Repository Istituzionale dei Prodotti della Ricerca del Politecnico di Bari

The role of surface treatments on fatigue design of aircraft components

This is a PhD Thesis

Original Citation:

Availability:
This version is available at http://hdl.handle.net/11589/251520 since: 2023-04-18

Published version
Politecnico di Bari
DOI:10.60576/poliba/iris/attolico-michele-angelo_phd2023

Terms of use:
Altro tipo di accesso

(Article begins on next page)

10 April 2024

Department of Mechanics, Mathematics and Management
MECHANICAL AND MANAGEMENT ENGINEERING
Ph.D. Program
SSD: ING-IND/14–MECHANICAL DESIGN AND MACHINE CONSTRUCTION

Final Dissertation

The role of surface treatments on fatigue design of aircraft components

by

Attolico Michele Angelo

Supervisors:

Prof.ssa Caterina Casavola

Prof. Vincenzo Moramarco

Coordinator of Ph.D. Program:
Prof. Giuseppe Pompeo Demelio

Course n°35, 01/11/2019-31/10/2022

Politecnico
di Bari

LIBERATORIA PER L'ARCHIVIAZIONE DELLA TESI DI DOTTORATO

Al Magnifico Rettore
del Politecnico di Bari

Il sottoscritto **MICHELE ANGELO ATTOLICO** nato a **BARI** il **11/04/1993**

residente a **BARI** in **TRAV. 126 VIA G. AMENDOLA 28** e-mail **micheleangelo.attolico@poliba.it**

iscritto al 3° anno di Corso di Dottorato di Ricerca in **INGEGNERIA MECCANICA E GESTIONALE** ciclo **XXXV**

ed essendo stato ammesso a sostenere l'esame finale con la prevista discussione della tesi dal titolo:

"THE ROLE OF SURFACE TREATMENTS ON FATIGUE DESIGN OF AIRCRAFT COMPONENTS"

DICHIARA

1) di essere consapevole che, ai sensi del D.P.R. n. 445 del 28.12.2000, le dichiarazioni mendaci, la falsità negli atti e l'uso di atti falsi sono puniti ai sensi del codice penale e delle Leggi speciali in materia, e che nel caso ricorressero dette ipotesi, decade fin dall'inizio e senza necessità di nessuna formalità dai benefici conseguenti al provvedimento emanato sulla base di tali dichiarazioni;
2) di essere iscritto al Corso di Dottorato di ricerca **INGEGNERIA MECCANICA E GESTIONALE** ciclo **XXXV**, corso attivato ai sensi del "*Regolamento dei Corsi di Dottorato di ricerca del Politecnico di Bari*", emanato con D.R. n.286 del 01.07.2013;
3) di essere pienamente a conoscenza delle disposizioni contenute nel predetto Regolamento in merito alla procedura di deposito, pubblicazione e autoarchiviazione della tesi di dottorato nell'Archivio Istituzionale ad accesso aperto alla letteratura scientifica;
4) di essere consapevole che attraverso l'autoarchiviazione delle tesi nell'Archivio Istituzionale ad accesso aperto alla letteratura scientifica del Politecnico di Bari (IRIS-POLIBA), l'Ateneo archivierà e renderà consultabile in rete (nel rispetto della Policy di Ateneo di cui al D.R. 642 del 13.11.2015) il testo completo della tesi di dottorato, fatta salva la possibilità di sottoscrizione di apposite licenze per le relative condizioni di utilizzo (di cui al sito http://www.creativecommons.it/Licenze), e fatte salve, altresì, le eventuali esigenze di "embargo", legate a strette considerazioni sulla tutelabilità e sfruttamento industriale/commerciale dei contenuti della tesi, da rappresentarsi mediante compilazione e sottoscrizione del modulo in calce (Richiesta di embargo);
5) che la tesi da depositare in IRIS-POLIBA, in formato digitale (PDF/A) sarà del tutto identica a quelle **consegnate**/inviate/da inviarsi ai componenti della commissione per l'esame finale e a qualsiasi altra copia depositata presso gli Uffici del Politecnico di Bari in forma cartacea o digitale, ovvero a quella da discutere in sede di esame finale, a quella da depositare, a cura dell'Ateneo, presso le Biblioteche Nazionali Centrali di Roma e Firenze e presso tutti gli Uffici competenti per legge al momento del deposito stesso, e che di conseguenza va esclusa qualsiasi responsabilità del Politecnico di Bari per quanto riguarda eventuali errori, imprecisioni o omissioni nei contenuti della tesi;
6) che il contenuto e l'organizzazione della tesi è opera originale realizzata dal sottoscritto e non compromette in alcun modo i diritti di terzi, ivi compresi quelli relativi alla sicurezza dei dati personali; che pertanto il Politecnico di Bari ed i suoi funzionari sono in ogni caso esenti da responsabilità di qualsivoglia natura: civile, amministrativa e penale e saranno dal sottoscritto tenuti indenni da qualsiasi richiesta o rivendicazione da parte di terzi;
7) che il contenuto della tesi non infrange in alcun modo il diritto d'Autore né gli obblighi connessi alla salvaguardia di diritti morali od economici di altri autori o di altri aventi diritto, sia per testi, immagini, foto, tabelle, o altre parti di cui la tesi è composta.

Luogo e data **BARI, 18/04/2023** Firma ____________________________

Il sottoscritto, con l'autoarchiviazione della propria tesi di dottorato nell'Archivio Istituzionale ad accesso aperto del Politecnico di Bari (POLIBA-IRIS), pur mantenendo su di essa tutti i diritti d'autore, morali ed economici, ai sensi della normativa vigente (Legge 633/1941 e ss.mm.ii.),

CONCEDE

- al Politecnico di Bari il permesso di trasferire l'opera su qualsiasi supporto e di convertirla in qualsiasi formato al fine di una corretta conservazione nel tempo. Il Politecnico di Bari garantisce che non verrà effettuata alcuna modifica al contenuto e alla struttura dell'opera.
- al Politecnico di Bari la possibilità di riprodurre l'opera in più di una copia per fini di sicurezza, back-up e conservazione.

Luogo e data **BARI, 18/04/2023** Firma ____________________________

Politecnico
di Bari

RICHIESTA DI EMBARGO

Sottoscrivere solo nel caso in cui si intenda auto-archiviare la tesi di dottorato nell'Archivio Istituzionale ad accesso aperto alla letteratura scientifica POLIBA-IRIS (https://iris.poliba.it)) non in modalità "Accesso Aperto", per motivi di segretezza e/o di proprietà dei risultati e/o informazioni sensibili o sussistano motivi di segretezza e/o di proprietà dei risultati e informazioni di Enti esterni o Aziende private che hanno partecipato alla realizzazione della ricerca.

Il/la sottoscritto/a____nato/a____

il____________ residente____________________ alla via________________ indirizzo e-mail________________________

________________ iscritto/a al corso di dottorato di ricerca____ ciclo_____

Autore della tesi di dottorato dal titolo____

e ammesso a sostenere l'esame finale:

NON AUTORIZZA

Il Politecnico di Bari a pubblicare nell'Archivio Istituzionale di Ateneo ad accesso aperto il testo completo della tesi depositata per un periodo comunque non superiore a 12 (dodici) mesi decorrenti dalla data di esame finale.

Specificare la motivazione *(apporre una crocetta sulla motivazione):*

☐ Brevetto
(*indicare nel campo libero la data della domanda di deposito*)____

☐ Segreto industriale, se è stato firmato un accordo di non divulgazione.
*(indicare nel campo libero gli estremi dell'accordo)*____

☐ Segreto d'ufficio a tutela di progetti ____

☐ Motivi di priorità nella ricerca (previo accordo con terze parti) ____

☐ Motivi editoriali ____

☐ Altro (*specificare*) ____

Saranno comunque consultabili ad accesso aperto i dati bibliografici e l'abstract.

Il sottoscritto dottorando dichiara in virtù di quanto sopra che si rende opportuno procrastinare la pubblicazione della tesi attraverso l'Archivio Istituzionale ad accesso aperto (POLIBA -IRIS) e di impostare la data di embargo, in fase di deposito della tesi di dottorato in formato elettronico (pdf/A) per un periodo *di embargo* non superiore a 12 (dodici) mesi decorrenti dalla data di esame finale.

Il sottoscritto dottorando dichiara di essere a conoscenza che a scadenza della data di embargo su riportata, la tesi verrà pubblicata attraverso l'Archivio Istituzionale ad accesso aperto alla letteratura scientifica del Politecnico di Bari.

Luogo e data ___________________________ Firma Dottorando _________________________________

Firma Relatore ___________________________________

Department of Mechanics, Mathematics and Management
MECHANICAL AND MANAGEMENT ENGINEERING
Ph.D. Program
SSD: ING-IND/14–MECHANICAL DESIGN AND MACHINE CONSTRUCTION

Final Dissertation

The role of surface treatments on fatigue design of aircraft components

---

by

Attolico Michele Angelo

Supervisors:

Prof.ssa Caterina Casavola

Prof. Vincenzo Moramarco

Coordinator of Ph.D. Program:
Prof. Giuseppe Pompeo Demelio

Course n°35, 01/11/2019-31/10/2022

Table of Content

Table of Content 1
List of Figures 4
List of Tables 9
INTRODUCTION 10
I. Motivation 10
II. Aims and Objective of Research 12
III. Structure of the thesis 13
IV. List of conferences 15
V. List of scientific publications 15
CHAPTER 1 16
SURFACE TREATMENTS FOR AIRCRAFT ALUMINUM ALLOYS 16
1.1. Preface 16
1.2. Aluminum Alloys 16
1.3. Overview of surface treatments 18
1.4. Laser Shock Peening (LSP) process 20
1.4.1. Historical background 20
1.4.2. Technological aspects of the LSP process 21
1.4.3. Laser Shock Peening parameters 23
1.4.4. Application of the Laser Shock Peening process 27
1.5. Shot Peening (SP) process 28
1.5.1. Applications of Shot Peening process 30
1.6. Comparison between Laser Shock Peening and Shot Peening 31
1.7. Corrosion protection systems 32
1.7.1. Anodizing 34
1.7.2. Anodic layer requirements for aerospace applications 35
1.7.3. Alternatives to the chromic acid anodizing (CAA) process 37
1.7.4. Tartaric-sulfuric acid (TSA) anodizing 37
1.7.5. Process Steps of Tartaric-sulfuric acid anodizing process 38
CHAPTER 2 40
RESIDUAL STRESS-BASED APPROACH FOR FATIGUE DESIGN 40
Preface 40
2.1. Theoretical framework of Fatigue and Fracture Mechanics 40
2.1.1. Definition of fatigue parameters 40
2.1.2. Physical interpretation of fatigue damage 42
2.1.3. Fatigue data analysis 43

2.2. Fatigue of notched components 46
2.3. Basics of linear elastic fracture mechanics 48
2.4. Overview of residual stresses 52
  2.4.1. Effects of residual stress field on fatigue 52
  2.4.2. Characteristics of residual stress profiles 54
2.5. Methods of experimental evaluation of residual stresses 55
2.6. Hole Drilling Method 58
  2.6.1. Hole Drilling Procedure 59
  2.6.2. Computation of the stresses during Hole Drilling 60
2.7. Residual stress determination using X-Ray Diffraction 62
  2.7.1. Basic Principles 62
  2.7.2. Measurement of lattice strain and stress computation 63
2.8. Application of Hole Drilling Method and X-Ray Diffraction technique for LSP residual stress evaluation 66

CHAPTER 3 70

EFFECTS OF LASER SHOCK PEENING ON SURFACE INTEGRITY AND RESIDUAL STRESS OF AA 7050-T7451 70

3.1. Preface 70
3.2. Introduction 71
3.3. Experimental activity 76
  3.3.1. Definition of material and sample geometry 76
  3.3.2. Surface roughness evaluation methods 79
  3.3.3. Residual stress field evaluation methods 81
3.4. Results and discussions 83
  3.4.1. Surface Roughness results 83
  3.4.2. Surface roughness discussion 89
  3.4.3. Residual stress results 90
  3.4.4. Residual stress discussion 98
3.5. Summary 101

CHAPTER 4 102

COUPLED EFFECT OF TARTARIC-SULFURIC ACID ANODIZING AND LASER SHOCK PEENING ON FOUR-POINT BENDING FATIGUE BEHAVIOR OF AL 7050-T7451 SAMPLES 102

4.1. Preface 102
4.2. Introduction 103
4.3. Experimental Activity 106
  4.3.1. Definition of material and sample geometry 106
  4.3.2. Tartaric-Sulfuric Acid Anodizing treatment 107
  4.3.3. Shot Peening and Laser Shock Peening Processes 108

4.3.4. **Microstructure and residual stress evaluation methods** 109
4.3.5. **Four-point bending fatigue tests** 111
4.4. **Results and discussions** 114
4.4.1. **Base material characterization** 114
4.4.2. **Morphology of the TSA anodic layer** 117
4.4.3. **Residual stress and microhardness analyses** 120
4.4.4. **Four-point bending fatigue tests results** 124
4.4.5. **Analyses of fatigue fracture surfaces by SEM** 128
4.5. **Summary** 134
CHAPTER 5 .... **136**
EVALUATION OF FATIGUE BEHAVIOR OF SINGLE EDGE NOTCHED COMPONENTS SUBJECTED TO LASER SHOCK PEENING PROCESS **136**
5.1. **Preface** 136
5.2. **Introduction** 137
5.3. **Experimental activity** 141
5.3.1. **Definition of material and sample geometry** 141
5.3.2. **Evaluation methods of stress concentration factor** 143
5.3.3. **Classification of components for fatigue testing** 145
5.3.4. **Residual stress evaluation methods and fatigue testing** 148
5.4. **Results** 149
5.4.1. **Stress concentration factor** 149
5.4.2. **Residual stress results** 153
5.4.3. **Results of fatigue test on single edge notched components** 157
5.4.4. **Analisys of fatigue fracture surfaces** 160
5.5. **Summary** 166
CONCLUSIONS **167**
I. **Summary** 167
II. **Future Research** 170
REFERENCES **172**

List of Figures

Figure 1-1: Classification of surface treatments according to the nature of underlying physical principle [11]. 19
Figure 1-2: Development of residual stresses due to localized plastic deformation following shock waves propagation. 22
Figure 1-3: Schematic of Laser Shock Peening (LSP) process in confined ablation mode configuration. 22
Figure 1-4: Onset of the dielectric breakdown phenomenon at different wavelengths in the aluminum alloy's laser shock peening treatment [31]. 24
Figure 1-5: Typical relationship between spot radius, laser intensity and focal length in LSP process [13]. 25
Figure 1-6: Influence of pulse repetition number on the intensity and penetration depth of the LSP-induced residual stress field [31]. 26
Figure 1-7: Schematic of Shot Peening process. 28
Figure 1-8: Typical shot peening parameters and their levels. 29
Figure 1-9: General trend of residual stresses generated by shot peening and laser shock peening [31]. 31
Figure 1-10: Schematic structure of a typical corrosion protection system for aircraft applications [79]. 33
Figure 1-11: Mobile species involved in the anodization process in sulfuric acid solution and explanation of ions migration [79]. 34
Figure 1-12: Contradictory requirements of oxide layers produced by anodizing process as a pre-treatment for painting. 36
Figure 1-13: Schematic representation of the process steps and the modifications that take place during the pre-treatments to anodizing [98]. 38
Figure 2-1: Constant amplitude cycling and the associate nomenclature: a) completely reversed stressing, b) non-zero mean stress, c) zero-to-tension stressing. 42
Figure 2-2: The fatigue stages and the parameters used to describe them [109]. 43
Figure 2-3: Rotating bending S-N curve for unnotched specimens of a steel with a distinct fatigue limit [110]. 44
Figure 2-4: Statistical methods to derive S-N curves of materials: a) Linear regression analysis; b) Normal distribution analysis [109]. 45
Figure 2-5: Stress concentration factor as a function of characteristic dimensions and applied loads [116]. 47
Figure 2-6: Comparison of S-N curves of an unnotched and a notched component [117]. 48
Figure 2-7: The basic modes of crack opening: opening mode, sliding mode and tearing mode. 49
Figure 2-8: Fatigue crack growth rates over a wide range of stress intensities for a ductile pressure vessel steel [121]. 51
Figure 2-9: Typical residual stress profile induced by Laser Shock Peening process. 54
Figure 2-10: Influence of geometry of the development of in-depth residual stress field. 55
Figure 2-11: Measurement penetration and spatial resolution of different residual stress measurement techniques [134]. 57
Figure 2-12: Application of a strain gauge rosette on the surface of the component and example of deformation caused by the presence of residual tensile stresses following the application of the Hole Drilling method [140]. 58
Figure 2-13: Three types of strain gauge rosettes proposed by ASTM E837 standard for Hole Drilling Method [98]. 59
Figure 2-14: Stepwise pattern of internal stresses in the definition of the integral method [98]. 61
Figure 2-15: Shift of the diffraction peak due to the application of external stress or the presence of a residual stress field [147]. 63
Figure 2-16: Definition of the coordinate systems of the sample and of the diffraction head [147]. 64
Figure 2-17: Hardness (a) and residual stress (b) profiles following nano and femto-second Laser Shock

Peening processes on 7050 AA [149]. 67
Figure 2-18: Distribution of residual stresses with different spot sizes: a) surface residual stresses along a line through the LSP treated region; b) in-depth residual stress profile measured in the centre of the treated region [150]. 67
Figure 2-19: Comparison of residual stress profiles measured by different evaluation methods on plates of different thicknesses: a) 6 mm thick plate; b) 1.6 mm thick plate [152]. 68
Figure 2-20: Influence of number of sequences and laser scanning direction on the development of the residual stress field: a) single sequence, horizontal scanning direction; b) single sequence, vertical scanning direction; c) double sequence, horizontal and vertical scanning directions; d) double sequence, vertical and horizontal scanning directions [153]. 69
Figure 3-1: Difference in longitudinal (S1) and transverse (S2) strain components following LSP process on 6xxx aluminum alloy. Strain profiles obtained by European Synchrotron Radiation Facility (ESRF) [172]. 72
Figure 3-2: Effect of overlap rate on surface roughness [174]. 73
Figure 3-3: Schematic of dimples formed in LSP process at different values of overlap rate: a) 0% overlap; b) 50% overlap [174]. 73
Figure 3-4: In-depth residual stress profiles induced by LSP (a) and SP (b) processes on AA 7050-T7451 [177]. 74
Figure 3-5: In-depth residual stress profiles at different values of number of layers [17]. 74
Figure 3-6: Distribution of residual stress on the surface and hole wall under different peak pressures [18]. 74
Figure 3-7: Geometry of the test specimens. All dimensions in mm. 77
Figure 3-8: Appearance of the laser peened areas of two specimens for roughness and residual stress measurements (30 mm thick) treated with different combinations of process parameters: on the left, higher pulse energy and smaller spot size; on the right, lower energy and larger spot size. 78
Figure 3-9: Schematic representation of peening strategy: definition of the main directions of peening and of overlap and offset parameters. 79
Figure 3-10: Measurement setup for surface roughness evaluation. 80
Figure 3-11: Definition of principal residual stress measurement directions. 81
Figure 3-12: Hole Drilling Method setup. 83
Figure 3-13: Roughness average (R_a) values along scanning and stepping directions at different level of nominal power densities (thickness 30 mm). 85
Figure 3-14: Roughness total height (R_t) values along scanning and stepping directions at different level of nominal power densities (thickness 30 mm). 85
Figure 3-15: Roughness average (R_a) values along scanning and stepping directions at different level of nominal power densities (thickness 10 mm). 86
Figure 3-16: Roughness total height (R_t) values along scanning and stepping directions at different level of nominal power densities (thickness 10 mm). 86
Figure 3-17: Mean response values at each level of the design parameters. 87
Figure 3-18: Contour plot of R_a and R_t versus thickness and NPD. 87
Figure 3-19: Effects of number of layers on roughness properties of LSPed specimens. 89
Figure 3-20: Effects of NPD, thickness and peening direction on surface residual stress values of LSPed specimens. 91
Figure 3-21: Effects of number of layers on surface residual stress values of LSP specimens. 93
Figure 3-22: In-depth residual stress profiles along scanning and stepping directions at 3.5 GW/cm^2 NPD level by XRD measurement method (specimen 05). 94
Figure 3-23: In-depth residual stress profiles along scanning and stepping directions at 4.5 GW/cm^2 NPD level by XRD measurement method (specimen 08). 95
Figure 3-24: Comparison between the RS profiles measured by XRD and HDM up to 0.7 mm for 3,5 GW/cm^2 specimens. 97
Figure 3-25: Comparison between the RS profiles measured by XRD and HDM up to 0.7 mm for 4,5 GW/cm^2 specimens. 97
Figure 3-26: Residual stress profiles obtained by HDM along scanning and stepping directions in the case of 12 layers (specimen 22). Surface point by XRD. 98
Figure 3-27: Residual stress profiles obtained by HDM along scanning and stepping directions in the

case of 20 layers (specimen 25). Surface point by XRD. ... 98
Figure 4-1: a) Shape and dimensions of fatigue specimens according to the EN 6072:2016 standard. All dimensions are in meters; b) Definition of section plane directions. ... 107
Figure 4-2: Identification of the shot and laser shock peened areas on four-point bending fatigue specimens. ... 108
Figure 4-3: Location of surface residual stress measurement points on the tensile surface of fatigue test specimens. ... 110
Figure 4-4: a) Schematic representation of the four-point bending setup; b) position of support and loading rollers on the surfaces of the specimens. ... 112
Figure 4-5: Schematic representation of the dimensions and positioning of the four-point bending testing fixture according to BS EN 6072:2010. ... 113
Figure 4-6: Experimental setup of four-point bending fatigue tests. ... 114
Figure 4-7: Microstructure of base material (As M.): a) optical, b) SEM micrographs of AA 7050-T7451 which depict the aligned stringers of intermetallic precipitates in the alloy matrix due to the forming steps aluminum plates are subjected to, and c) SEM image of large and spherical Al2CuMg particles and rod-shaped Al7Cu2Fe particles. ... 115
Figure 4-8: Appearance of the surface of AA7050 T7451 specimens: a) longitudinal section (LT-L plane) and b) cross-section (ST-LT plane) of As M. specimen. While: c) microstructure on the longitudinal section (LT-L plane) and d) microstructure on the cross-section (ST-LT plane) of As M.+TSA specimen; as expected, the grain structure is elongated with a typical flat pancake-shaped structure, especially in the rolling direction. ... 116
Figure 4-9: Top view (a-f) SEM images (L-LT plane) of the untreated as-machined specimen (a-b) and anodized specimen (c-d) at different magnifications: e) high magnification detail of a defect present on the surface of As M. specimen; f) high magnification detail of a cluster of micro voids on the surface of As M.+TSA specimen. ... 118
Figure 4-10: SEM micrograph of the cross-section (LT-ST) of the anodic film formed in TSA bath. ... 118
Figure 4-11: Top view (a-f) SEM images (L-LT plane) of the As M.+SP+TSA (a-b) and As M.+LSP+TSA specimen (c-d) at different magnifications: e) high magnification detail of a defect present on the surface of As M. specimen; f) high magnification detail of a cluster of micro voids on the surface of As M.+TSA specimen. ... 119
Figure 4-12: SEM cross-sectional views of As M.+SP+TSA and As M.+LSP+TSA specimens at different magnifications. ... 120
Figure 4-13: Residual stress values at three different positions on the surface of As M., As M.+TSA, As M.+SP+TSA and As M.+LSP+TSA specimens along the longitudinal direction. ... 122
Figure 4-14: Residual stress values at three different positions on the surface of As M., As M.+TSA, As M.+SP+TSA and As M.+LSP+TSA specimens along the transverse direction. ... 122
Figure 4-15: In-depth residual stress profile at the midpoint of the tensile surface of As M.+LSP+TSA specimen. ... 123
Figure 4-16: Microhardness profile of As M., As M.+SP+TSA and As M.+LSP+TSA samples. ... 124
Figure 4-17: S-N curves of As M., As M.+TSA, As M.+SP+TSA and As M.+LSP+TSA specimens obtained by 4-parameters Weibull interpolation function. ... 126
Figure 4-18: SEM images of the As M. and As M.+TSA fatigue specimens in HCF regimes: a and c) representative macrographs of an overall view of the fracture surface of As M.+TSA-03 and As M.-08 specimens after fatigue tests, respectively; b and d) SEM enlarged images of the spot fringe at 50X where the tear ridges that run across the entire crack propagation area can be observed. ... 129
Figure 4-19: SEM images of the As M. and As M.+TSA fatigue specimens in LCF regimes: a and c) representative macrographs of an overall view of the fracture surface of As M.-04 and As M.+TSA-01 specimens after fatigue tests, respectively; b and d) SEM enlarged images of the spot fringe at 50X where the tear ridges that run across the entire crack propagation area can be observed. ... 130
Figure 4-20: SEM analysis of the fracture surface of the treated sample: a) cross-section of fracture surface in the region of the crack initiation due to defects: crack initiation occurs at the surface. Moreover, fracture surface exhibits cleavage-like fracture. b) crack initiation sites occurred on the surface, c) longitudinal section of fracture surface showing defects with angular morphology that act as stress concentrations points, resulting in areas with micro-crack formation and d) magnification of the

fracture surface showing the presence of the voids at the vertices of which the micro-cracks occur. 132
Figure 4-21: SEM analysis of the fracture surface of the treated sample: a) magnification of fracture surface of region of stable crack growth and b) fracture surface contains regions with lots of striations. Striation's width is about 1.13 µm. 132
Figure 4-22: SEM images of the As M.+SP+TSA and As M.+LSP+TSA fatigue specimens in HCF regimes: a and d) representative macrographs of an overall view of the fracture surface of As M.+SP+TSA-05 and As M.+LSP+TSA-04 specimens after fatigue tests, respectively; b-c and e-f) SEM enlarged images of the spot fringe where the tear ridges that run across the entire crack propagation area can be observed. 133
Figure 5-1: Influence of radius of curvature on the residual stress field induced by LSP process on convex and concave geometry: a) Ti-6Al-4V, b) AA 2024-T3 [226]. 137
Figure 5-2: Comparison between simulated and measured tri-directional residual stress distributions on convex and concave geometry: a-b-c) convex geometry; d-e-f) concave geometry; a-d) axial direction; b-e) radial direction; c-f) depth [227]. 138
Figure 5-3: a) Cross section of the hole region and identification of measurement surfaces by contour method; b) stress maps obtained by contour method using different LSP patterns [228]. 139
Figure 5-4: Residual stress maps in different cross sections of a notched component subjected to laser peening obtained by FEM based on eigenstrain theory [231]. 140
Figure 5-5: Geometric properties of single edge notch fatigue specimen. 142
Figure 5-6: Schematic definition of the two different loading configurations: a) full-clamped configuration and b) Pin-Load configurations. 143
Figure 5-7: Details of the employed tetrahedral mesh on single edge notched component. 144
Figure 5-8: Location of strain gauge for the experimental evaluation of the stress concentration factor at the notch. 144
Figure 5-9: Setup for digital image correlation measurement: a) Overall view of the measurement system; b) detail of the black dotted pattern on the surface of the single edge notched component. .. 145
Figure 5-10: Single edge notched components for fatigue testing: a) overall view of each type of component; b) magnified view of the shot peened region of As M.+SP+TSA components; c) magnified view of the shot peened region of As M.+LSP+TSA components. 147
Figure 5-11: Definition of the two measurement grids on the front surface and on the lateral surface of single edge notched components for residual stress evaluation. 148
Figure 5-12: Normal stress maps (Y-direction) of single-edge notched components under pin load (a) and full clamped (b) load configurations. 150
Figure 5-13: Maximum normal stress at the notch as a function of nominal stress in single-edge notched components under pin load and full clamped load configurations. 150
Figure 5-14: Unexpected failures of single edge notched components: a) fatigue crack starting from the transition zone between flat section and clamping region; b) fatigue crack nucleating at the most stressed part of the loading hole. 151
Figure 5-15: Stress concentration factor at the notch obtained by applying an HBM strain gauge in the inner surface of the notch. 153
Figure 5-16: a) Displacement map obtained by Digital Image Correlation technique applied on the front surface of the component; b) Displacement map obtained by numerical simulation. 153
Figure 5-17: Residual stress maps on the front surfaces of single-edge notched components; a) As M.; b) As M.+TSA; c) As M.+SP+TSA and d) As M.+LSP+TSA. 154
Figure 5-18: Average values of residual stresses as a function of the distance from the notch tip. ... 154
Figure 5-19: Residual stress maps in the inner surface of the notch of a) As M. and b) As M.+TSA components. 156
Figure 5-20: Residual stress maps in the inner surface of the notch of a) As M.+SP+TSA and b) As M.+LSP+TSA components. 156
Figure 5-21: S-N fatigue curves of single edge notched components under constant amplitude uniaxial cyclic loading. 159
Figure 5-22: Typical failure mode of a single edge notched component subjected to uniaxial fatigue test. 161
Figure 5-23: Fracture surface of As M. component at different magnifications: a) overall view of the fracture surface; b) location of the crack nucleation site; c) microstructural feature inducing crack

nucleation. 162
Figure 5-24: Fracture surface of As M.+TSA component at different magnifications: a) overall view of the fracture surface; b) location of the crack nucleation site; c) semicircular-shaped defect inducing fatigue crack nucleation.. 163
Figure 5-25: Fracture surface of As M.+SP+TSA component at different magnifications: a) overall view of the fracture surface; b-c) location of the crack nucleation site; d) magnification of the boundary region between two indentation footprints. 163
Figure 5-26: Fracture surface of As M.+LSP+TSA component at different magnifications: a) overall view of the fracture surface; b) location of the crack nucleation site; d) magnification of the boundary region between two indentation footprints. 164

List of Tables

Table 1-1: Strength ranges of various wrought aluminum alloys [2]. 17
Table 1-2: Comparison of roughness parameters following the application of shot peening and laser shock peening processes on steel and aircraft aluminum alloy specimens [31]. 32
Table 2-1: Definition of all the possible parameters used to define fatigue load cycle. 41
Table 3-1: Chemical composition of AA 7050-T7451 [2]. 76
Table 3-2: Mechanical properties of AA 7050-T7451 [2]. 76
Table 3-3: Laser parameters employed for the surface treatment of the AA 7050-T7451 specimens. 77
Table 3-4: Definition of process parameters identifying each group of specimens. 78
Table 3-5: XRD measurement parameters. 82
Table 3-6: Identification codes and technological properties of specimens for surface roughness and residual stress evaluation. 83
Table 3-7: Factorial plane for surface roughness evaluation: analysis of power density, thickness and peening strategy influence. 84
Table 3-8: Identification codes and technological properties of specimens for the evaluation of the effects of variation in the number of layers. 88
Table 3-9: Factorial plane for surface roughness evaluation: analysis of the influence of the number of layers. 88
Table 3-10: Summary of surface residual stress measurements: analysis of NPD, thickness and peening strategy influence. 91
Table 3-11: Summary of surface residual stress measurements: analysis of the number of layers influence. 92
Table 3-12: In-depth RS measurements by XRD on specimens 05 (a) and 08 (b). 96
Table 4-1: Chemical composition of 7050-T7451 aluminum alloy in wt.% 106
Table 4-2: Mechanical properties of 7050-T7451 aluminum alloy. 106
Table 4-3: X-Ray Diffraction measurement parameters. 110
Table 4-4: Parameters for the calculation of maximum tensile stress. 113
Table 4-5: Fatigue test data: a) As M. specimens, b) As M.+TSA specimens, c) As M.+SP+TSA specimens, d) As M.+LSP+TSA specimens. 125
Table 4-6: Estimated values of Weibull parameters using non-linear regression analysis based on the least square method. 126
Table 5-1: Chemical composition of 7050-T7451 aluminum alloy in wt.% 141
Table 5-2: Mechanical properties of 7050-T7451 aluminum alloy. 141
Table 5-3: Classification of components for fatigue testing according to the surface treatments they were subjected. 146
Table 5-4: X-Ray diffraction process parameters 149
Table 5-5: Values assumed by residual stresses at the measurement grid points located on the inner surface of the notch. 156
Table 5-6: Number of cycles to failure and maximum net stress level for each component: a) As M. components; b) As M.+TSA components; c) As M.+SP+TSA components; d) As M.+LSP+TSA components 158
Table 5-7: Estimated values of Weibull parameters using non-linear regression analysis based on the least square method. 158

INTRODUCTION

I. Motivation

The aviation industry is constantly looking for design solutions to cost-effectively address the long-standing problem of fatigue and fatigue-related damage. The design philosophy based on the damage-tolerant approach is nowadays the main design criterion for critical aircraft structures and provides significant benefits in terms of weight savings, increased reliability and structural integrity in the presence of damage occurring during manufacturing processes or service. Despite advances in the development of new aluminum alloys with increased mechanical properties and the availability of modern methods for predicting the fatigue behavior of aircraft frames, further increasing the fatigue crack resistance of metal components could offer the possibility of developing more economical and environmentally sustainable structures in accordance with the most recent and restrictive regulations imposed by airworthiness authorities. Within this context, over the past decade, the concept of residual stress-based engineering has emerged as an interesting field of research in both academia and industry to achieve improved fatigue and damage tolerance capabilities in fatigue-critical metal structures. Compressive residual stress fields induced by specific surface treatments can be appropriately designed and applied at particularly critical hot spots to delay fatigue crack nucleation and propagation by increasing the durability of the component and its ability to withstand cyclic stresses. Some surface technologies that are based on the residual stress principle are already solidly established in the aerospace industrial landscape: cold expansion (CX) technology has been widely used since the 1970s by aircraft manufacturers to increase the fatigue life of fastener holes, or the Shot Peening (SP) technique used for several industrial applications such as the treatment of the root section of a gear tooth profile that is critically stressed with intense bending loads, or for the treatment of shafts, compression springs, and turbine blades. Each surface treatment technology is suitable for a limited range of applications defined by the ability of the technique to adapt to specific geometric features (notches, fillets, holes), the characteristics of the induced residual stress field (intensity, depth of penetration, volumetric distribution) or the possibility of being integrated within a production context or being used for maintenance, repair and overhaul (MRO) activities. In recent years, research supported by large industrial aircraft manufacturers has led to the identification of a new and promising technology for fatigue and damage tolerance enhancement of structural critical components: the Laser Shock Peening (LSP) process. In the LSP process, a metal component is subjected to short-duration laser pulses generating a confined plasma on the surface of the part. The controlled expansion of the plasma leads to the formation of a very high-pressure pulse that, when properly driven into the thickness of the component, results in local plastic deformation of the surface and sub-surface region and the subsequent generation of compressive residual stresses. The potential of LSP technology lies in its ability to provide much greater penetration depths of residual stress field along with peak intensities generally comparable to or greater than conventional peening techniques. In addition, the LSP process is an attractive process concerning accessibility in the internal structures of airframes: fatigue critical points are often located in positions that are difficult to inspect, so the use of an optical system that does not involve contact with the treated part can be an advantage in the development of transportable systems for in situ application of LSP treatment. Although the advantages of this technology have been widely documented in the scientific literature, some research issues have not been adequately explored and require further investigation.

Firstly, only limited application of LSP technology can be found on one of the most industrially interesting aircraft aluminum alloys, AA 7050-T7451, which is largely employed for its excellent specific mechanical properties and high resistance to stress corrosion cracking and exfoliation. Most scientific studies focus on the investigation of a single combination of process parameters and do not provide comparative analyses between different process strategies. For the LSP process to be effectively applied, it is necessary to know in detail the effect of the main process parameters on the induced residual stress field to calibrate the process and accurately meet the design requirements. In addition, it is necessary to assess the impact of the process on the surface integrity of the part since LSP involves severe surface plastic deformation causing a change in roughness parameters. Another aspect almost completely unexplored in the scientific literature is the simultaneous application of the LSP process and anodizing treatment. The operating service conditions of aircraft components can be particularly severe due to the presence of high thermal gradients and chemical agents that promote corrosion. High-strength aluminum alloys are particularly susceptible to this phenomenon and therefore require the use of specific protection methods, such as anodizing, which allow corrosion resistance to be increased by electro-chemical processes that act at the surface level by increasing the thickness of the anodic layer normally present on the material. However, anodizing processes reduce the component’s fatigue life due to the increased hardness of the anodic layer compared to the substrate and the presence of microstructural defects that act as preferential sites of fatigue crack nucleation. Some studies have attempted to demonstrate the ability of the SP process to compensate for the reduction in fatigue life caused by the presence of the anodic layer when used as a pre-treatment to anodizing. However, very few attempts have been made in verifying whether the LSP process is equally capable of providing the desired increase in fatigue life of an anodized component.

The third aspect concerns the possibility of employing the LSP process on components with special geometric features, such as notches, fillets, or sharp edges, that may be difficult to be peened. The presence of such geometric discontinuities is typical of real components and usually originates from manufacturing constraints. The residual stress field in the vicinity of a geometric discontinuity may be affected by the lack of elastic material conveying stress development, and as a result, a reduction in the intensity of residual compressive stresses can be observed, limiting the effectiveness of the treatment. It is, therefore, necessary to carefully analyze the residual stress state at these features to verify the compatibility of the selected LSP process with the geometry of the treated component, identifying regions where unexpected reductions in stress intensity occur and trying to propose operational solutions that can limit their influence.

II. Aims and Objective of Research

Based on the reasons stated above, this research activity aims to evaluate the ability of the LSP process to improve the fatigue performance of 7050-T7451 aircraft aluminum alloy components subjected to the anodizing process. Specifically, the objectives of the thesis can be summarized as follows:

- Identification of the combination of LSP process parameters that provide an optimum trade-off between induced residual stress field properties and the least impact on component surface integrity. According to the findings of the reviewed technical and scientific literature, several different sets of process parameters will be considered, with a particular focus on the individual role and the interrelation between nominal power density, number of layers, specimen thickness and peening strategy.
- Application of the identified LSP process on smooth components (K_t=1) for the evaluation of material fatigue properties. The LSP process will be applied in conjunction with a sulfuric tartaric acid anodizing treatment to verify the ability of the laser peening process to compensate for the reduction in fatigue life caused by the presence of the anodic layer. The results will be compared with the fatigue behavior of the same material under the same anodizing conditions but subjected to a shot peening

process to provide a direct correlation between the two main surface treatments investigated.

- Evaluation of fatigue behavior of a notched component representative of a real aircraft part. First, the geometry and loading configuration that allow a stress concentration factor at the notch comparable to that of the real component will be identified. Then the residual stress fields induced by the LSP process near the notch will be analyzed to verify the possible influence of the geometric discontinuity on the residual stress distribution. Finally, the fatigue properties of the component will be assessed by performing constant amplitude uniaxial fatigue tests to estimate the fatigue life increase factor guaranteed by the identified LSP process. Again, the LSP process will be combined with the tartaric-sulfuric acid anodizing process, and a comparison with the results of fatigue tests performed on identical components subjected to shot peening will be presented.

III. Structure of the thesis

This thesis work is organized into 7 chapters.

INTRODUCTION explains the motivation behind the research activity, describes its main objectives and activities and defines the structure of the thesis.

Chapter 1 presents an overview of the main surface treatments applied to aluminum alloys of aircraft interest. In particular, a broad focus will be devoted to the technological processes of Laser Shock Peening, Shot Peening and Tartaric-Sulfuric Acid Anodizing to highlight their basic physical principles, technological characteristics and process parameters, advantages and disadvantages, and main fields of application. The description of the processes will be based on a careful and detailed review of the relevant scientific literature.

Chapter 2 recalls the main concepts related to the phenomenon of fatigue in metallic materials and explores the role of residual stresses in defining the fatigue behavior of a component. The main experimental methods commonly employed for the evaluation of the fatigue behavior of material will then be identified and discussed. Finally, an in-depth look at experimental techniques for measuring residual stresses will be proposed with a special focus on X-ray diffraction and hole drilling methods, which will be extensively used in the continuation of the research activity.

Chapter 3 presents experimental results of residual stress measurement and surface integrity evaluation on 7050-T7451 aluminum alloy components subjected to the LSP process at different combinations of process parameters. Two different factorial planes will be defined to evaluate the single and combined effects of the factors of nominal power density, component thickness, deposition strategy, and the number of laser passes on the characteristics of residual stress profiles and the main material roughness parameters. Based on the results obtained, an optimized LSP process will be identified for the treatment of structural components, which will be described in subsequent chapters.

Chapter 4 concerns the evaluation of fatigue properties of smooth unnotched components subjected in series to the LSP process and tartaric-sulfuric acid anodizing. The objective of the analysis is to verify the ability of the LSP process to compensate for the reduction in fatigue life caused by the presence of the anodic layer on the surface of the component. The fatigue behavior of an untreated and a simply anodized material will initially be compared to quantify the reduction in fatigue life caused by the anodizing process alone. Then, the effects of shot peening and laser shock peening processes in combination with the anodizing process will be evaluated to compare their effectiveness and provide useful operational guidance for improving the LSP process.

Chapter 5 focuses its attention on the application of the LSP process on notched components (K_t>1). Specifically, a representative geometry of a real component for aircraft applications will be defined and a laser pattern will be applied at the geometric discontinuity to evaluate the ability of the LSP process to provide local reinforcement in the most stressed area of the component. Before the evaluation of fatigue behavior, a detailed analysis of the residual surface stress state induced by the LSP process in the vicinity of the geometric discontinuity will be performed to identify any reduction in fatigue life determined by incompatibility between the process specifications and the geometric characteristics of the component.

CONCLUSIONS presents a summary of the research activity and the main conclusions. A perspective on future research activity will also be provided.

IV. List of conferences

- Date: September 1-3, 2021, Title: “Numerical modelling and experimental evaluation of crack growth rate in components obtained by Selective Laser Melting” at the 50th national conference of the “Società Scientifica Italiana di Progettazione Meccanica e Costruzione di Macchine (AIAS), online (speaker).
- Date: March 27-30, 2022, Title: “Fatigue performance enhancement of laser peened aircraft components” at the 11th International Conference on Residual Stresses (ICRS11), Nancy, France (speaker).
- Date: September 4-7, 2022, Title: “Effects of Laser Shock Peening-induced residual stresses on fatigue life of anodized AA 7050-T7451 components” at the 14th International Conference on Shot Peening (ICSP14), Milan, Italy (speaker).
- Date: September 7-10, 2022, Title: “Analisi del comportamento a fatica di componenti in lega di alluminio aeronautica sottoposti a trattamenti di anodizzazione in soluzione tarta-solforica e pallinatura laser” at the 51th national conference of the “Società Scientifica Italiana di Progettazione Meccanica e Costruzione di Macchine (AIAS), Padova, Italy (speaker).

V. List of scientific publications

- J.M. Mercado-Colmenero, C. Martin-Doñate, V. Moramarco, **M.A. Attolico**, G. Renna, M. Rodriguez-Santiago, C. Casavola, Mechanical characterization of the plastic material GF-PA6 manufactured using FDM technology for a compression uniaxial stress field via an experimental and numerical analysis, Polymers (Basel). 12 (2020). https://doi.org/10.3390/polym12010246.
- **M.A. Attolico**, C. Casavola, A. Cazzato, V. Moramarco, G. Renna, Effect of extrusion temperature on fused filament fabrication parts orthotropic behaviour, Rapid Prototyp J. 26 (2020) 639–647. https://doi.org/10.1108/RPJ-08-2019-0207.
- **M.A. Attolico**, C. Barile, C. Casavola, V. Moramarco, D. Furfari, D.O. Busse, Effects of Laser Shock Peening on Surface Roughness and Residual Stress of AA 7050-T7451, J Mater Eng Perform. 31 (2022) 7973–7988. https://doi.org/10.1007/s11665-022-06857-7.
- **M.A. Attolico**, C. Casavola, V. Moramarco, G. Renna, D. Furfari, D.O. Busse, Influence of tartaric-sulfuric acid anodic film on four-point bending fatigue behavior of AA 7050-T7451 samples, Fatigue Fract Eng Mater Struct. 45 (2022) 3716–3730. https://doi.org/10.1111/ffe.13844.

CHAPTER 1

SURFACE TREATMENTS FOR AIRCRAFT ALUMINUM ALLOYS

1.1. Preface

The application of surface treatments plays a crucial function in designing and fabricating particularly stressed components or structures subjected to demanding service conditions. The rationale behind their use lies mainly in improving the performance of the material, imparting special physical properties, changing the appearance or altering the size of the treated component. These objectives can be achieved by different types of mechanical, thermal, chemical or electrochemical treatments, each with its peculiarities or disadvantages depending on the particular material to which it is applied, whether metallic, polymeric or ceramic. The macroscopic and microscopic effects resulting from the application of surface treatments on the surface integrity of the material can be assessed by topographical analysis (roughness and erosion), evaluation of mechanical properties (residual stresses and hardness), the study of metallurgical states (phase changes and microstructure), or observation of any properties that can be appropriately related to the process employed.

This chapter will provide an overview of the main types of surface processes for the treatment of aeronautical aluminum alloys, with particular reference to the alloys belonging to the 7xxx series as the main object of study. An in-depth analysis will be dedicated to peening technology and in particular to two of its most common variants, the "shot peening" and the "laser shock peening" processes, focusing on the physical principles underlying the two different processes, on the technological implications, on the fields of application and on the main methodologies for evaluating the mechanical and physical properties induced in the material. Similarly, a detailed analysis of the main anodizing processes of aluminum alloys will be provided to contemplate all those cases of real applications in which, in addition to high mechanical performance, high corrosion and wear resistance are required.

1.2. Aluminum Alloys

The unique properties of aluminum and its alloys make it one of the most versatile, economical and attractive metallic materials for various engineering applications. The low density coupled with the high mechanical properties typical of some aluminum alloys enables the design and construction of lightweight and high-strength structures ideal for aerospace applications, particularly highly stressed components or parts of aircraft and space vehicles. In addition, the inherent corrosion resistance properties offered by the thin natural oxide layer formed by exposure of the material's free surface with oxygen favor application in scenarios characterized by high thermal gradients in the presence of chemical and physical media [1,2].

The designation system proposed by the Aluminum Association (ANSI/AA system) divides aluminum alloys into nine different families. Other recognized classification systems, such as the unified numbering system (UNS) or the European designation (EN) refer to the ANSI/AA system with only minor modifications. In the case of wrought aluminum, each family is distinguished by a four-digit identification code in which the first digit indicates the main alloying element. Table 1-1 shows the nominal composition, strength range and strengthening mechanism under each family.

Table 1-1*: Strength ranges of various wrought aluminum alloys* [2].

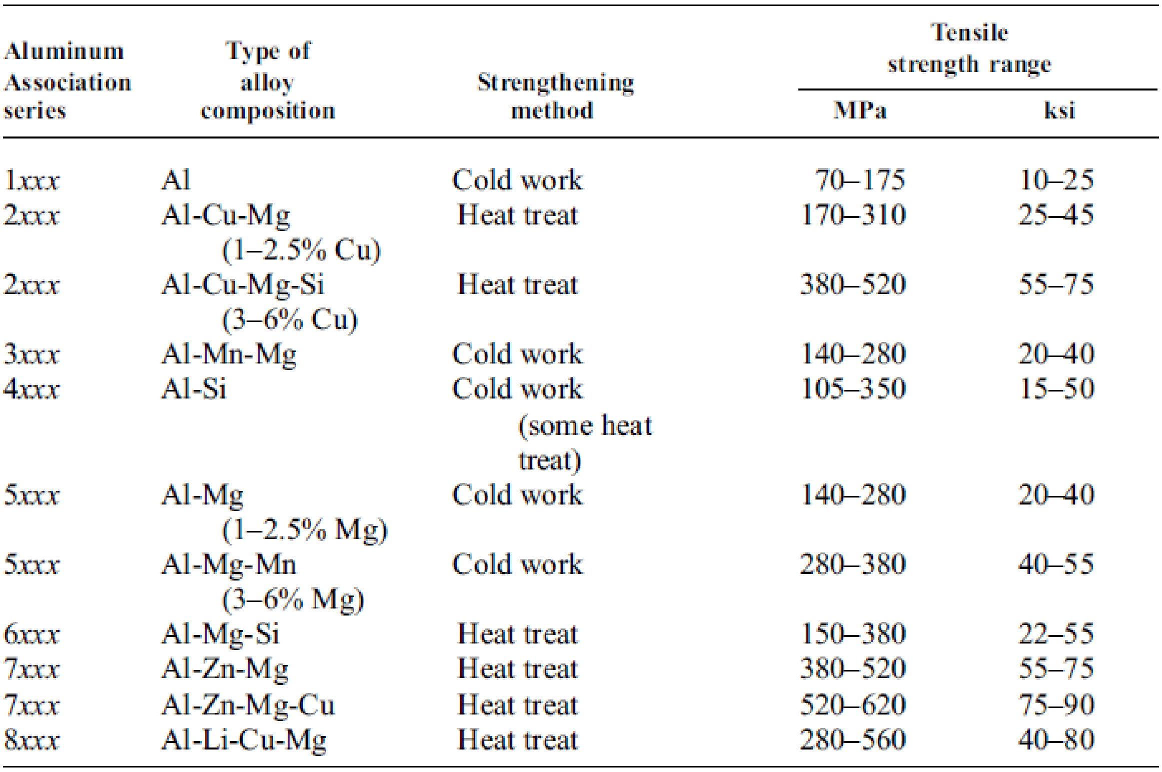

Aluminum Association series	Type of alloy composition	Strengthening method	Tensile strength range	
			MPa	ksi
1*xxx*	Al	Cold work	70–175	10–25
2*xxx*	Al-Cu-Mg (1–2.5% Cu)	Heat treat	170–310	25–45
2*xxx*	Al-Cu-Mg-Si (3–6% Cu)	Heat treat	380–520	55–75
3*xxx*	Al-Mn-Mg	Cold work	140–280	20–40
4*xxx*	Al-Si	Cold work (some heat treat)	105–350	15–50
5*xxx*	Al-Mg (1–2.5% Mg)	Cold work	140–280	20–40
5*xxx*	Al-Mg-Mn (3–6% Mg)	Cold work	280–380	40–55
6*xxx*	Al-Mg-Si	Heat treat	150–380	22–55
7*xxx*	Al-Zn-Mg	Heat treat	380–520	55–75
7*xxx*	Al-Zn-Mg-Cu	Heat treat	520–620	75–90
8*xxx*	Al-Li-Cu-Mg	Heat treat	280–560	40–80

The alloys of greatest interest within the aircraft industry belong to the 2xxx, 7xxx and 8xxx series [3]. In the 2xxx series, copper is the main alloying element, often with magnesium as a secondary addition. Following solution heat treatment, these alloys can exhibit mechanical properties comparable to or even superior to low-carbon steels [4]. While exhibiting excellent mechanical properties that make it an ideal candidate for the fabrication of parts and structures requiring high strength-to-weight ratios, this alloy has limited corrosion resistance compared to most other alloys and is prone to intergranular corrosion under particular service conditions [5]. One of the most representative alloys belonging to this family is 2024, used in many structural aeronautical applications but also in the automotive field for the production of cylinders, pistons, and gear wheels.

7xxx alloys have zinc as the main alloying element, together with magnesium or magnesium and zinc, depending on the desired degree of strength. Copper-containing alloys show the highest strength and have been one of the most widely used structural solutions in aviation for the past 50 years [6]. However, the presence of copper makes these alloys among the most susceptible to stress corrosion cracking (SCC) [7] and are for that reason often used in a slightly aged temper to provide a better combination of mechanical properties, corrosion resistance and fracture toughness. The two most representative alloys in this family are 7050 and 7075: the former, the subject of the present research activity, uses Zr instead of Cr to ensure deeper hardening and exhibits high strength and toughness along with a high ability to resist SCC and exfoliation, especially in the T7 condition; the latter, although exhibiting excellent mechanical properties, shows poor resistance to corrosion, SCC phenomenon and exfoliation [8].

The latest family of aluminum alloys of industrial interest is alloy 8xxx. The 8xxx series alloys cover a wide range of chemical compositions depending on the requirements of the specific application. They are generally characterized by the presence of tin, lithium and/or iron in various combinations. The lithium-containing alloys are of particular interest since they are precipitation hardenable and characterized by high stiffnesses and low densities. They can be considered excellent alternatives to the medium-to-high-strength alloys of the 2xxx and 7xxx series in some aerospace or aeronautical applications [9].

1.3. Overview of surface treatments

The surface characteristics of materials significantly influence the performance of an engineering component. The different surface treatments to which they are subjected aim to obtain physical and mechanical properties that cannot be obtained from primary manufacturing processes without resorting to more performing and expensive materials [10].

A possible classification of surface treatments proposed by Qutaba [11] is shown in Figure 1-1 and identifies four different categories of processes according to the nature of the underlying physical principle: mechanical, chemical, electrochemical and case hardening.

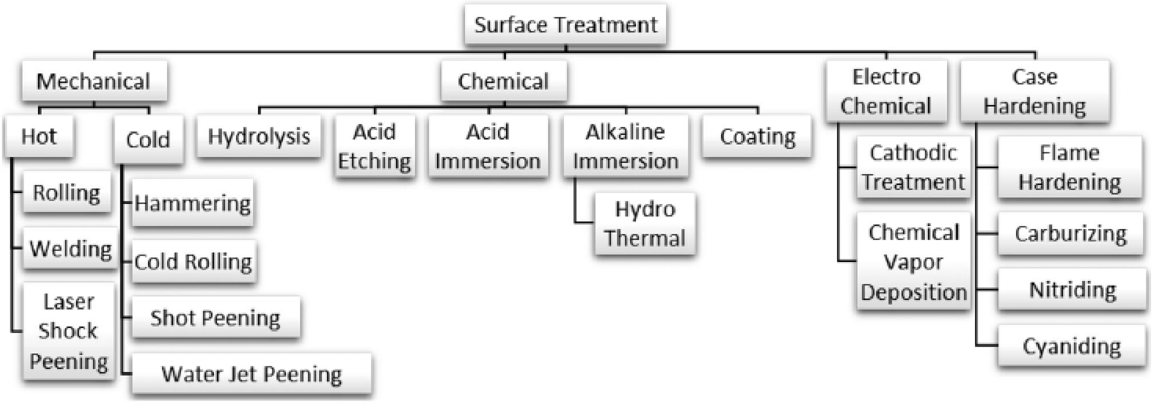
Surface Treatment
Mechanical
Chemical
Electro Chemical
Case Hardening
Hot
Cold
Hydrolysis
Acid Etching
Acid Immersion
Alkaline Immersion
Coating
Rolling
Welding
Laser Shock Peening
Hammering
Cold Rolling
Shot Peening
Water Jet Peening
Hydro Thermal
Cathodic Treatment
Chemical Vapor Deposition
Flame Hardening
Carburizing
Nitriding
Cyaniding

***Figure 1-1**: Classification of surface treatments according to the nature of underlying physical principle* [11].

Mechanical treatments, one of the main topics of this research activity, can in turn be divided into two subcategories: hot treatments and cold treatments. In hot working the material is plastically deformed when its temperature is higher than the recrystallization temperature, on the contrary, in cold working the deformation occurs at temperatures lower than the recrystallization temperatures [12]. The mechanical processes include hot and cold rolling, shot peening and laser shock peening, hammering and water jet peening. Although the Laser Shock Peening process has been included among the hot mechanical surface treatments, it is necessary to remark that since the plastic deformation is caused by the propagation of the shock wave induced by the rapid expansion of the plasma on the surface of the material, this process could be included in the cold working sub-category as well, as proposed in several related scientific articles [13–17].

It is important to observe how most of these processes are commonly employed for the development of residual stress fields in the surface and sub-surface region of the mechanical components in order to ensure significant increases in their fatigue life [18,19]. Plastic deformations localized on the surface of the component result in an elastic response of the material surrounding the plasticized zone leading to the development of the desired stress field. The physical principle underlying the plasticization process varies with the type of treatment employed, as will be shown in the following sections.

Chemical processes take advantage of particular chemical reactions to provide specific physical properties to the surface of the treated material, typical examples being the process of immersion in acid or alkaline solution or the coating treatments, or to change the geometry of the component, as occurs in the chemical etching process. Electrochemical processes use a combination of chemical and electrical processes to change the surface layer properties of the material. Some processes of this nature, particularly the anodizing process which will be covered extensively later in this chapter, are widely used in the aerospace industry for the treatment of aluminum alloys in order to significantly improve the corrosion and wear resistance of the material and thus enable its use in critical structural applications [20].

Case hardening is a special type of process to increase the surface hardness of a component by diffusing additional amounts of carbon (carbonization), nitrogen (nitriding), boron (boriding) or cyanide (cyaniding) at high temperatures within the surface layer and then heat treated to the desired hardness [21,22]. In this way, it is possible to obtain a structure characterized by high hardness values near the surface of the component, where wear phenomena are mainly concentrated due to sliding contact with hard and abrasive materials, and a soft core capable of bearing stresses without cracking. These processes find wide application in the automotive industry for treating low-carbon steels (usually less than 0.3%) which are not normally hardenable due to the small amount of carbon, so the surface of the steel is chemically altered to increase the hardenability [23].

1.4. Laser Shock Peening (LSP) process

1.4.1. Historical background

In the Laser Shock Peening (LSP) process, laser pulses of high intensity and short duration (on the order of 10 ns on average) impact the surface of the component, generating a plasma bubble whose expansion results in plastic deformation of the surface and sub-surface region of the component. The use of a confining material directs the plasma expansion along the thickness of the part causing plastic deformation and the subsequent generation of a compressive residual stress field in the treated region of the part. The theoretical basis of the process dates back to the mid-20th century when Askaryan and Moroz [24] from the P.N. Lebedev Physics Institute conducted the first experiments aimed at generating shock waves using high-intensity laser pulses. Their main merit was to thoroughly analyze laser-matter interaction and to observe that the pressure generated by high-intensity laser pulses acting on a surface was much greater than the pressure of the laser beam itself. The high-pressure values are closely related to the phenomenon of vaporization of the material caused by the very high temperatures reached by the irradiated region.

A further turning point was the insight that it was possible to achieve benefits in the final stress state of the component by confining the plasma expansion through a transparent envelope and directing the expansion of pressure shock waves within the material [25]. Despite these early and encouraging results, LSP technology took some time before it was attractive for industrial use. It is a technique that requires multidisciplinary knowledge in the fields of plasma physics, laser physics, and mechanical and metallurgical engineering combined with a solid understanding of high-energy laser systems [13].

Early laser systems, such as the one developed by the Battelle Memorial Institute in the United States, could not justify industrial use due to the lack of laser sources (low repetition rates) to provide real industrial potential, but they were nonetheless important in understanding how to improve the mechanical properties of metallic materials using LSP [26–28]. Indeed, the first works on the analysis of the fatigue behavior of some alloys of great aeronautical interest, such as AA 7075-T6 [29] and AA 2024-T3 [30], following LSP treatment date back to this period. In the following years many French research centers, such as the CLFA (Cooperation Laser Franco-Allemande), the LALP (Laboratoire d'Application des Lasers de Puissance) and the LULI (Laboratoire d'Utilisation des Lasers Intenses) focused their attention on improving the technological process to make it possible its use in an industrial context [31]. In America, therefore, the first patents relating to small-sized laser systems capable of generating high-intensity laser pulses with a relatively high pulse rate (up to 1 Hz) were registered, which finally made a possible industrial application economically viable. In the 90s the US Air Force in collaboration with General Electric (GE) aviation and the Battelle Memorial Institute tried to solve the problem of Foreign Object Damage (FOD) through the application of Laser Shock Peening technology and the first LSP systems were integrated within the production lines of GE Aviation [32,33]. In 2002 the Metal Improvement Company (MIC) started production of LSP systems for the treatment of Rolls-Royce turbine blades and is still one of the largest providers of LSP services in the world.

1.4.2. Technological aspects of the LSP process

When high-intensity and short-term laser pulses are projected onto the surface of a material, the vaporization of the surface layer allows the formation of a high-temperature and pressure plasma whose expansion, if suitably controlled and directed, can plastically deform the treated region [13,14]. The condition that must occur for the material to be plastically deformed is that the peak pressure of the shock wave is greater than the dynamic yield stress of the material (Huguniot elastic limit - HEL). According to Johnson and Rhode [34], the HEL is defined as:

$$HEL = \frac{1-\nu}{1-2\nu}\sigma_y^{dyn} \tag{1}$$

where ν is the Poisson’s ratio and σ_y^{dyn} is the dynamic yield strength at high strain rates.

Residual compressive stresses develop as a result of the elastic response of the surrounding material to the inelastic deformation of the plasticized region (Figure 1-2).

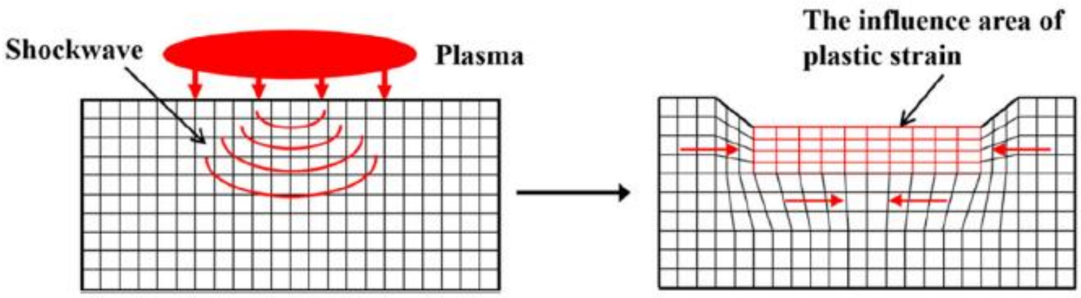
Shockwave
Plasma
The influence area of plastic strain

Figure 1-2*: Development of residual stresses due to localized plastic deformation following shock waves propagation.*

A typical RS profile can be characterized by a compressive region underneath the treated surface with a peak value of compressive stress near the surface and a tensile region surrounding the compressive region to balance the compressive stress state. The penetration depth of the process depends on the extension of the plasticized region and therefore on the characteristics of the LSP process and the properties of the employed material.

The LSP process in confined ablation mode is schematically shown in Figure 1-3.

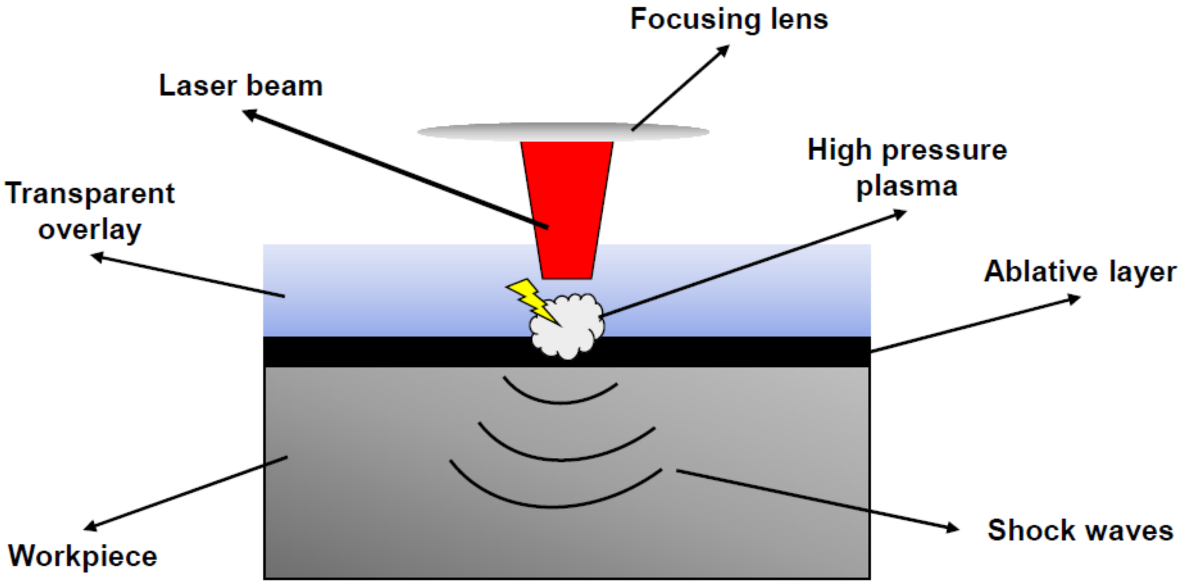
Focusing lens
Laser beam
High pressure plasma
Transparent overlay
Ablative layer
Workpiece
Shock waves

Figure 1-3*: Schematic of Laser Shock Peening (LSP) process in confined ablation mode configuration.*

To prevent any thermal phenomena due to the direct application of short-duration laser pulses (in the range of tenths of nanoseconds) on the surface of the component, such as melting or laser ablation which could induce the presence of localized residual tensile stresses, a sacrificial ablative layer is applied on the surface of the piece, in the form of paint or black adhesive tape or metallic coatings, which serves a dual function: to protect the surface from the aforementioned thermal effects and to increase the pressure peak of the shock waves [28,35,36]. Studies have shown that black paint has the best ability to absorb the laser energy and therefore is the ideal candidate for use as an ablative material layer [37]. It is important to underline that the thickness of the ablative layer must ensure the protection of the material substrate during the application of the laser pulse. It is the vaporization of the ablative layer that triggers the formation of the plasma by preserving the surface of the part from the occurrence of thermal phenomena.

Another key element for the proper application of LSP treatment is the presence of a transparent overlay that prevents the free expansion of plasma away from the surface of the treated component. The overlay allows the efficient conversion of laser-supplied energy into pressure waves by appropriately directing wave propagation in the material [38–40]. Its absence would result in a reduction of the intensity and duration of the shock pulse and thus the development of lower compressive residual stresses [41,42]. Materials characterized by the highest acoustic impedance values are the ideal choice as transparent overlays because they allow higher peak pressures to be achieved for the same incident laser power densities. The most commonly used materials are glass, water or quartz. Although glass has higher acoustic impedance values, water is usually preferred since glass is prone to breakage due to shock [38].

1.4.3. Laser Shock Peening parameters

The complexity of the Laser Shock Peening process caused by the coexistence of different physical phenomena such as plasma generation, pressure wave propagation and plasticization, is perfectly reflected in the complexity of process parameters and their optimization.

The parameters that must be considered in defining any Laser Shock Peening process are the wavelength of the laser beam [nm], the laser energy [J], the laser frequency [Hz], the pulse duration (FWHM) [ns] and the laser spot geometry and size [mm^2].

The first aspect that should be analyzed as the main element of LSP technology is the type of laser system employed. A typical system for LSP must be able to deliver laser pulses of energy between a few hundreds of mJ and a few tens of J with pulse lengths of less than 100 ns [31,43]. These requirements can be met only by Q-switched laser system based on neodymium such as Nd-doped glass (Nd:Glass), yttrium aluminum garnet (Nd:YAG), yttrium orthovanadate (Nd:YVO4) or ytterbium-doped YAG (Yb:YAG).

The most common and easiest to produce wavelengths are 1064 nm (near infrared), 532 nm (green) and 355 nm (ultraviolet). The choice of wavelength is closely related to the occurrence of the dielectric breakdown phenomenon. This phenomenon consists of the formation of the plasma at a different position from the surface of the material causing a reduction in the energy absorbed for the generation of the shock wave [39,44,45]. It has been verified that although the use of shorter wavelengths (UV range) improves the photon-metal interaction favoring the formation of the shock wave, it also causes the reduction of the breakdown threshold in water confinement limiting the maximum peak pressure [45], as shown in Figure 1-4.

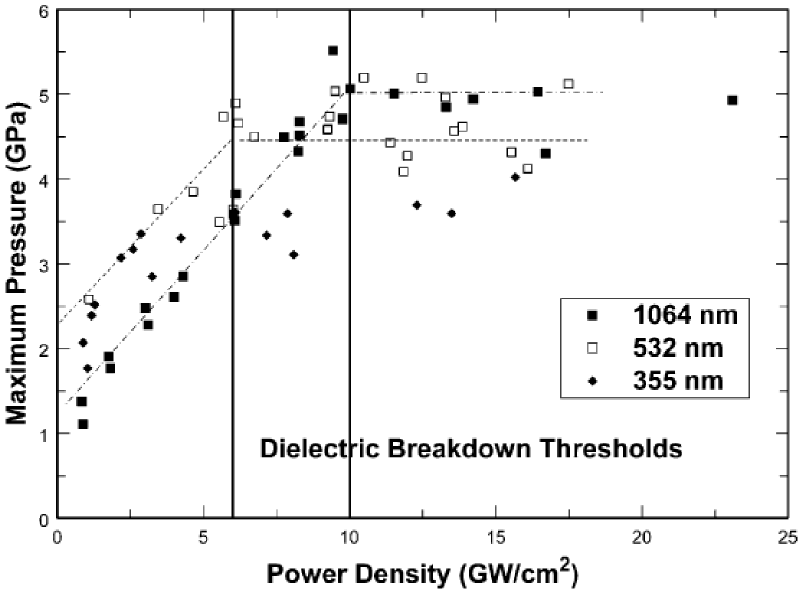

Figure 1-4: *Onset of the dielectric breakdown phenomenon at different wavelengths in the aluminum alloy's laser shock peening treatment* [31].

In the case of low laser energies, a lens system can be used to focus the laser beam on the surface of the workpiece to be laser peened: by keeping the component close to the focal plane, high power densities can be achieved while employing low source energy values. This is related to the fact that the spot beam size varies in the direction of laser propagation, being minimum at the focal plane and increasing moving away from it (Figure 1-5).

Since the laser intensity is inversely proportional to the square of the spot radius (r), higher power intensities are obtained at higher energies and lower spots.

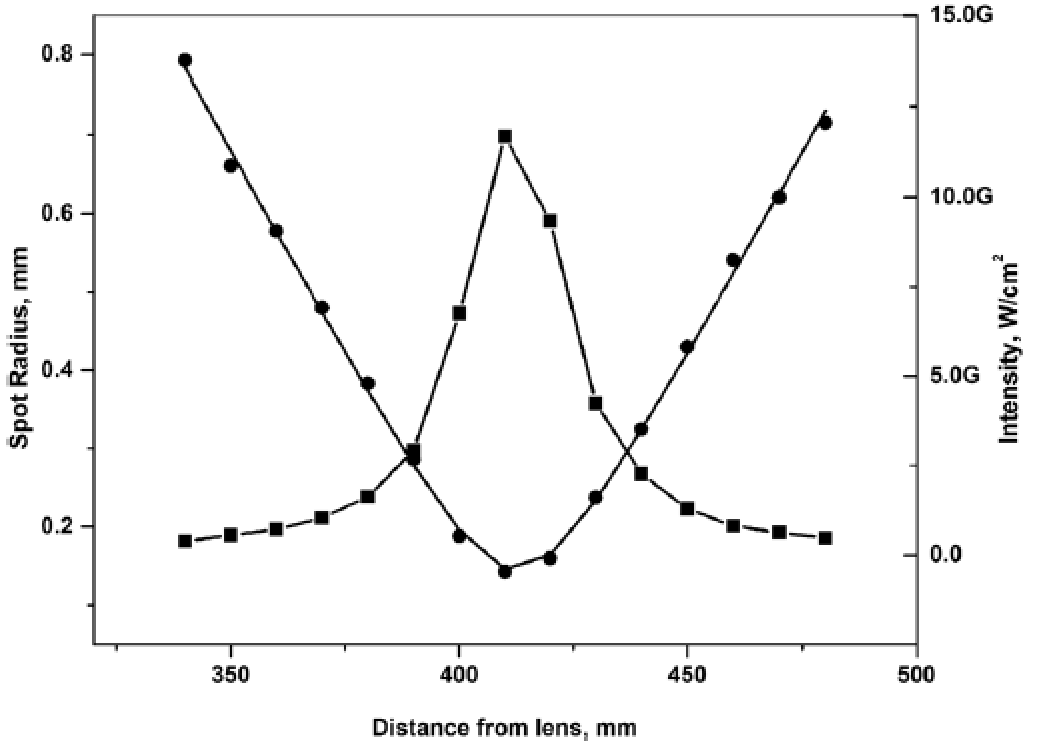

***Figure 1-5**: Typical relationship between spot radius, laser intensity and focal length in LSP process* [13].

The size of the laser spot on the target significantly affects the intensity and penetration depth of the generated compressive residual stress field. Shock waves generated using small laser spots have an attenuation rate inversely proportional to the square of the spot radius ($\propto 1/r^2$) because it acts as a point source (sphere expansion); in the case of larger laser spots, the attenuation rate is inversely proportional to the spot radius ($\propto 1/r$), since shock waves behave like a planar front resulting in greater penetration within the material. At the same time, however, larger spots lead to lower energy intensities and consequently lower pressure peaks. It is therefore essential to find an ideal compromise suited to the specific requirements of the application in which laser peening technology is to be used [31,46].

The use of small laser spots can also have important application implications. If the target surface has an extension much larger than the size of the laser spot, it will be necessary to provide for the presence of a translation stage that allows displacements in two directions to be able to peen the entire region of interest, and a controller will also have to be used that allows synchronization of the motion system with the laser source.

A quantity derived from the energy and spot size parameters commonly used in the definitions of any Laser Shock Peening process is the nominal power density. The nominal power density is defined as the amount of energy delivered in the unit of time by the laser source over the laser spot area:

$$Power\ Density\ \left[\frac{GW}{cm^2}\right] = \frac{Laser\ energy\ [J]}{Laser\ spot\ area\ [cm^2] * Pulse\ duration\ [ns]} \tag{2}$$

Two additional highly relevant process parameters are the overlap rate and the number of repetitions of the laser pulse. The overlap rate is a parameter that indicates the percentage of coverage of the surface subjected to the Laser Shock Peening process and is calculated as the ratio of the coincidence length between two adjacent spots to the diameter of the spot on the target surface. It is common to indicate two different overlap rates in the two main peening directions, conventionally identified as scanning direction and stepping direction according to the laser handling system. The scanning direction defines the advancing direction to form a row of laser pulses, while the stepping direction refers to the advancing direction of multiple rows of laser pulses [16].

The number of repetitions of laser pulses, or "number of layers," indicates the number of repetitions of laser patterns on the surface of the part, or more simply the number of times the same surface is subjected to the same peening process [17,47,48]. Two different laser patterns can be repeated in the same position or a non-perfectly overlapping manner by introducing an appropriately selected offset value. It has been observed in the scientific literature that at specific parameters of overlap and number of repetitions there is a greater uniformity of residual stresses in the two main directions of laser peening allowing the development of a nearly equal-biaxial stress field as well as a greater intensity of the residual stress field in comparison with the standard procedure (Figure 1-6) [47,48].

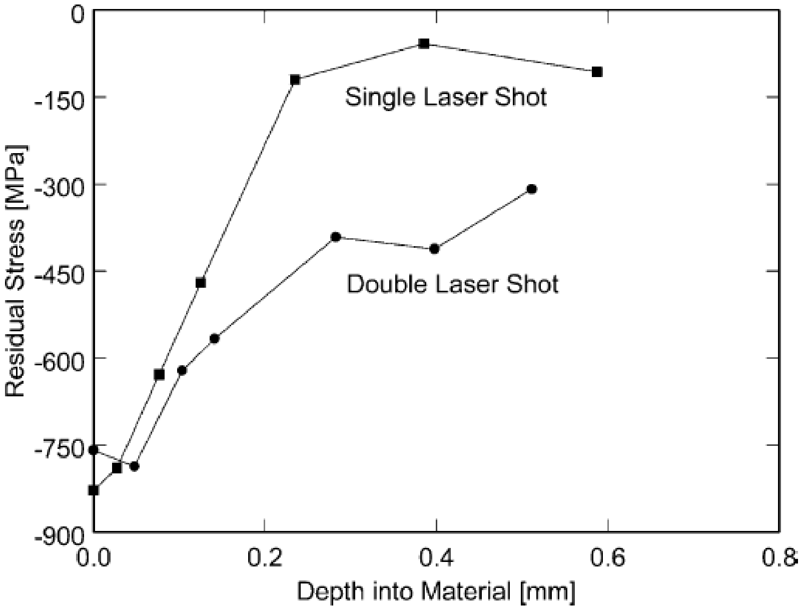

***Figure 1-6**: Influence of pulse repetition number on the intensity and penetration depth of the LSP-induced residual stress field* [31].

.

1.4.4. Application of the Laser Shock Peening process

At the current state of the art, the Laser Shock Peening process has been successfully applied to numerous materials including steel, aluminum and nickel alloys, copper, and molybdenum. The main applications involve increasing fatigue life [49], reducing fretting fatigue damage [50], increasing corrosion resistance [51], and increasing Foreign Object Damage (FOD) resistance [52]. Within the aerospace industry, there are numerous papers in the scientific literature concerning the application of the LSP process on wing attachment fittings (F-22 lugs) [53], landing gear [54], critical fatigue components (F-16 bulkheads) [55], fasteners and fastener holes [56], aluminum and titanium welded aircraft parts [57], and finally helicopter components [58].

The process can be applied to components of widely varying thicknesses, from thin plates less than 3 mm thick (typical values for aircraft fuselage skins) to thick components up to 30 mm thick. Sano [57] demonstrated the possibility of significantly increasing the fatigue limit of a 6061-T6 aluminum alloy by applying a coating-free LSP treatment on 3 mm thick specimens. Toparli and Fitzpatrick [59] observed that although it is possible to induce compressive stress states by LSP on thin plates (1.8 mm) of 2024-T351, distortion of the component as a result of the process can cause a reduction in the stress state and an anisotropy of stresses in the two main laser peening directions.

Several studies have focused on the study of crack nucleation and crack propagation phenomena in 2024-T3 aluminum components with different notch geometries. Results have shown the ability of the LSP process to suppress the crack propagation phenomenon when applied near the stress concentration site and the ability to deflect the crack trajectory by changing the geometry and location of the LSP-treated region [60].

A different type of research work has focused instead on the effects of individual process parameters on the results of LSP treatment. The parameters typically monitored were the nominal power density, the pulse duration, the number of layers or repetitions and the thickness of the treated component. Cellard [61] verified that all the above parameters influenced the magnitude of the induced residual stress field, however, only a minimal influence on the roughness and work-hardening parameters was observed.

Jiang [62] observed that fatigue life improved as the number of LSP passes increased until a plateau was reached beyond which the effects on fatigue life were found to be negligible if not worsening. An ideal number of passes of three had been identified.

Finally, several researchers have tried to compare the benefits derived from the LSP process with those induced by the conventional SP process [63–65]. In particular, the crack propagation rate in AA 7075-T7351 friction stir welded plates was investigated showing a significant reduction in fatigue crack growth in components subjected to LSP compared with untreated welded components and base material. In addition, fatigue striation spacing in laser shock peened specimens was found to be small compared to shot peened specimens, demonstrating the ability of LSP to delay fatigue crack propagation due to the greater extent of the residual stress field.

1.5. Shot Peening (SP) process

The Shot Peening process is a cold working process in which a workpiece is subjected to the impact of small spheres made of metal, ceramic, or glass material (Figure 1-7).

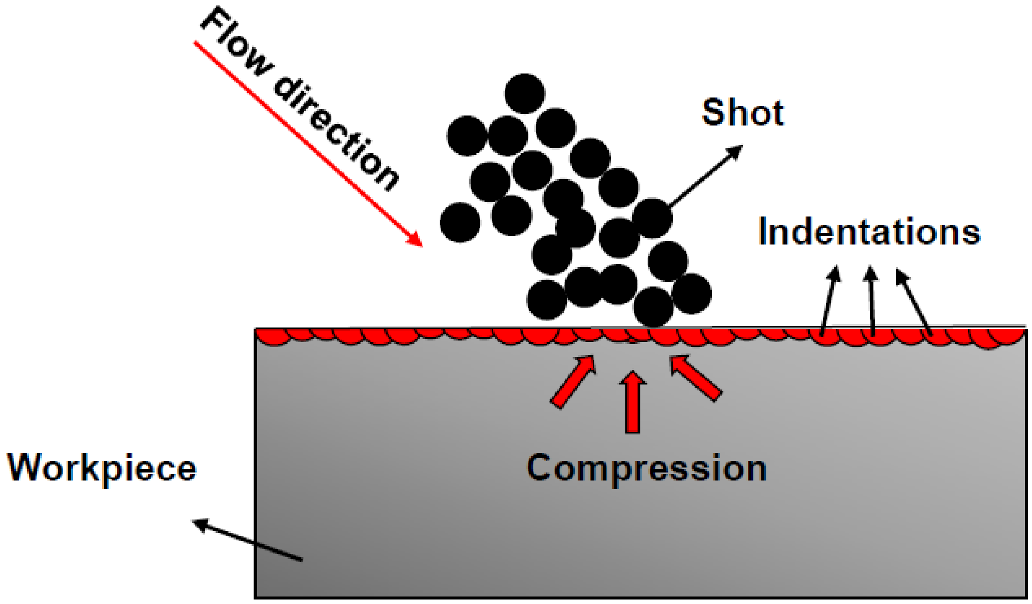

Figure 1-7: *Schematic of Shot Peening process.*

The particles are combined with a volume of compressed air whose purpose is to direct the spheres onto the surface of the part and provide the amount of energy required to cause plastic deformation of the surface layer of the material. Each impact results in the formation of grooves or indentation sites of semi-spherical shape that induce modification of the metallurgical state and topography of the surface state, thus altering the mechanical properties of the part. Specifically, the overlapping of multiple indentations results in the formation of a uniform surface layer of compressive residual stresses that significantly increase the fatigue performance of the part [66].

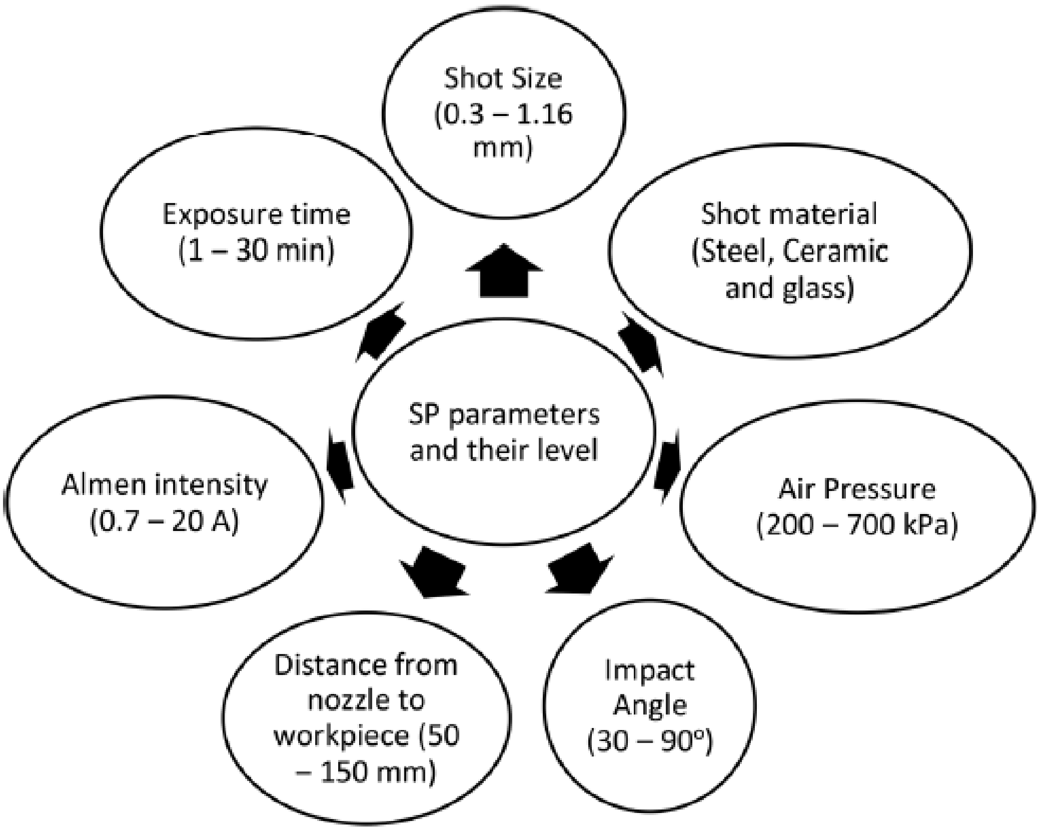
Shot Size (0.3 – 1.16 mm)
Shot material (Steel, Ceramic and glass)
Air Pressure (200 – 700 kPa)
Impact Angle (30 – 90°)
Distance from nozzle to workpiece (50 – 150 mm)
Almen intensity (0.7 – 20 A)
Exposure time (1 – 30 min)
SP parameters and their level

Figure 1-8: *Typical shot peening parameters and their levels.*

The process parameters of a shot peening treatment include shot material and size, air flow velocity, angle of incidence, nozzle distance from the workpiece surface and degree of coverage (Figure 1-8) [67]. The shot should be at least as hard as the surface being peened: typical values of the hardness of the shot are in the range of 45-65 HRC. Most shot peening processes are carried out with ferrous shots that are characterized by high-impact energy and good durability. However, glass beads are used when lower shot peening intensity levels are allowed, especially in the case of thin parts peening. Their use avoids the decontamination step after the treatment of nonferrous parts using ferrous shots, but there is an increased risk of the presence of irregularly shaped particles in the air stream due to the higher risk of glass breakdown. Ceramic particles are characterized by higher hardness values but lower density than ferrous shots; they are less prone to breakage than glass particles but the purchase costs are higher. The ideal shape of the shots should be spherical and therefore free of sharp edges or irregularities while the size is closely related to the required finishing characteristics: smaller shot diameters provide better coverage but also cause an increase in surface roughness, conversely larger diameters allow for smoother finishes but with lower coverage rates. Shot velocity determines the amount of kinetic energy possessed by the particles upon impact with the surface and is closely related to compressed air pressure. Coverage indicates the percentage of the treated area affected by indentation. The methods for verifying coverage are defined in SAE J2277 recommended practice and usually include a visual inspection through a magnifying glass to identify areas not affected by the blast, especially in applications where full coverage is not required and the application of a liquid tracer on the surface of the workpiece before peening and then the examination of the peened area under UV light to verify that all the tracer liquid coating has been removed.

The most important shot peening parameter is the shot intensity. This parameter is defined by a quantity called "Almen intensity," which represents the maximum deflection of a thin steel plate, or strip, constrained through four screws to a metal block and subjected to the shot peening process with the same shot peening conditions as the component. Three different types of thin plates are commercially available depending on their thickness denoted respectively by the letters N, A and C whose specific application depends on the level of shot peening intensity employed. The curvature or arc height of the strip is measured with the aid of a dial gauge after the strip is placed and retained magnetically against two pairs of ball contacts a fixed distance apart. Almen intensity plays a key role in defining the shot peening process because it encapsulates the contribution of all the different process parameters involved without the need to measure them individually. It is also extremely simple to measure and does not require knowledge of external quantities [68,69].

1.5.1. Applications of Shot Peening process

The shot peening process can be used on components of almost any shape, even for the treatment of complex geometric parts. The most common applications are in the automotive sector, especially for the treatment of springs, shafts, and connecting rods, but several applications can be found also in the aviation field, such as turbine vanes or blade bases and welded joints [70]. The residual stress field induced by the shot peening process can delay the nucleation phenomenon and the initial crack propagation phase, due to the very limited depth of the tension/compression transition point in the residual stress profile [71]. For the same reason, shot peening is not suitable for the treatment of components in which through-the-thickness cracks already exist in the component. An interesting application of the shot peening process on aluminum alloys of aviation interest was proposed by Aghaie-Khafri [72]: in fact, the author analyzed the effects of heat treatment and shot peening on an aircraft wheel made of AA 7050-T7451 and verified that both types of treatment were able to provide an improvement in the fatigue life of the component. Furthermore, it was observed that the order in which the treatments were pursued influenced the increase in fatigue life and in particular that the best result was obtained when the shot peening process was preceded by heat treatment. The range of residual stresses was uniform in the first 200 microns from the surface of the part with an intensity between about -300 and -400 MPa.

1.6. Comparison between Laser Shock Peening and Shot Peening

As reviewed in the previous paragraphs, the main objective of peening treatments is to generate a compressive residual stress state in the surface and sub-surface region of the component through local plastic deformation. The employment of shot peening technology is widely established in the aircraft industry, however, laser shock peening technology has unique characteristics that may justify its alternative use to shot peening in industrial settings as well. Although similar from a technological point of view, the two processes have different outputs in terms of induced compressive residual stress field, surface integrity following treatment, and microstructural changes. Regarding residual stresses, several studies have highlighted that SP treatment can induce higher compressive residual stresses within the component than LSP, with peaks located mainly near the surface (Figure 1-9). LSP on the contrary allows far greater penetration depths than typical SP process, with compressive residual stress field extending as far as 1.5-2 mm from the surface and compressive peaks located at a depth of 0.5-0.6 mm inside the component, providing additional protection against the phenomenon of fatigue crack propagation [73,74].

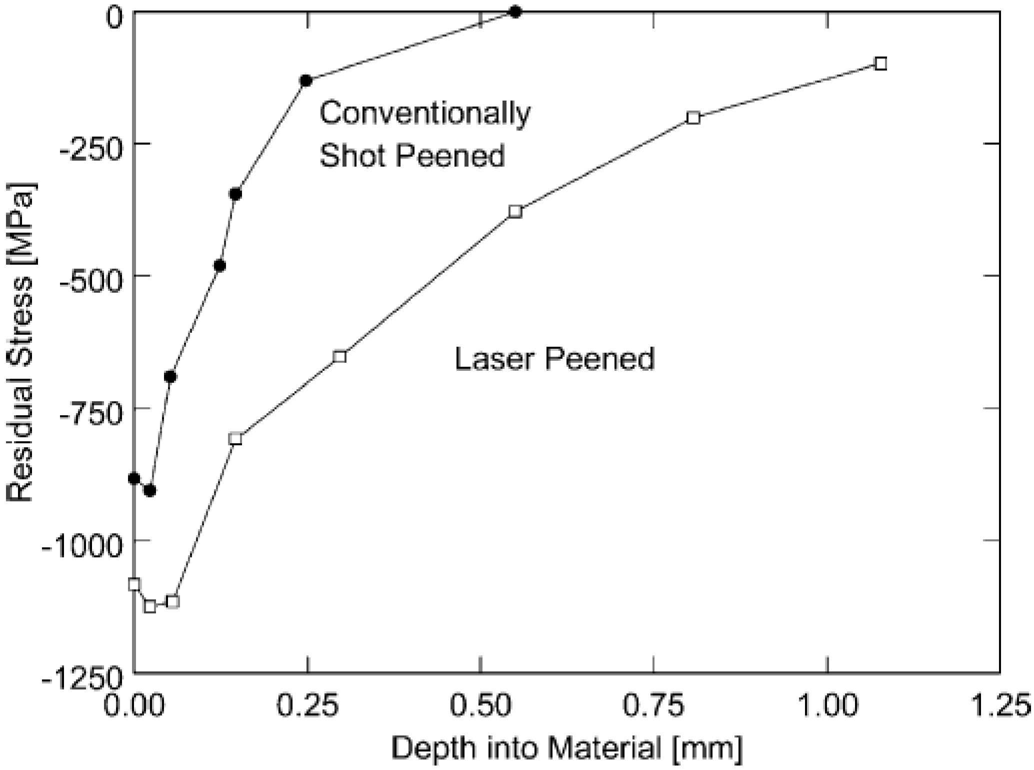

***Figure 1-9**: General trend of residual stresses generated by shot peening and laser shock peening* [31].

The second aspect concerns the influence of the peening processes on the surface integrity of the component. The conventional shot peening process generates a very rough surface characterized by high average and peak roughness values (Table 1-2). While this is favorable for adhesion properties, at the same time it results in a deterioration of fatigue and wear performance. Sometimes, for wear applications, removal of the roughened surface is a necessity. However, due to the thinness of the SP compressive layer, the removal of the rough surface also produces a reduction of the compressive layer, nullifying the main advantage of the process.

Table 1-2*: Comparison of roughness parameters following the application of shot peening and laser shock peening processes on steel and aircraft aluminum alloy specimens* [31].

Material and processing	**Ra (µm)**	**Rt (µm)**
A356 as milled	0.7	6.2
A356 LSP (2GW/cm2, two impacts)	1.1	7.5
A356 SP (F38-50N, 0.3 mm beads)	5.8	33
7075 as milled	0.6	5.2
7075 LSP (4GW/cm2, three impacts)	1.3	11
7075 SP (20-23A, 125%, 0.6 mm beads)	5.7	42

Concerning Laser Shock Peening, a distinction must be made: in the case of the LSP process without a protective coating, especially in the treatment of aluminum alloys, the occurrence of thermal phenomena on the surface of the component causes local melting and vaporization leading to the formation of droplets and craters and thus to a very rough surface [75]. In the case of LSP with an ablative layer, thermal phenomena are localized on the surface of the ablative layer and do not affect the substrate, inducing any deterioration of surface integrity other than the appearance of circular grooves due to shock wave expansion. Thus, in the latter case, there is an increase in the waviness of the treated surface but only a minimal effect on the roughness parameters [73]. As fatigue initiation is mainly a surface phenomenon the greater impact of the SP process on surface integrity can lead to significant implications in terms of fatigue strength. Regarding microstructural changes, LSP is often associated with a significant increase in dislocation density in the case of application on aluminum alloys. It has also been observed that LSP results in an increase in the hardness of the under-aged alloy 2024-T351, while it does not seem to affect the hardness values of peak-aged alloys, such as 2024-T851, 7075-T651 or 7075-T73.

1.7. Corrosion protection systems

Aluminum and aluminum alloys are widely used as materials of construction in the aerospace industry due to their low density and high specific mechanical properties. Pure aluminum also possesses high corrosion resistance compared to most metals, making the use of special additional protection unnecessary, except for high and low pH environments. The same is not true for aluminum alloys: the secondary phases formed by the presence of alloying elements in the aluminum matrix possess a different electrochemical potential from that of the matrix. This can lead to the onset of micro-galvanic couplings in the presence of an electrolyte and thus make them more susceptible to corrosion. The 2xxx and 7xxx aluminum series have the most desirable mechanical properties in structural design, however, they are deficient in resistance to general corrosion and stress corrosion cracking, necessitating the use of special processes to protect the exposed surface of the components [76,77]. The problem takes on even sharper contours when one considers that the typical service conditions of aircraft components for critical structural applications are characterized by very high thermal gradients, with temperatures ranging from -50 to 80°C or higher, and the presence of chemicals such as water, fuel, antifreeze fluid and others.

Hence, there is a need to adopt surface protection systems that are stable over a long period and capable of providing the required resistance to corrosion phenomena throughout the entire life cycle of the component. A typical aerospace corrosion protection system is a multilayer system consisting of a porous anode layer, an organic primer loaded with corrosion inhibitors, and an organic top coating (Figure 1-10) [78].

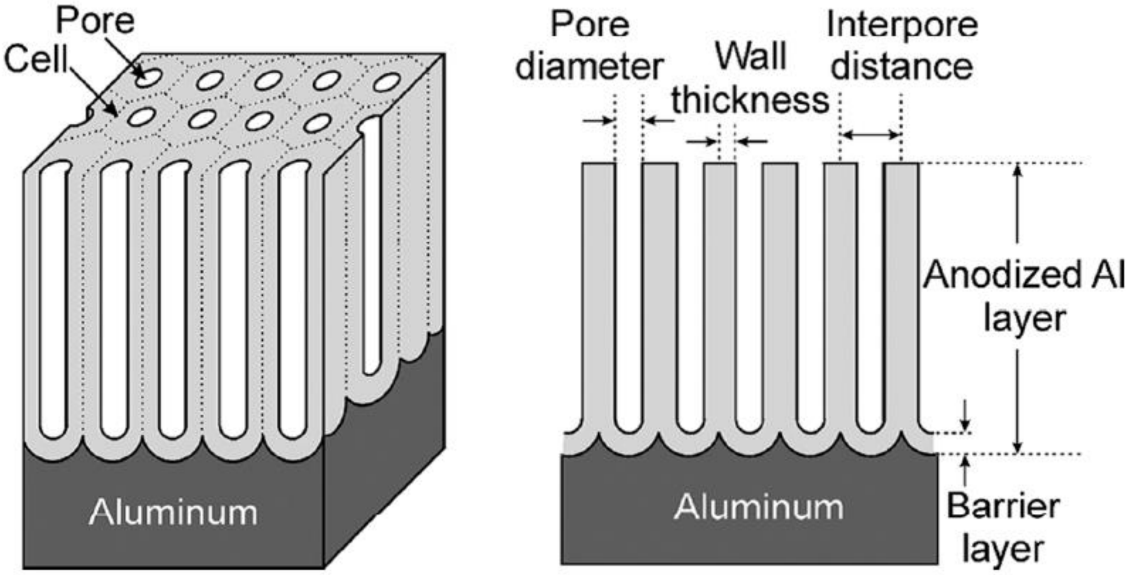

Figure 1-10*: Schematic structure of a typical corrosion protection system for aircraft applications* [79].

The different layers isolate the material substrate from the external environment by preventing contact with aggressive electrolytes and in some cases promote the adhesion of paint to the substrate due to the porous nature of the anodic part.

Protection systems in aviation have long relied on the use of hexavalent chromium (Cr-(VI)), which has outstanding corrosion inhibition capabilities. Unfortunately, however, compounds containing this element are carcinogenic and its use has been significantly reduced due to health and environmental concerns [80]. For this reason, research in recent years aims to identify environmentally sustainable alternatives to Cr-(VI)-based protection systems that can provide comparable corrosion protections [81,82]. One of the recently developed alternatives is tartaric-sulfuric solution anodizing (TSA). Some additional information on the anodizing process is necessary before delving into this topic.

1.7.1. Anodizing

Anodizing is an electrochemical process that aims to thicken the anodic layer naturally present on the surface of a metallic material. This phenomenon originates when a current at a sufficient voltage passes through an electrolyte within which aluminum represents the anode and a suitable material serves as the cathode. The mobile species involved in the anodization of pure aluminum in an aqueous solution are Al^{3+} cations and O^{2-} and OH^- anions. The Al^{3+} cations are generated at the aluminum/oxide interface as a result of aluminum oxidation, the latter are formed at the oxide/solution interface by the removal of H^+ from H_2O molecules. Migration of ions then occurs due to a high-intensity electric field (in the order of 10^8-10^9 V/m) promoting the formation of the anodic layer (Figure 1-11) [40-41].

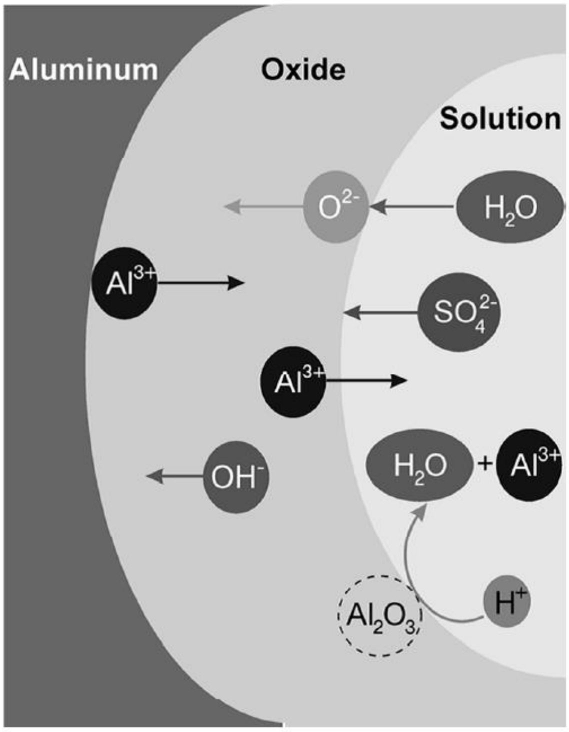

***Figure 1-11**: Mobile species involved in the anodization process in sulfuric acid solution and explanation of ions migration* [79].

At the same time as oxide formation, other chemical reactions, known as side reactions, occur, which depend on the nature of the substrate and electrolyte and can have a significant impact on the effectiveness of the anodizing process. Alloying elements can be embedded within the anodic layer leading to the formation of defects and micro-galvanic couplings deleterious to corrosion resistance. In the case of 7xxx series alloys, the main alloying elements are magnesium, zinc and copper. Magnesium has a lower Gibbs free energy of oxide formation than aluminum and therefore will oxidize earlier than aluminum due to the application of electrical voltage forming mainly MgO [83]. The volume occupied by magnesium oxide is less than that occupied by elemental magnesium, so voids will form within the anodic layer [84]. Part of these voids will be covered by alumina, which has a larger volume than molecular aluminum. In contrast, copper has a higher Gibbs free energy of oxide formation than aluminum and will eventually oxidize during the anodizing process [70]. In the first phase therefore, there will be preferential oxidation of aluminum at the oxide/aluminum interface and simultaneous accumulation of copper in solid solution or intermetallic phase under the anode film leading to the formation of a copper-enriched zone. When a limiting copper content is reached, its oxidation begins and witnesses the simultaneous formation of Al_2O_3, MgO and CuO.

1.7.2. Anodic layer requirements for aerospace applications

The basic aspects that need to be examined when analyzing the influence of a corrosion protection system for aviation applications are mainly three: corrosion resistance; the effects of the presence of the anode layer on the fatigue properties of the component; and adhesion ability (Figure 1-12).

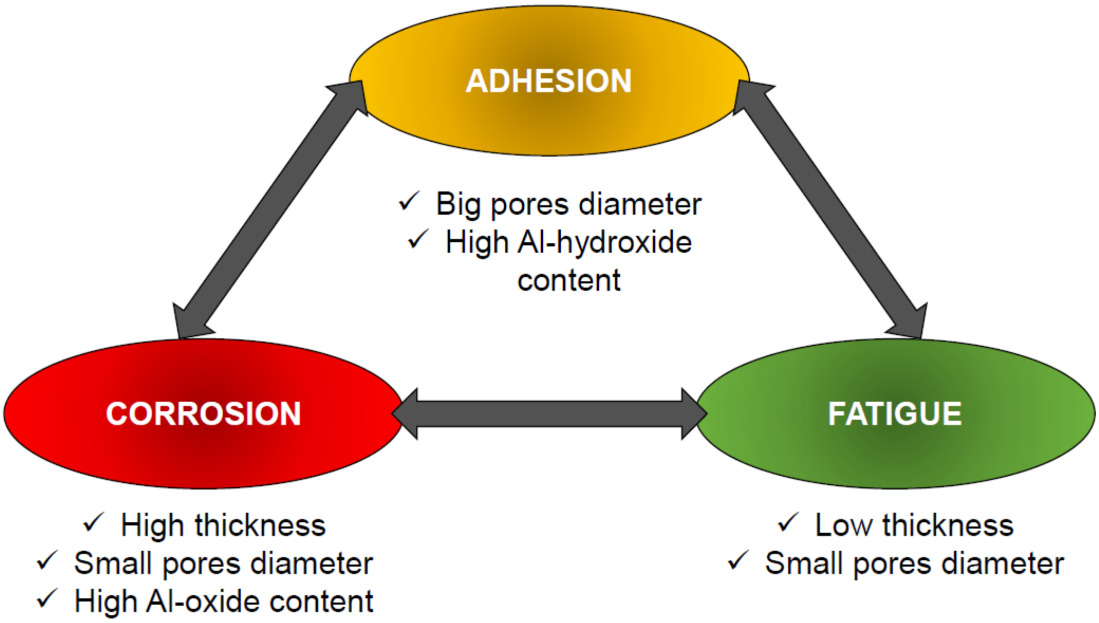

***Figure 1-12**: Contradictory requirements of oxide layers produced by anodizing process as a pre-treatment for painting.*

The porous anodic layer is used as a protective barrier against corrosion and also plays a key role as a base for paint and organic coatings loaded with corrosion inhibitors. Corrosion resistance is found to be increased as the thickness of the oxide layer increases, on the other hand, the presence of pores improves adhesion to organic coatings while improving anticorrosive properties. However, from a purely mechanical point of view, the pores act as stress concentration sites as geometric singularities on the surface of the component and thus represent preferential fatigue crack nucleation locations under the action of external cyclic loads. Smaller pores affect fatigue life less significantly but reduce the adhesion capabilities of the anode layer, thicker films provide more pores and higher oxide concentration favoring corrosion resistance at the expense of fatigue life. It has been widely reported that the presence of an anodic layer is deleterious to the fatigue properties of the aluminum substrate [85–88]. The higher brittleness of the anodic film, typical of ceramic-like materials, compared to the substrate promotes crack formation in the anodic layer. Considering that the fatigue life of in component is 90% represented by the crack nucleation phase, it is easy to understand the effect of increased sensitivity to crack initiation determined by the presence of the anodic layer. Studies have shown a fatigue limit reduction of about 50 percent in the case of anode layer thicknesses of 10 microns and up to 75 percent for thicknesses of 60 microns on 7xxx aluminum alloy anodized in a sulfuric acid electrolyte [89].

It is therefore immediate to observe how the achievement of the three fundamental requirements for the realization of an ideal anodic layer for aeronautical applications is based on a careful balancing of the physical properties of the anodic film, specifically the thickness and density and size of the pores.

1.7.3. Alternatives to the chromic acid anodizing (CAA) process

For years, chromic acid has been the ideal solution for corrosion protection systems in aviation applications because it can offer an excellent balance of adhesion characteristics, corrosion resistance and fatigue performance [90,91]. Restrictions imposed on the production and use of Cr-(VI)-based compounds due to environmental and health concerns has driven research toward finding alternative solutions that can provide a similar balance of properties. The main candidate electrolytes for chromic acid replacement fall mainly into two groups: phosphoric acid-based electrolytes and sulfuric acid-based electrolytes. The two processes resulting from the use of these two classes of electrolytes are phosphoric acid anodizing (PAA) and sulfuric acid anodizing (SAA), respectively. Phosphoric anodizing provides excellent adhesion properties but reduced corrosion resistance due to the open-pore morphology of the anodic layer, characteristics that make this process ideal for structural bonding applications only [92]. The sulfide solution anodizing process results in the formation of a dense, sulfate-enriched anodic layer that provides excellent wear and corrosion resistance properties, however, its low porosity and the greater thicknesses of the anodic layer compared to those obtained with CAA result in lower susceptibility to adhesion and reduced fatigue strength [93–96]. However, some studies have shown that the addition of weak organic acids, such as tartaric, malic or citric acid, to the sulfuric solution leads to the formation of porous anodic layers typical of aircraft protection systems [97]. The anodization process resulting from the integration of an organic tartaric acid into a sulfuric solution is called tartar-sulfuric acid anodization and will be discussed extensively in the next section.

1.7.4. Tartaric-sulfuric acid (TSA) anodizing

Sulfuric tartaric acid anodizing was first introduced into the industrial environment in the early 2000s once it was known that its addition to a sulfuric acid electrolyte helped to increase the corrosion resistance provided by the anodic layer. Initially, the function of tartaric acid within the solution was not well understood: studies showed that the addition of tartaric acid causes a significant reduction in steady-state current at constant voltage during 2xxx aluminum anodizing and that the concentration of tartaric acid in solution corresponds to a reduction in steady-state current density until a minimum is reached [95]. The reduction in steady-state current may be caused by the increase in electrical resistance caused by the incorporation of tartaric acid into the anode layer. On the other hand, the increase in corrosion resistance of the TSA layer compared with an SAA layer has been associated with the repelling properties of tartaric acid and compounds derived from it, particularly tartrates resulting from the reaction of aluminum cations with tartaric acid that are deposited within the pores generated during the anodizing process [95,97]. Aluminum tartrates have a very high solubility in acidic environments; however, the solubility is drastically reduced in water. When the anodized surface is exposed to an aggressive environment, the aluminum tartrates deposited within the pores solubilize, creating an additional barrier to oxidation phenomena.

1.7.5. Process Steps of Tartaric-sulfuric acid anodizing process

Anodizing is not a stand-alone process but is embedded within a more complex and structured process consisting of a series of pre- and post-surface treatments. Pre-treatments are intended to prepare the surface for the subsequent anodizing process and are divided into three types: degreasing, alkaline etching, and an d pickling (Figure 1-13).

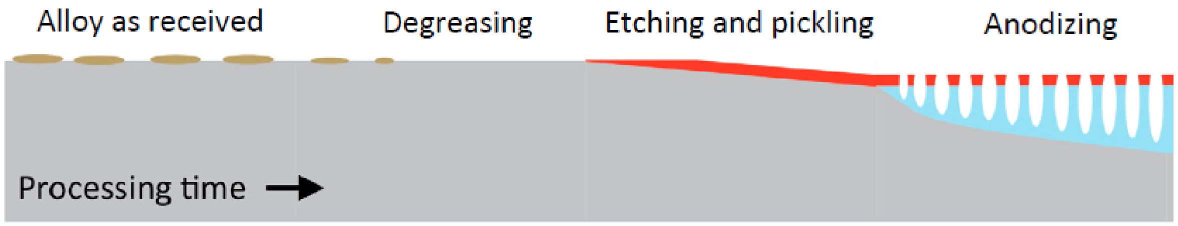

***Figure 1-13**: Schematic representation of the process steps and the modifications that take place during the pre-treatments to anodizing* [98].

Degreasing consists of removing any traces of residues or contamination, such as oils and lubricants, related to the previous technological processing and aims to ensure maximum wettability of the surface that will undergo anodizing. This is done using a low-alkaline cleaner due to the rapid dissolution of aluminum in alkaline solutions [90].

Alkaline etching consists of immersing the component within an aqueous solution based on sodium hydroxide. The purpose of this step is to eliminate surface changes (changes in composition, breakdown of intermetallics in the matrix, etc.) caused by the high shear deformations experienced during the technological processing. During this step, it is important to pay close attention to the presence and number of additives in the solution and the temperature of the bath as they may trigger unwanted reactions at the aluminum/oxide interface. Chemical etching can also affect the chemical composition of the substrate material: in particular, the removal of the magnesium-enriched layer and enrichment of alloying material, such as copper, in the substrate is generally observed [99–102].

The difference between alkaline etching and acid pickling is not well defined since both steps involve modification of the component surface by chemical dissolution. In general, the pickling process should be aimed at removing insoluble products formed during the previous alkaline etching steps. For this, a solution consisting of a combination of acids, usually sulfuric acid, nitric acid and ferric sulfate, is used, within which the sulfuric acid reacts with tin, zinc and copper to form the corresponding salts, the nitric acid neutralizes the copper compounds present at the oxide layer and the iron sulfate acts as an oxidizing agent [103].

Post-treatments include sealing and painting. Sealing is used for parts that are intended to be used without being painted and involve soaking the anodized component in boiling water, with additives added if necessary, or sealing electrolytes to close the pores formed during the previous anodizing. During immersion, there is the dissolution of aluminum oxide in water, deposition of gel-type aluminum hydroxide on the anodized surface, and subsequent formation of an aluminum compound, pseudo-boehmite, due to condensation of the gel [104]. This process, which is also referred to as the alumina hydration mechanism, allows the corrosion resistance of the anodic layer to be increased.

CHAPTER 2

RESIDUAL STRESS-BASED APPROACH FOR FATIGUE DESIGN

Preface

Evaluation of mechanical properties plays a major role in materials design in the aerospace industry. Structural components are subjected to the action of cyclic loads during all phases of flight, from takeoff to landing, making the study of fatigue properties a fundamental prerequisite to designing Residual stresses can significantly influence the fatigue behavior of a component. They are self-balancing stresses that overlap with external stresses altering the overall stress state and leading to different effects depending on the sign of the stresses: tensile residual stresses near the surface of the part tend to accelerate the nucleation and propagation phases of fatigue cracks; conversely, compressive residual stresses can prolong fatigue life by opposing the crack tip aperture. Generally, tensile residual stresses are introduced unintentionally within the material as a result of technological processes of welding, forging, bending; on the other hand, compressive residual stresses are purposefully generated through the application of specific surface treatments aimed at improving the fatigue properties of the material. This chapter will initially propose a brief review of the concept of fatigue and the basic principles of fracture mechanics. Next, the role of residual stresses on the fatigue behavior of metallic materials will be analyzed, focusing on the characteristics of residual stress fields required in fatigue-critical aircraft applications and the main experimental methods for the evaluation of residual stresses.

2.1. Theoretical framework of Fatigue and Fracture Mechanics

2.1.1. Definition of fatigue parameters

The application of cyclic loads results in the formation of microscopic physical damage that accumulates during load cycles leading to the development of fatigue cracks and eventually to material failure. This phenomenon is known as fatigue and occurs even at stress values significantly lower than the yield strength of the material. Fatigue failure has been a subject of study for more than 150 years and is still a concern for engineering design. Indeed, the fatigue phenomenon is associated with most mechanical component failures during service life, and its economic impact is compounded by the need for component replacement and preventive interventions. To date, however, the phenomenon of fatigue in metallic materials is well understood, and there are numerous textbooks available that comprehensively describe and analyze the theoretical and practical fundamentals needed to understand, evaluate, and predict fatigue and fracture of materials and structures [105–108].

At least two stress-related parameters are required to identify a stress cycle, in addition to frequency. In the absence of corrosion phenomena, the frequency parameter is supposed to have no influence on the fatigue behavior of a metallic material for loading frequencies below 100 Hz. In the case of periodic and constant-amplitude cyclic stress, maximum and minimum stress, mean stress and alternating stress, or stress ratio and stress range can be chosen indifferently as representative parameters of the load cycle. The definition of each parameter and the nomenclature associated with the load cycles are proposed in Table 2-1 and Figure 2-1, respectively. Similar parameters can be found if strains, tangential stresses or loads are used instead of normal stresses.

Table 2-1*: Definition of all the possible parameters used to define fatigue load cycle.*

Parameter	**Definition**
Maximum Stress	σ_{max}
Minimum Stress	σ_{min}
Mean Stress	$\sigma_m = \frac{\sigma_{max} + \sigma_{min}}{2}$
Alternating Stress	$\sigma_a = \frac{\sigma_{max} - \sigma_{min}}{2}$
Stress Range	$\Delta\sigma = \frac{\sigma_{max} - \sigma_{min}}{2} = 2\sigma_a$
Stress Ratio	$R = \frac{\sigma_{min}}{\sigma_{max}}$
Amplitude Ratio	$R_a = \frac{\sigma_a}{\sigma_m}$

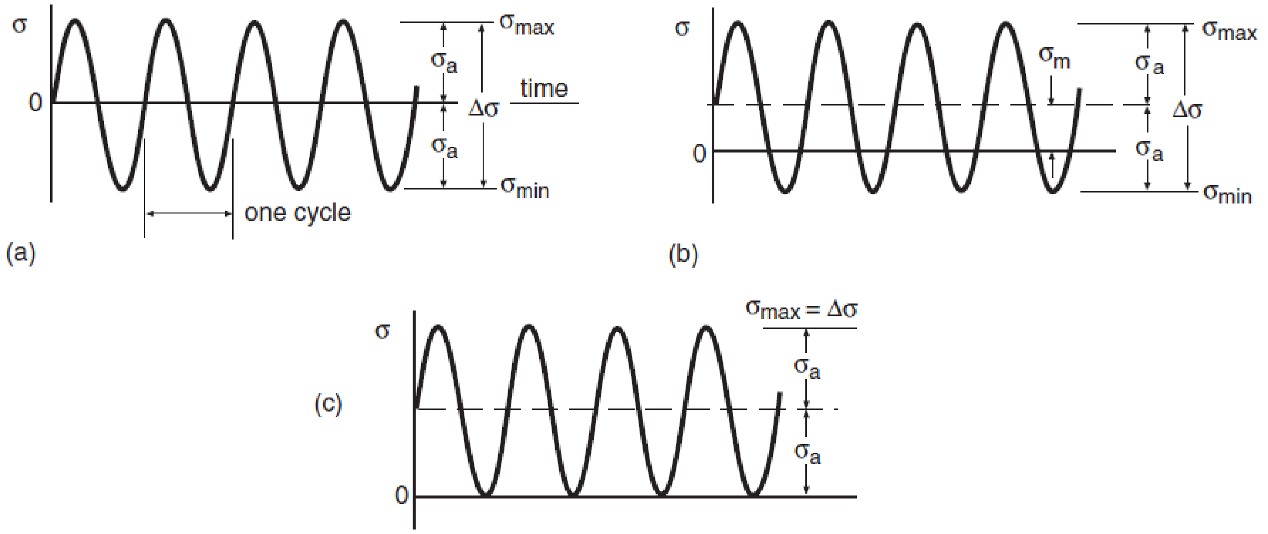

Figure 2-1: *Constant amplitude cycling and the associate nomenclature: a) completely reversed stressing, b) non-zero mean stress, c) zero-to-tension stressing.*

2.1.2. Physical interpretation of fatigue damage

The fatigue failure process can be divided into three stages: crack nucleation, stable crack propagation and final fracture.

The nucleation phase generally occurs at the surface of the component. The motion of dislocations favored by the favorable orientation of some surface grains generates sliding between crystalline planes at 45° to the direction of load application. This sliding leads to the formation of micro-cracks that act as nucleation sites for fatigue cracks. As the stress continues, the slip bands tend to enlarge and extend to adjacent grains. When the slip bands manage to penetrate to a distance of a few grains from the surface of the material, they tend to coalesce and thus propagate perpendicularly to the loading direction, initiating the propagation phase. Propagation can occur by striation formation, by coalescence of microvoids (especially for ductile materials) or by micro cleavage (especially for brittle materials). When the crack reaches a critical size, brittle fracture or plastic collapse of the part occurs. The number of cycles corresponding to the various phases varies with the applied stress amplitude. The nucleation phenomenon is generally predominant at lower stress amplitudes and gradually becomes less important as the stress amplitude increases leading to an increase in the duration of the stable crack propagation phase.

The phenomena of crystal plane slippage, nucleation and microcracks propagation occur entirely at the microscopic level and are mainly influenced by the material free surface conditions and the heterogeneity of the stress distribution around the grain boundaries. Local stresses can take on very different values from global stresses in the presence of stress concentrators such as microstructural defects (pores, voids) or geometric singularities (holes, fillets). For this reason, the parameter governing the nucleation phase of fatigue cracks is the stress concentration factor K_t which will be examined in detail later in this chapter. The stable crack propagation phase, on the other hand, is controlled by the stress intensity factor K, which is a measure of the severity of the crack situation as affected by the crack size, the stress state and the component geometry. Instead, final failure is described by the fracture toughness factors K_{1c} and K_c which represent the resistance to brittle fracture in the presence of a crack (Figure 2-2).

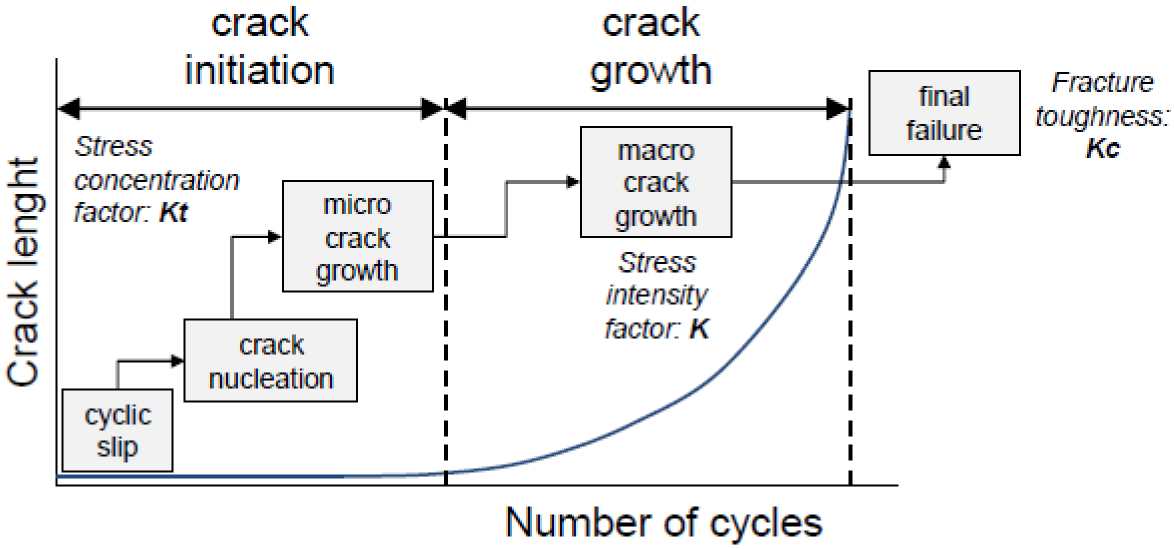
crack initiation
crack growth
Crack lenght
Stress concentration factor: **Kt**
micro crack growth
macro crack growth
final failure
Fracture toughness: **Kc**
Stress intensity factor: **K**
crack nucleation
cyclic slip
Number of cycles

***Figure 2-2**: The fatigue stages and the parameters used to describe them* [109].

2.1.3. Fatigue data analysis

As just highlighted, the fatigue life of a component is the sum of the period of fatigue crack nucleation and the period of fatigue crack propagation to final failure. In structural components characterized by small bearing sections, the macroscopic crack growth phase is negligible compared to the crack initiation period due to the absence of bulky material. In these cases, it is possible to describe the fatigue phenomenon using the so-called fatigue life approach. If a specimen of an engineered material or component is subjected to cyclic loading of sufficient intensity, the specimen will show fatigue damage or possibly failure after a certain number of loading cycles. If we repeat the test at different load values, we will notice that the fatigue life of the component will vary as the load level changes (Figure 2-3).

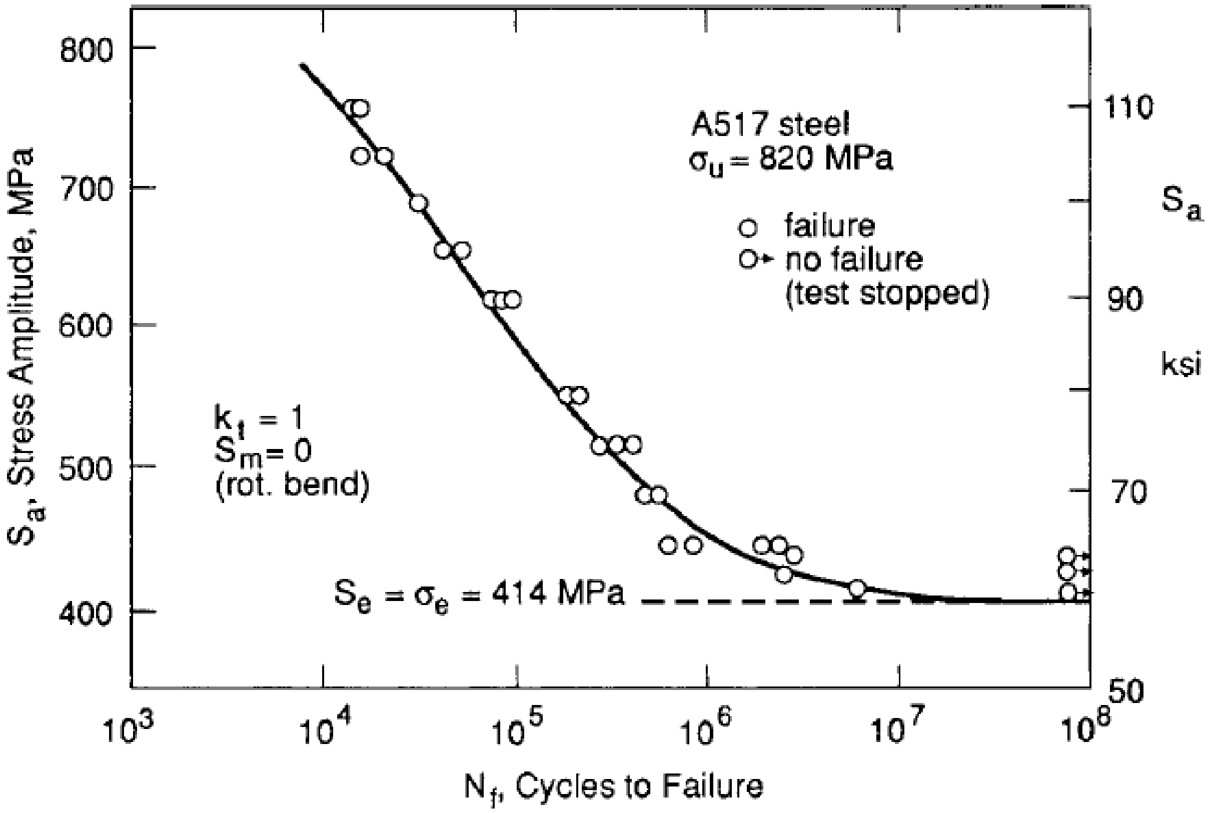

Figure 2-3: *Rotating bending S-N curve for unnotched specimens of a steel with a distinct fatigue limit* [110].

Basic fatigue data are obtained from tests with uniaxial nominal stresses of constant amplitude and are normally represented in diagrams with the natural logarithm of the number of cycles to failure on the abscissa and the applied stress on the ordinate. These diagrams are called Wohler diagrams or S-N diagrams. The diagram mainly consists of three regions: in the first zone, up to about 10^4 cycles, the maximum stress value is slightly above the yield strength of the material, and the trend of the curve is almost horizontal: it represents the oligocyclic fatigue region. In the second zone, the stress is lower than the yield strength of the material, and the region extends to about 10^6 cycles. This is the region of finite fatigue life. The third zone has a horizontal asymptote as the fatigue life of the component becomes theoretically infinite below a specific stress value. This stress value was defined by Wohler as the fatigue limit. The fatigue limit occurs for many metallic materials, particularly steels and cast irons, but may not exist as in the case of some high-strength steels or aluminum alloys. Recent research has also demonstrated the existence of a second horizontal asymptote at a lower level than the fatigue limit, which falls within the scope of very high cycle fatigue (VHCF) theory and will not be addressed in this research activity [111,112].

Basically, there are two different statistical methods to determine the S-N curve:

- Linear regression analysis: several samples at different load amplitude levels are tested. The resulting set of points is plotted on a double logarithmic diagram, and a linear relationship is identified between the logarithm of the load amplitude and the logarithm of the number of cycles to failure (Figure 2-4a).
- Normal distribution analysis: different stress levels within the finite life range of the component are identified and a number of fatigue test repetitions are performed at each level. Assuming a Gaussian distribution, the point corresponding to a 90% of survival probability is derived for each stress level. The linear interpolation of the points obtained at each stress level will form the S-N curve of the material (Figure 2-4b).

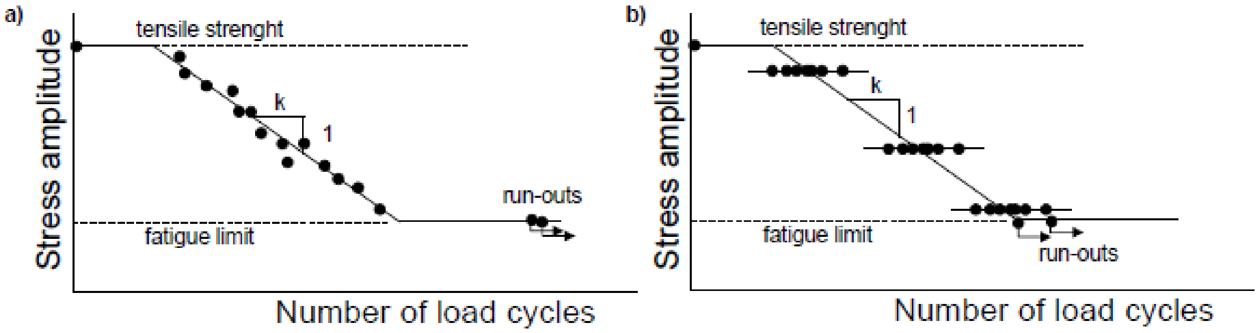

Figure 2-4*: Statistical methods to derive S-N curves of materials: a) Linear regression analysis; b) Normal distribution analysis* [109].

With appropriate statistical methods, it is possible to obtain S-N curves corresponding to a particular probability of survival or rupture. The diagrams showing the S-N curves as the probability changes are called S-N-P [113]. Fatigue life data are usually described with a log-normal distribution, although more refined distributions, such as the Weibull distribution [114], can provide more accurate results, especially in the fatigue limit zone. The most widely used statistical method for constructing S-N-P plots is least-squares interpolation. This method cannot account for run-outs, which are usually ignored thus losing valuable information. In some cases, the elimination of run-outs may lead to incorrect results, especially in the fatigue limit zone. In addition, one of the conditions underlying the least squares method is that the dispersion of fatigue data must be constant at all stress levels. Unfortunately, it is very common to observe low values of dispersion of fatigue data at high-stress values and conversely high dispersion at low-stress values due to the physical nature of the fatigue phenomenon. For this reason, another method of statistical analysis of fatigue data is often used, the maximum likelihood method, which allows the evaluation of both the influence of run-outs and non-constant dispersion of fatigue data [115]. However, such statistical analysis is not widespread in the industry, and there is still a tendency to prefer the least-squares interpolation method assuming constant dispersion and log-normal distribution of lifetime data at different stress levels.

2.2. Fatigue of notched components

Geometric discontinuities such as holes, fittings and keyways are termed stress raisers because they locally induce an intensification of the stress state applied to the component. Stress raisers, generally referred to as notches require close attention as their presence reduces the fatigue strength of a component. To address the problem of their influence on fatigue strength, however, it is necessary to preliminarily evaluate their influence on the stress state in the static case. In the areas where a notch is present, the assumptions of the Saint-Venant solid are negated. Notch always leads both to an increase in the average stresses in the notch section, due to the reduction in the resisting section, and to an alteration of the stress distribution over the section itself. In the context of elastic analysis, the stress distribution around the notch can often be determined analytically: it depends only on geometric factors, and the stress distribution is independent of the absolute size of the notch but depends only on its shape. In order to have a characteristic quantity that gives the essential information for calculation, the stress concentration factor was introduced:

$$K_t = \frac{\sigma_{max}}{\sigma_{nom}} \tag{1}$$

which is the ratio of the maximum stress in the notch to the nominal stress. It is important to note that the stress concentration factor does not provide information about either the trend of stresses within the part or the value of the stresses in directions other than that of the nominal uniaxial stress. The determination of stress concentration factors can be done analytically, many geometries, however, do not have closed-form analytical solutions; numerically by the finite element method (FEM) but the reliability of the solutions is strongly influenced by the size of the bottom notch radius; and experimentally by optical methods or application of strain sensors limiting the analysis to the elastic field. Several handbooks have been published that report stress concentration factor values for various geometries and types of applied loads [116]. An example of a diagram is shown in Figure 2-5. The K_t factor is given as a function of the dimensionless quantities that define the geometry of the component: the abscissa always shows the dimensionless bottom notch radius with respect to a characteristic dimension, while the various curves are parameterized with the ratio of the characteristic dimensions.

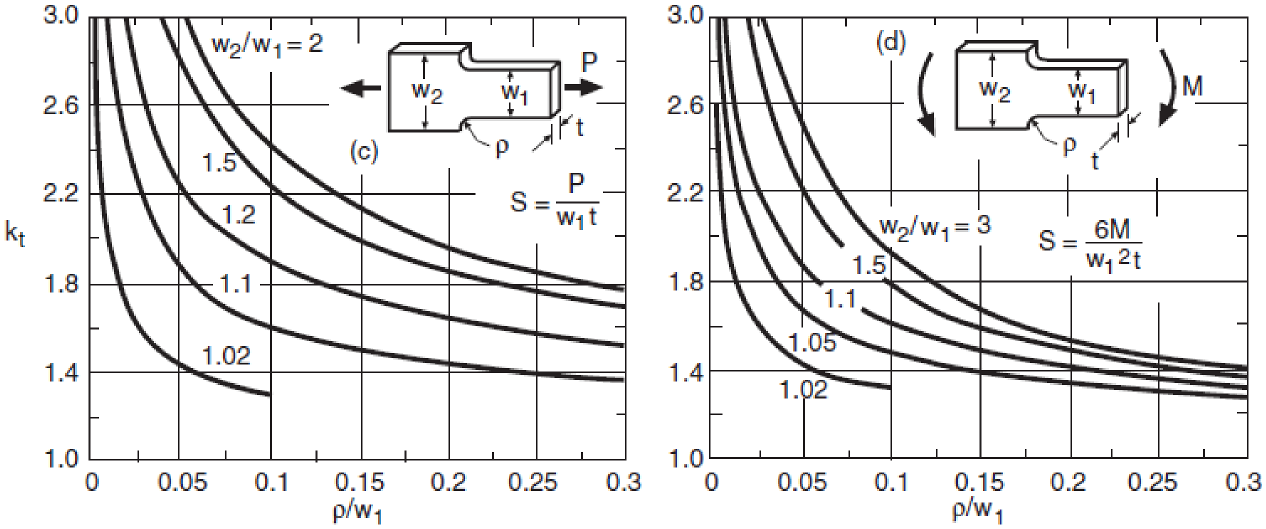

Figure 2-5*: Stress concentration factor as a function of characteristic dimensions and applied loads* [116].

From a simplified view of the problem, it might be expected that an unnotched and a notched component should exhibit the same fatigue life if the stress state σ_{nom} in the unnotched component is the same as the stress state $\sigma_{max} = K_t\ \sigma$ at the notch in the notched component, i.e., that the effect of the presence of the notch on an S-N diagram would be to reduce the stress amplitude corresponding to any given life by the factor K_t. However, it has been observed that this does not always correspond to reality and that notches generally have a lower effect on fatigue life than expected based on K_t value (Figure 2-6). It is therefore useful to introduce a new factor, the fatigue stress concentration factor K_f, which represents the actual reduction in the fatigue limit to which a notched component is subjected compared with an unnotched component and is thus defined as the ratio of the un-notched endurance limit to that for the notched members.

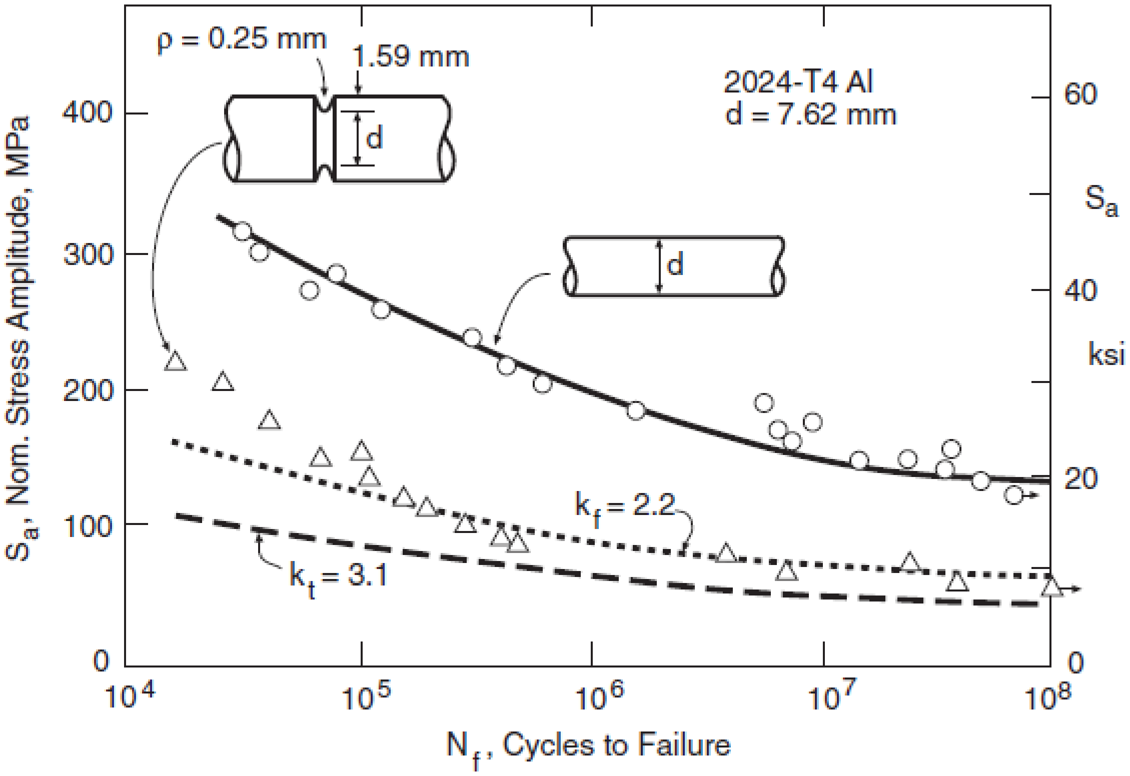

***Figure 2-6**: Comparison of S-N curves of an unnotched and a notched component* [117].

One reason why the presence of a notch affects the fatigue life of a component less significantly than expected can be associated with the local plasticization phenomena that may occur at the notch tip. The maximum local stress predicted by means of the K_t factor is based on elastic considerations and in no way contemplates plastic phenomena. The actual stress experienced by the component in the vicinity of the notch is lower than that estimated using K_t because the material would not be able to withstand stresses higher than the its yield strength limit without yielding. The occurrence of plasticization phenomena or local damage alters the stress distribution within a region of finite extent located near the notch tip, termed the process zone. Thus, the stress that controls fatigue crack initiation is not the peak stress calculated at the notch tip by means of K_t approach, but a lower-value average stress calculated over the process zone, hence the difference in behavior observed in the S-N diagrams. A second reason may be related to the fact that the fatigue crack in the case of the notched component propagates within a rapidly decreasing stress region, due to the local stress gradient induced by the presence of the notch, as opposed to uniform stress state typical of the unnotched component. The phenomenon of fatigue crack propagation will be examined in detail in the next section.

2.3. Basics of linear elastic fracture mechanics

The mechanical behaviour of a component containing a defect or crack is studied by fracture mechanics. To evaluate the stress state around a defect, the three basic modes of crack opening under the action of external loads must be considered (Figure 2-7).

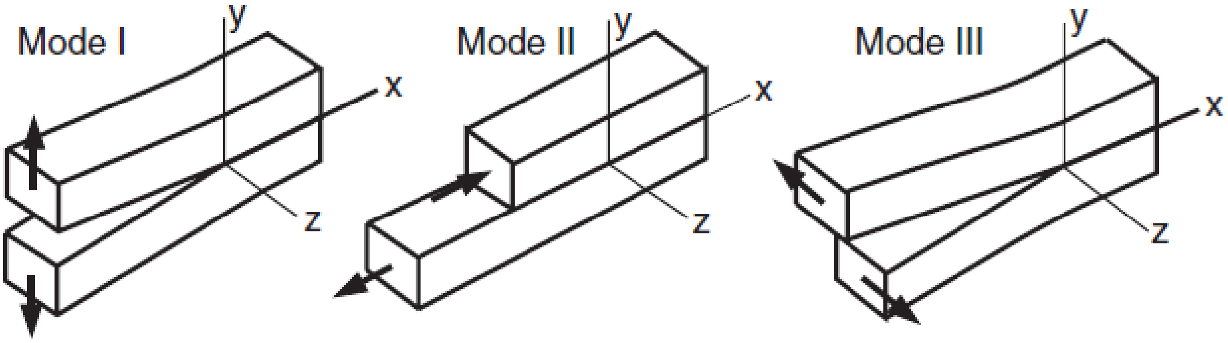

Figure 2-7*: The basic modes of crack opening: opening mode, sliding mode and tearing mode.*

Mode I is called the opening mode and consists of the detachment of the two faces of the crack. In Mode II, the sliding mode, the two crack faces slide over each other in a direction normal to the leading edge of the crack. Mode III, the tearing mode, always consists of mutual sliding of the two crack faces but in a direction parallel to the crack leading edge. Mode I is generally caused by tensile loading, whereas the other two modes are caused by shear loading in different directions. Most crack problems of engineering interest involve or can be linked to Mode I opening, so we will limit the discussion to this type of loading.

Let us consider an infinite plate containing a through-the-thickness crack of a length of *2a* which is loaded in tension (Mode I opening).

The components of the stress tensor in the x-y plane at the crack tip can be calculated using the formulas derived by Westergard [118].

$$\sigma_x = \frac{K_I}{\sqrt{2\pi r}}\cos\frac{\theta}{2}\left(1-\sin\frac{\theta}{2}\sin\frac{3\theta}{2}\right)+o(r) \tag{2}$$

$$\sigma_y = \frac{K_I}{\sqrt{2\pi r}}\cos\frac{\theta}{2}\left(1+\sin\frac{\theta}{2}\sin\frac{3\theta}{2}\right)+o(r) \tag{3}$$

$$\tau_{xy} = \frac{K_I}{\sqrt{2\pi r}}\cos\frac{\theta}{2}\sin\frac{\theta}{2}\cos\frac{3\theta}{2}+o(r) \tag{4}$$

or concisely:

$$\sigma_{ij} = \frac{K_I}{\sqrt{2\pi r}} f_{ij}^{I}(\theta) \tag{5}$$

where r and θ are the polar coordinates of the point under consideration, assuming the origin of the system at the crack tip, and K_I is a constant that depends on the geometric factor of the crack β, the nominal applied tension σ and the absolute size of the defect a. This constant is called the stress intensity factor and is obtained as follow:

$$K = \beta\sigma\sqrt{\pi a} \tag{6}$$

Analyzing the equations of the stress state in the crack's surroundings, it can be seen that the intensity of the stress field depends only on the stress intensity factor: the mechanics of the fracture is therefore based on what happens in the defect's surroundings and not on what happens at a single point in the structure. It is also important to observe what happens in the x-direction, i.e., the crack propagation direction: normal stresses tend to infinity for r tending to zero. As analyzed in the previous section, this is not possible because in real materials the stress cannot exceed the yield limit without local plasticization phenomena occurring. Therefore, a region of plasticization will be generated near the crack tip and the extent of this region will depend on the type of stress to which the component is subjected, as demonstrated by Irwin [119].

If the value of the stress intensity factor at the maximum stress does not exceed the fracture toughness value of the material and there are no plastic failure phenomena, the crack can propagate stably until it reaches a critical size that leads to failure. From a microscopic point of view, defect propagation during a loading cycle can be explained as follows: as loads increase, localized plastic sliding occurs at the crack tip, leading to rounding of the tip itself. In the unloading phase, the material that has undergone the plastic deformation cannot return to the initial condition, and thus crack elongation occurs. From a mathematical point of view, crack growth turns out to be a function of the stress range, or equivalently the stress intensity factor range, and the stress ratio and will thus be given by:

$$\frac{da}{dN} = f(\Delta K, R) \tag{7}$$

The systematic study of defect propagation under cyclic loads was carried out by Paris [120], who first proposed an empirical formula that describes crack propagation and is commonly called "Paris's law". Paris observed that increasing the stress value increases the rate of crack propagation and decreases both fatigue life and defect length at failure. He also found that increasing the initial length of the defect increases the rate of propagation and decreases the fatigue life. Based on these observations he then formulated the expression to approximate this experimental trend:

$$\frac{da}{dN} = C(\Delta K)^n \tag{8}$$

where C and n are two parameters that depend on the material, stress ratio and other secondary variables such as test conditions. Based on the above relation, the following observations can be drawn: for defects of zero initial size, even at very high stress values, the change in crack length turns out to be zero; for stress values below a lower limit, crack propagation results to be zero; for stress intensity factor values higher than the fracture toughness of the material, the crack growth rate reaches very high values, approaching the sound propagation velocity in the material.

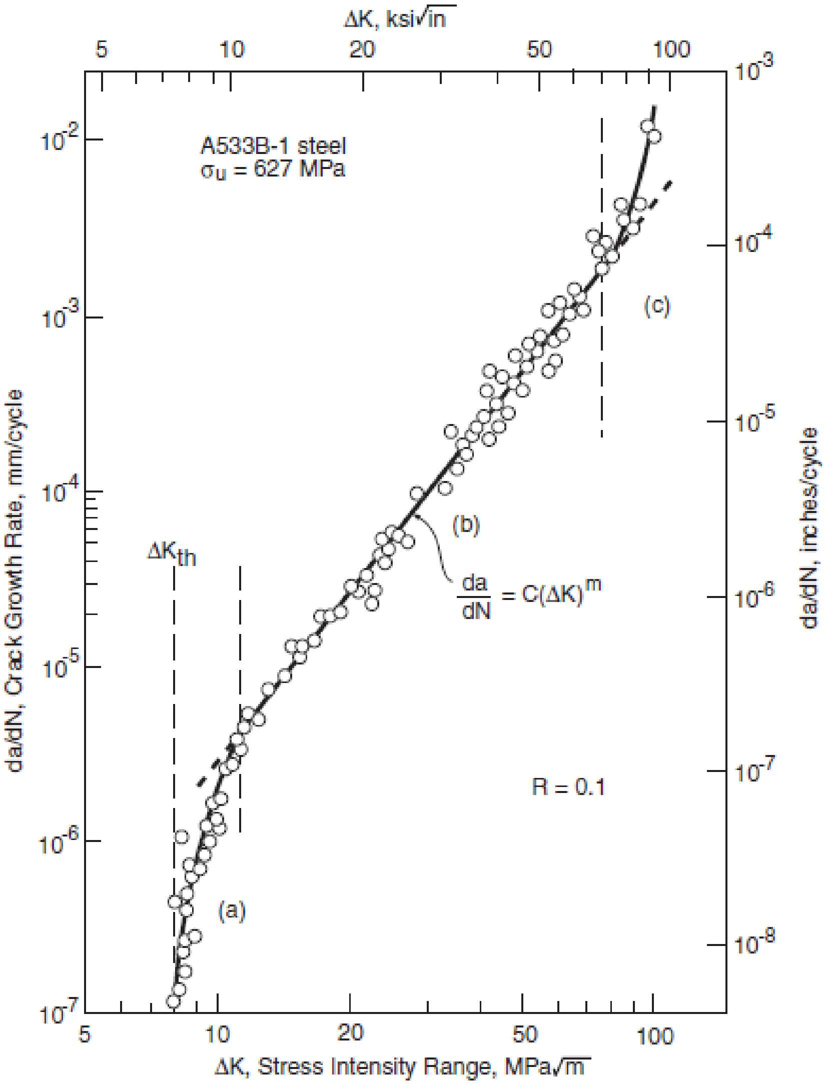

Figure 2-8: *Fatigue crack growth rates over a wide range of stress intensities for a ductile pressure vessel steel* [121].

The entire Paris curve (Figure 2-8) actually has a characteristic S-shape in which three characteristic regions can be identified: the first region corresponds to the period of crack nucleation and is characterized by a threshold K_{th} below which no appreciable crack growth is observed; the second region corresponds to the period of subcritical crack growth and represents the true range of application of Paris's law; and the third region corresponds to the transition from stable to unstable crack propagation that occurs when the stress intensity factor reaches the limiting value K_c.

Paris' law had some initial difficulties in being accepted. The main reason is that it uses concepts valid in the elastic field, particularly the stress intensity factor, to describe a phenomenon that is governed by plastic phenomena and that at the apex of the crack there is an area of plastically deformed material with possible residual stresses. This objection is overcome, however, if one considers that the coefficients of Paris' law are calculated under stress conditions similar to those that the real component will experience in the presence of a defect of similar size and thus contemplate the plasticization effects that this empirical relationship is accused of neglecting.

2.4. Overview of residual stresses

2.4.1. Effects of residual stress field on fatigue

Residual stresses are self-equilibrating stresses that exist within any material and structure regardless of the presence of any external load. Residual stresses can be generated during any manufacturing process or during service life as a result of the elastic response of the material to an incompatible local deformation, such as non-uniform plastic deformation. The material surrounding the plasticized region deforms elastically to preserve dimensional continuity leading to the formation of residual stresses. Because of their self-balancing nature, the presence of residual stresses can be ignored or underestimated during mechanical design leading to catastrophic consequences. In fact, these stresses add to external loads and their contribution can be beneficial or deleterious depending on their sign and location within the component.

The fatigue phenomenon is strongly influenced by the presence of residual stress fields, whether tensile or compressive, and their spatial distribution in the bulk of the material [122]. The fatigue behavior of a mechanical component or structure is strongly determined by the loading history it experiences. As analyzed in the previous sections, two of the main parameters that impact the fatigue properties of a material are the load amplitude and the stress ratio. Residual stresses do not cycle as applied external loads; they are effectively static stresses, and therefore do not affect the stress amplitude. However, they do affect the stress mean value and consequently the stress ratio by inducing changes in the fatigue life of the component. Consider, for example, the stress ratio obtained by adding the contribution of any residual stress field σ_{res} to the external stress components σ_{max} and σ_{min}.

$$R' = \frac{\sigma_{min} + \sigma_{res}}{\sigma_{max} + \sigma_{res}} \tag{9}$$

or equivalently using the stress intensity factor

$$R' = \frac{K_{min} + K_{res}}{K_{max} + K_{res}} \tag{10}$$

where K_{min}, K_{max} indicate the stress intensity factor due to the minimum and maximum values of the cyclic load, respectively, while K_{res} denotes the stress intensity factor due to the residual stress distribution alone. Let ΔK be the stress intensity factor range not considering residual stress and ΔK_{eff} be the stress intensity factor range in the presence of residual stress field.

It is assumed that fatigue damage does not occur when compression is transmitted across the crack faces.

If the residual tension field is tensile, the corresponding value of K_{res} will be positive and consequently R_{eff} will be greater than R and the value K_{eff} will be equal to K. On the other hand, if $K_{min}+K_{res} < 0$, then under the assumption that the residual stress field is compressive and its magnitude of such intensity as to balance the minimum load during the loading cycle, R will change according to Eq. 10 and ΔK_{eff} will be equal to

$$\Delta K_{eff} = K_{max} + K_{res} - 0 < \Delta K \tag{11}$$

as a result of the assumption that the crack is closed when a compressive load is applied. In this way Paris's law is modified as follows:

$$\frac{da}{dN} = C\left(\Delta K_{eff}\right)^n \tag{12}$$

with a consequent decrease in crack growth rate for a given ΔK.

This approach for evaluating the effects of the presence of a residual stress field on the crack propagation phenomenon is easy to apply since it only involves superimposing the residual stress field on the external stress state however, it has theoretical inaccuracies: it does not consider the nonlinearity of the contact conditions occurring between the crack flanks and it does not consider the nonlinearity between external loads and K_{eff}. As a result, the superposition principle should not be applied because the linearity condition is lost. Some studies have proposed alternative calculation methods, such as the weighted function method [123–125] and the finite element method [126,127], for the evaluation of K_{eff} and the proper application of this approach.

2.4.2. Characteristics of residual stress profiles

Residual stress profiles within a material can differ substantially depending on the technological process from which they originated, the geometric and physical properties of the material, and the service conditions. For illustrative purposes, a typical residual stress profile induced by the Laser Shock Peening process is shown in Figure 2-9.

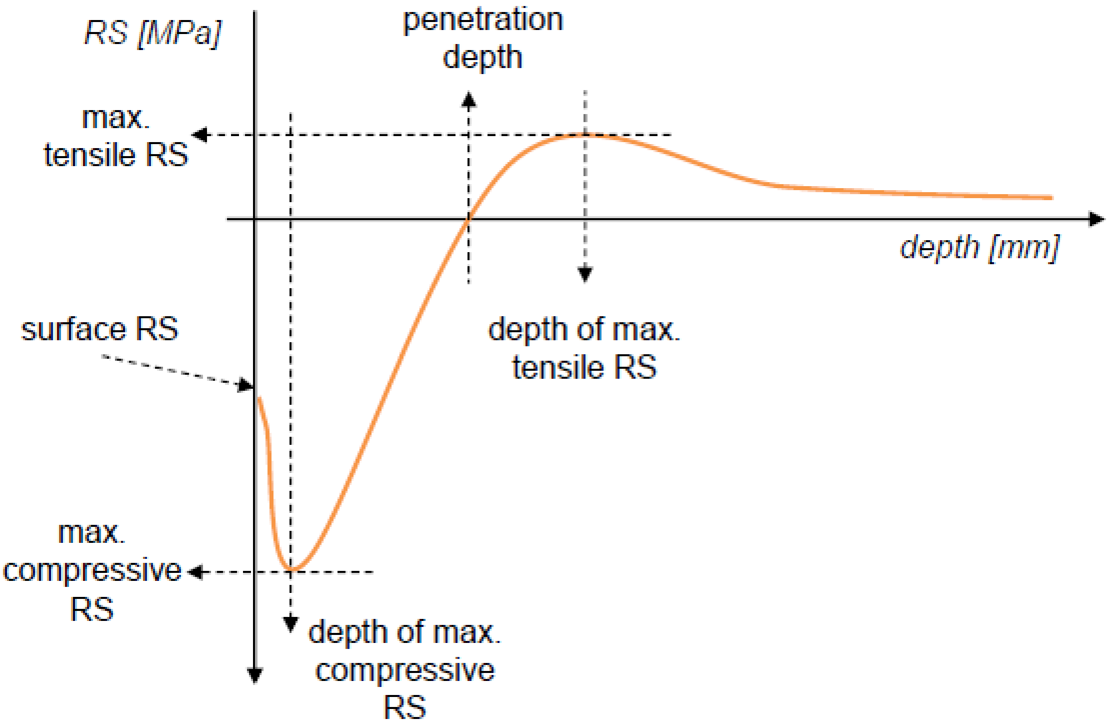

Figure 2-9: *Typical residual stress profile induced by Laser Shock Peening process.*

The residual stress profile can be fully defined by identifying the following characteristics: the value of the residual stresses at the surface of the workpiece; the peak value of the residual stresses, both tensile and compressive, and the corresponding depths of measurement; and the tensile/compression transition point or penetration depth. The surface residual stress state provides fundamental information on the condition of the region most affected by fatigue phenomena. This measurement can also be used for verification of the correct application of the technological process. The location and magnitude of the residual stress peak significantly influence the crack propagation phase, altering its growth rate and in some cases its trajectory. Often the residual stress peak is located close to the surface of the workpiece, a typical example being the residual stress field generated by the shot peening process, while in other cases, as in laser shock peening, the extent of the residual stress field is such that the location of the compressive peak can be as far away as 0.5-0.6 mm from the surface of the workpiece, depending on the adopted process parameters. However, it should be remembered that residual stresses constitute a self-equilibrating stress field and so the presence of local compression is always accompanied by the presence of tension at a different position in the component. Consequently, the greater the depth of penetration of the residual compressive stress field, the greater the extent of the region subjected to tensile stresses to ensure the overall equilibrium of the stress state. The geometry of the component also plays a key role because the amount and distribution of elastic material around the area affected by plastic deformation determines the characteristics of the residual stress field and the position of the equilibrating tensile stresses (Figure 2-10).

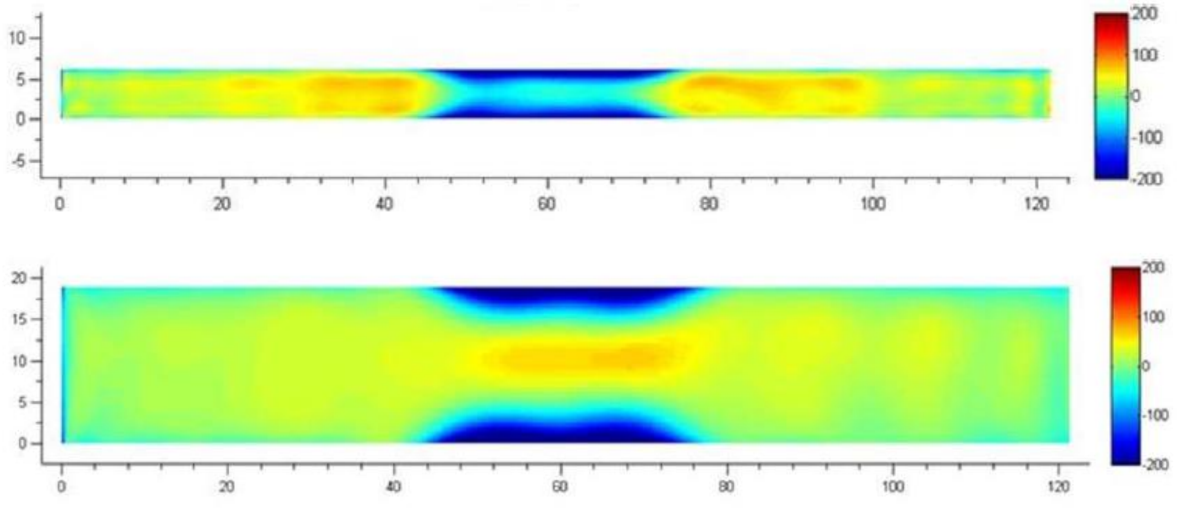

Figure 2-10*: Influence of geometry of the development of in-depth residual stress field.*

2.5. Methods of experimental evaluation of residual stresses

Residual stress measurement methods are indirect since they require the measurement of different quantities for their interpretation. There are different families of residual stress measurement methods: in the relaxation-based methods the deformations caused by the redistribution of residual stresses after cutting or removal of the material are used as the basis for estimating the originally existing residual stress field [128]. The deformations associated with material relaxation are elastic in nature, and therefore it exists a linear relationship between the deformation and the released residual stresses. There are different measurement technologies based on the relaxation method and they differ mainly in the cutting geometry, however all can be classified as destructive or semi-destructive measurement methods. For some specimen geometries the strain/stress relationship can be derived analytically, in other cases calibration by finite element methods is required. In almost all cases, however, the search for this relationship is complicated by the fact that the strain measurement is made in a region other than the one where material removal takes place and thus less affected by relaxation phenomena. The most popular and commonly used relaxation methods are the splitting method [129], sectioning method [130], layer removal method [131], hole drilling method, ring-core method [132] and contour method [133]. The hole drilling method is probably the most widely used relaxation method for measuring residual stresses and consists of making a small hole in the surface of the material and measuring strains in the surrounding region using strain gauges or full-field optical techniques. This method will be reviewed in detail in the following paragraphs.

Another class of residual stress measurement techniques is that based on the physical phenomenon of diffraction. In its most common variant, diffraction method is a nondestructive measurement method for evaluating surface residual stresses and is based on the ability of an electromagnetic radiation to measure the distance between atomic planes in a crystalline or polycrystalline material. The crystalline inter-plane distance can be associated with the intensity and direction of the stress state existing within the material, regardless of the nature of the stress, whether applied or residual. The measurement method based on the diffraction principle will also be addressed in detail later in this chapter.

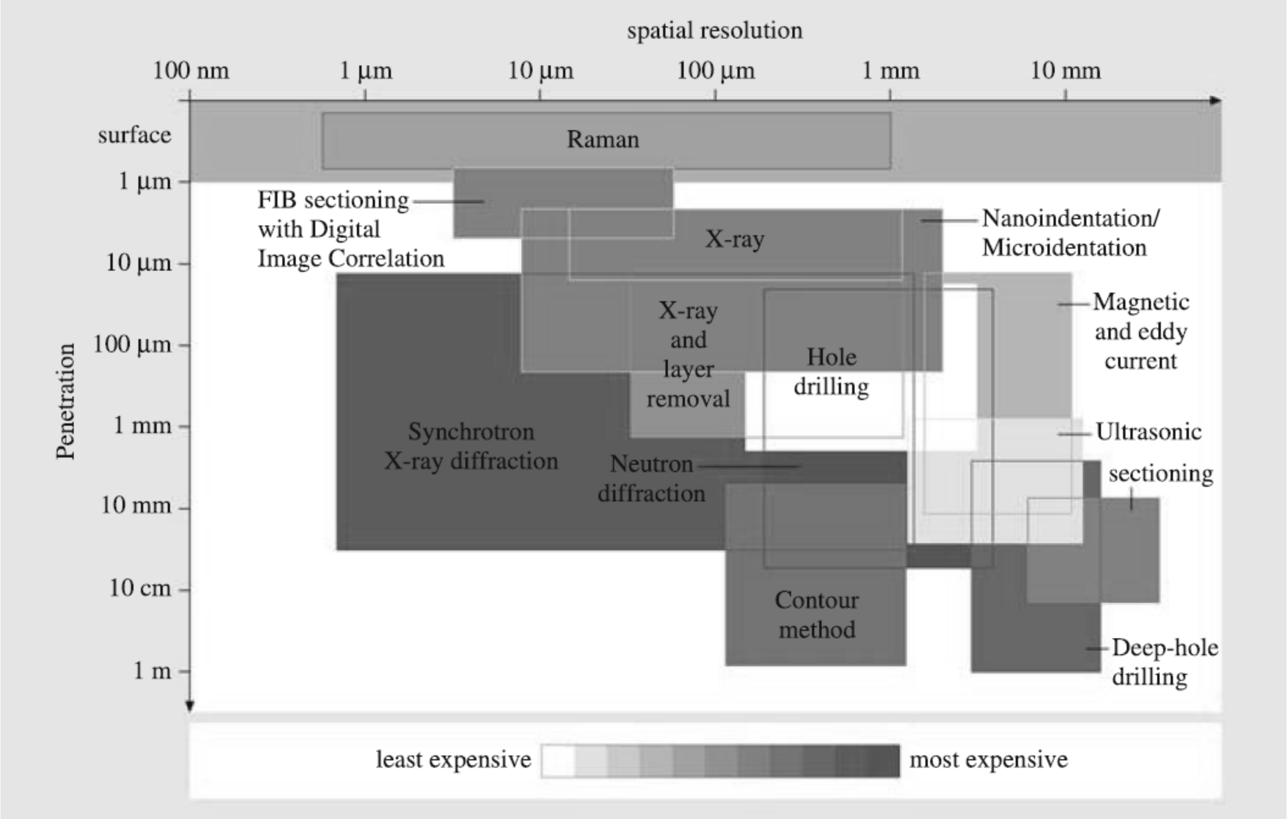

***Figure 2-11**: Measurement penetration and spatial resolution of different residual stress measurement techniques* [134].

Other methods of residual stress measurement include non-destructive and semi-destructive measurement techniques that rely on the measurement of properties associated with deformation. Magnetic methods, such as Barkhausen magnetic noise [135], consist of measuring the number and intensities of re-orientations of magnetic domains during the magnetization process of a ferromagnetic material. The ultrasonic method consists of measuring the speed of propagation of sound waves within the materials [136]. The thermoelastic method associates the field of elastic strain with the change in thermal energy of an elastic material [137]. The photoelastic method exploits the phenomenon of birefringence whereby a particular class of materials shows variable refractive index under the action of a stress field. By transmitting a polarized light through the material, a pattern of fringes representing shear stresses within the material is observed [138]. The last type of residual stress measurement method is indentation, which is based on the change in hardness experienced by a material in the presence of a residual stress state [139]. The different types of measurement are shown schematically in Figure 2-11, indicating for each of them the depth of penetration, or the ability of the technique to measure residual stresses within the material, and the spatial resolution. From the description of the different methods, it is evident that each has specific ranges of applicability, and the choice of the most suitable technique for the specific application must be made according to the type of material being investigated, the type of residual stresses to be evaluated and the geometry of the component, as well as on economic and time motivations.

2.6. Hole Drilling Method

The Hole Drilling method is the most widely used for residual stress measurement because it is relatively inexpensive, has standardized procedures and offers good accuracy and reliability. Although the method involves drilling a hole in the investigated region, it is sometimes classified as a semi-destructive technique because the damage is often tolerable or repairable. The hole is drilled on a component of linear elastic, isotropic and homogeneous material and on a flat, smooth surface away from any other surface, discontinuity or edge. The creation of the hole results in redistribution of residual stresses and in deformation of the surrounding region (Figure 2-12). These strains are measured by strain gauges or full-field optical methods and are subsequently associated with the original residual stress field through algorithms that take into account the geometry of the component.

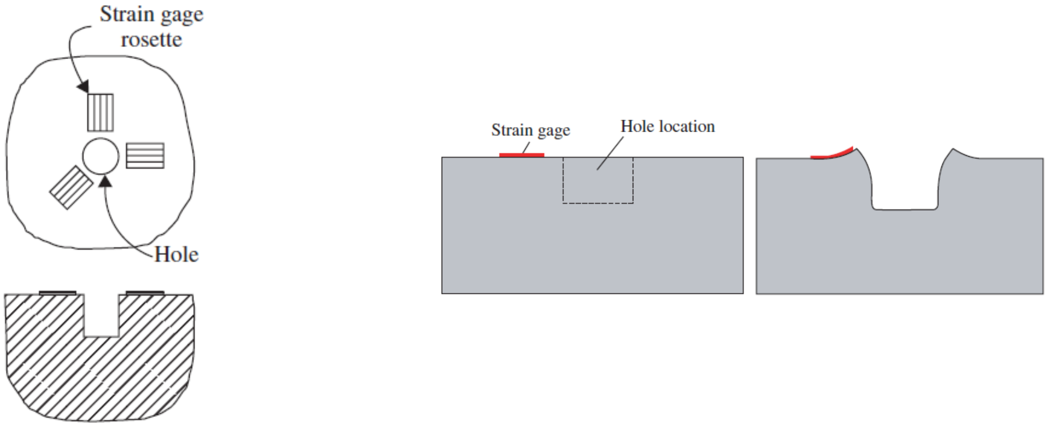

***Figure 2-12**: Application of a strain gauge rosette on the surface of the component and example of deformation caused by the presence of residual tensile stresses following the application of the Hole Drilling method* [140].

Strain gauges have proven to be a robust and reliable measurement method for measuring strains that develop during the measurement of residual stresses during hole drilling. ASTM E837 [140] describes the use of three different types of strain gauge rosettes to suit the required measurement range: Type A is a general-purpose design suitable for most measurement needs; Type B has the three strain gauge grids located on the same side with respect to the hole location and is therefore useful for making measurements near an obstacle; Type C, on the other hand, is a special type of rosette for measuring low residual stresses and for materials characterized by low thermal conductivity such as plastics (Figure 2-13).

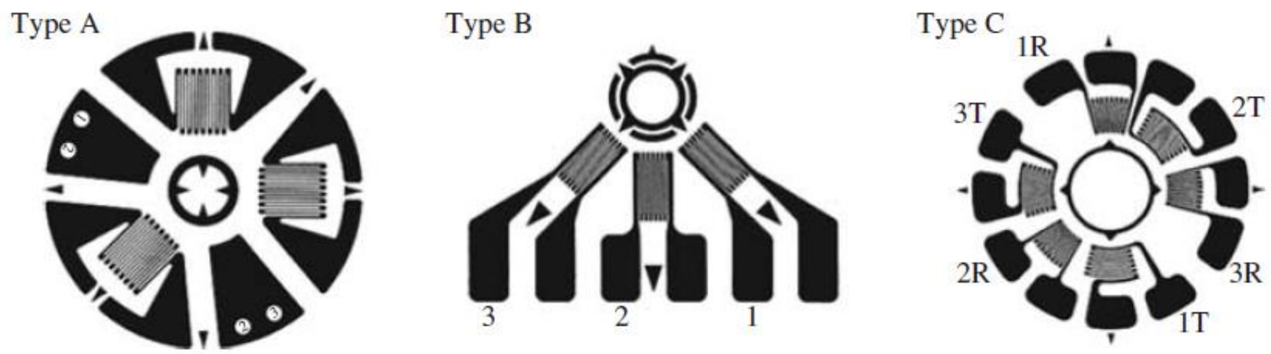

Figure 2-13*: Three types of strain gauge rosettes proposed by ASTM E837 standard for Hole Drilling Method* [98].

The nominal hole diameter is generally 0.4 times the average diameter of the hole on the rosette. The use of smaller diameters causes a reduction in output, particularly at the surface, while larger diameters can cause damage to the sensor. The maximum drilling depth is defined by the size and geometry of the rosette used and is 1.4 mm for Type B rosettes. The maximum depth at which residual stresses can be evaluated is lower than the maximum drilling depth and is again defined by the geometric characteristics of the employed rosette. The reason is that stresses calculated for each hole increment are evaluated in the center of the increment, so half of the final increment is subtracted from the total depth of penetration resulting in a lower evaluation depth. In the case of a Type B rosette, the maximum evaluation depth is therefore 1 mm. Another important aspect to be considered is the thickness of the component being examined. In the case of thin specimens, the drilling process can induce significant bending of the component depending on the intensity of the residual stress field present within the material. For Type B rosettes a minimum specimen thickness of 5 mm is recommended.

2.6.1. Hole Drilling Procedure

ASTM E837 gives the nominal hole diameters for Type A, B, and C rosettes. From a practical point of view, the drill size will be smaller than the suggested nominal size because during the drilling process, the presence of clearance or vibration causes holes of larger diameters to form compared to the dimension of the cutting tool. The size of the drill also depends on how the hole is made: in the case of orbital drilling, the size of the tool will be smaller than in the case of conventional plunge drilling. The cutting tool consists of a tungsten carbide head with an inverted cone shape with a 5° inclination on each side to facilitate chip removal. The drilling machine consists of a motor equipped with a spindle to hold the cutting tool, an alignment system to allow correct positioning with respect to the rosette, a depth control, tools to measure the diameter of the hole, and auxiliary tools for setting and clamping the component.

Once the strain gauge rosette is installed and the connection with the strain signal acquisition system is verified, the hole drilling machine is positioned so that the center of the drilling axis coincides with the center of the rosette. The drilling tool is then inserted into the spindle and locked into position. At this point, it is necessary to locate the point of contact between the drilling tool and the surface of the workpiece. Electrical contact or visual inspection will establish the point at which the tool tip makes contact with the surface of the workpiece after passing the back of the sensor and the adhesive layer. This location will represent the starting point of the drilling stage. The first drilling step is performed at a low feed rate, and once completed, the acquired strain values will be monitored until they stabilize as a result of material relaxation. The drilling and acquisition steps are repeated until the final drilling depth is reached. At the end of the measurement phase, any loss of adhesion of the rosette around the hole area is checked through the optical head to avoid alteration of the strain gauge measurements due to improper adhesion of the sensor. A check is also made for burrs at the edges of the hole, which may be an indication that plasticization of the drilling region has occurred. Following these preliminary checks, the rosette is removed and the hole size is measured averaging two perpendicular diameters. This data will represent will be provided as input for the application of the calculation based on the integral method.

2.6.2. Computation of the stresses during Hole Drilling

In the general case, residual stresses have different values at different measurement depths. The surface strain measured by the strain gauge grids will therefore be the combination of the individual strain contributions corresponding to each drilling step [141]. In the case of isotropic strains and stresses:

$$p(h) = \frac{1+v}{E}\int_0^h \hat{a}(H,h)\, P(H)\, dH \tag{13}$$

where $p(h)$ represents the combination of strain released when the hole reaches a depth h, $P(H)$ is the combination of the stresses that exists at a depth H from the surface, and $a(H,h)$ is a kernel function that contains the stress calibration constants. This relationship is mathematically classified as a Volterra equation of the first kind. It is an inverse problem since the quantity to be determined, namely the residual stresses, lies within an integral at the second member of the equation. A solution to this equation can be obtained using so-called inverse methods designed specifically for equations of this type. The most commonly employed computational approach is the integral method [142]. Internal stresses are assumed to be locally constant within each drilling step leading to a stepwise stress profile in the depth of the material (Figure 2-14).

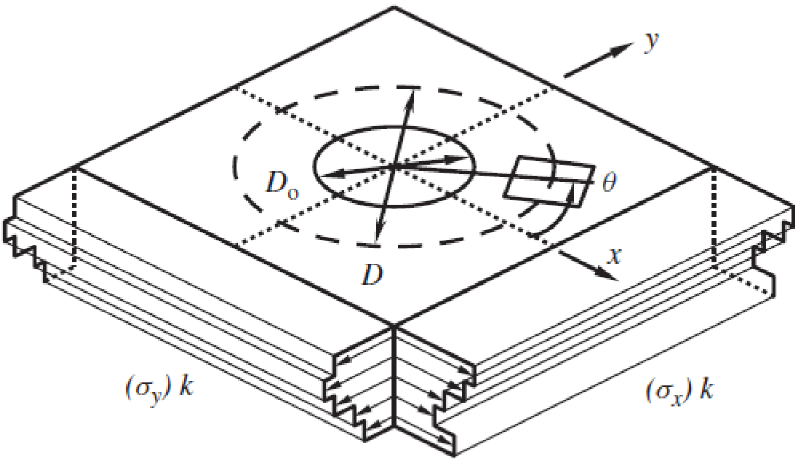

Figure 2-14: *Stepwise pattern of internal stresses in the definition of the integral method* [98].

With this approach, the problem of stress determination in the case of variable stress profile with depth can be traced back to the uniform stress case. Each element of the calibration constants *a* and *b,* expressed in matrix form, associates the stresses within the depth increment *j* with the strains measured with a hole *i*-increments deep.

$$\overline{a_{ij}} = \int_{h_{j-1}}^{h_j} \hat{a}(H, h_i)\, dH \qquad \overline{b_{ij}} = \int_{h_{j-1}}^{h_j} \hat{b}(H, h_i)\, dH \qquad (14)$$

From a physical point of view, the quantity $\overline{a_{ij}}$ represents the strain caused by a unit stress within increment *j* of a hole *i*-increments deep. With this generalization, it is possible to associate each stress component with its corresponding strain component using the following relations:

$$\overline{\boldsymbol{a}}\,\boldsymbol{P} = \frac{E}{1+\upsilon}\,\boldsymbol{p} \qquad \overline{\boldsymbol{b}}\,\boldsymbol{Q} = E\,\boldsymbol{q} \qquad \overline{\boldsymbol{b}}\boldsymbol{T} = E\,\boldsymbol{t} \qquad (15)$$

Where ***P***, ***Q*** and ***T*** respectively represent the isotropic, 45° shear and axial shear stresses and ***p***, ***q*** and ***t*** represent the isotropic, 45° shear and axial shear strains corresponding to the combination stresses ***P***, ***Q*** and ***T***.

There is a limit to the depth of stress assessment within the component. The farther the stresses are from the surface of the part, the less effect they will have on the strain measurement. Using the definition of the calibration matrix elements, the elements on the diagonal will approach values close to zero as drilling depth increases because they represent the strain corresponding to unit stresses applied to the bottom of the hole. The matrix then becomes singular and no longer invertible, consequently the stresses are no longer computable [143,144]. Hence the limit placed on the maximum residual stress evaluation depth established by the ASTM E837 standard.

2.7. Residual stress determination using X-Ray Diffraction

2.7.1. Basic Principles

The residual stress measurement by diffraction method measures the distance between atomic planes in crystalline materials in the presence of stress fields. The measurement of interatomic distance is carried out by exploiting the principle of diffraction: this phenomenon occurs when electromagnetic radiation, X-rays in our specific application, interacts with an ordered configuration of atoms and is absorbed and re-radiated in different orientations [145,146]. The angle at which constructive interference occurs between waves diffracted from the crystal lattice is defined by Bragg's law and is related to the interatomic distance through the relationship:

$$n\,\lambda = 2d\sin\theta \tag{16}$$

where n is an integer, λ is the wavelength of the electromagnetic radiation, d is the distance between the interatomic planes, and θ is the Bragg angle (Figure 2-15).

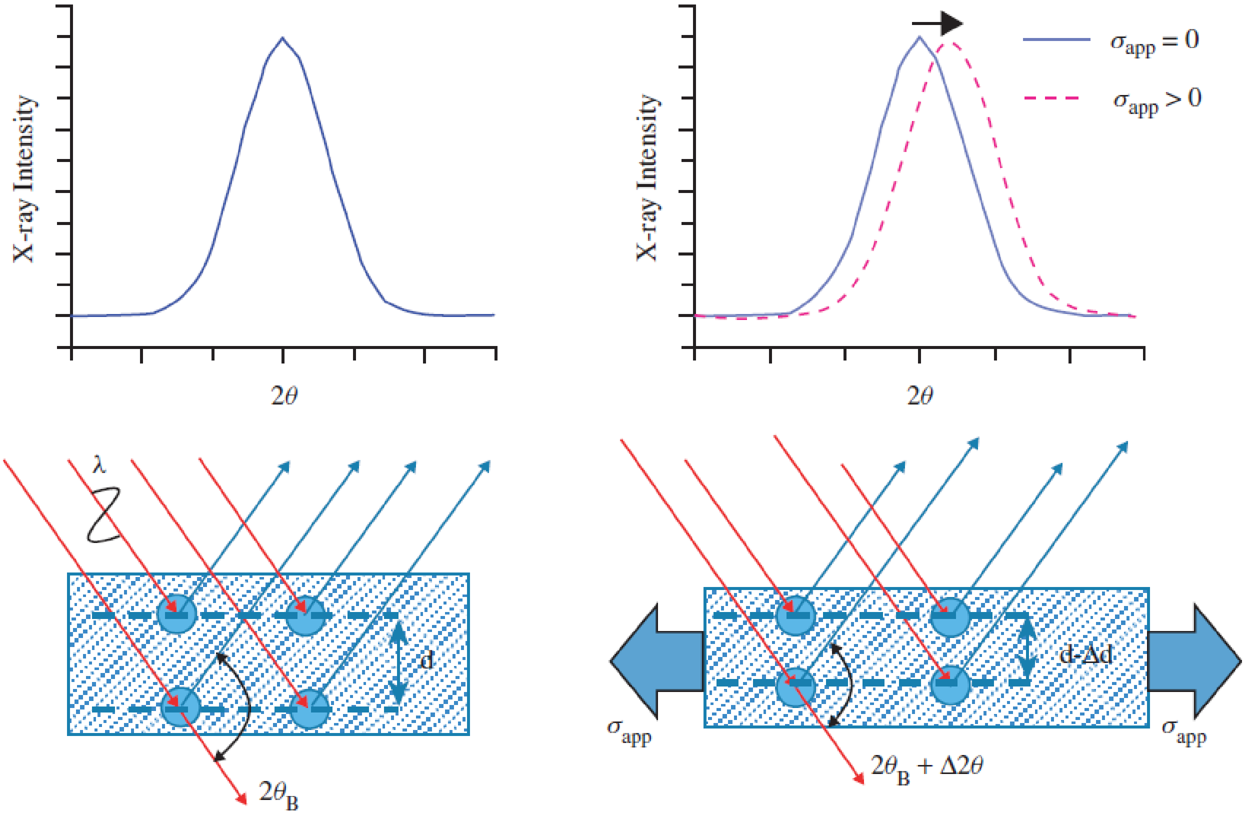
X-ray Intensity
2θ
X-ray Intensity
2θ
$\sigma_{app} = 0$
$\sigma_{app} > 0$
λ
d
$2\theta_B$
d-Δd
σ_{app}
σ_{app}
$2\theta_B + \Delta 2\theta$

***Figure 2-15**: Shift of the diffraction peak due to the application of external stress or the presence of a residual stress field* [147].

The possible presence of external or residual stresses alters the potential energy of the system of atoms by causing the atomic planes to shift to a new equilibrium position characterized by a different value of interatomic distance. Through the measurement of the new interatomic distance, it is possible to determine the stress state present within the material.

2.7.2. Measurement of lattice strain and stress computation

Let S_i: $\{S_1, S_2, S_3\}$ and L_j: $\{L_1, L_2, L_3\}$ be the reference systems of the specimen and the measuring device, which can be correlated through the two angles Φ and Ψ (Figure 2-16).

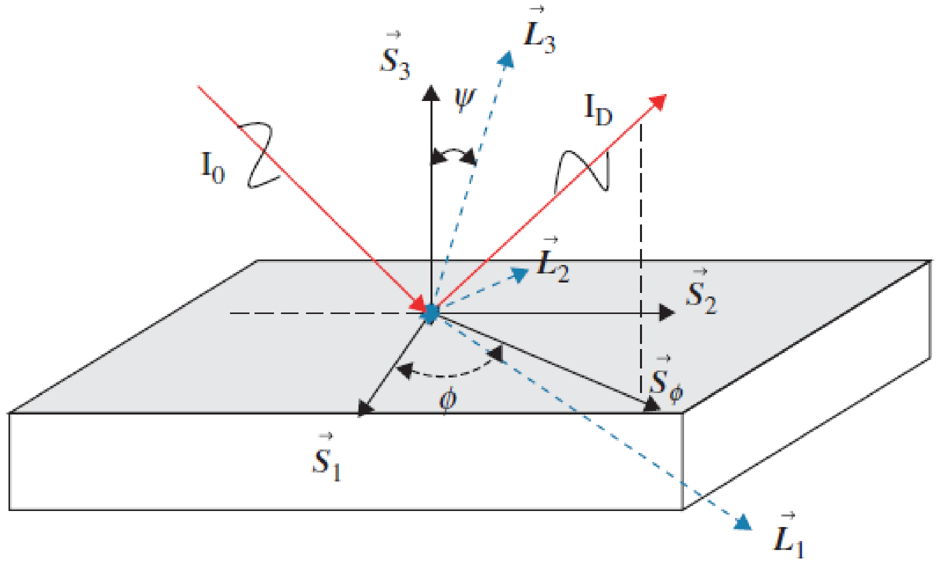

Figure 2-16*: Definition of the coordinate systems of the sample and of the diffraction head* [147].

The strain ε'$_{33}$ in the reference system *L* along the *L$_3$* direction can be derived by comparing the interatomic distance calculated using Bragg's law at the reflection plane identified by Miller's indices *(hkl)* and the reference interatomic distance *d$_0$* (undeformed material).

$$(\varepsilon'_{33})_{\Phi\Psi} = \frac{((d_{hkl})_{\Phi\Psi} - d_0)}{d_0} \tag{17}$$

The strain can be similarly expressed in the specimen reference system using a transformation matrix, obtaining:

$$\varepsilon'_{33} = a_{3k}a_{3l}\varepsilon_{kl} \tag{18}$$

Where a_{3k} and a_{3l} are the direction cosines between *L$_3$* and *S$_i$* axes. *Φ* and *Ψ* angles are known as they represent the relative position of the X-ray source to the sample. Combining the two previous equations yields the main equation for the determination of residual stresses by X-ray diffraction.

$$\begin{aligned}(\varepsilon'_{33})_{\Phi\Psi} &= \frac{((d_{hkl})_{\Phi\Psi} - d_0)}{d_0} \\ &= \varepsilon_{11}\cos^2\Phi\sin^2\Psi + \varepsilon_{12}\sin 2\Phi\sin^2\Psi + \varepsilon_{22}\sin^2\Phi\sin^2\Psi + \varepsilon_{33}\cos^2\Psi \\ &+ \varepsilon_{13}\cos\Phi\sin 2\Psi + \varepsilon_{23}\sin\Phi\sin 2\Psi\end{aligned} \tag{19}$$

It is a linear equation in six unknowns representing the six strain components in the reference system *L_j*. The equation can be solved by measuring six values of *d* along six independent directions. However, it is preferable to have a larger number of measurement points so as to reduce statistical errors. The main solving methods are the Dolle-Hauk Method and Winholtz-Cohen least-squares analysis. A detailed description of these methods is beyond the scope of this research and can be found in some reference texts.

Once the strain tensor is known, the stresses can be calculated using Hooke's law:

$$\sigma_{ij} = C_{ijkl}\varepsilon_{ij} \tag{20}$$

Under conditions of linearity and isotropy, this equation can be rewritten as follows:

$$\sigma_{ij} = \frac{1}{\frac{1}{2}S_2}\left(\varepsilon_{ij} - \delta_{ij}\left(\frac{S_1}{\frac{1}{2}S_2 + 3S_1}\varepsilon_{kk}\right)\right) \tag{21}$$

where δ_{ij} is the Kronecker delta and S_1 and S_2 the two X-ray elastic constants [148] defined as follows:

$$\frac{1}{2}S_2 = \left(\frac{1+\upsilon}{E}\right) \qquad\qquad S_1 = -\frac{\upsilon}{E} \tag{22}$$

There is an alternative method for stress evaluation that disregards the calculation of the strain tensor and the subsequent application of Hooke's law. If we consider Equation 19 again and express the strain components as a function of the corresponding stress components, under the assumption of isotropic material we obtain:

$$\begin{aligned}(\varepsilon'_{33})_{\Phi\Psi} &= \frac{((d_{hkl})_{\Phi\Psi} - d_0)}{d_0} \\ &= \frac{1+\upsilon}{E}(\sigma_{11}\cos^2\Phi + \sigma_{12}\sin 2\Phi + \sigma_{22}\sin^2\Phi - \sigma_{33})\sin^2\Psi + \frac{1+\upsilon}{E}\sigma_{33} \\ &- \frac{\upsilon}{E}(\sigma_{11} + \sigma_{22} + \sigma_{33}) + \frac{1+\upsilon}{E}(\sigma_{13}\cos\Phi + \sigma_{23}\sin\Phi)\sin 2\Psi\end{aligned} \tag{23}$$

which in the case of biaxial stress state is reduced to:

$$d_{\Psi} = \frac{1+\upsilon}{E} d_0 (\sigma_{11}\cos^2\Phi + \sigma_{12}\sin 2\Phi + \sigma_{22}\sin^2\Phi)\sin^2\Psi - \frac{\upsilon}{E}(\sigma_{11}+\sigma_{22})d_0 + d_0 \qquad (24)$$

It can be seen from Equation 24 that the relationship between the interplanar distance and the value of $\sin^2\Psi$ is linear and that the slope of the interpolation line represents the stress σ_{Φ} along the direction S_{Φ}. This technique is known as the "$\sin^2\Psi$ method". σ_{Φ} can be therefore determined directly from the slope of the d_{Ψ} vs. $\sin^2\Psi$ data.

2.8. Application of Hole Drilling Method and X-Ray Diffraction technique for LSP residual stress evaluation

Hole drilling and X-ray diffraction techniques are commonly used for the evaluation of residual stress fields induced by surface processes on metallic components. On the basis of the measurement methodology and the employed sensors, the Hole Drilling method allows the evaluation of residual stresses up to depths of about 1 mm from the surface of the component and thus the identification of the stress profile within the material. However, measurements near the surface are affected by a higher percentage of uncertainty due to the large effect of input uncertainties and the low level of strain measured in the small hole increment. The same is true for the last evaluation steps because of the reduced sensitivity of strain gauges placed at a high distance from the bottom of the hole. For this reason, it is advisable to supplement residual stress data obtained from a technique based on relaxation phenomenon with surface stress evaluation by X-ray diffraction technique. The non-destructive nature of the X-ray diffraction technique for surface residual stress evaluation allows the two measurement methods to be used in series for a complete and rigorous characterization of the residual stress state within the material. It is also possible to use the X-ray diffraction technique for the evaluation of the in-depth residual stress state by associating a material removal technique such as electropolishing, which allows the removal of material layers of defined thickness without altering the distribution of residual stresses originally present within the material.

Numerous examples related to the application of the Hole Drilling and X-Ray Diffraction method for the evaluation of residual stress fields induced by the Laser Shock Peening process on aluminum alloys of aerospace interest are present in scientific literature.

Guo [149] analyzed the differences in residual stress fields induced by nanosecond Laser Shock Peening (NLSP) and femtosecond Laser Shock Peening (FLSP) processes on 7050 aluminum alloy using X-ray diffraction technology (Figure 2-17). In both cases, high ranges of compressive residual stresses were observed in the investigated region with higher stress peaks in the case of NLSP (-320 MPa at a depth of about 0.3 mm from the surface) than FLSP (only about -130 MPa at the surface).

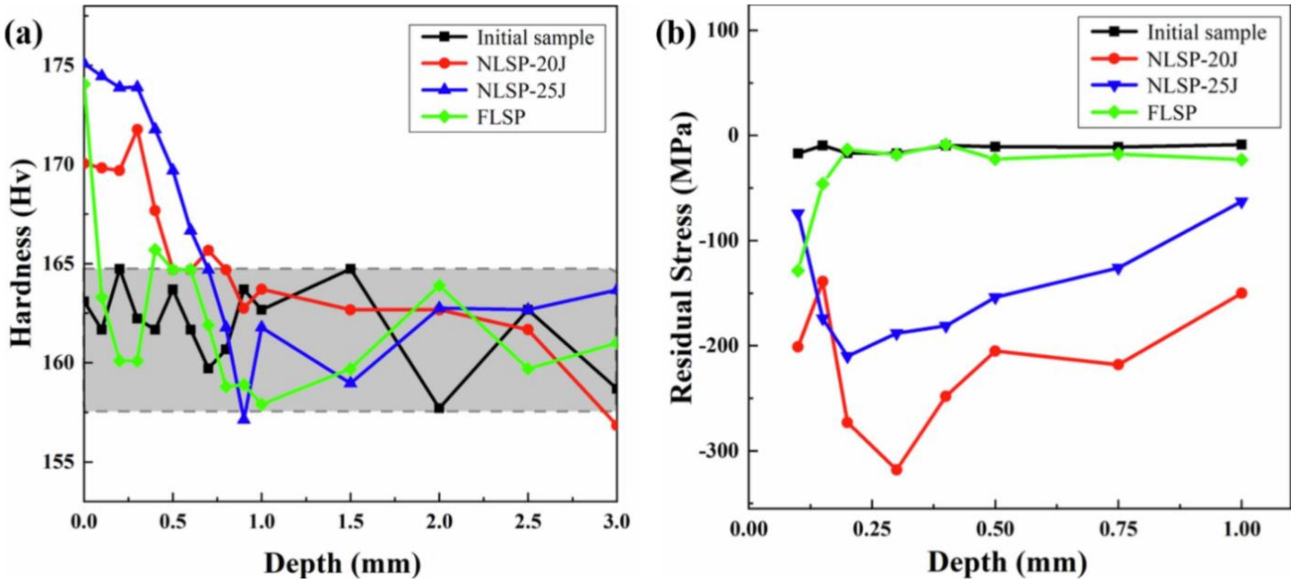

Figure 2-17*: Hardness (a) and residual stress (b) profiles following nano and femto-second Laser Shock Peening processes on 7050 AA* [149].

Sun [150] evaluated the influence of using a square spot size on the process-induced residual stress field using X-ray diffraction for both surface and depth stress evaluation. He showed that increasing values of the spot size result in higher surface stresses (up to about -200 MPa) and greater penetration depths (up to about 0.98 mm from the workpiece surface), as reported in Figure 2-18. In contrast, Sikhamov [151] employed the Hole Drilling technique to characterize the residual stress profile in a 2024-T3 alloy treated by a Laser Shock Peening process at a fastener hole. A maximum compressive value of about -220 MPa was observed near the treated surface, and a non-equibiaxiality of residual stresses in the two main peening directions was also noted.

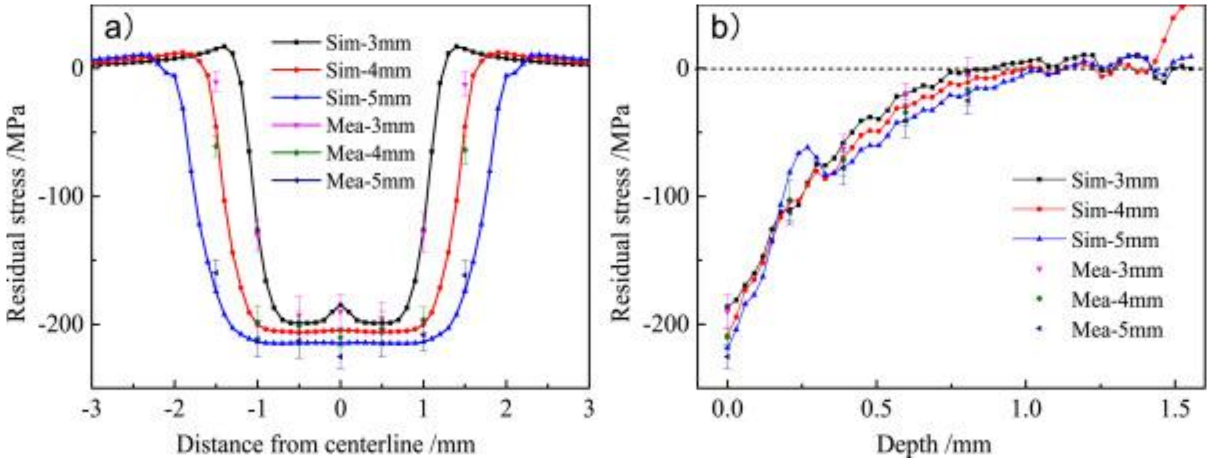

Figure 2-18*: Distribution of residual stresses with different spot sizes: a) surface residual stresses along a line through the LSP treated region; b) in-depth residual stress profile measured in the centre of the treated region* [150].

Nobre [152] evaluated the possibility of measuring the residual stresses induced by the Laser Shock Peening process on plates of different thicknesses in AA 7075-T651 by Incremental Hole Drilling method and compared the results with those obtained by methods based on the diffraction method (Figure 2-19). He observed a high discrepancy between the results measured by the two evaluation techniques at the thinner plate thickness (1.6 mm), with incremental hole drilling providing overestimated residual stress values compared to those expected.

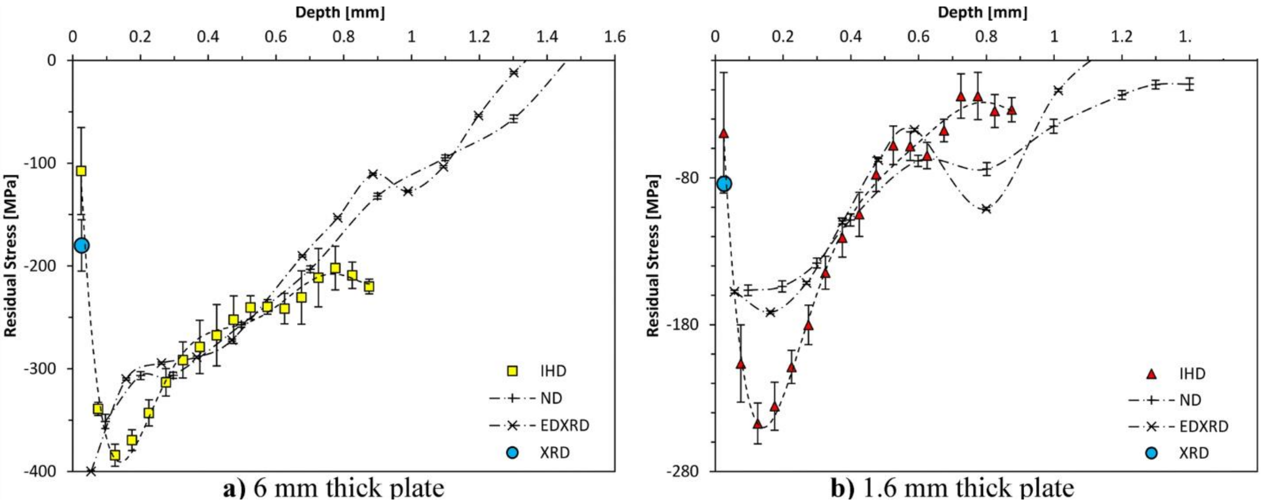

a) 6 mm thick plate **b)** 1.6 mm thick plate

Figure 2-19*: Comparison of residual stress profiles measured by different evaluation methods on plates of different thicknesses: a) 6 mm thick plate; b) 1.6 mm thick plate* [152].

Kallien [153] investigated the residual stresses generated by the LSP process on a 2024-T3 aluminum alloy at different peening strategies (number of sequences, overlap, protective layer) and using the Incremental Hole Drilling method. He showed that a single shot peening sequence, i.e., a single layer, leads to the formation of a non-equibiaxial stress field and that, on the other hand, the use of two layers with different laser scanning directions reduces the difference between the stresses in the two measurement directions (Figure 2-20).

Several other studies address the issue of measuring residual stresses in components of different materials subjected to Laser Shock Peening process, such as titanium alloys [154–157] or steels [158–161], but they are beyond the scope of this research.

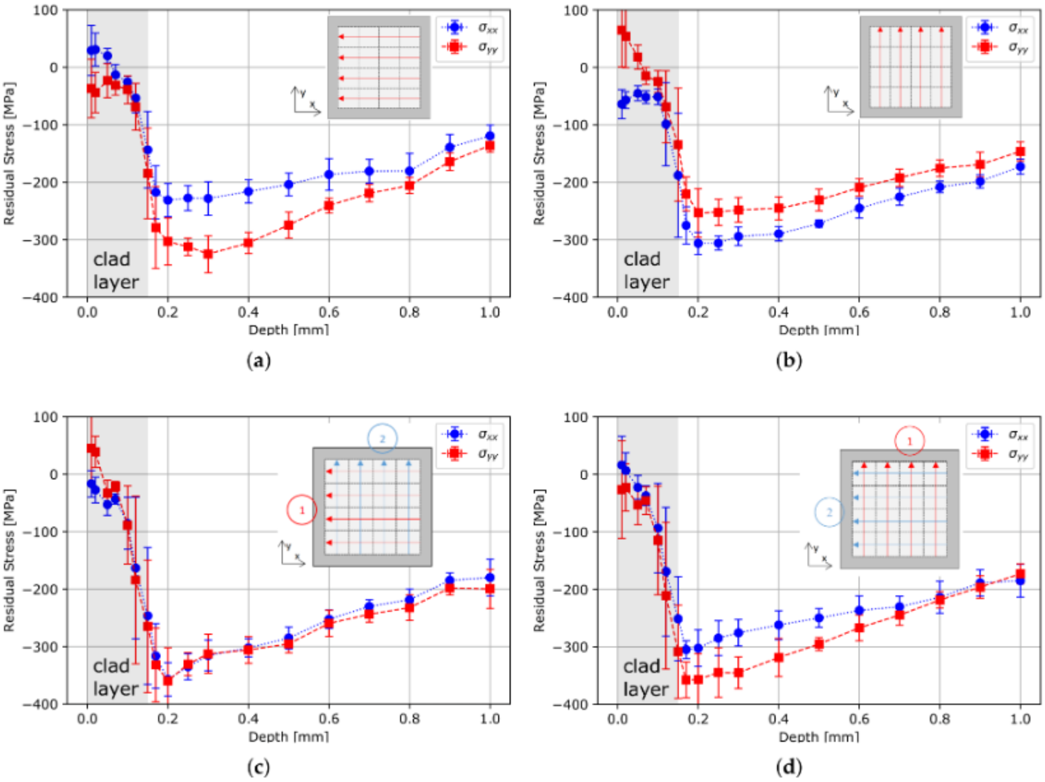

(a) (b)

(c) (d)

***Figure 2-20**: Influence of number of sequences and laser scanning direction on the development of the residual stress field: a) single sequence, horizontal scanning direction; b) single sequence, vertical scanning direction; c) double sequence, horizontal and vertical scanning directions; d) double sequence, vertical and horizontal scanning directions* [153].

CHAPTER 3

EFFECTS OF LASER SHOCK PEENING ON SURFACE INTEGRITY AND RESIDUAL STRESS OF AA 7050-T7451

3.1. Preface

Surface treatment techniques such as Laser Shock Peening (LSP) represent a consolidated strategy to induce the presence of compressive residual stresses beneath the treated surface of various metallic alloys. They are widely employed in the aeronautical sector to significantly improve the fatigue strength of identified hot spots without modifying the initial design concept of a component. However, surface roughening caused by the process must be closely monitored, since it may negatively affect fatigue life, resulting in earlier crack initiation. For this reason, the interplay between the key factors affecting both the surface integrity and the development of residual stresses needs to be fully clarified. In this chapter, the individual and combined effects of different LSP process parameters such as nominal power density, specimen thickness, peening strategy and number of passes of the laser will be experimentally examined and discussed. The surface integrity will be assessed through the determination of roughness average and roughness total height values, whereas residual stresses induced by laser shock peening process will be analysed using X-ray diffraction technique and hole drilling method to obtain detailed information about the stress status of the components. It will be demonstrated that the approach to use lower values of nominal power density together with higher number of layers allows to obtain the same surface stress condition determined by the use of the highest value of nominal power density but a significantly lower impact on the surface integrity. At the same time, however, there is a reduction in the depth of penetration of residual stresses that undermines the use of this combination of parameters for critical structural applications.

3.2. Introduction

The use of surface technologies inducing residual stresses is usually employed in aeronautical industries as a design feature for new-generation aircraft to provide additional integrity margins for identified hot spots by reducing the potential for initiation and propagation of cracks [162]. This engineering approach aims at improving the economic and ecological impact on future aircraft structures by controlling the residual stresses and it is particularly suited to applications where fatigue and crack growth performance cannot be further optimized through standard design techniques[163]. In this context, laser shock peening (LSP) can be considered a rapidly advancing and promising technique for the surface treatment of metal parts which guarantees deeper compressive residual stress fields, more uniform stresses distribution and less impact on surface integrity compared to other conventional surface treatment methods [164], such as Shot Peening which represents one of the most established techniques in the aeronautical sector for the surface treatment of different metal alloys [165–167].

From a technical point of view, the LSP process consists of exposing the sample to short-duration pulses of a laser to initiate the formation of a plasma cloud at the workpiece surface. The component is usually covered with a thin laser-absorbent sacrificial coating to absorb the laser energy and permit the formation of plasma between the material surface and the transparent confining layer. The plasma is characterized by a very high pressure which is transmitted into the sample via shock waves that plastically deform the near-surface region causing compressive residual stresses to develop at the surface and up to a certain depth into the component. As a consequence, the effectiveness of the process can be naturally assessed by analyzing residual stress field jointly with plastic strain and surface roughening [168]: the process must ensure a minimum depth of compressive residual stress and a magnitude sufficient to guarantee the part has the desired enhancement in fatigue performance. Hence, it is of paramount importance to investigate the effects of different combinations of LSP parameters on the aforesaid factors and to numerically assess their interdependence.

The area of applicability of LSP technology is exceptionally wide and includes the employment of several different metallic materials [169–171]. Thus far, many researchers have provided their contribution to the understanding of phenomena connected to the LSP technique and to the development of robust and qualified strategies aiming at optimizing the overall performance of laser-peened components.

As concerns the application of laser shock peening treatment on aluminum alloy, Toparli and Fitzpatrick [172] verified the feasibility of the LSP process on thin aluminum plates focusing their attention on the detrimental effects of distortions due to laser peening on the entity of in-plane compressive residual stresses (Figure 3-1). They also confirmed the role of the pulse energy and the number of passes as key factors affecting induced residual stresses. The thickness of the component subjected to LSP can significantly affect the residual stress field due to the backscattering of elastic shock waves occurring at the rear surface of the part; this is especially true for thin plates, as confirmed by the above-mentioned study; however, it is worth analyzing the effects of thickness on residual stresses entity of thicker plates or components, especially in conjunction with specific values of pulse energy and spot dimensions.

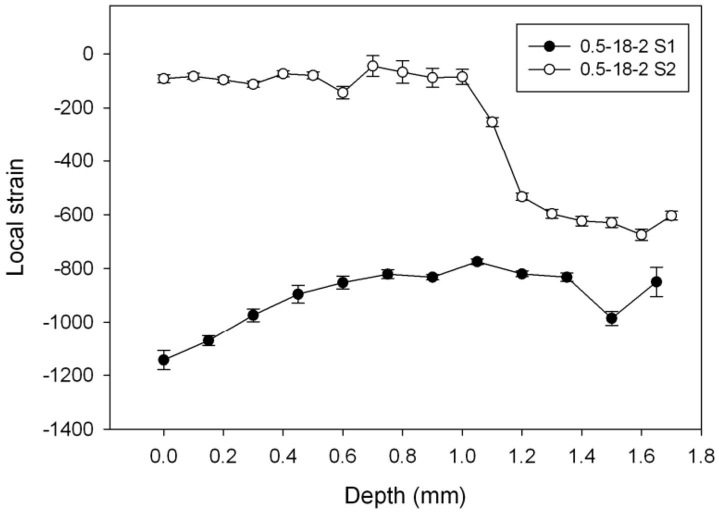

***Figure 3-1**: Difference in longitudinal (S1) and transverse (S2) strain components following LSP process on 6xxx aluminum alloy. Strain profiles obtained by European Synchrotron Radiation Facility (ESRF)* [172].

Glaser [173] performed residual stress measurements on laser peened AA 6056-T4 samples and observed a pronounced residual stress anisotropy between scanning and stepping directions of the laser, especially at lower values of irradiance. Furthermore, surface roughness was observed to increase for both irradiance and spot coverage. Salimianrizi [174] investigated the effects of beam overlap rates, the number of laser shots and scanning pattern on surface roughness: specifically, it was observed that roughness values, as well as residual stress measurements, were different along scanning and stepping directions due to adopted scanning pattern and overlap rate and that the higher the overlap, the less roughness occurs until a critical threshold is reached (Figures 3-2 and 3-3). Consequently, it can be stated that the directionality of the process, namely the scanning pattern, as well as some key factors, such as overlap rates, spot size, beam energy and offset between two consecutive layers, can modify the overall behavior or the component, in terms of residual stresses and surface integrity.

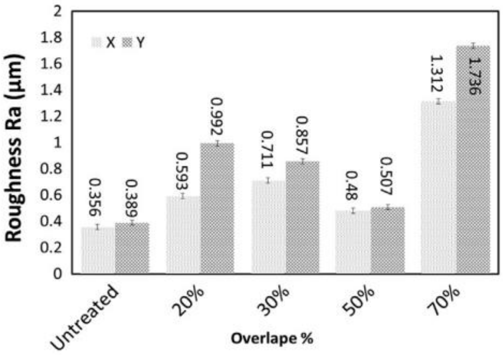

***Figure 3-2**: Effect of overlap rate on surface roughness* [174].

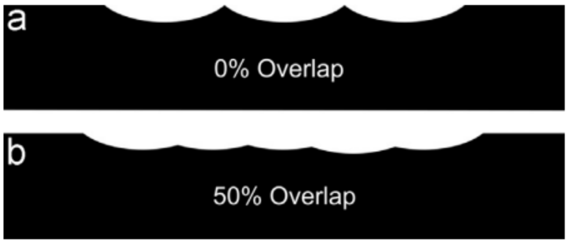

***Figure 3-3**: Schematic of dimples formed in LSP process at different values of overlap rate: a) 0% overlap; b) 50% overlap* [174].

As regards the application of LSP on materials other than aluminum alloys, Tursky [175] presented an overview of main mechanical surface treatments employed to induce compressive residual stress fields in austenitic stainless-steel structure and considered the merits of each of them in terms of their effects on surface roughness and residual stress distribution.

Petan [176] investigated the influence of different combinations of pulse density and spot size on the surface integrity and residual stress measurements of laser peened Maraging steel X2NiCoMo18-9-5: larger spot size at constant pulse energy was observed to have a greater mechanical effect due to a lower energy attenuation rate and a higher overlapping rate. Consequently, spot size, or equivalently power density, can be deservedly included in the list of the most influential process parameters.

Very few papers in the literature provide an overview analysis of the various LSP process parameters with specific reference to aluminum alloy 7050-T7451. Moreover, most articles concerning LSP applications on 7050-T7451 aluminum alloy use a single combination of process parameters and do not provide comparative analyses between different process strategies. This material is widely used in aerospace applications for its high strength, stress corrosion cracking resistance and fracture toughness and can be conveniently designed to suit specific heavy plate applications, such as fuselage frames, bulkheads and wing skins. Luong [177] studied the effects of SP and LSP on fatigue performance of AA-7050-T7451 focusing on residual stress measurements and surface quality assessment before four points bending fatigue testing. Based on the reported results, surface quality resulted to be less affected by LSP surface treatment than SP, but it was observed a significant variation in waviness above AM conditions. Moreover, regarding the residual stresses, LSP produced slightly lower near-surface compressive stresses but concurrently the largest depth of compression inside the component (Figure 3-4).

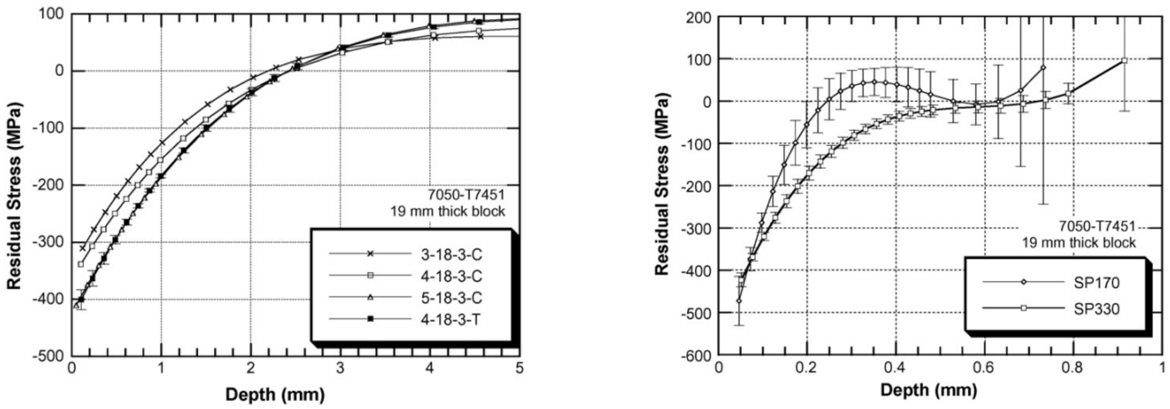
a)

b)

***Figure 3-4**: In-depth residual stress profiles induced by LSP (a) and SP (b) processes on AA 7050-T7451* [177].

Similarly, Gao [178] verified the beneficial effects of LSP treatment on fatigue performance of 7050-T7451 aluminum alloy as a consequence of deeper compressive residual stress fields and good surface finish. Jiang [179] evaluated the influence of power density on fatigue life and fracture characteristics of 7050-T7451 aluminum alloy fastener hole specimens showing a close correlation between the residual stress field induced by the laser peening process and the power density parameter (Figure 3-5 and 3-6).

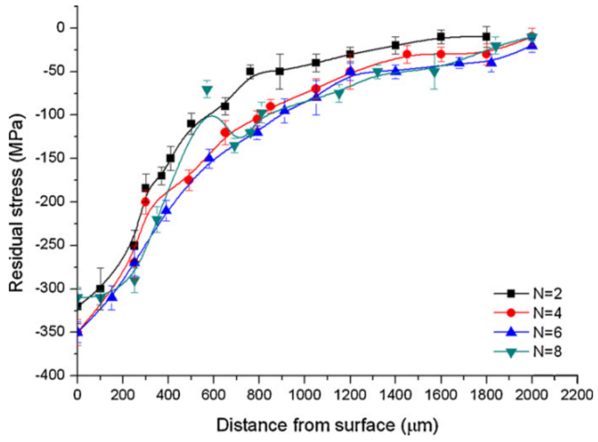

***Figure 3-5**: In-depth residual stress profiles at different values of number of layers [17].*

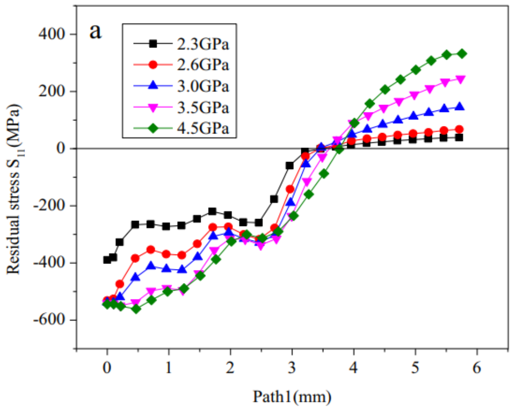

***Figure 3-6**: Distribution of residual stress on the surface and hole wall under different peak pressures [18].*

Nowadays, however, a comprehensive understanding of the effects of the above-mentioned most influencing laser peening process parameters on the development of residual stresses and on surface roughness has not been achieved yet.

Consequently, the objective of this work was primarily the evaluation of surface roughness of laser shock peened square-shaped AA 7050-T7451 specimens through the determination of roughness average (R_a) and roughness total height (R_t) values as the most commonly employed indicators of the validity of the treatment.

Secondary, residual stress field induced by laser shock peening process on the same specimens was assessed using the XRD technique and HDM to obtain detailed information about the stress status of the components. According to the findings of the reviewed technical and scientific literature, several different sets of process parameters were considered, with a particular focus on the individual role and the interrelation between nominal power density, number of layers, specimen thickness and peening strategy. In particular, the possibility of using a higher number of layers (greater than or equal to 4) associated with a lower power density will be verified and the results obtained will be compared with those resulting from the use of increasing power density with a constant number of passes to assess the applicability of this new peening strategy.

3.3. Experimental activity

3.3.1. Definition of material and sample geometry

In this study, the effects of the laser shock peening process on the surface roughness and the residual stress induced on Al 7050-T7451 were analyzed. The experimental work was conducted on 7050-T7451 aluminum alloy. The corresponding nominal chemical composition is listed in Table 3-1, while the mechanical properties of the wrought material are shown in Table 3-2.

***Table 3-1**: Chemical composition of AA 7050-T7451* [2].

Composition	**Si**	**Fe**	**Cu**	**Mn**	**Mg**	**Cr**	**Zn**	**Ti**	**Others**
Content [wt%]	Max 0,12	Max 0,15	2,0-2,6	Max 0,1	1,9-2,6	Max 0,04	5,7-6,7	Max 0,06	0,15

***Table 3-2**: Mechanical properties of AA 7050-T7451* [2].

Modulus of Elasticity, E [GPa]	**Ultimate Tensile Strength, σu [MPa]**	**Tensile Yield Strength, σy [MPa]**	**Elongation at Break [%]**	**Poisson's Ratio, ν**
71,7	524	469	11	0,33

Square-shaped specimens were cut out of an aluminum rolled plate with a thickness of 30 mm. The blocks thus obtained were available in two different thicknesses, namely 10 mm and 30 mm, to further explore and clarify the role of thickness in the development of residual stresses inside the components. The geometrical properties of the test specimens are indicated in Figure 3-7.

The LSP treatment was performed at the ZAL Center of Applied Aeronautical Research in Hamburg, Germany. It was applied only to one side of the specimen. The experiments were conducted using a YLF:Nd laser with a wavelength of 1053 nm operating at a maximum 20 Hz pulse frequency. The laser pulse width was set to 18 ns. The beam shape was round and a flat-top beam profile was employed. For the sake of completeness, all laser parameters are schematically shown in Table 3-3.

***Table 3-3**: Laser parameters employed for the surface treatment of the AA 7050-T7451 specimens.*

Laser Source	Wavelength	Laser power	Pulse energy	Pulse length	Pulse frequency	Beam shape	Beam profile	Spot diameter
YLF:Nd	1053 nm	200 W	Up to 10 J	16 ns to 21 ns	1 Hz to 20 Hz	Round	Flat Top	2 mm to 6 mm

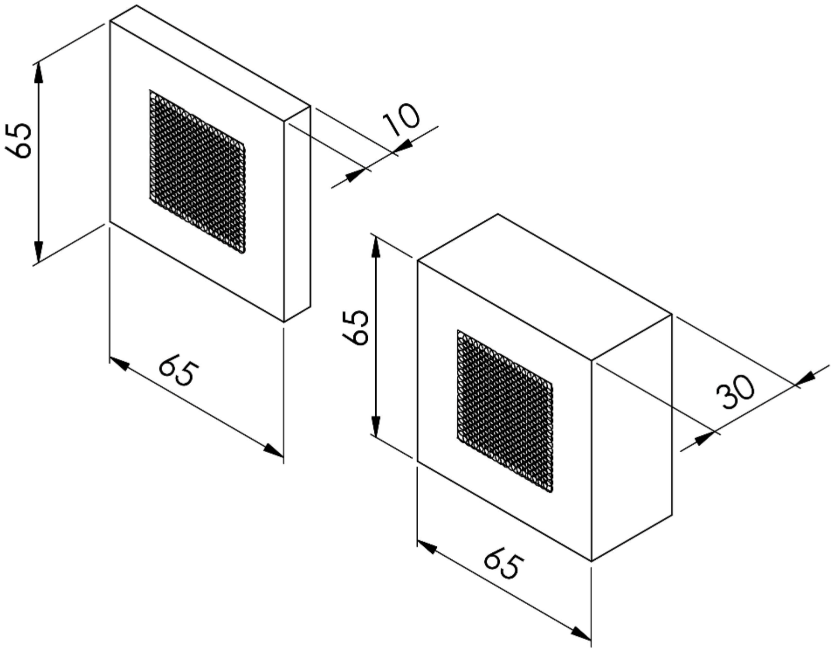

***Figure 3-7**: Geometry of the test specimens. All dimensions in mm.*

The treated zone is placed in the middle of the upper face of the specimens and has dimensions of approximately 35 mm x 35 mm. The surface of the treated area was covered with a sacrificial adhesive coating (a commercial black paint with a thickness of approximately 30-40 μm) before the peening process and a water film (distilled water with a thickness of approximately 2 mm) was used as a transparent confining layer. A total of 27 specimens were available for residual stress evaluation and surface roughness analysis: 9 thick samples and 18 thin samples. Samples were divided into groups of three and each group, identified by a capital letter, differs from each other for the specific combination of the LSP process parameters applied. Consequently, 3 different combinations of parameters were considered for thick samples and 6 for thin samples. Among the most critical parameters, nominal power density (NPD), number of laser passes, specimen thickness and peening strategy have been considered, as shown in Table 3-4. The values selected for these process parameters derive from a careful analysis of the scientific literature related to the application of the LSP process on AA 7050-T7451 components. The parameters range, including the laser power density, the spot size and the overlap rate, represents the most commonly used for that kind of alloy, as reported in the literature [46,169,171,179,180]. On the other hand, referring to the additional process parameters such as the number of laser passes or the percentage of offset between consecutive layers, only limited experimental data are available in the literature. It was therefore considered necessary to explore new process strategies for evaluating the effects of the chosen parameters on the properties examined (Figure 3-8).

Table 3-4: *Definition of process parameters identifying each group of specimens.*

Group of specimens	**Thickness**	**NPD**	**Nominal Energy**	**Layers**	**Offset**
	[mm]	[GW/cm^2]	[J]		[%]
A	30	2,5	5,31	3	33,0/33.0
B	30	3,5	7,43	3	33,0/33.0
C	30	4,5	9,55	3	33,0/33.0
D	10	2,5	5,31	3	33,0/33.0
E	10	3,5	7,43	3	33,0/33.0
F	10	4,5	9,55	3	33,0/33.0
G	10	0,8	4,99	4	25,0/25.0
H	10	0,8	4,99	12	8,5/8.5
I	10	0,8	4,99	20	5,0/5.0

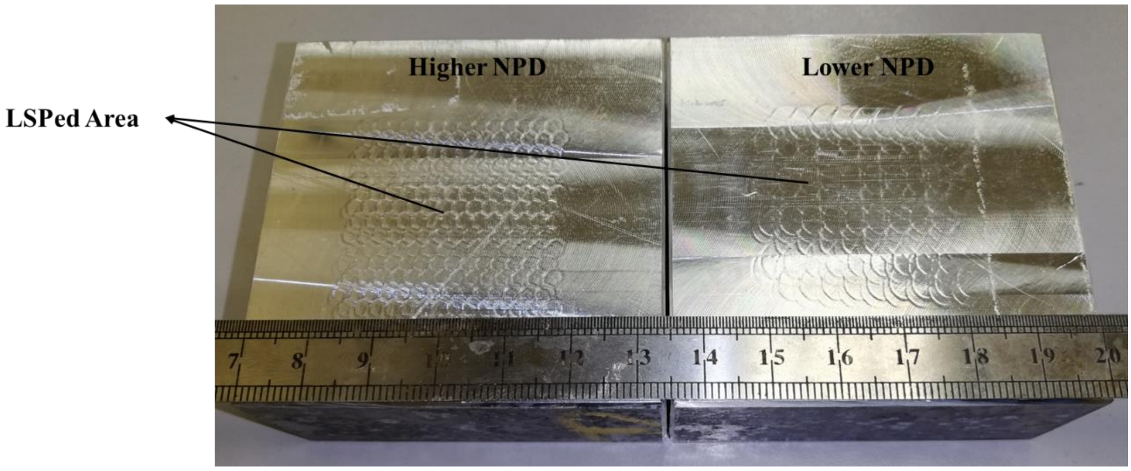

Figure 3-8: *Appearance of the laser peened areas of two specimens for roughness and residual stress measurements (30 mm thick) treated with different combinations of process parameters: on the left, higher pulse energy and smaller spot size; on the right, lower energy and larger spot size.*

The peening pattern can be identified by two conventional directions, namely X and Z, indicating the scanning and stepping direction of the laser beam (Figure 3-9) respectively. The overlap percentage indicates the overlapping between two adjacent laser spots measured along both scanning and stepping directions. The offset parameter represents the mismatch between two consecutive layers and its value is inversely related to the number of layers.

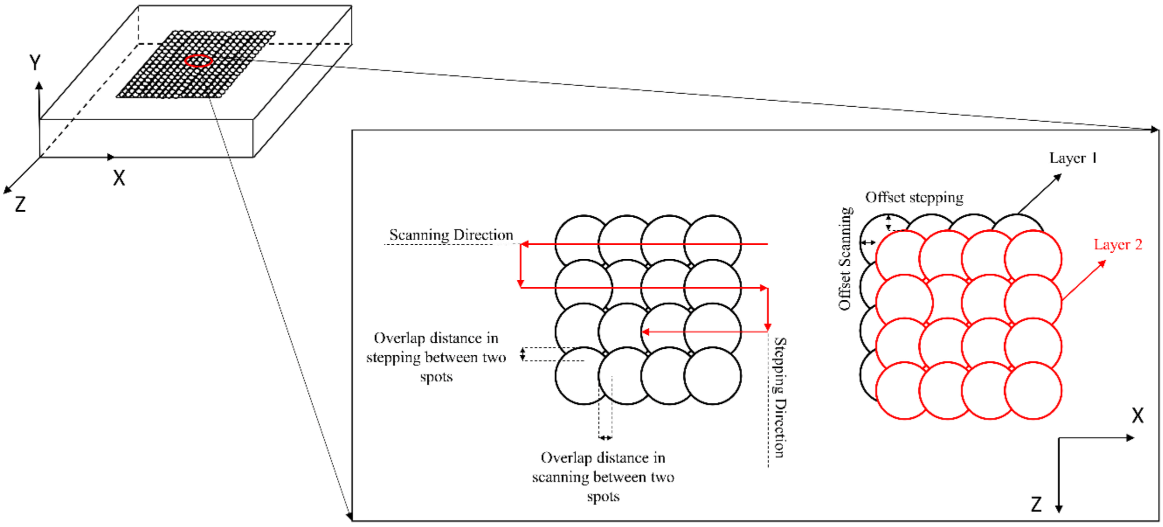
Y
X
Z
Scanning Direction
Overlap distance in stepping between two spots
Overlap distance in scanning between two spots
Stepping Direction
Offset Scanning
Offset stepping
Layer 1
Layer 2
X
Z

***Figure 3-9**: Schematic representation of peening strategy: definition of the main directions of peening and of overlap and offset parameters.*

3.3.2. Surface roughness evaluation methods

Roughness measurements were performed on each specimen after laser shock peening treatment through a Surtronic 25 contact profilometer (Taylor Hobson), as shown in Figure 3-10. First of all, each specimen was cleaned with isopropyl alcohol to prevent the presence of grease or abrasive materials. They were then positioned on a linear translation stage fixed to an optical table with dampers and pneumatic isolation to ensure both the specimen and the profilometer were completely steady and free of vibration during the measurement.

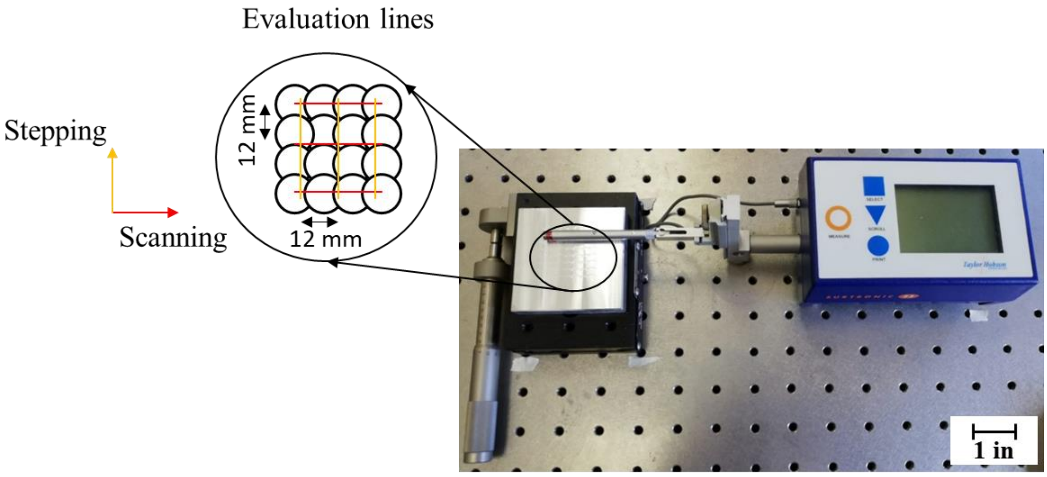

Figure 3-10*: Measurement setup for surface roughness evaluation.*

Based on the indications provided by reference standard [181], a cut-off length of 0.8 mm and an evaluation length of 4 mm were selected. The tip of the stylus had a diameter of 2 µm and the traverse speed was constant and equal to 1 mm/sec. Six individual roughness measurements for each specimen were carried out, three of which were aligned with the scanning direction of the laser beam, while the other three were aligned with the stepping direction. Three repetitions of each measure were performed to allow for proper statistical analysis of the results. The measuring lines, along both scanning and stepping directions, were positioned within the treated area at a distance of approximately 12 mm from each other. The values of roughness average (R_a) and roughness total height (R_t) were evaluated along the two laser directions, based on an arithmetical average of values obtained along each measuring line.

Two different analyses were carried out to estimate the influence of NPD, peening strategy, thickness and the number of layers on the surface roughness of LSP specimens.

Firstly, a 23 factorial design was used to statistically estimate the correlation between NPD, peening strategy, thickness and the considered roughness properties. In this case, the selected design factors were the laser NPD, the number of layers of peening and the specimen thickness. NPD and number of layers factors were run at three levels (respectively 2.5, 3.5, 4.5 GW/cm^2 and 4, 12 and 20 layers), while thickness factor was run at two levels (10 and 30 mm). The design was replicated three times, as being three the number of specimens characterized by the same set of process parameters. The response variables were the roughness average value (R_a) and the roughness total height value (R_t), commonly employed as indicators of surface roughness. Secondly, a single factor analysis of variance was employed as a statistical method for the assessment of the influence of the number of layers on roughness properties. In this case, as well, R_a and R_t values were used as response factors in the factorial design.

3.3.3. Residual stress field evaluation methods

The evaluation of the residual stress field due to the laser shock peening process was performed through two different techniques: XRD and HDM.

Surface residual stresses analysis was performed using Xstress 3000 G3R X-ray diffractometer (Stresstech). It was instrumented with a Cr tube (λ = 0.2291 nm) and a 2 mm collimator. The residual stress measurements were carried out in the center of each specimen along two different directions: the stepping direction and the scanning direction, as indicated in Figure 3-11.

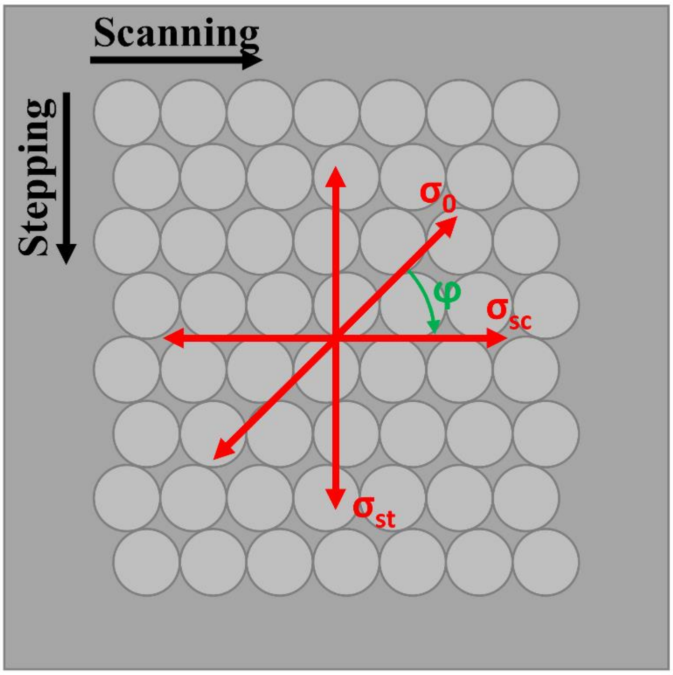

Figure 3-11: *Definition of principal residual stress measurement directions.*

The residual stress measurements were performed using the sen-square-psi technique as required by UNI EN 15305 standard [182]. The diffracted intensity, the peak width and the position of K-alpha 1 of the diffraction peak were determined by interpolating the peak profile with the Pearson VII function. Table 3-5 summarizes the parameters used during the residual stress measurements.

***Table* 3-5**: *XRD measurement parameters.*

Tube	Diffraction Angle [°]	Exposure time [sec]	No. of Tilt	Tilt angle [°]	Tilt oscillation [°]	Collimator diameter [mm]	Voltage [kV]	Current [mA]
Cr	139,3	25	4	±45	±3	2	30	8

Miller Indexes	Poisson's ratio	Young's Modulus [GPa]	Absorption coefficient [1/mm]
(311)	0.345	70.6	42.7

In-depth residual stress fields were evaluated both by the X-ray method and HDM. As concerning XRD, in-depth measurements were performed after removing the material by an electrochemical attack with a Movipol-3 Struers and A2 electrolyte applying a voltage of 70 V for time intervals of 5 sec so as to obtain a current intensity of about 0.8 A. At these process parameters, the material removal rate is equivalent to approximately 1 μm/sec. The following nominal depths were analyzed: 0, 10, 20, 30, 40, 50, 100, 150, 200, 250, 500, 750, 1250, 1500, 1750, 2000, 2250, 2500, 2750, 3000 × 10-3 mm. In any case, the measure was stopped before 3 mm when traction stress was measured. For the in-depth measurement of residual stresses by XRD, the same diffractometric parameters employed for surface measurements were adopted.

HDM was carried out by using the SINT Technology Hole Drilling system, according to the ASTM E837-13 [98]. Type B strain gauge rosette (CCW) was applied in the middle of the treated surface. The "a" grid was oriented along to the scanning direction of the specimen: it represents the x-direction of the residual stresses. The angle β defines the direction of the most tensile principal stress σ_{max}, according to the standard. The latter was measured counterclockwise from the gauge a.

The hole was carried out up to 1 mm in 20-hole steps located according to a polynomial distribution. A tungsten carbide end mill, TiAlN coated, inverted cone-shaped 1.6 mm diameter was used. The drilling phase was controlled by a compressed air unit at 400000 rpm speed of rotation (Figure 3-12). Residual stress results were evaluated by using the Integral method along the x and y directions.

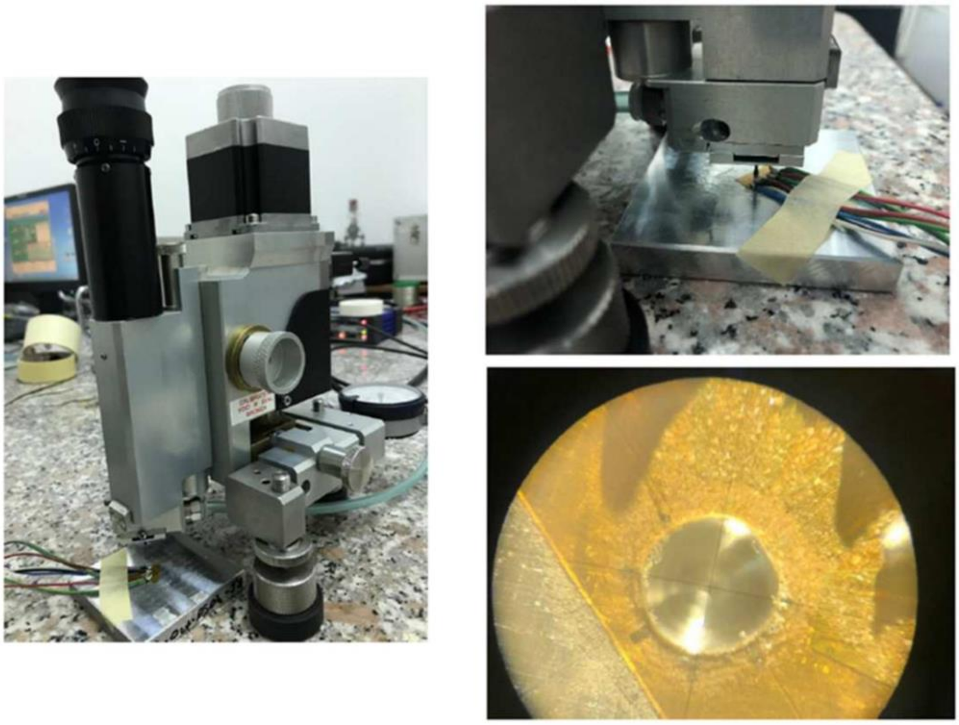

***Figure 3-12**: Hole Drilling Method setup.*

3.4. Results and discussions

3.4.1. Surface Roughness results

Surface roughness investigations were performed to infer the effects of variations in NPD, the number of layers, laser pattern and specimen thickness on surface integrity of laser shock peened components. First of all, the combined effects of NPD, laser pattern and specimen thickness were analyzed. For this purpose, two groups of specimens different in thickness were taken into consideration: inside every single group, three different levels of NPD, namely 2.5, 3.5 and 4.5 GW/cm^2 and two laser directions, specifically scanning and stepping directions, were considered, keeping constant all other LSP parameters. For a clear overview, a summary table reporting the identification code of each specimen and a breakdown of technological aspects was reported in Table 3-6.

***Table 3-6**: Identification codes and technological properties of specimens for surface roughness and residual stress evaluation.*

ID Codes	Thickness [mm]	Nominal Power Density [GW/cm^2]	Spot Size [mm]	Overlap	Nominal Energy [J]	Layers	Offset
01-02-03	30	2,5	3,5	30%/30%	5,31	3	33%/33%
04-05-06	30	3,5	3,5	30%/30%	7,43	3	33%/33%
07-08-09	30	4,5	3,5	30%/30%	9,55	3	33%/33%
10-11-12	10	2,5	3,5	30%/30%	5,31	3	33%/33%
13-14-15	10	3,5	3,5	30%/30%	7,43	3	33%/33%
16-17-18	10	4,5	3,5	30%/30%	9,55	3	33%/33%

The average results of R_a and R_t along both the scanning and the stepping directions of the laser were acquired and employed as response factors in the considered factorial plane, as shown in Table 3-7. The significance level of the test was fixed to 0.01.

Table 3-7: *Factorial plane for surface roughness evaluation: analysis of power density, thickness and peening strategy influence.*

	Coded Factors			**R_a [µm]**			**R_t [µm]**		
Run	**Power Density [GW/cm^2]**	**Thickness [mm]**	**Laser Direction**	**Replicate 1**	**Replicate 2**	**Replicate 3**	**Replicate 1**	**Replicate 2**	**Replicate 3**
1	2,5	10	Scanning	0,96 (±0.11)	0,93 (±0.15)	1,34 (±0.14)	4,70 (±0.7)	4,30 (±0.7)	6,20 (±0.7)
2	2,5	10	Stepping	1,28 (±0.06)	1,32 (±0.14)	1,13 (±0.12)	5,80 (±0.3)	6,10 (±0.6)	4.90 (±0.5)
3	2,5	30	Scanning	1,38 (±0.12)	1,33 (±0.14)	1,07 (±0.14)	6.60 (±0.7)	6,60 (±0.9)	5.20 (±0.7)
4	2,5	30	Stepping	1,22 (±0.21)	1,18 (±0.12)	1,42 (±0.16)	6,10 (±1.7)	6,20 (±1.3)	6,90 (±0.8)
5	3,5	10	Scanning	1,89 (±0.27)	1,67 (±0.41)	2,00 (±0.37)	9,60 (±1.5)	8,90 (±2.9)	11,40 (±2.8)
6	3,5	10	Stepping	1,36 (±0.31)	1,78 (±0.19)	2.02 (±0.44)	6.30 (±1.9)	8.40 (±0.9)	11,10 (±2.3)
7	3,5	30	Scanning	1,78 (±0.23)	1,33 (±0.14)	1.24 (±0.17)	8.70 (±1.7)	6,30 (±0.9)	6,10 (±1.1)
8	3,5	30	Stepping	1,38 (±0.21)	1,60 (±0.17)	1,73 (±0.14)	6,20 (±1.4)	7,10 (±0.6)	8,10 (±1.1)
9	4,5	10	Scanning	2,27 (±0.22)	2,08 (±0.2)	1,98 (±0.44)	11,60 (±1.4)	10,10 (±1.5)	11,30 (±4.0)
10	4,5	10	Stepping	1,98 (±0.29)	1,84 (±0.26)	1,69 (±0.11)	11.40 (±2.4)	10,30 (±1.9)	8,80 (±1.0)
11	4,5	30	Scanning	1,98 (±0.16)	1,67 (±0.40)	1,67 (±0.26)	9.90 (±1.1)	8,40 (±2.4)	8,90 (±1.5)
12	4,5	30	Stepping	1,64 (±0.31)	2,02 (±0.19)	2,00 (±0.14)	9,00 (±2.5)	10,20 (±1.4)	10,00 (±1.3)

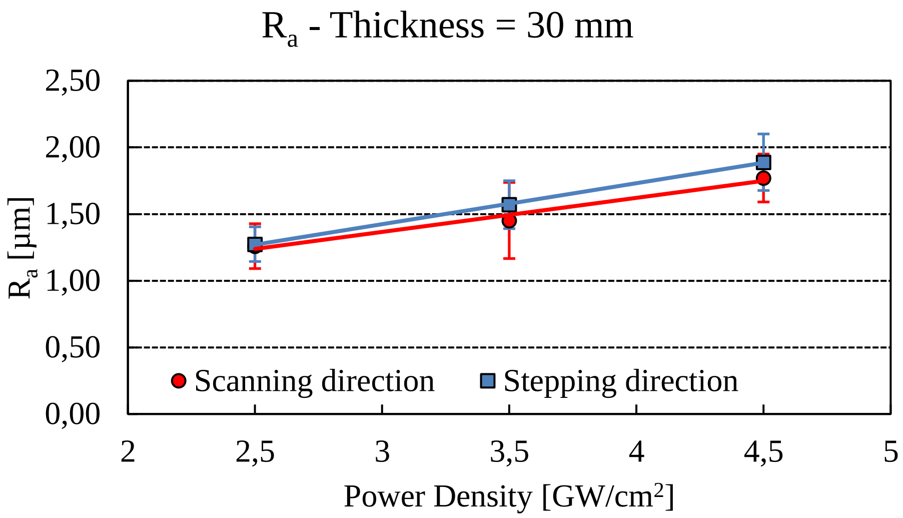

Figure 3-13: Roughness average (R_a) *values along scanning and stepping directions at different level of nominal power densities (thickness 30 mm).*

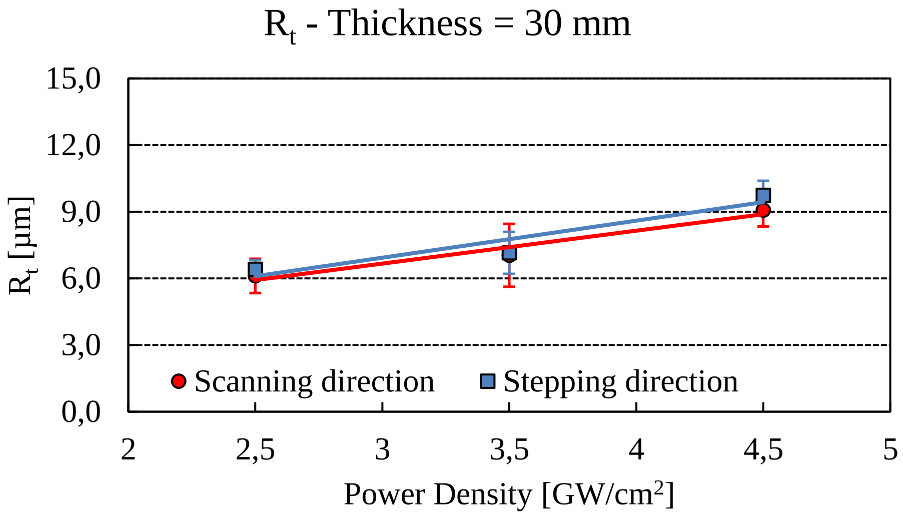

Figure 3-14: Roughness total height (R_t) *values along scanning and stepping directions at different level of nominal power densities (thickness 30 mm).*

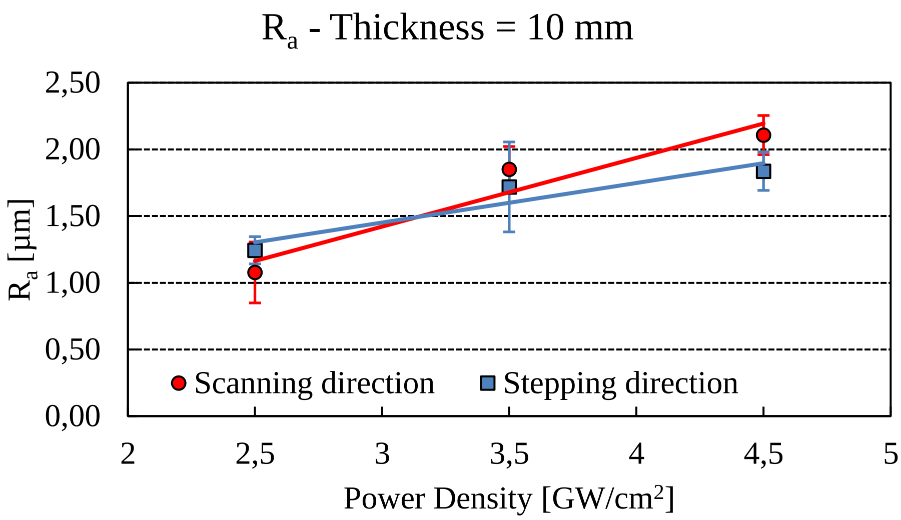

***Figure 3-15**: Roughness average (R_a) values along scanning and stepping directions at different level of nominal power densities (thickness 10 mm).*

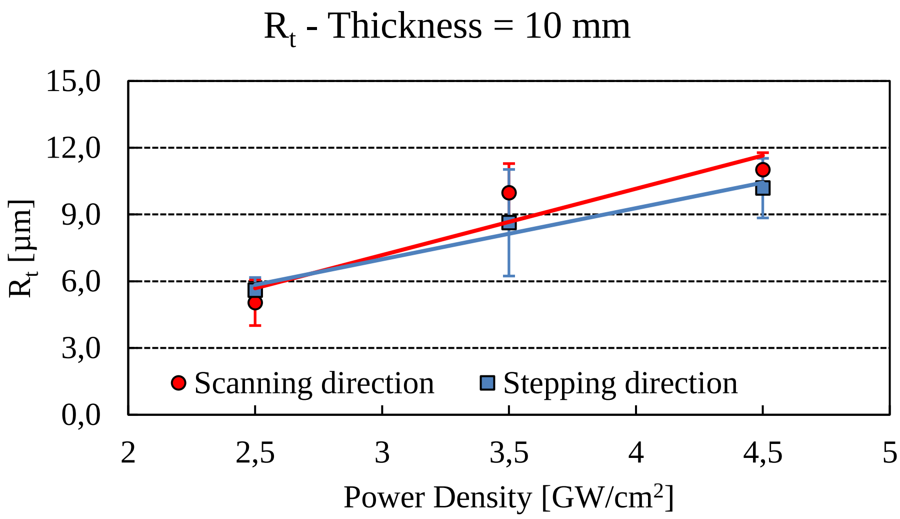

***Figure 3-16**: Roughness total height (R_t) values along scanning and stepping directions at different level of nominal power densities (thickness 10 mm).*

The average results of R_a and R_t were reported in Figures 3-13, 3-14, 3-15 and 3-16. Higher values of NPD determine a significant and measurable increase in roughness properties both along scanning and stepping directions, as a consequence of the greater depth and intensity of plastic deformation to which the component is subjected as NPD increases [46]. However, roughness properties seem not to be significantly affected by variation in laser direction at constant values of NPD, confirming the validity of the peening strategy. Indeed, a variation of the roughness parameters in the two main directions of the laser could have indicated a non-uniformity of the process most likely associated with a wrong combination of the LSP process parameters. Moreover, thickness does not play a major role as a parameter affecting surface roughness. The ANOVA was used to confirm the magnitude of the effects of each parameter. It can be noted from the main plot diagrams in Figure 3-17 that the main effect of NPD is highly significant ($P < .001$), suggesting that this factor dominates the process.

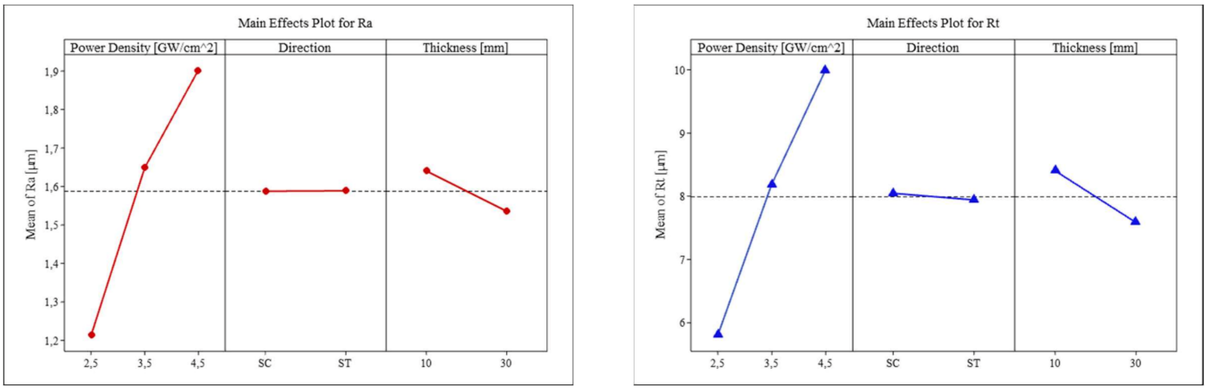

Figure 3-17*: Mean response values at each level of the design parameters.*

The interaction between NPD and thickness factors can also be considered significant according to the chosen value of significance level, but the closeness of the corresponding p-value ($P = .079$ for R_a and $P = .091$ for R_t) to the significance level would suggest a greater number of tests to be run to verify the effective influence of this interaction on the process output. All other main effects and factors interactions have a very low value of significance. All findings obtained were briefly and effectively reported in the following contour plots (Figure 3-18), where the effect of laser direction was considered negligible for the reasons given above.

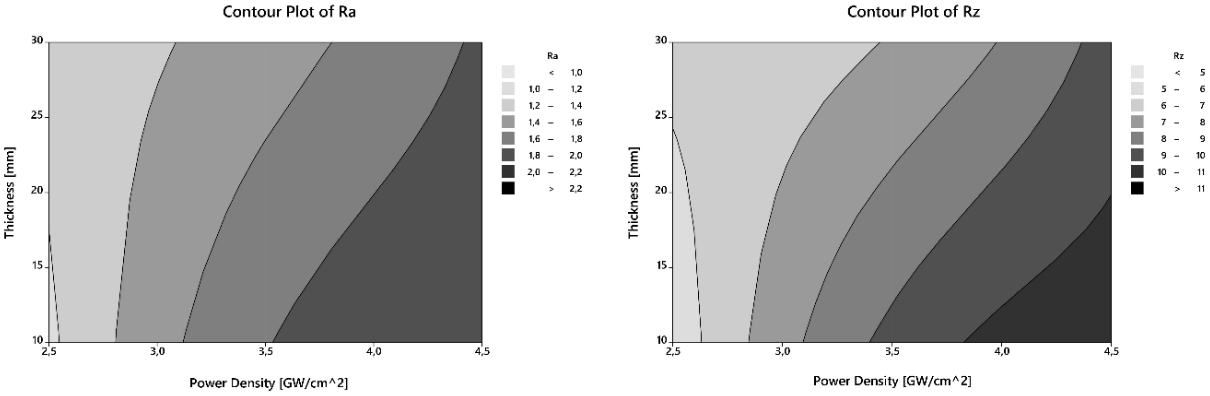

Figure 3-18*: Contour plot of R_a and R_t versus thickness and NPD.*

As regards the second objective of this research activity, the influence of the number of layers on the surface roughness of laser peened specimens was investigated. In this respect, three different levels of the number of layers factor were considered, namely 4, 12 and 20 and three replicates of the same experiment were run. Given that the NPD factor has a predominant effect on the roughness properties, these specimens were laser peened by using a lower value of laser NPD, specifically 0.8 GW/cm^2, to minimize its impact on the surface and better distinguish the specific contribution of each factor. All other process parameters, such as thickness, spot size and spot overlap, were kept constant, as schematized in Table 3-8.

***Table 3-8**: Identification codes and technological properties of specimens for the evaluation of the effects of variation in the number of layers.*

ID Code	**Thickness** [mm]	**Nominal Power Density** [GW/cm^2]	**Spot Size** [mm]	**Overlap**	**Nominal Energy** [J]	**Layers**	**Offset** [%]
19-20-21	10	0,8	6,0	25%/25%	4,99	4	25,0%/25,0%
22-23-24	10	0,8	6,0	25%/25%	4,99	12	8,5%/8.5%
25-26-17	10	0,8	6,0	25%/25%	4,99	20	5,0%/5.0%

In this case, as well, R_a and R_t values were used as response factors in the factorial plane and single-factor analysis of variance was employed as a statistical method for the assessment of results since only one factor, i.e. the number of layers is investigated (Table 3-9).

***Table 3-9**: Factorial plane for surface roughness evaluation: analysis of the influence of the number of layers.*

	Coded Factor	**R_a [µm]**			**R_t [µm]**		
Run	**Number of Layers**	**Replicate 1**	**Replicate 2**	**Replicate 3**	**Replicate 1**	**Replicate 2**	**Replicate 3**
1	4	0,54	0,53	0,55	5,00	4,70	4,80
2	12	0,62	0,64	0,67	6,80	6,20	6,70
3	20	0,82	0,81	0,85	9,20	8,90	8,60

The number of layers parameter results to have a great impact on surface roughness of LSP-treated specimens as testified by diagrams in Figure 3-19. Increasing its value from 4 to 20, R_a value shows an increase of 53.7%, while R_t value shows an increase of 84.5%. The ANOVA analysis confirmed that the number of layers significantly affects ($P < .001$) the surface roughness of the component, in terms of both R_a and R_t values. As with the laser power density parameter, the increase in surface roughness caused by the higher number of laser passes is due to the increased degree of plastic deformation of the surface of the treated component. Repeated LSP impacts contribute to extending the depth of the plasticized zone, which is directly reflected in the roughness profile characteristics.

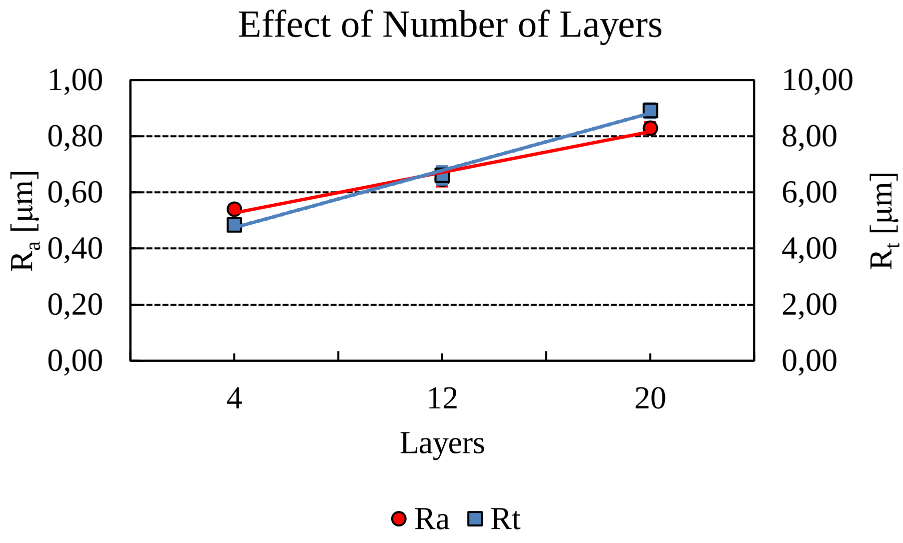

Figure 3-19: *Effects of number of layers on roughness properties of LSPed specimens.*

3.4.2. Surface roughness discussion

One of the main effects of the laser peening process is the increase of the surface roughness in the treated component compared to the unprocessed one. This phenomenon is a direct consequence of the local plastic deformation caused by the shock waves induced by the plasma's-controlled expansion on the component's surface. When the pressure of the plasma exceeds the dynamic yield strength of the material, plastic deformation occurs thus altering near-surface microstructure and properties. The peak pressure is strictly related to the laser power density: generally, higher power density values result in higher peak pressure increasing the depth and the magnitude of plastic deformation [13,15,31,183]. This explains the increase in surface roughness associated with the use of higher power densities. The R_a e R_t values found at the three power density levels examined, specifically 2.5, 3.5 and 4.5 GW/cm^2, are consistent with results presented in other studies conducted on the same or similar materials and using comparable process parameters set [183–185]. It is important to note that no significant changes in surface properties were observed in the two directions of the laser, i.e., scanning and stepping directions, demonstrating the validity of the peening strategy. Some studies, in fact, associated variation in surface properties along the two peening directions with the scanning pattern and specifically, the selected overlap parameter: the higher the overlap, the less roughness occurred until a limit value was reached beyond which a drastic increase in surface roughness was observed due to the consumption of the sacrificial layer and the consequent material ablation [186]. Overlap values of less than 70% along both directions, such as those used in this study, guarantee the absence of the ablation phenomenon and help to keep the surface roughness of the component within the design requirements.

Similar to laser power density, the use of a higher number of laser passes, i.e., the number of layers, results in a deterioration of the surface roughness of the laser peened component. The repetition of the laser pulses determines a greater amount of local plastic deformation on the component surface, which increases the characteristic roughness parameters. To the best of the authors' knowledge, few studies in the scientific literature, both numerical and experimental, have addressed the evaluation of the effects of the number of passes on the surface roughness of the component and none have ever used a number of passes greater than five [180,187–190]. Therefore, it is not possible to compare the results obtained with those provided by previous studies. However, the low values of surface roughness found in the correspondence of high values of the number of passes suggest the possibility to adopt this peening strategy to applications that require high surface integrity of the component (wear resistance, fretting fatigue, etc.). Moreover, the association of these roughness values with the corresponding residual stress profiles allows the application of this laser peening strategy also for structural applications in fatigue critical points.

3.4.3. Residual stress results

Residual stress measurements were carried out on the same groups of specimens used for surface roughness evaluation to find an optimal set of parameters that guarantee simultaneously surface integrity and the desired residual stress field.

In Table 3-10 mean residual stress values along both scanning and stepping directions of the laser obtained through the XRD technique applied on the surface of each specimen in the center of the treated zone were reported.

In Figure 3-20 the effects of NDP on the surface residual stresses on 10 mm and 30 mm thick specimens were shown. As regards 10 mm thick specimens, it was observed a decrease in compressive RS from -184,2 ± 12,1 MPa to -164,9 ± 14,6 MPa in the scanning direction and from -162,0 ± 15,6 MPa to -135,3 ± 14,7 MPa in the stepping direction as the NPD increases from 2.5 to 4.5 GW/cm2. This reduction could be associated with the phenomenon of reflection of the elastic waves on the lower surface of the specimen, although this phenomenon is more typically found in components with a slightly lower thickness than that considered and in correspondence with specific process parameters, as will be highlighted in the following discussion paragraph.

As concerning 30 mm thick specimens, variations in NPD seems not to significantly affect residual stress measurement on the surface of the components, both along scanning as well stepping direction.

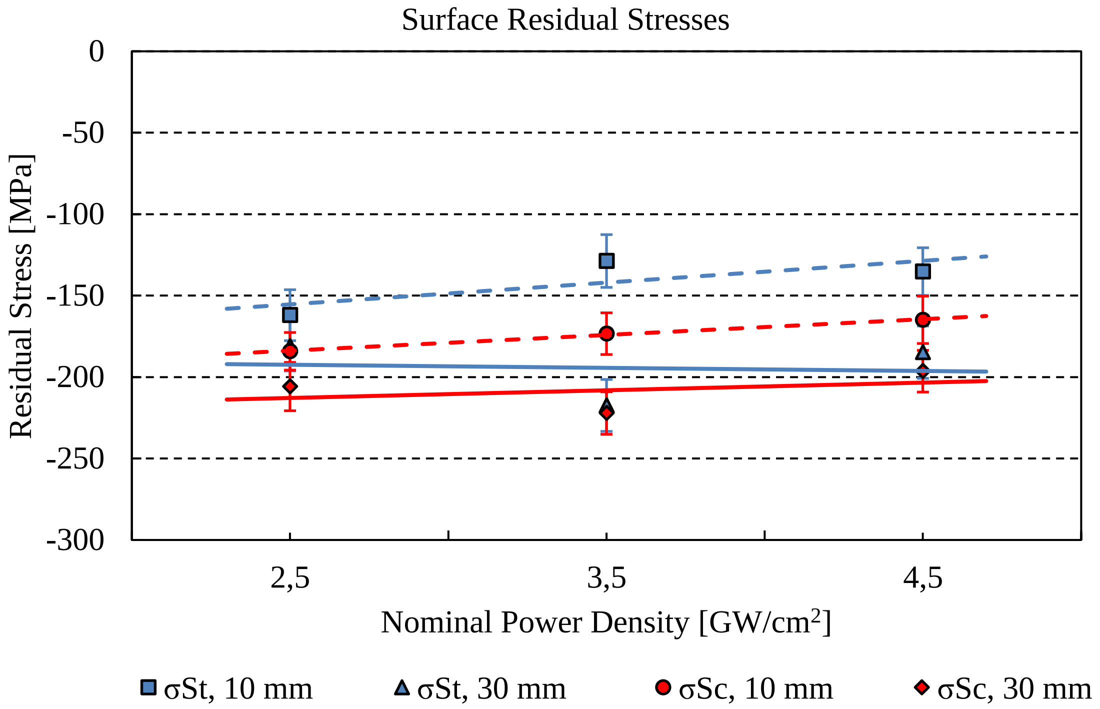

Figure 3-20: *Effects of NPD, thickness and peening direction on surface residual stress values of LSPed specimens.*

Table 3-10: *Summary of surface residual stress measurements: analysis of NPD, thickness and peening strategy influence.*

Specimens' ID	Nominal PD [GW/cm²]	Thickness [mm]	$\sigma_{St, 30\ mm}$ [MPa]	$\sigma_{Sc, 30\ mm}$ [MPa]	Err_{St} [MPa]	Err_{Sc} [MPa]
01-02-03	2,5	30	-180,9	-205,8	15,3	14,8
04-05-06	3,5	30	-217,4	-222,1	16,0	13,1
07-08-09	4,5	30	-184,7	-196,4	16,1	12,8

Specimens' ID	Nominal PD [GW/cm²]	Thickness [mm]	$\sigma_{St, 10\ mm}$ [MPa]	$\sigma_{Sc, 10\ mm}$ [MPa]	Err_{St} [MPa]	Err_{Sc} [MPa]
10-11-12	2,5	10	-162,0	-184,2	15,6	11,5
13-14-15	3,5	10	-128,8	-173,4	16,2	12,8
16-17-18	4,5	10	-135,3	-164,9	14,7	14,6

Therefore, it can be generally stated that an increase in NPD determines a slight decrease in compressive residual stresses on the surface of 10 mm thick laser peened specimens, independently of the direction of the laser, whereas almost constant values of residual stresses were observed on the surface of 30 mm thick specimens.

As concerns the influence of the number of layers, it was observed that compressive residual stresses on the surface of the specimens increase with the number of layers. In particular, the compressive stress along stepping direction increases from -206,9 ± 18,0 MPa to -239,2 ± 29,9 MPa while the one along scanning direction increases from -162,1 ± 11,5 MPa to -232,6 ± 31,8 MPa when the number of layers increases from 4 to 20, as shown in Table 3-11 and Figure 3-21. This result is a direct consequence of the greater depth of plastic deformation induced by the increased number of laser passes.

As a consequence of the reported results, it is important to point out that it is possible to obtain higher compressive residual stresses at the surface of the component using lower values of NPD but a higher number of layers, with the additional advantage of obtaining lower values of surface roughness, in terms of R_a and R_t and consequently better surface integrity. In-depth residual stress analysis was carried out through both the XRD technique and HDM. Specifically, specimens identified by ID code 04-05-07-08-13-16, as being representative of the highest values of nominal NPD and both values of thickness, were analyzed using both methods, whereas specimens identified by ID code 22-25, which were obtained using the highest number of layers, were analyzed using only HDM.

Table 3-11: *Summary of surface residual stress measurements: analysis of the number of layers influence.*

Specimens' ID	**Number of layers**	**σ_{St} [MPa]**	**σ_{Sc} [MPa]**	**Err_{St} [MPa]**	**Err_{Sc} [MPa]**
19-20-21	4	-206,9	-162,1	18,0	11,5
22-23-24	12	-221,3	-241,5	19,5	18,3
25-26-27	20	-239,2	-232,6	29,9	31,8

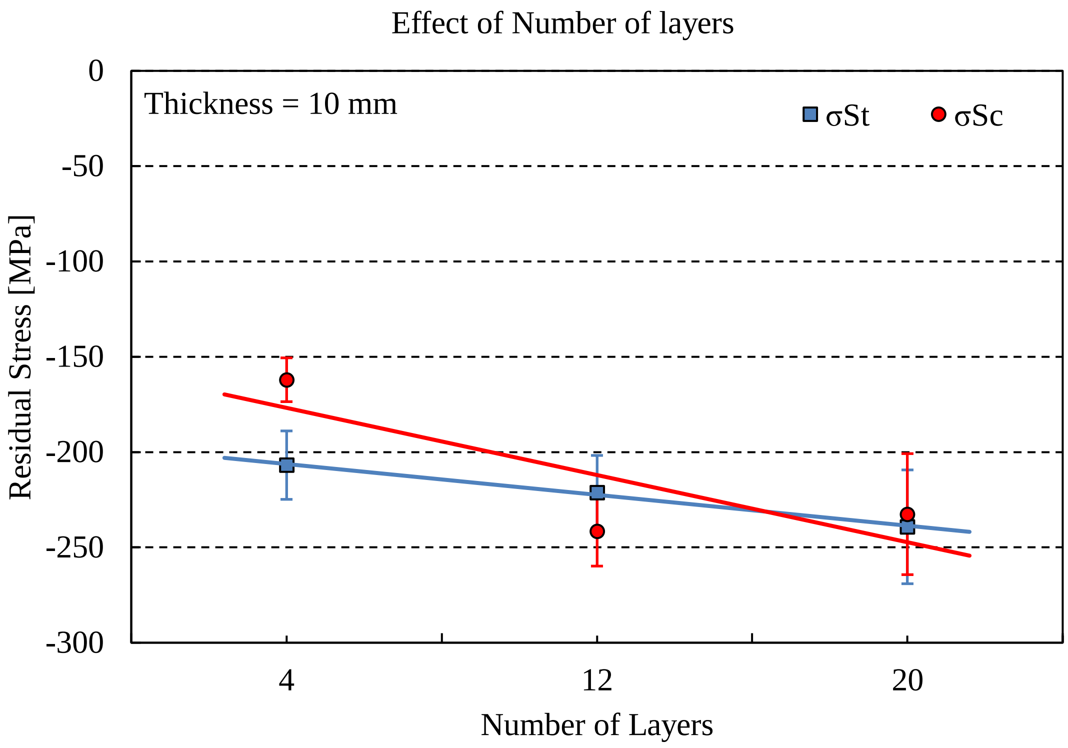

***Figure 3-21**: Effects of number of layers on surface residual stress values of LSP specimens.*

Figures 3-22 and 3-23 show the comparison between the RS profiles of specimen 05 (NPD = 3,5 GW/cm^2) and specimen 08 (NPD = 4,5 GW/cm^2) along both scanning and stepping directions. The actual evaluation depths, residual stress values and corresponding measurement errors were reported for both Specimen 05 and Specimen 08 in Table 3-12a-b, respectively. In general, specimens that were laser peened using the highest value of nominal NPD show higher values of compressive stresses in both directions compared to those characterized by lower values of NPD. As concerning specimen 05, the maximum compression stress in stepping direction is σ_{St} = -296,7 ± 39,1 MPa at a depth of 0,248 mm while in scanning direction is σ_{Sc} = -310,3 ± 35,5 MPa at a depth 0,502 mm. As regards specimen 08, the maximum compression stress in stepping direction is σ_{St} = -341,8 ± 18,9 MPa at a depth of 0,155 mm while in scanning direction is σ_{Sc} = -349,7 ± 14,3 MPa at a depth of 0,251 mm.

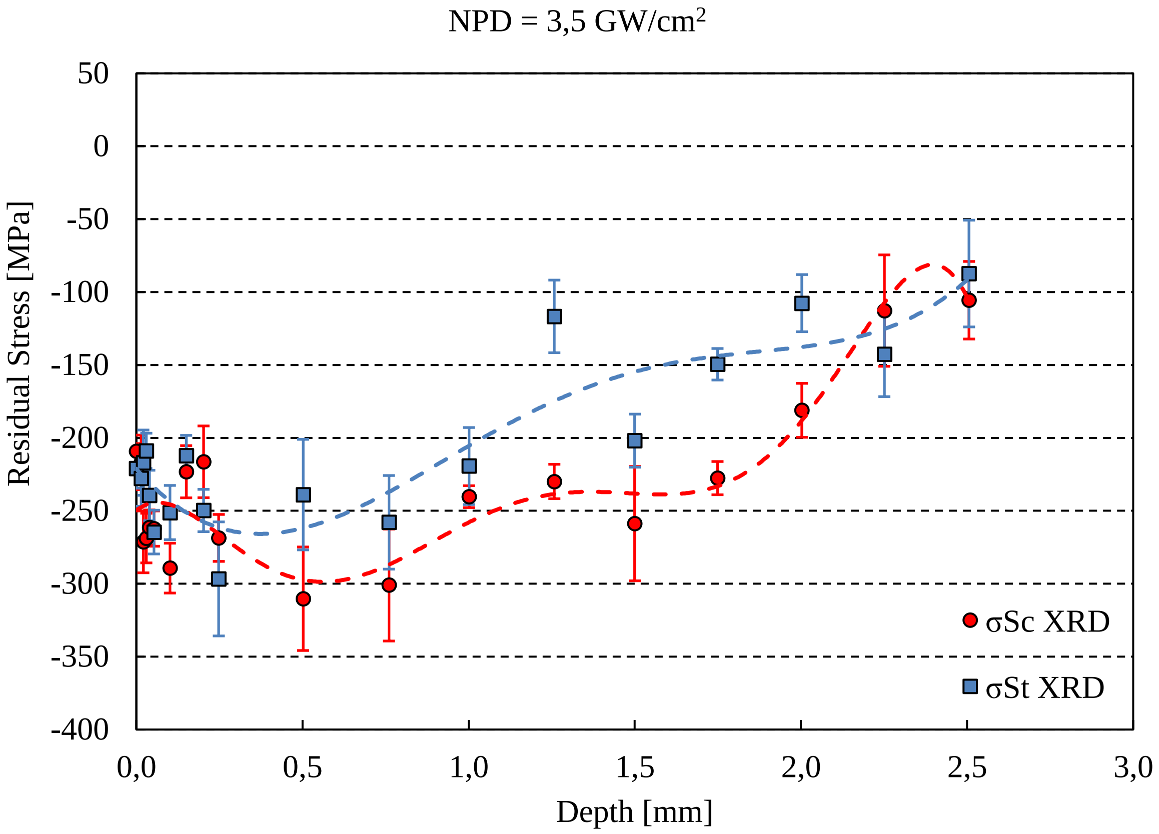

Figure 3-22: *In-depth residual stress profiles along scanning and stepping directions at 3.5 GW/cm^2 NPD level by XRD measurement method (specimen 05).*

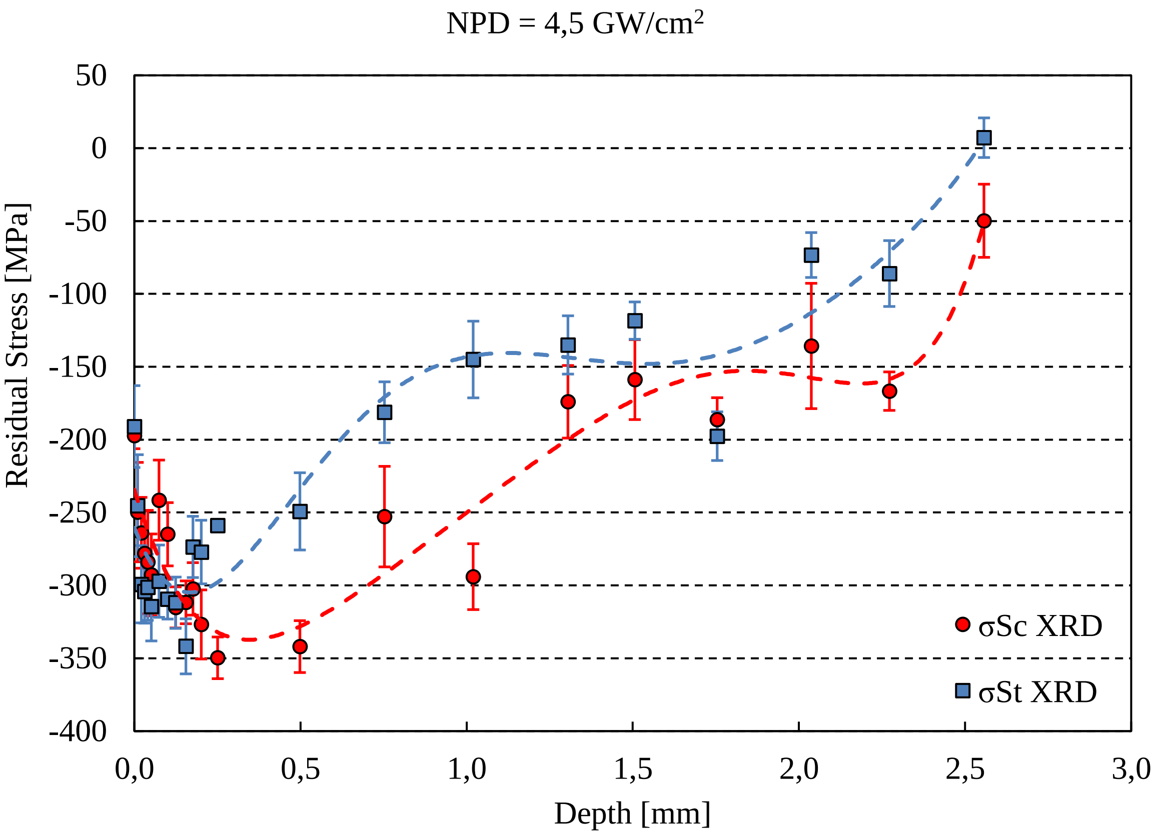

Figure 3-23: *In-depth residual stress profiles along scanning and stepping directions at 4.5 GW/cm^2 NPD level by XRD measurement method (specimen 08).*

In Figures 3-24 and 3-25 the comparison between the RS profile measured by XRD and HDM was shown. They refer respectively to specimens 04-05 and 07-08. Results show a good concordance between the two measurement methods. For both methods, in fact, at a depth between 0.1 and 0.7 mm, with an NDP of 3,5 GW/cm^2, the RS is quite constant between -250 MPa and -350 MPa. Moreover, using an NDP of 4,5 GW/cm^2, it was found very good accordance along the scanning direction, increasing tension from -400 MPa to -250 MPa, while some discrepancies were found in the stepping direction.

***Table 3-12**: In-depth RS measurements by XRD on specimens 05 (a) and 08 (b).*

(a) Specimens 05: NPD = 3,5 GW/cm^2

Depth [mm]	$\sigma_{St\ XRD}$ [MPa]	Err σ_{St} [MPa]	$\sigma_{Sc\ XRD}$ [MPa]	Err σ_{Sc} [MPa]
0,000	-220,9	±13,6	-209,1	±5,2
0,014	-227,8	±19,1	-216,8	±18,7
0,021	-217,0	±22,4	-271,3	±21,2
0,030	-208,9	±12,1	-268,7	±17,0
0,039	-239,5	±17,3	-261,4	±12,0
0,053	-264,6	±15,0	-262,2	±12,1
0,101	-251,2	±18,6	-289,3	±17,1
0,150	-212,2	±13,9	-223,2	±17,9
0,202	-249,8	±14,5	-216,4	±24,6
0,248	-296,7	±39,1	-268,6	±16,1
0,502	-238,9	±37,9	-310,3	±35,5
0,760	-257,9	±32,1	-300,9	±38,4
1,001	-219,3	±26,4	-240,3	±7,5
1,258	-116,7	±24,9	-229,9	±11,8
1,500	-201,9	±18,2	-258,8	±39,2
1,749	-149,5	±10,8	-227,6	±11,4
2,003	-107,6	±19,6	-181,1	±18,5
2,251	-142,6	±29,1	-112,7	±38,2
2,506	-87,3	±36,6	-105,6	±26,6
2,760	-92,1	±47,8	-165,6	±42,5
3,002	-65,9	±34,5	-241,0	±62,9

(b) Specimens 08: NPD = 4,5 GW/cm^2

Depth [mm]	$\sigma_{St\ XRD}$ [MPa]	Err σ_{St} [MPa]	$\sigma_{Sc\ XRD}$ [MPa]	Err σ_{Sc} [MPa]
0,000	-191,0	±28,1	-197,2	±9,0
0,010	-245,3	±35	-249,7	±34,1
0,021	-299,2	±26,5	-263,9	±24,3
0,031	-304,2	±21,7	-278,0	±29,2
0,040	-301,3	±22,7	-284,0	±35,5
0,051	-314,4	±23,7	-292,8	±28,1
0,074	-297,1	±24,8	-241,5	±27,5
0,100	-309,5	±13,6	-264,9	±21,7
0,124	-311,9	±17,6	-315,1	±14,1
0,155	-341,8	±18,9	-311,6	±14,7
0,176	-273,6	±21,0	-302,4	±18,0
0,201	-277,1	±21,8	-326,8	±23,7
0,251	-259,0	±2,0	-349,7	±14,3
0,498	-249,2	±26,5	-342,0	±17,8
0,753	-181,2	±20,9	-252,8	±34,5
1,020	-145,0	±26,3	-294,0	±22,6
1,305	-135,0	±20,0	-174,0	±24,9
1,506	-118,3	±12,8	-158,8	±27,4
1,754	-197,6	±16,7	-186,2	±15,0
2,037	-73,3	±15,4	-135,7	±43,0
2,272	-86,0	±22,6	-166,7	±13,2
2,557	7,2	±13,6	-49,8	±25,1

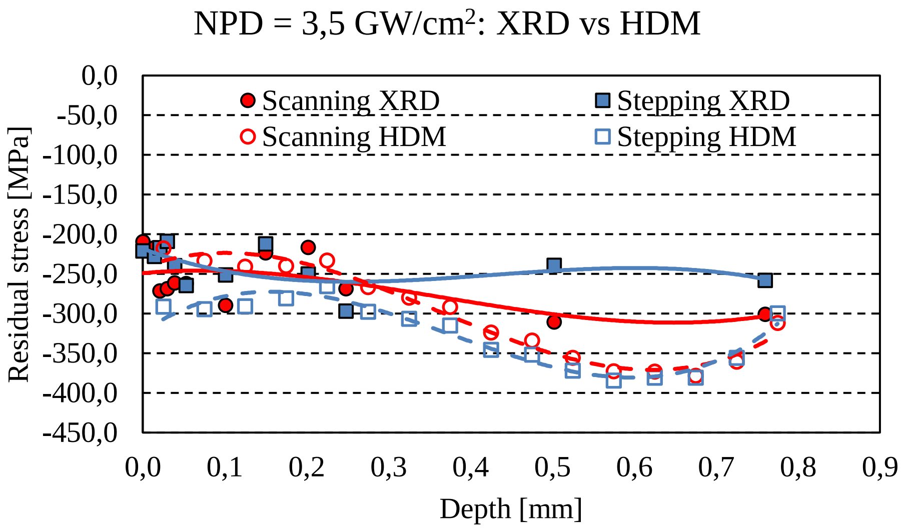

Figure 3-24: *Comparison between the RS profiles measured by XRD and HDM up to 0.7 mm for 3,5 GW/cm^2 specimens.*

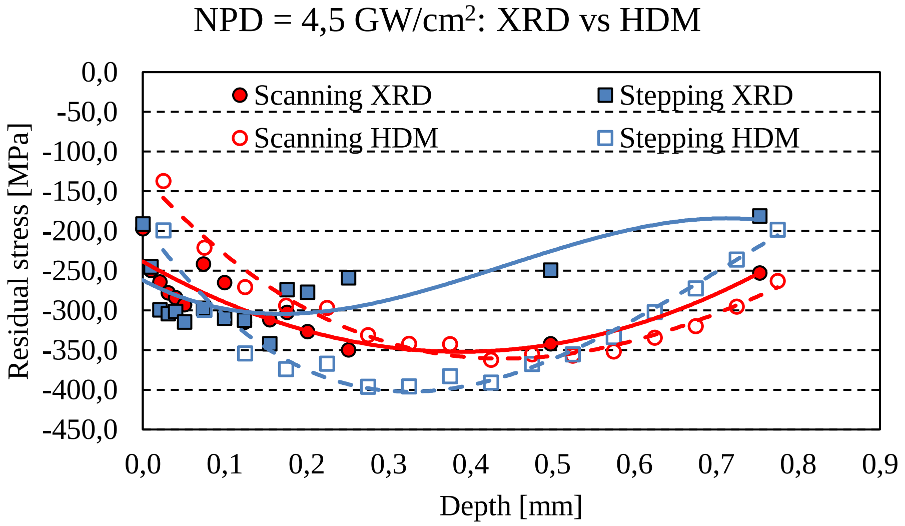

Figure 3-25: *Comparison between the RS profiles measured by XRD and HDM up to 0.7 mm for 4,5 GW/cm^2 specimens.*

As concerning specimens 22 and 25, characterized by a number of layers equal to respectively 12 and 20 at a constant NPD value of 0.8 GW/cm^2, the RS profiles obtained through HDM were shown in Figures 3-26 and 3-27. To provide complete information, the value of residual stress on the surface of each component previously achieved by XRD was indicated on the same diagrams. It is possible to observe that when the NPD is the same, the greater number of layers generates higher compressive stresses. Moreover, the increasing trend of the RS profile starts at a depth deeper than the corresponding value at the lowest value of the number of layers.

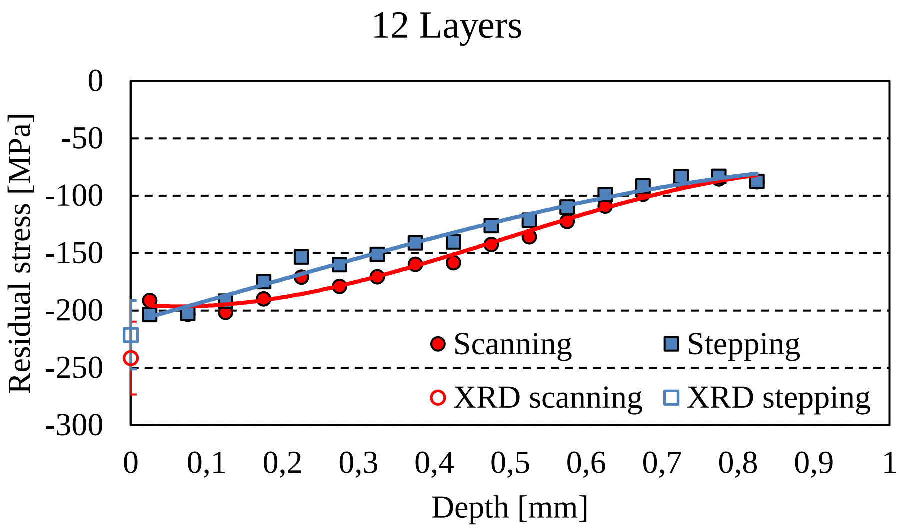

Figure 3-26: *Residual stress profiles obtained by HDM along scanning and stepping directions in the case of 12 layers (specimen 22). Surface point by XRD.*

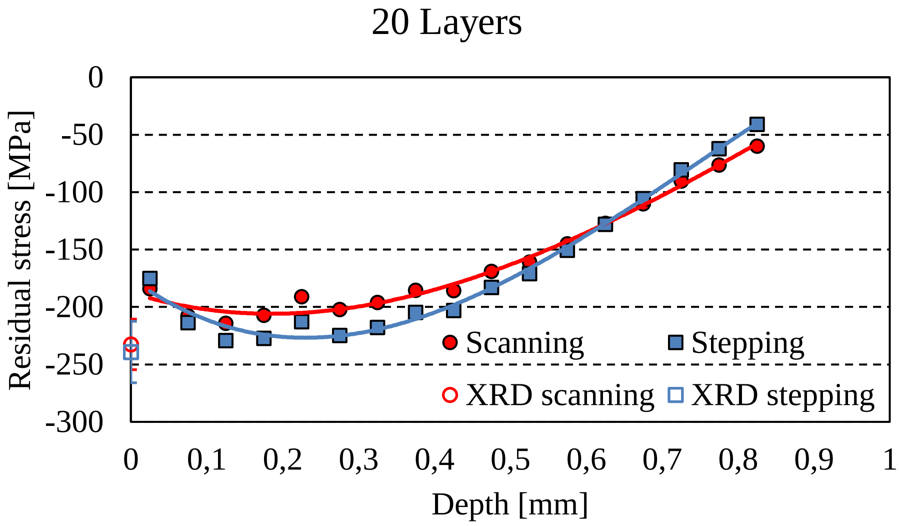

Figure 3-27: *Residual stress profiles obtained by HDM along scanning and stepping directions in the case of 20 layers (specimen 25). Surface point by XRD.*

3.4.4. Residual stress discussion

The development of a compressive residual stress field can be considered as the primary objective of the laser shock peening process. The physical phenomenon on which the development of compressive residual stresses is based recalls concepts related to processes involving plastic deformations: when the plasma pressure exceeds the dynamic yield stress of the material, the irradiated region undergoes an expansion in the plane as a direct consequence of the mechanical action exerted by the shock waves. This expansion, however, is constrained by the presence of the surrounding material whose confinement action determines the development of residual compressive stresses. The analysis of the experimental results showed that all the examined samples present high compressive stresses at the surface: this aspect can be related primarily to the employment of the absorbent coating which protects the substrate from thermal ablation [191] and prevents surface tensile stresses to develop during the LSP process; secondly, the development of tensile residual stresses on the surface of the peened component is usually associated with the occurrence of the “reverse straining” effect due to LSP process performed with smaller spot diameters [192]. Under this assumption, the surface release waves starting from the edge of the laser spot propagate toward the center of the laser spot, increasing in intensity, thereby changing the residual stress field. Based on past research, this phenomenon occurs up to spots as small as 3 mm in size [192], however, based on the available experimental results, it is not possible to draw any conclusion about the possible occurrence of this phenomenon in the case of the study under examination.

Moreover, it was observed that an increase in NPD determined a slight decrease in compressive residual stresses on the surface of 10 mm thick specimens compared to 30 mm thick ones. This behavior can be associated with the phenomenon of the back-reflected shockwaves typical in the LSP process: the induced plastic deformation can be altered by the arrival of the back-reflected stress waves, especially in thin samples, thus altering the residual stress profile within the thickness of the component. In components of reduced thickness, multiple reflections of the shock waves can interfere destructively by hindering the plastic deformation phenomenon still in progress near the irradiated surface of the component and consequently altering its distribution. A critical thickness of 2.5 times the spot diameter has been identified as the limit within which this phenomenon occurs [192]. In the case of 10 mm thick samples belonging to groups D-E-F defined in Table 3-4, 3.5 mm spot size was employed. Therefore, the critical thickness beyond which the effect of back reflection of stress waves is theoretically negligible is approximately 8.75 mm, a value quite close to the thickness of the above-mentioned groups of specimens. The absence of this phenomenon cannot be therefore excluded with certainty. It is also important to note that no other factors were found that could induce a reduction in the surface residual stress field, such as burns or surface cracks.

In addition, the analysis showed that the two in-plane stress components along scanning and stepping directions show similar trends thus highlighting the absence of distortion of the component that would have otherwise led to the relaxation of some of the compressive stresses [180].

As regards residual stresses into the depth of the material, it is important to point out some aspects: minimum residual stress field requirements for fatigue critical applications include a maximum magnitude of approximately 75% of the material yield strength at 1.5% of the component thickness and the zero-crossing point located at about 10% of the component thickness. As it is possible to observe in Figures 3-24 and 3-25 where the RS profiles measured by XRD and HDM are shown, 30 mm thick samples which were laser peened using NPD values of 3.5 and 4.5 GW/cm2 accurately meet the design requirements. As concerning specimens characterized by a higher number of layers and lower NPD values (Fig. 14), the maximum value of compressive residual stresses is located approximately between 0.1-0.2 mm depth, but its magnitude is lower than expected, as a consequence of using lower NPD values compared to the samples considered above. The zero-crossing point is instead located at the desired depth.

The information gathered so far regarding the residual stress field characteristics and the roughness properties at different combinations of process parameters represent an ideal starting point for the evaluation of the fatigue properties of mechanical components treated with LSP, as these are among the main factors influencing the fatigue life of a component. Future work will test from an experimental point of view the ability of the LSP processes analyzed in this work to enhance the resistance of load-bearing components to various types of stress-induced damage, particularly about applications in the aeronautical field.

3.5. Summary

In this chapter, the effects of different combinations of laser shock peening process parameters on the surface roughness and residual stress development of treated components were examined. The following observations emerged from the analysis of the results:

- NPD and number of layers turned out to be the most influential factors affecting roughness properties, determining an increasing trend of both R_a and R_t values shifting from the lowest to the highest level of each parameter. No significant variation in roughness properties was observed along the scanning and stepping directions of the laser and as the thickness of the treated component varied.
- Surface residual stress measurements obtained using the XRD technique pointed out that 10 mm thick specimens present lower values of compressive stress on the surface than 30 mm thick specimens when all other process parameters were kept constant. Moreover, it was observed that compressive residual stresses on the surface of the specimens increase with the number of layers and that the maximum compressive stress is comparable with that obtained using the maximum NPD. In addition, similar trends of the two in-plane stress components along scanning and stepping directions were observed.
- In-depth residual stress analysis revealed that specimens that were laser peened using higher values of NPD showed higher values of maximum compressive stress both along scanning and stepping direction and that residual stresses remained approximately constant up to a depth of about 0.7-0.8 mm beneath the treated surface. Moreover, the influence of the number of layers on in-depth RS profiles was examined: when the number of layers increases, higher compressive stresses are induced and greater stability of residual stress value was observed. It was found that 30 mm-thick samples which were laser peened using NPD values of 3.5 and 4.5 GW/cm^2 accurately met the residual stress design requirements for fatigue critical applications.

CHAPTER 4

COUPLED EFFECT OF TARTARIC-SULFURIC ACID ANODIZING AND LASER SHOCK PEENING ON FOUR-POINT BENDING FATIGUE BEHAVIOR OF AL 7050-T7451 SAMPLES

4.1. Preface

The effects of the Laser Shock Peening (LSP) process and Tartaric-Sulfuric Acid Anodizing (TSA) treatment on the fatigue behavior of 7050-T7451 aluminum alloy will be investigated through four-point bending fatigue tests. Anodizing processes, including TSA, are widely used in aerospace applications to increase components corrosion and wear resistance, but at the same time result in a significant reduction in fatigue properties of the base material. The possibility of combining the anodizing process with laser peening treatment allows this drawback to be overcome by exploiting the unique properties of the residual stress fields induced by the optimized LSP process to increase the fatigue life of the component.

To better understand the mechanisms and application possibilities of these two surface treatments, morphological and microstructural analyses will be carried out on anodized and laser peened components, and the residual stress field induced by a specific laser shock peening process for the pre-treatment of the anodized surface will be evaluated. It will be demonstrated that TSA anodizing determines an appreciable reduction in the fatigue life of the material especially at lower values of stress amplitude, due to the presence of defects at the interface between the substrate and the anodic layer which act as stress concentrators and promote the nucleation of fatigue cracks. The compressive residual stress field induced by the laser shock peening process used as a pre-treatment to anodizing can compensate for the negative effects introduced by anodizing and at the same time offer greater safety margins useful for the design of critical aeronautical structures.

4.2. Introduction

Aluminum alloys from the 7xxx series, with zinc, magnesium and copper as main alloying elements, are one of the most commonly employed for aerospace applications [193–197]. Their high specific mechanical properties make them ideal candidates for structural components or highly stressed parts, especially when the main requirement is fatigue strength [198–200]. However, the difference in electrochemical potential between the secondary phases formed by alloying elements and the aluminum matrix often results in a reduction in the corrosion resistance of the alloy, thus making it necessary the use of specific surface treatments aimed at providing additional corrosion protection [201,202]. The oxide layer that naturally forms on the surface of aluminum components when they are exposed to air is not sufficient to ensure adequate corrosion resistance for the severe service conditions of aerospace environments, characterized by high-temperature gradients and the presence of several chemical agents.

The anodizing process is certainly one of the most widely used solutions for improving the corrosion resistance of aluminum alloys: an artificial stable oxide layer is generated on the surface of the component to ensure appropriate wear and corrosion resistance [203]. Depending on the process parameters adopted, such as anodizing voltage and time, chemical composition and electrolyte temperature, the thickness of the anodic layer can vary from a few micrometers up to several millimeters, with a different impact on the mechanical properties and corrosion resistance of the component [204]. In particular, it has been widely demonstrated in the scientific literature that the anodizing process has a significant influence on the fatigue behavior of materials and this was attributed mainly to the following reasons: firstly, the brittle and porous nature of the anodic layer that easily cracks under cyclic tensile loading and its strong adhesion to the substrate; secondly, the development of tensile residual stresses due to the elastic mismatch between the anodizing film and the substrate and, lastly, the formation of pit-like defects that could act as preferential sites for the nucleation of fatigue cracks.

Typically, for application in the aerospace industry, corrosion resistance and fatigue properties must be simultaneously ensured, and to achieve this, the anodizing process must be optimized so that the thickness and morphology of the anodic layer allow the design requirements to be met. This logically results in the use of lower anodic coating thicknesses, typically in the range of 2-7 µm, to provide an excellent compromise between fatigue resistance and corrosion protection of the material.

For decades, chromic acid was the optimal choice for aeronautical applications because the physical and chemical characteristics of the anodic layer provided an optimal balance between corrosion resistance, adhesion and fatigue properties [205,206]. However, due to the toxic and carcinogenic nature of hexavalent chromium compounds, the European Union Regulation on Registration, Evaluation, Authorization and Restriction of Chemicals (REACH) has placed stringent restrictions on the production and use of these compounds, which has led to the development of different anodizing electrolytes with a lower environmental impact, but capable of guaranteeing similar physical, chemical and mechanical properties. The most widely used processes as an alternative to chromic anodizing are sulfuric, tartaric, tartaric-sulfuric and phosphoric acid anodizing and numerous studies in the scientific literature have attempted to provide detailed information about the morphology, physical and chemical properties, and effects on the mechanical properties for some of the above processes [205,206]. In particular, the tartaric-sulfuric acid anodizing treatment is an environmentally friendly solution, recently developed by Airbus, which favors the formation of an anodic layer with comparable corrosion resistance to that obtained by chromic anodizing [207–209]. However, little information has been provided on the effects of the anodizing process in a TSA bath on the fatigue behavior of the treated components.

The reduction in fatigue performance is usually associated with the presence of pits that act as stress concentrators during fatigue loading. Generally, these pits occur during the pickling process, which is a pre-treatment step that prepares the surface for anodizing and aims at removing the insoluble products generated during the previous etching process. In this respect, Chaussumier [210] developed a numerical model to predict the fatigue life of chromic acid anodized AA 7050-T7451 specimens through the identification of sizes and locations of pickling pits and the evaluation of their contribution to crack nucleation. The feasibility of the model was verified by comparing numerical outputs to experimental results obtained by four-point bending fatigue testing on prismatic specimens that pointed out an important decrease in fatigue resistance due to the anodization process, especially in the HCF region of the S-N curve. Shahzad [211] correlated the presence of pits, due to the pickling process, to the reduction of fatigue performance of chromic anodized 7050 Al alloy. The fractographic observations confirmed that almost all crack initiation sites started from pits whose depth was greater than 8 µm. Lee [212] compared the fatigue behavior of 7050-T7451 specimens after CAA, sulfuric acid anodizing (SAA) and tartaric acid anodizing (TAA) processes and observed that TAA specimens showed the greatest resistance at the lowest applied stress and addressed such result to the presence of irregular pits in the pre-anodized layer.

The presence of tensile residual stresses due to the anodization process can contribute to the degradation of stress-life fatigue behavior of the base material, as confirmed by a study carried out by de Camargo [213] about the effects of anodic films grown on axial fatigue of CAA, SAA and hard anodized specimens.

To balance the negative effects of the anodizing process on the fatigue life of structural components and at the same time guarantee the high mechanical performance required in the aeronautical field, it is possible to adopt specific surface treatments before anodizing, such as peening processes, capable of introducing residual compressive stress fields in the surface and sub-surface region of the component to slow down the propagation of fatigue cracks or even prevent their nucleation [214,215]. In order for such processes to provide the required increase in fatigue life, the induced residual stress field must possess certain characteristics, such as an adequate depth of penetration, a predetermined depth and intensity of the residual stress peak and a well-defined trend reversal point, which can only be achieved by careful design of the peening process. In addition, a thorough analysis of the surface integrity and morphological and microstructural properties of the component following the peening process is essential to ascertain the absence of factors, such as high surface roughness or the presence of surface defects, which may affect the fatigue behavior of the material.

This research activity aims to investigate the effects of residual stresses induced by anodizing and laser peening processes on the fatigue behavior of components made of aluminum alloy 7050-T7451. Specifically, the possibility of using laser shock peening as a pre-treatment to anodizing will be verified to compensate for the reduction of fatigue life due to the formation of the anodic layer. Initially, a study of the residual stress field induced by an optimized laser peening process for aeronautical applications will be carried out to compliance with the design requirements, then the microstructure and morphology of the anodic layer will be analyzed to identify the causes related to the reduction of the fatigue life of the components. Finally, the results of four-point bending fatigue tests conducted on prismatic bending bars (K_t=1) in untreated, anodized, and peened-anodized conditions will be proposed and discussed.

4.3. Experimental Activity

4.3.1. Definition of material and sample geometry

AA7050 (rolled plate) alloy 80 mm thick was supplied in T7451 condition (solution heat-treated, stress-relieved by controlled stretching and then artificially overaged). The chemical composition and the mechanical properties of the AA 7050-T7451 used in the investigations are reported in Table 4-1 and 4-2, respectively. Test specimens were obtained from a rolled plate with the thickness of the specimens parallel to the longitudinal rolling direction of the plate. Figure 4-1 illustrates the shape and dimensions of the fatigue specimens according to the EN 6072:2016 standard.

Table 4-1: *Chemical composition of 7050-T7451 aluminum alloy in wt.%*

Elements	Zn	Mg	Cu	Zr	Fe	Si	Mn	Cr	Ti
Concentration (%)	6.2	2.25	2.3	0.1	0.15	0.12	≤0.10	≤0.04	≤0.06

Table 4-2: *Mechanical properties of 7050-T7451 aluminum alloy.*

Tensile Yield Strength, σy	Ultimate Tensile Strength, σu	Ductility	Modulus of elasticity, E	Poisson’s ratio, ν
MPa	*MPa*	*%*	*GPa*	*#*
469	524	11	71.7	0.33

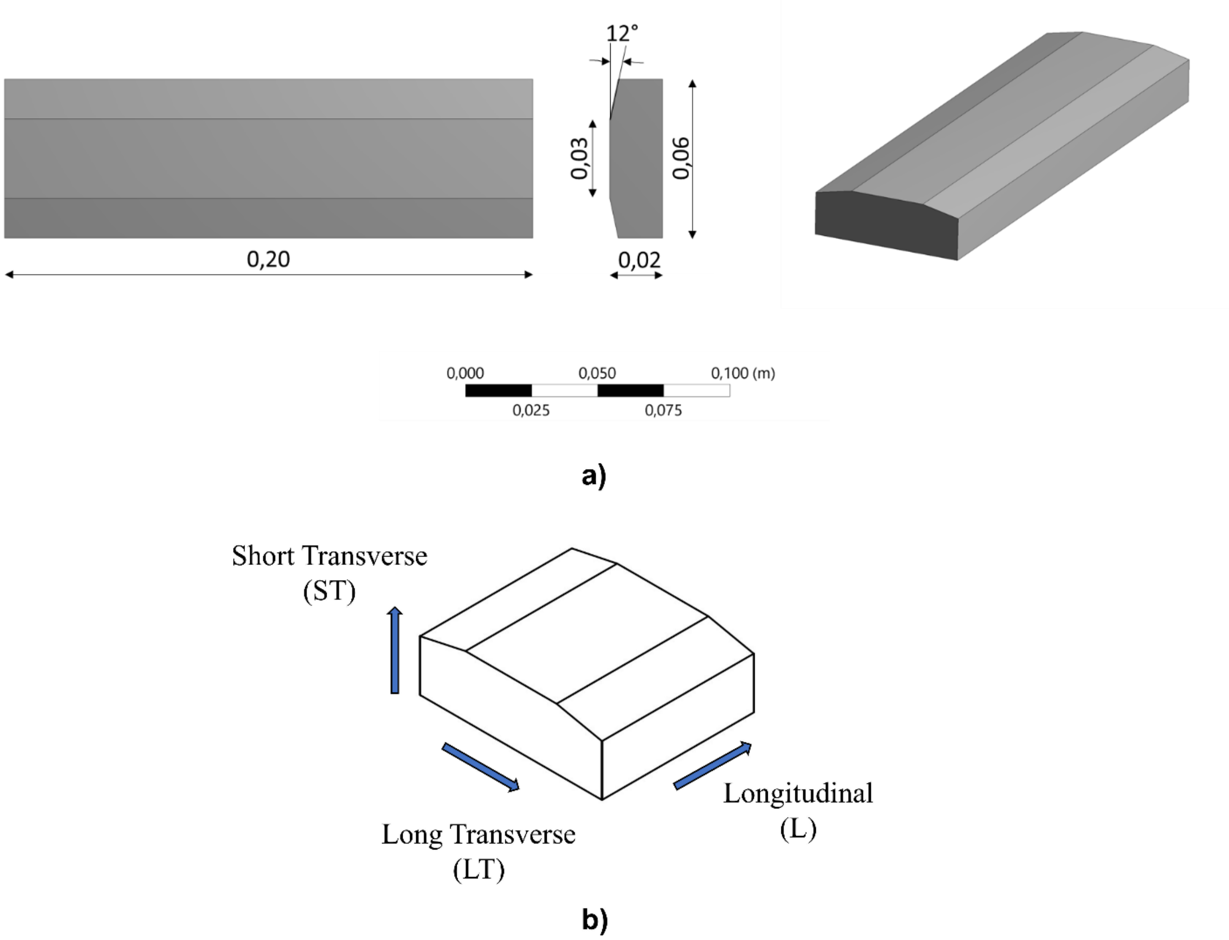

***Figure 4-1**: a) Shape and dimensions of fatigue specimens according to the EN 6072:2016 standard. All dimensions are in meters; b) Definition of section plane directions.*

Fatigue tests were carried out on four different groups of specimens, characterized by different surface conditions: as machined specimens (As M.); specimens subjected only to the anodizing process in a tartaric-sulfuric acid solution (As M.+TSA); specimens subjected in series to mechanical shot peening and TSA anodizing treatments (As M.+SP+TSA); and finally, specimens subjected to laser shock peening and TSA anodizing treatments (As M.+LSP+TSA).

Based on this classification, it will be possible to analyze individually the influence of the anodizing process when applied to the base material as well as to evaluate the effectiveness of the laser peening process when used as a pre-treatment to anodizing, comparing the relative mechanical performance with that derived from an established process such as shot peening.

4.3.2. Tartaric-Sulfuric Acid Anodizing treatment

Prior to anodizing, the specimens were degreased with an alkaline cleaner to remove any contamination from the metallurgical process and then subjected to the pickling process in an aqueous solution of sulfuric acid, nitric acid and ferric sulfate to allow the formation of a homogeneous anodic layer. Anodizing of the specimen in sulfur-tartaric bath was carried out using the following concentrations: 80 g/l $C_4H_6O_4$ and 40 g/l H_2SO_4. The temperature of the bath was set between 37-43°C and a fixed anodizing potential difference of 13-15 V was applied for 22 min in the case of As M.+TSA and As M.+SP+TSA samples and 45 min in the case of As M.+LSP+TSA samples. As a consequence of the different treatment times, the anodic layer of the As M.+LSP+TSA specimens will be about twice the thickness of the anodic layer of the As M.+TSA and As M.+SP+TSA specimens. The objective is to verify whether the Laser Shock Peening process can still provide fatigue performance comparable to that offered by shot peening despite the increased thickness of the TSA layer.

4.3.3. Shot Peening and Laser Shock Peening Processes

Both mechanical and laser peening processes were carried out before the TSA anodizing treatment so as not to damage the anodic layer. The shot peening process was applied in the central portion of the specimen surface subjected to tensile stress during fatigue testing (Figure 4-2). The specimens were initially shot peened to full coverage using cast steel shots with an average size of 600 µm at an intensity of 0.20 to 0.24 mmA. Next, the specimens were subjected to a decontamination process using glass shots of smaller size (300 µm) and with a resulting Almen intensity of 0.26-0.32 mmN.

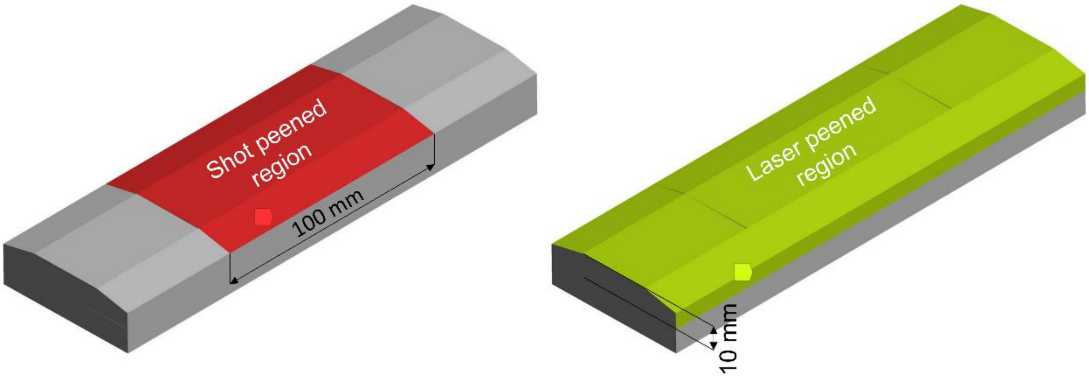

***Figure 4-2**: Identification of the shot and laser shock peened areas on four-point bending fatigue specimens.*

Laser peening treatment was performed on the entire tensile surface and part of the side surfaces of the fatigue specimen, as shown in Figure 4-2. A neodymium-doped yttrium lithium fluoride (ND:YLF) laser system characterized by a wavelength of 1053 nm and operating at a frequency of 10 Hz was employed. The treated surface was preliminarily covered with a layer of ablative material (aluminum tape) in order to promote the formation of the plasma cloud, and a laminar flow of water was made to flow over the surface of the component in order to confine the plasma expansion by directing it toward the thickness of the component. Laser pulses with a nominal energy of 2.5 J and duration of 20 ns were then projected through a circular spot of 2 mm diameter onto the surface of the part according to a predefined pattern to ensure complete coverage of the treated region. Specifically, adjacent spots had an overlap rate of 33% in both the scanning and stepping directions to ensure complete coverage and uniformity of the induced residual stress state. In the present case, the scanning and stepping directions correspond with the transverse and axial direction of the fatigue specimen, respectively. In addition, three different laser peening layers with a 33% phase shift between them in both main directions of the laser pattern were employed. The parameters of the LSP process were selected in accordance with the results of the residual stress profiles and surface integrity parameters that emerged during the investigation described in the Chapter 4 of this research activity. The nominal power density corresponding to the employed values of energy, spot size, and pulse duration turns out to be 4 GW/cm^2, a value between the two levels of nominal power density at which the suitability of the residual stress profiles to the design requirements had been previously verified. In addition, the parameters of overlap between adjacent spots, number of layers and offset between layers were kept unchanged from the values used in the previous analysis.

4.3.4. Microstructure and residual stress evaluation methods

The base material microstructure, after being ground and mechanically polished, was revealed by conventional analytical techniques: Optical Microscope (OM) Nikon Eclipse TE2000-U supplied by computer-assisted image analysis (NIS Elements BR) and Scanning Electron Microscope (SEM) Zeiss EVO-MA10. SEM examination was conducted to evaluate the thickness of the anodic layer obtained by the anodizing process of the specimen along the Short Transverse-Long Transverse plane (ST-LT) (see Figure 4-1). The thickness of the anodic layer was calculated as the average of ten thickness values obtained by examining five different randomly chosen cross-section micrographs of the anodized specimen. Two thickness values were extrapolated from each micrograph. The surface morphology of as-received specimens' longitudinal section, before and after the anodizing process, was characterized by scanning electron microscopy. Moreover, void areas of specimens in the longitudinal section were obtained using NIS software for imaging analysis. In particular, void area percentage was measured as the sum of the void areas divided by the total area of the examined surface.

The surface residual stresses were evaluated using the X-ray diffraction technique in accordance with the indications given in the reference standard UNI EN 15305 (2016). The Xstress 3000 G3R X-ray diffractometer (Stresstech) equipped with a Cr tube ($\lambda = 0.2291$ nm) and a 2 mm diameter circular collimator was employed. Measurements were based on the (311) diffraction reflection of Kα radiation assuming the elastic constants S_1 and $S_2/2$ equal to respectively 1.905×10^{-6} MPa^{-1} and -4.887×10^{-6} MPa^{-1}. The residual stress values were computed by the $\sin^2\Psi$ technique. All other measurement parameters are reported in the Table 4-3.

Table 4-3: *X-Ray Diffraction measurement parameters.*

Diffraction Angle *[°]*	Exposure time *[sec]*	No. of Tilts *[#]*	Tilt angle *[°]*	Tilt oscillation *[°]*	Voltage *[kV]*	Current *[mA]*
139,3	40	9	±45	±3	30	7.5

Surface residual stresses were evaluated for each type of specimen at three points located on the longitudinal axis of the tensile surface of the fatigue specimens, as shown in Figure 4-3. Biaxial stress measurements were made along the axial (σ_x) and transverse directions (σ_y) of the fatigue specimen.

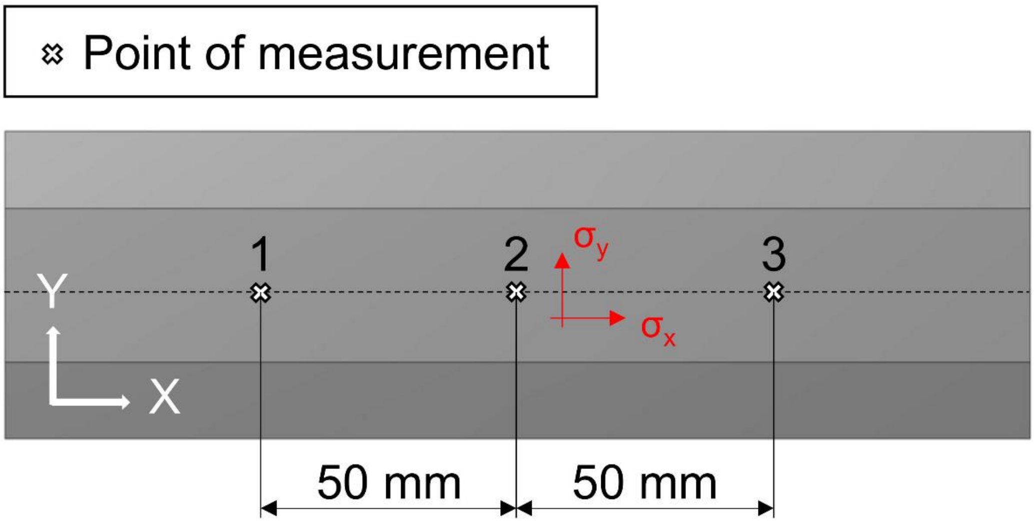

Figure 4-3*: Location of surface residual stress measurement points on the tensile surface of fatigue test specimens.*

An AM+LSP+TSA specimen was randomly selected to measure the in-depth residual stress profile induced by the simultaneous application of the laser peening process and TSA anodizing treatment. The measurement was made at the midpoint of the tensile surface of the fatigue specimen (point 2 in Figure 4-3) to a depth of about 1.75 mm from the component surface along the scanning and stepping direction of the laser pattern. The analysis was conducted by removing layers of materials through a step-by-step electrolytic-polishing procedure using a Movipol-3 equipment (Struers) and A2 electrolyte. Different removal steps were selected depending on the depth of evaluation: 10 µm of removal up to a depth of 50 µm, 25 µm at depths between 50 and 200 µm, 50 µm between 200 and 500 µm, 100 µm between 500 and 1000 µm, and 250 µm between 1000 to 1750 µm. Material removal operations were conducted by applying a voltage of 85 V for 20-sec intervals to ensure a current intensity of about 0.8 A. The measurement parameters adopted for the evaluation of surface residual stresses were similarly employed for in-depth measurements.

To approximately estimate the effective depth of the SP and LSP processes, microhardness measurements were made in the cross section of a single sample belonging to the As M., As M.+SP+TSA and As M.+LSP+TSA groups. Each sample was sliced perpendicularly to the treated surface, hot mounted in transparent resin and polished by silicon carbide abrasive papers in sequential steps. The microhardness was measured with a load of 100 g and a dwelling time of 15 sec using Shimadzu HMV-G2 automatic loading and unloading Vickers microhardness tester. Hardness values were acquired at depth intervals of 100 µm from the treated surface.

4.3.5. Four-point bending fatigue tests

Fatigue tests were carried out through a four-point bending test fixture. The device, designed and built expressly for these tests, consisted of two HE-A profiled steel beams connected to a servo-hydraulic load frame (Schenk PC 400M) through two bolted flanges. The support and loading rollers (15 mm diameter) were mounted on V-shaped grooves to allow free rotation under load and were placed on the upper and lower beam, respectively, according to indications reported on reference standard [216]. The span between outer and inner rollers was adjusted by sliding the grooves inside the adjustment slots built on the flanges of each beam. Their distance was measured to the nearest 0.1 mm. The load was measured by a 250 kN load cell directly mounted on the testing machine crosshead (Figure 4-4).

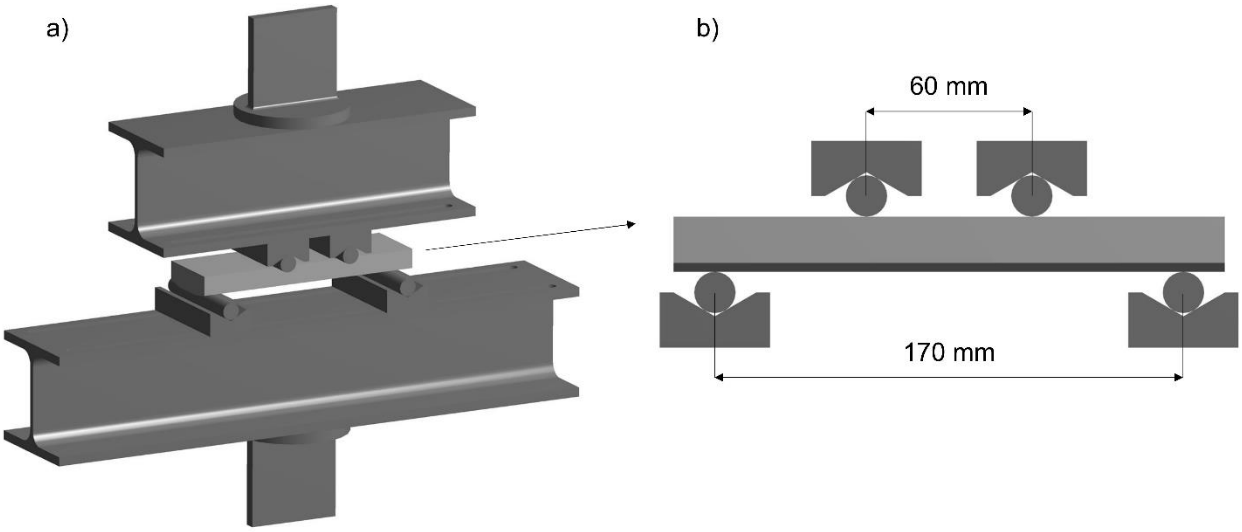

Figure 4-4: *a) Schematic representation of the four-point bending setup; b) position of support and loading rollers on the surfaces of the specimens.*

Fatigue testing was conducted under load control with a maximum cyclic frequency of 15 Hz (sinusoidal waveform) at a stress ratio $R = \frac{\sigma_{min}}{\sigma_{max}}$ of 0.1 and under constant amplitudes cyclic loads. All experiments were carried out at room temperature. With such a stress ratio, the face in contact with the lower rollers was submitted to time-varying in-plane tensile stresses, while the face in contact with the upper rollers was submitted to time-varying in-plane compressive stresses.

The tests were interrupted when 3×10^6 cycles were reached without any sign of cracking and when the failure occurred or cracks were visually observed. To generate S-N data, fatigue tests were performed at stress levels that provided lifetimes between about 3×10^4 and 3×10^6 cycles.

The nominal maximum tensile stress σ_{max} within the loaded specimen was calculated using Equation 1 where M_f is the constant maximum bending moment between the two inner supports, z_{max} is the maximum distance between the sample surfaces and the neutral axis in the cross-section, I_{yy} is the true moment of inertia about the y-y axis (Figure 4-3).

$$\sigma_{max} = \frac{M_f z_{max}}{I_{yy}} \tag{1}$$

The maximum and minimum stress at respectively the stretched and compressed specimen surface was then calibrated through the application of two HBM strain gages (type 3/120 LY11) at the center of both surfaces along the axial direction.

The bending moment raises linearly from the outer roller to the inner one. The portion of the specimen between the inner and the outer roller is loaded with a constant bending moment (shear force is zero), given by Equation 2

$$M_f = \frac{(L - L_i)F}{4} \tag{2}$$

where L and L_i are respectively the distances between outer and inner rollers and F is the total applied force (Figure 4-5).

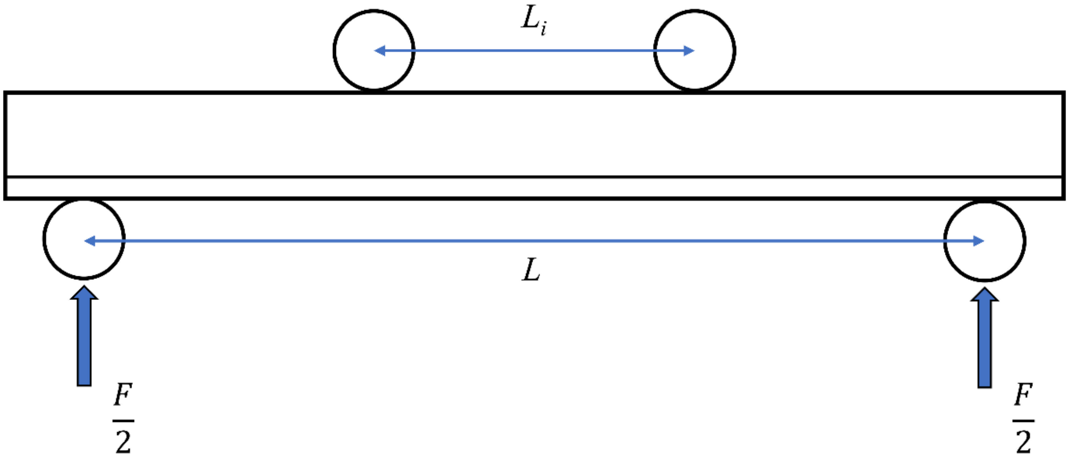

***Figure 4-5**: Schematic representation of the dimensions and positioning of the four-point bending testing fixture according to BS EN 6072:2010.*

All the parameters used for the calculation of the maximum tensile stress at the stretched surface of 4PB coupons are listed in Table 4-4.

***Table 4-4:** Parameters for the calculation of maximum tensile stress.*

L *[mm]*	**L_i** *[mm]*	**Elastic modulus/E** *[GPa]*	**I_{yy}** *[m^4]*	**z_{max}** *[m]*
170	60	71.7	3.6×10^{-8}	0.01037

Specimens that failed in fatigue were subsequently cycled to complete fracture at a high-stress ratio for fractographic examinations (Figure 4-6). The fracture surfaces of As M., As M.+TSA, As M.+SP+TSA and As M.+LSP+TSA specimens were evaluated by SEM to identify both nucleation sites and propagation of fatigue cracks.

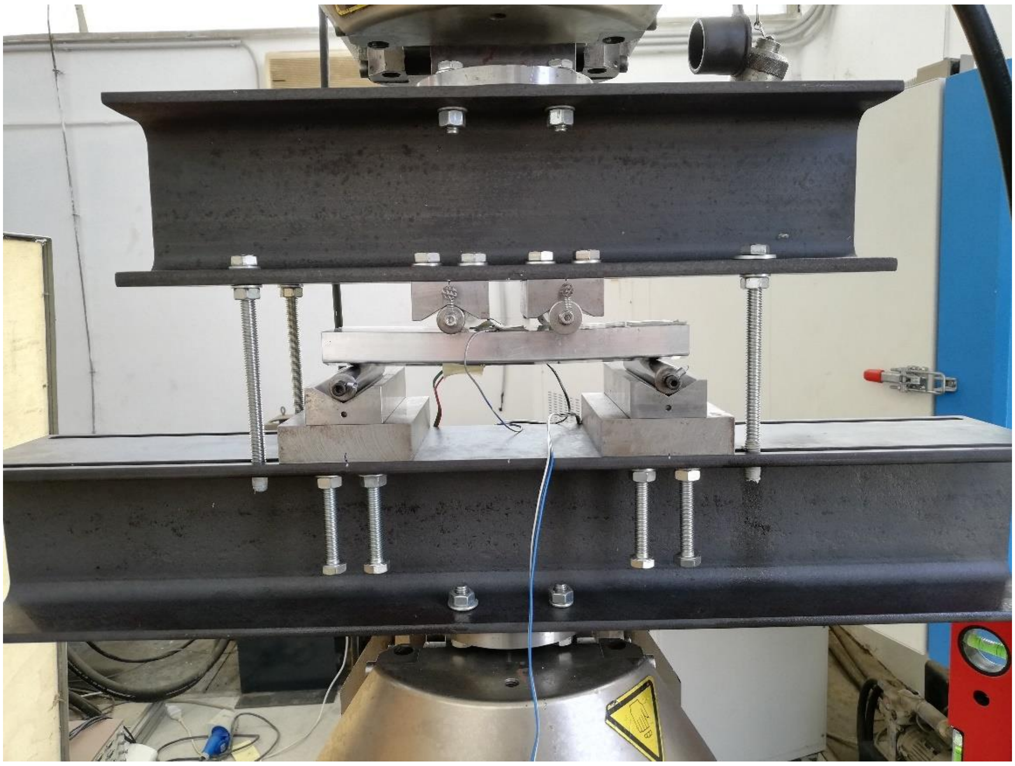

Figure 4-6: *Experimental setup of four-point bending fatigue tests.*

4.4. Results and discussions

4.4.1. Base material characterization

The base material (substrate) is an AA7050-T7451 alloy based on the Al-Zn-Mg-Cu system. This is an over-aged Al alloy that is characterized by high fracture toughness and minimal loss of tensile strength. Figure 4-7 depicts optical (Figure 4-7a) and SEM (Figure 4-7b, c) micrographs of the microstructure of the AA 7050-T7451 specimen. OM and SEM observations reveal the presence of the aluminum matrix (solid solution phase) together with coarse intermetallic compounds, whose shape can be spheroidal and elongated or irregular. These intermetallic compounds, often referred to as constituent particles [200], between 0.5-16 µm in size, are aligned as stringers in the direction of working metal (rolling direction) (Figure 4-7a, b). Based on particles morphology and previous works [198,200,217] it can be concluded that the large and spherical particles are Al_2CuMg (Figure 4-7c) and the elongated (rod-shape) or irregularly shaped ones are Al_7Cu_2Fe (Figure 4-7c).

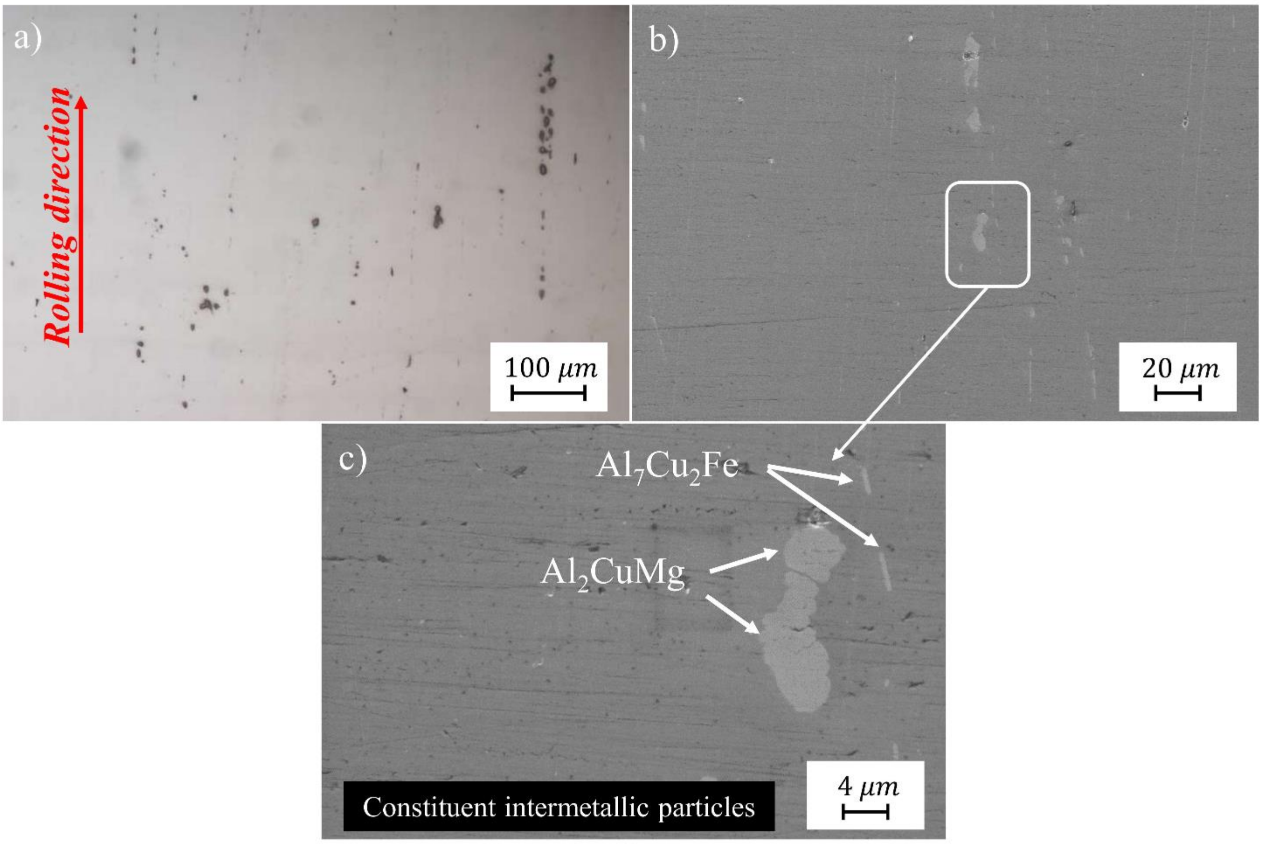
a)
Rolling direction
100 μm
b)
20 μm
c)
Al_7Cu_2Fe
Al_2CuMg
Constituent intermetallic particles
4 μm

Figure 4-7: *Microstructure of base material (As M.): a) optical, b) SEM micrographs of AA 7050-T7451 which depict the aligned stringers of intermetallic precipitates in the alloy matrix due to the forming steps aluminum plates are subjected to, and c) SEM image of large and spherical Al2CuMg particles and rod-shaped Al7Cu2Fe particles.*

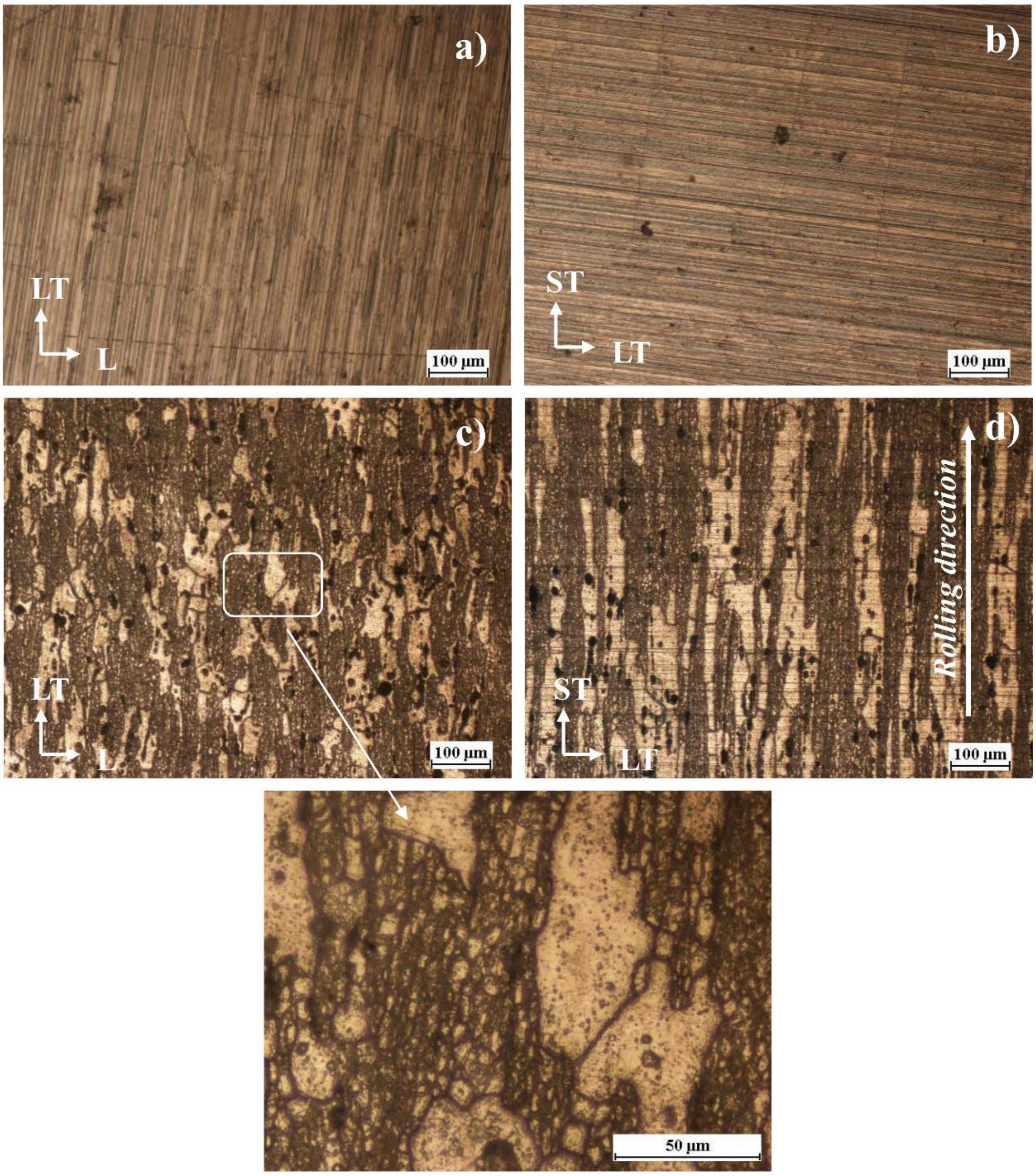

Figure 4-8: *Appearance of the surface of AA7050 T7451 specimens: a) longitudinal section (LT-L plane) and b) cross-section (ST-LT plane) of As M. specimen. While: c) microstructure on the longitudinal section (LT-L plane) and d) microstructure on the cross-section (ST-LT plane) of As M.+TSA specimen; as expected, the grain structure is elongated with a typical flat pancake-shaped structure, especially in the rolling direction.*

The effect of the TSA anodizing process on surface appearance of the specimens, corresponding to the transverse (Short Transverse-Long Transverse (ST-LT) plane) and longitudinal section (Transverse-Longitudinal (LT-L) plane), are shown in Figure 4-8. The untreated As M. specimen shows the texture of the existing scratches produced by milling on the surface (Figure 4-8a, b). While the anodizing process points out the microstructure of the substrate alloy. Especially, the optical micrographs (Figure 4-8c, d) show that the alloy, due to the forming steps to which aluminum plates were subjected, consists of highly elongated, bandlike grains aligned with the rolling direction and some fine grains (partially recrystallized grain structure). Moreover, it can be noted that the constituent particles, responsible for the high mechanical properties of the alloy, are mainly distributed at grain boundaries and/or within grains.

4.4.2. Morphology of the TSA anodic layer

Analysis using SEM was performed to evaluate the surface morphology of the anodic layer on simply anodized and peened+anodized samples. Figure 4-9 shows the typical plane view SEM images of the As M. specimen surface (top view) and of the TSA anodized surface. The As M. specimen (Figure 4-9a and b) exhibits homogeneous and featureless surface morphology with a small number of surface defects, such as pin-holes resulting from either substrate imperfections (Figure 4-9b) or local chippings due to standard mechanical preparation of the surface performed before the anodizing treatment. On the other hand, the As M.+TSA specimen surface appeared morphologically tailored to bond well with the surface of the specimen (Figure 4-9c). Besides, as expected, due to the high reactivity of the intermetallic particles, TSA anodizing leads to the formation of an anodic layer with some surface defects (Figure 4-9d). The defects consist mainly of small cavities and micro-pores between 0.6 – 20.5 µm in diameter (Figure 4-9c and d). A careful inspection of the anodic layer (Figure 4-9d) reveals that the percentage area fraction of defects induced by anodizing is approximately equal to 2.6%. This value was obtained by dividing the sum of the void areas by the total area of the examined surface. In addition, it was noted that the cavities have similar shapes and dimensions to those of Al_2CuMg particles. Consequently, the formation of these cavities depends mainly on the preferential dissolution of these particles enriched with Cu and Mg, occurring in a three-step process: homogeneous dissolution, copper deposition, and local dissolution of the surrounding matrix. Contrariwise, the formation of micro-pores is considered a consequence of the dissolution of grain or sub-grain boundary precipitates [201,217,218]. Furthermore, it was observed that the defects distribution is irregular and in some areas the defects are rather close forming clusters (Figure 4-9d and f). Usually, these pore clusters can significantly weaken the mechanical properties of the specimen, serving as primary sites for the nucleation of fatigue cracks [200].

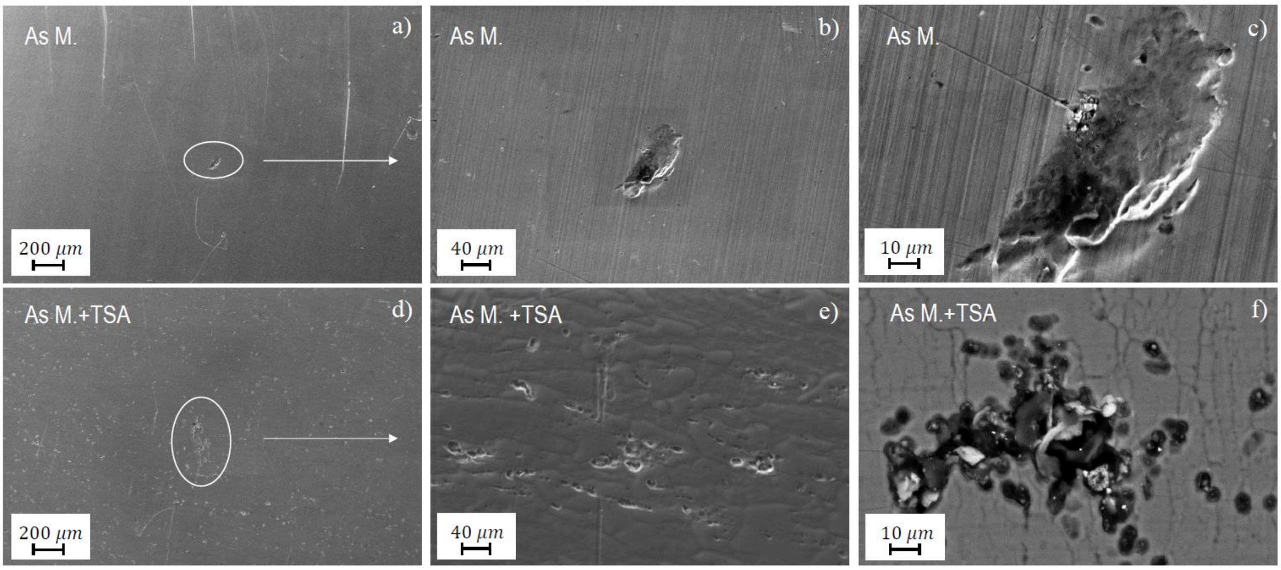

Figure 4-9: *Top view (a-f) SEM images (L-LT plane) of the untreated as-machined specimen (a-b) and anodized specimen (c-d) at different magnifications: e) high magnification detail of a defect present on the surface of As M. specimen; f) high magnification detail of a cluster of micro voids on the surface of As M.+TSA specimen.*

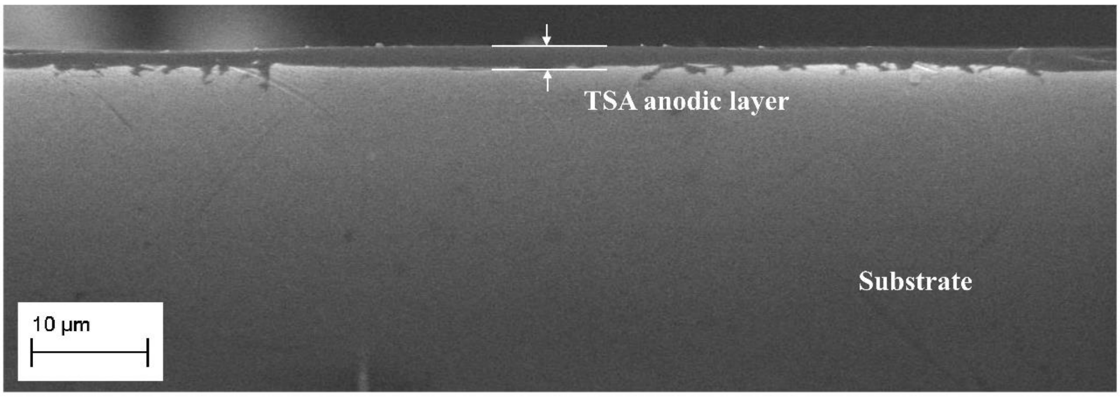

Figure 4-10: *SEM micrograph of the cross-section (LT-ST) of the anodic film formed in TSA bath.*

Figure 4-10 displays the cross-section SEM image of the As M.+TSA specimen. The SEM micrograph shows a dense anodic layer forming along the upper part (top) of the specimen substrate. It can be observed that the anodic layer inherited relief of the specimen surface. Especially, a closer examination of the film regions near the interface suggests that the anodic oxidation penetrates inside the cavities already present on the surface of the specimen, filling them. The anodic film thickness was about 2.16 ± 0.4 μm. For the used experimental conditions this result agrees with the literature [205].

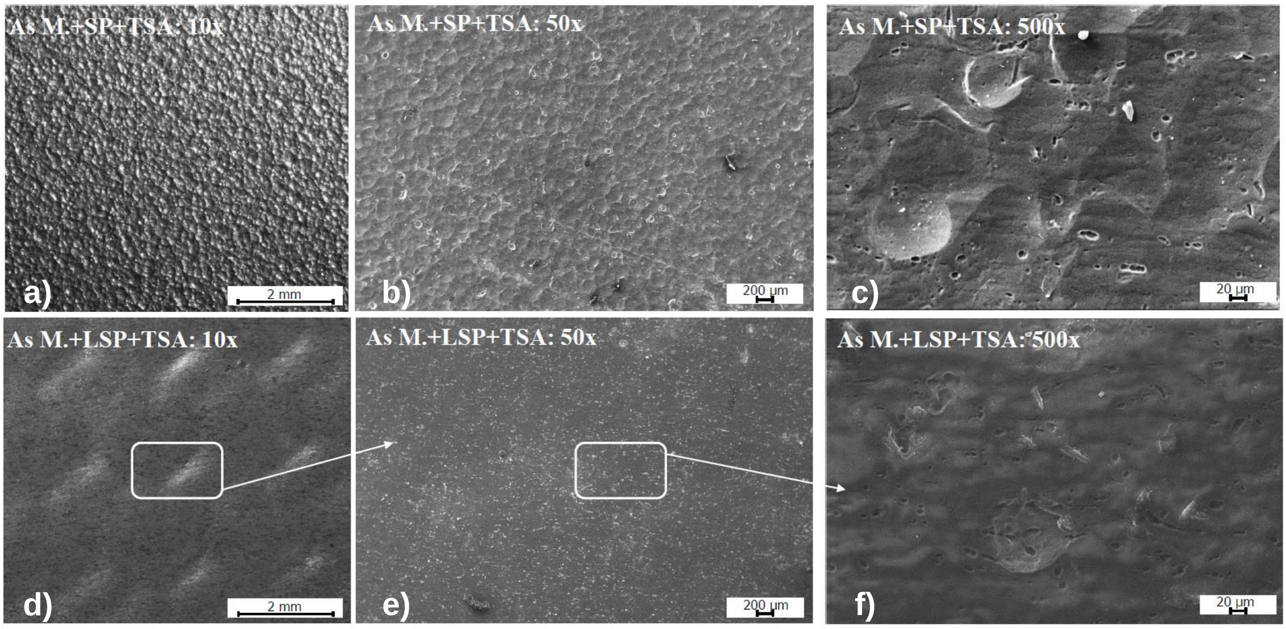

Figure 4-11: *Top view (a-f) SEM images (L-LT plane) of the As M.+SP+TSA (a-b) and As M.+LSP+TSA specimen (c-d) at different magnifications: e) high magnification detail of a defect present on the surface of As M. specimen; f) high magnification detail of a cluster of micro voids on the surface of As M.+TSA specimen.*

Figure 4-11 shows SEM micrographs of the surface of As M.+SP+TSA and As M.+LSP+TSA component at different levels of magnification. The two peening processes affect the surface morphology of the examined samples differently: the surface of the shot peened sample exhibits the typical indentations (Figure 4-11a-b) induced by the impact of glass shots on the surface during the decontamination phase of the shot peening process. The TSA layer develops on this starting morphology and leads to the formation of a final rough surface characterized by the presence of pores and voids similar in type, density and size to those found in the case of simply anodized sample (Figure 4-11c). In the case of As M.+LSP+TSA samples, the surface of the component does not show the presence of visible indentations as in the case of shot peened sample (Figure 4-11d-e). This is due both to the systematic nature of the LSP process (ordered pattern of laser spots) as opposed to the randomness of impacts in the SP process, and to the different size of the laser spots as compared to the diameter of the shots used in the SP treatment. As a result, the surface appears similar to that of a simply anodized component rather than that of a shot peened component. The type, density and size of defects induced by the TSA anodizing process is comparable to that observed in the case of anodized and shot peened samples (Figure 4-11f).

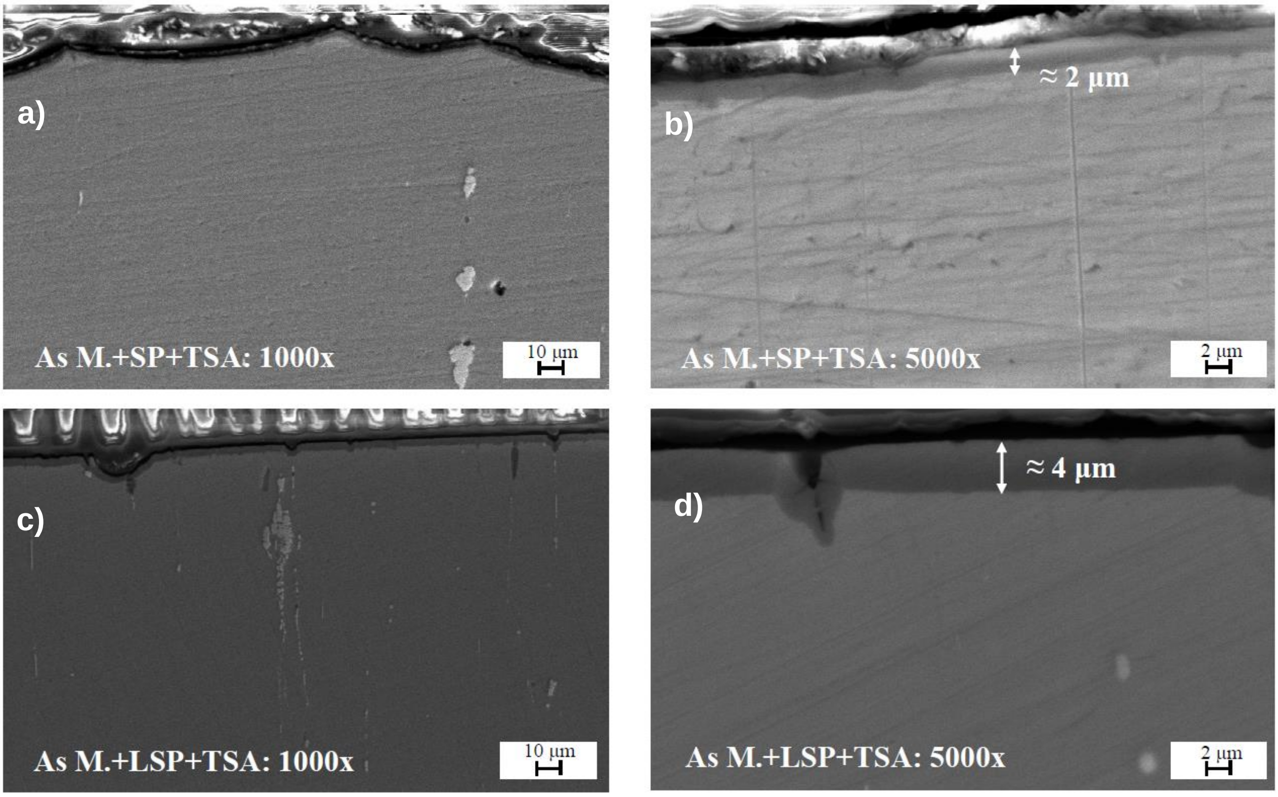

Figure 4-12: *SEM cross-sectional views of As M.+SP+TSA and As M.+LSP+TSA specimens at different magnifications.*

Cross-sectional analysis of the As M.+SP+TSA specimen confirmed the presence of an anodic layer about 2.08 ±0.3 µm thick well bonded to the material substrate despite the high surface roughness induced by the shot peening process. This thickness coincides with that measured in the case of simply anodized sample as a result of the employment of the same anodizing time (Figure 4-12a-b). In the case of As M.+LSP+TSA sample, a TSA layer thickness of 4.16 ± 0.4 µm is observed due to twice the anodization time in tarta-sulfuric solution compared to the shot peened sample. No lack of adhesion between the anodic layer and substrate is visible, however, some microcracks generally less than 15 microns in length are observed originating on the surface of the anodic layer and propagating through the substrate of As M.+LSP+TSA samples (Figure 4-12c-d).

4.4.3. Residual stress and microhardness analyses

The diagrams shown in Figures 4-13 and 4-14 show the values assumed by the surface residual stresses in the axial and transverse directions at the three measurement points on the tensile surface of the fatigue specimens. The data were obtained by averaging the results of residual stresses measured on a batch of four specimens in each group. Linear interpolation functions were used to evaluate the trend of axial and transverse residual stresses as the measurement position on the specimen surface changed.

Compressive stress states of different magnitudes are observed in all four categories of specimens considered. As expected, the stress state is almost uniform on the surface of the component, and only a slight deviation from linearity is found in the measurement of transverse residual stresses on As M. specimens, probably associated with the technological processes to which the component has been subjected. The As M. specimens exhibit an average compressive stress state of about -100 MPa along both evaluation directions. Generally, in the scientific literature, anodizing processes are associated with the presence of tensile stress fields on the surface of the component. However, the analysis of the reported data shows a trend contrary to expectations, in which the anodizing process in tartaric-sulfuric solution appears to induce a slight increase in the compressive stress state on the surface of the component, both in the axial and transverse directions. It should be pointed out, however, that the extremely small thickness of the anodic layer causes residual stress measurements by X-ray diffractometry (penetration depth of about 10 microns) to be made on a volume of material that does not consist entirely of the anodic layer, but rather largely of base material. Consequently, surface residual stress measurements in TSA specimens are not to be considered as residual stresses within the anodic layer, but measurements on a volume of material that also includes the anodic layer. Much more interesting, however, is to analyze the results of specimens consecutively subjected to peening and anodizing processes. Regarding surface residual stresses, in the case of SP specimens, a compressive average residual stress field of about -190 MPa is observed in both longitudinal and transverse directions. The uniformity of stresses in the two measurement directions is a direct consequence of the stochastic nature of the shot peening process and the choice of appropriate coverage and intensity values.

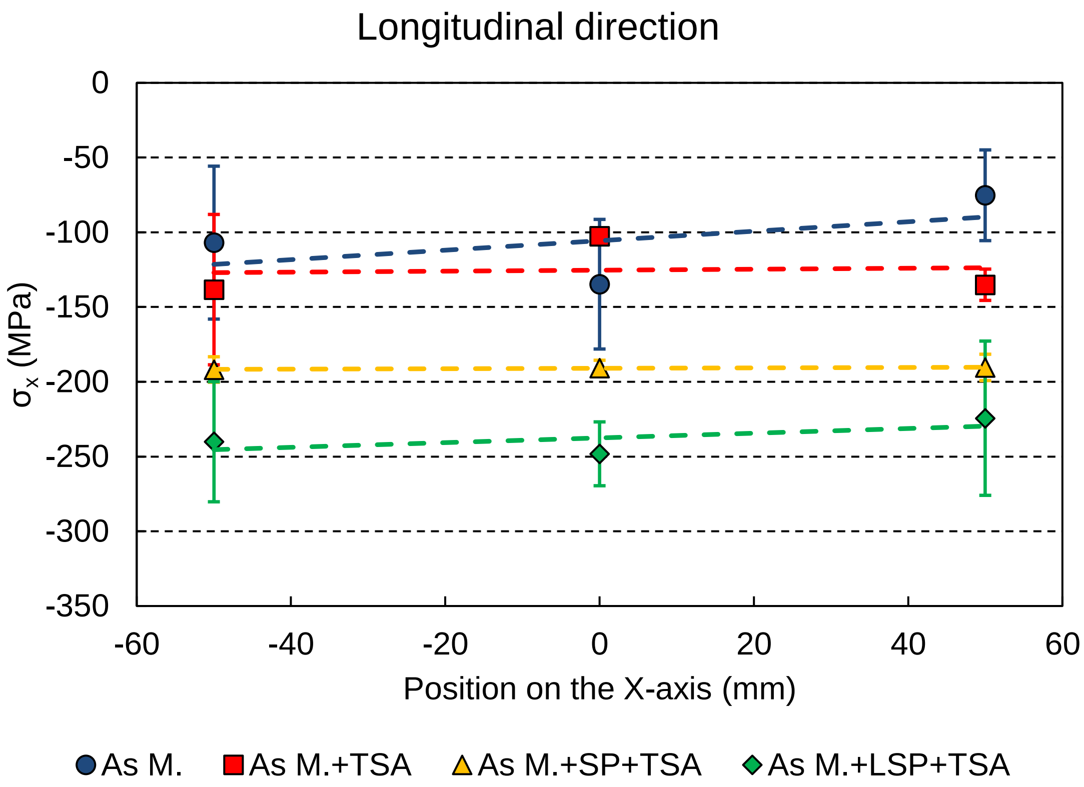

***Figure 4-13**: Residual stress values at three different positions on the surface of As M., As M.+TSA, As M.+SP+TSA and As M.+LSP+TSA specimens along the longitudinal direction.*

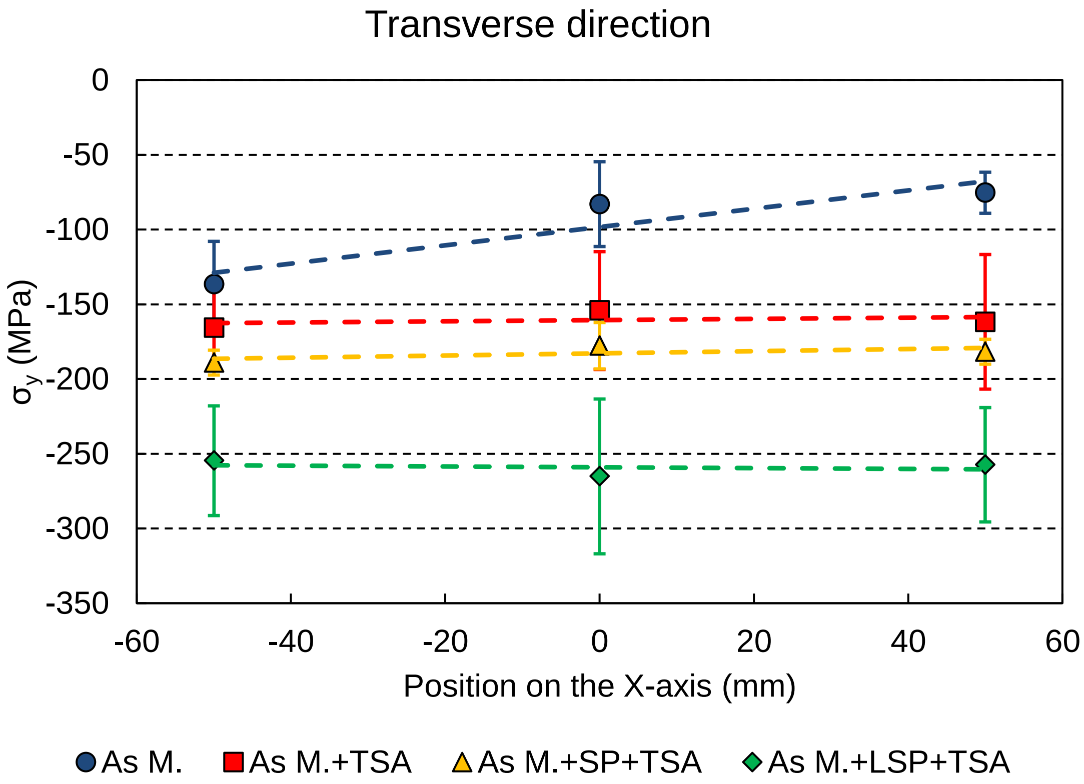

***Figure 4-14:** Residual stress values at three different positions on the surface of As M., As M.+TSA, As M.+SP+TSA and As M.+LSP+TSA specimens along the transverse direction.*

As.M+LSP+TSA specimens exhibit higher compressive surface residual stresses than As.M+SP+TSA specimens. On average, a value of about -250 MPa is measured in both axial and transverse directions. The presence of compressive residual stresses on the surface of the component following the laser peening treatment highlights the absence of local burns, which was previously confirmed by visual inspection of the component, while the uniformity of stresses in the two directions suggests that the overlapping strategy between adjacent laser spots and the offset interposed between consecutive layers favored the formation of a nearly equibiaxial stress state. The intensity of residual surface stresses induced by the laser peening process is in line with results published in other scientific papers concerning LSP applications on aircraft aluminum alloys and that, despite the application of the TSA anodizing process, the values do not deviate from those measured on only laser peened samples shown in the previous chapter.

To verify the compliance of the LSP process with the design requirements, a As M.+LSP+TSA fatigue test specimen was sacrificed to perform the measurement of the in-depth residual stress profile using the X-ray diffraction method. Figure 4-15 shows the trend of residual stresses in the longitudinal direction measured at the midpoint of the laser peened region (see Figure 4-2). This evaluation direction was chosen since it coincides with the main direction of loading on the tensile surface resulting from the four-point bending test configuration.

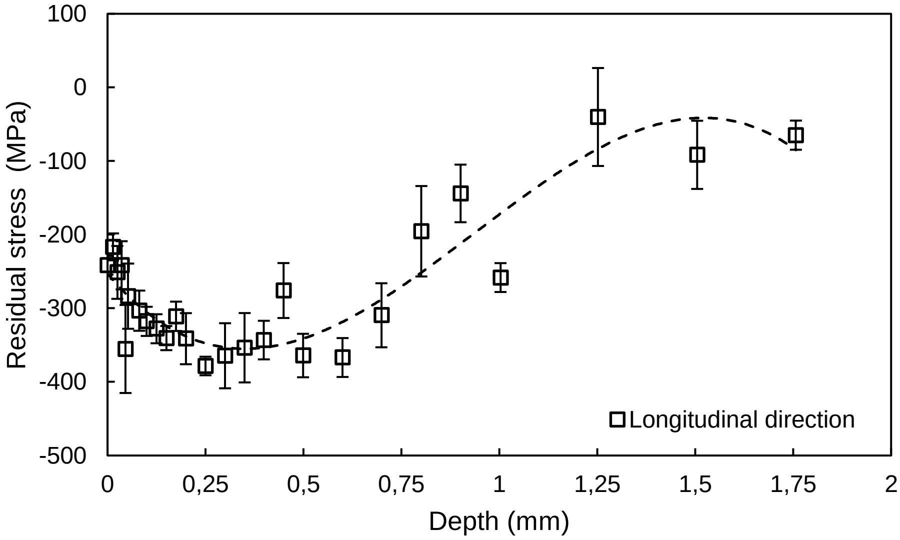

Figure 4-15: *In-depth residual stress profile at the midpoint of the tensile surface of As M.+LSP+TSA specimen.*

The values of residual stresses at the different measurement depths were interpolated using a cubic function. The resulting profile shows a peak compressive residual stress intensity of about -350 MPa (approximately 75% of the yield stress of the material) at about 0.4 mm from the surface and a depth of penetration of the residual compressive stress field greater than 1 mm.

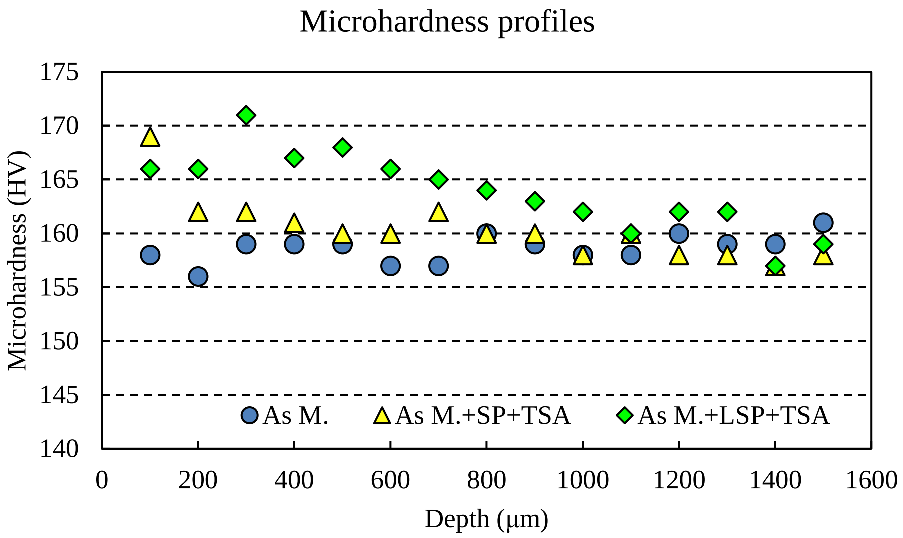

Figure 4-16: *Microhardness profile of As M., As M.+SP+TSA and As M.+LSP+TSA samples.*

The microhardness profiles for the As M., As M.+SP+TSA and As M.+LSP+TSA samples are shown in Figure 4-16. The surface hardness of the base material not subjected to the anodizing and peening process is about 158 HV and remains approximately constant along the entire evaluation depth. In the case of As M.+SP+TSA, the hardness value reaches a maximum of about 169 HV at the 100 μm depth and then gradually decreases as the distance from the surface increases, conforming to the hardness values of the As M. material. As M.+LSP+TSA specimens exhibit a hardness peak of 171 HV at a depth of 300 μm and a subsequent descent toward the typical values of the untreated material. It is important to point out the small difference between the hardness values of peened samples compared with the base material. This phenomenon was already discussed in the scientific literature and predicts little influence of the peening processes on the hardness of peak aged aluminum alloys, such as 7050-T7451 aluminum alloy [14].

4.4.4. Four-point bending fatigue tests results

Tables 4-5a-d report the number of cycles to failure as a function of the maximum applied bending stress for the base material in the as machined and anodized conditions, respectively. The fatigue data were then plotted on a semi-logarithmic graph (Figure 4-17). Run-out points were considered part of the population and were marked with an arrow on the chart.

Table 4-5: *Fatigue test data: a) As M. specimens, b) As M.+TSA specimens, c) As M.+SP+TSA specimens, d) As M.+LSP+TSA specimens.*

a)

ID Code	Maximum stress [MPa]	Cycles to failure
As M.-01	400	48697
As M.-02	350	85466
As M.-03	450	46023
As M.-04	500	33190
As M.-05	280	>3×10^6
As M.-06	300	>3×10^6
As M.-07	320	154872
As M.-08	310	2357290
As M.-09	375	62227
As M.-10	315	196801

b)

ID Code	Maximum stress [MPa]	Cycles to failure
As M.+TSA-01	350	62272
As M.+TSA-02	300	110258
As M.+TSA-03	250	2603447
As M.+TSA-04	250	1196699
As M.+TSA-05	280	236342
As M.+TSA-06	375	58807
As M.+TSA-07	325	94471
As M.+TSA-08	270	216466
As M.+TSA-09	290	118204
As M.+TSA-10	260	>3×10^6
As M.+TSA-11	265	201066

c)

ID Code	Maximum stress [MPa]	Cycles to failure
As M.+SP+TSA-01	400	170776
As M.+SP+TSA 02	425	95973
As M.+SP+TSA-03	385	115023
As M.+SP+TSA-04	360	243734
As M.+SP+TSA-05	350	354643
As M.+SP+TSA-06	450	84786
As M.+SP+TSA-07	375	241841
As M.+SP+TSA-08	330	2849198
As M.+SP+TSA-09	475	75582
As M.+SP+TSA-10	335	>3×10^6
As M.+SP+TSA-11	345	324102

d)

ID Code	Maximum stress [MPa]	Cycles to failure
As M.+LSP+TSA-01	400	149293
As M.+LSP+TSA-02	450	80134
As M.+LSP+TSA-03	375	231313
As M.+LSP+TSA-04	350	271432
As M.+LSP+TSA-05	425	116932
As M.+LSP+TSA-06	340	294415
As M.+LSP+TSA-07	330	371623
As M.+LSP+TSA-08	320	467332
As M.+LSP+TSA-09	310	>3×10^6
As M.+LSP+TSA-10	475	71465

The experimental data were fitted using the 4-parameters Weibull equation shown in Equation 3

$$S = b(N + B)^a + S_e \tag{3}$$

Where S denotes the maximum stress, N is the number of cycles at a specified stress level, S_e the fatigue endurance strength at 3×10^6 cycles, B is a term introducing an inflexion point in the curve, and a and b are constants depending on the material. The unknown constants were estimated using a non-linear regression analysis based on the least square method. The parameters obtained for each type of specimen are shown in Table 4-6.

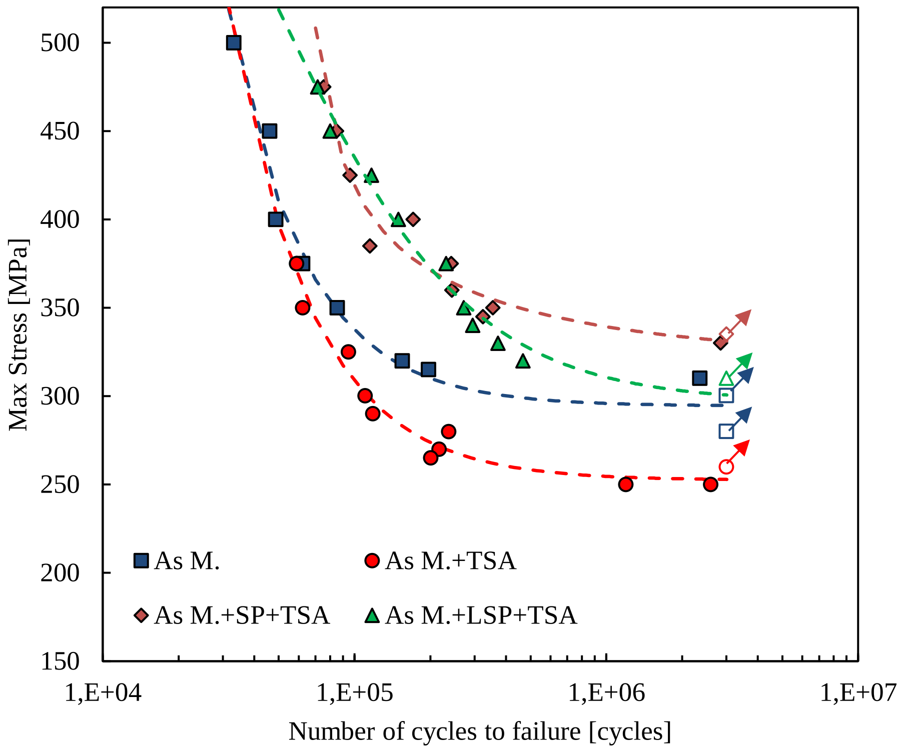

Figure 4-17: *S-N curves of As M., As M.+TSA, As M.+SP+TSA and As M.+LSP+TSA specimens obtained by 4-parameters Weibull interpolation function.*

Table 4-6: *Estimated values of Weibull parameters using non-linear regression analysis based on the least square method.*

Weibull parameters	As M.	As M.+TSA	As M.+SP+TSA	As M.+LSP+TSA
b	8.55×10^{8}	7.67×10^{8}	3.46×10^{4}	1.83×10^{8}
B	1410	3182	-57200	51400
a	-1.458	-1.423	-0.5524	-1.182
S_e	294	252	322	297

As it is possible to observe by comparing the S-N curves in Figure 4-17 of both As M. and As M.+TSA specimens, the presence of the anodic film on the surface of anodized specimens determined an overall reduction in the fatigue performance of the base material. It is generally recognized that the decrease in fatigue life is a typical consequence of the presence of pits developed during the pickling process and of tensile residual stresses induced by anodization [213]. However, based on the residual stress information reported in the previous section, it is not possible to establish a direct correlation between the variation in fatigue properties and the observed values of residual stresses on the surface of the specimens. Consequently, the main reason for the decrease in fatigue performance can be primarily ascribed to the presence of micro-voids/pits that facilitate crack initiation.

This assumption is further corroborated by the observation of the differences between S-N curves in the low and high cycle fatigue regions: after curve fitting, in low cycle fatigue, there is only a slight difference between the number of cycles to failure of anodized and as-machined specimens attributable to the small number of cycles responsible for crack initiation and to the plasticization phenomena which tend to reduce the stress gradients that develop at the stress concentration sites minimizing the effects of the presence of the anodic layer on the fatigue performance of the component. On the other hand, at low values of applied stress, the difference between the stress-life curves becomes much more noticeable as a consequence of the greater impact of the presence of pits on fatigue life. Fares [219] attributed this phenomenon to differences in the relative importance of crack nucleation and crack propagation phenomena in low- and high-cycle fatigue. It is well known that the propagation phenomenon is dominant in the Low Cycle Fatigue (LCF) region, while the nucleation phenomenon predominates in the High Cycle Fatigue (HCF) region. The anodic layer is expected to influence the nucleation phase more significantly than the crack propagation phase due to the characteristic presence of a high density of defects in the surface region. Savas [220] and Hemmouch [221] came to similar conclusions, attributing the reduction in fatigue life to the brittle nature of the oxide layer and the heterogeneous microstructure of the anodic film. Chanyathunyaroj [222] observed that the pickling process before anodizing promotes the formation of pits at the surface, which together with the brittleness of the anodic layer facilitates the creation of microcracks that act as nucleation sites for fatigue failure.

From a quantitative point of view, based on the experimental fatigue results, tests at maximum cyclic stress of 350 MPa show that As M. specimens provide an average lifetime 1.37 times longer than As M.+TSA specimens; at lower stress levels the discrepancy becomes even more pronounced: at 300 MPa As M. tests were all run-outs, while As M.+TSA specimens averaged 110000 cycles, denoting a fatigue life at least 30 times lower than As M. specimens. As concerns anodized specimens, the first run-out was observed at 260 MPa.

The employment of shot peening and laser shock peening as pre-treatments to TSA anodizing certainly provides a significant increase in the fatigue life of the component. However, it is necessary to dwell carefully on the performance of the two fatigue curves noting that the thickness of the anodic layer on the two types of specimens is different: in fact, As M.+LSP+TSA specimens have an anodic layer twice as thick as As M.+SP+TSA specimens as a result of the different treatment time in tartar-sulfuric acid solution. In the LCF regime of the S-N diagram, the trends of the two fatigue curves of the As M.+SP+TSA and As M.+LSP+TSA specimens exhibit almost coincident trends and very significant increases in fatigue life compared to the As M. and As M. +TSA: specifically, at a maximum stress level of 450 MPa both the SP and LSP provide fatigue life increases of about 100 percent compared to both the base material and the simply anodized specimens, while at a maximum stress level of 375 MPa fatigue life more than three times higher than those of the As M. and As M.+TSA components are estimated in the shot and laser peened components. The curve trends of the two groups of peened specimens vary in the transition region between the LCF regime and the MCF and HCF regimes. The As M.+SP+TSA specimens exhibit an estimated fatigue limit 1.08 times higher than the As M.+LSP+TSA specimens. It is also interesting to observe that the fatigue limit of As M.+LSP+TSA specimens is almost coincident with that of As M. specimens. Thus, it seems evident that the presence of an anodic layer twice as thick as that on the As M.+SP+TSA specimens significantly affects the fatigue behavior in the HCF regime of the fatigue curves of the As M.+LSP+TSA specimens. Although the residual stress field induced by the laser peening process exhibits higher compressive surface stresses and that the depth of stress penetration is greater than that of the peened components, it can be supposed that the presence of surface microcracks observed in the cross section of the As M.+LSP+TSA components are responsible for the phenomenon of fatigue crack nucleation by acting as preferential sites of stress concentration. This is a likely explanation because no significant changes in behavior are observed in the LCF region of the fatigue curves of both shot and laser peened components, a region in which local plasticization phenomena at the surface defects induced by the TSA anodizing process tend to attenuate and equalize the resulting maximum stress states ensuring comparable fatigue properties.

4.4.5. Analyses of fatigue fracture surfaces by SEM

To identify crack nucleation sites and the fracture morphology, the fracture surfaces of the As M., As M.+TSA, As M.+SP+TSA and As M.+LSP+TSA specimens after fatigue tests in HCF regime were observed using SEM. The images in Figure 4-18 and 4-19 display the overall view of the fatigue crack morphology of As M. and As M.+TSA specimens.

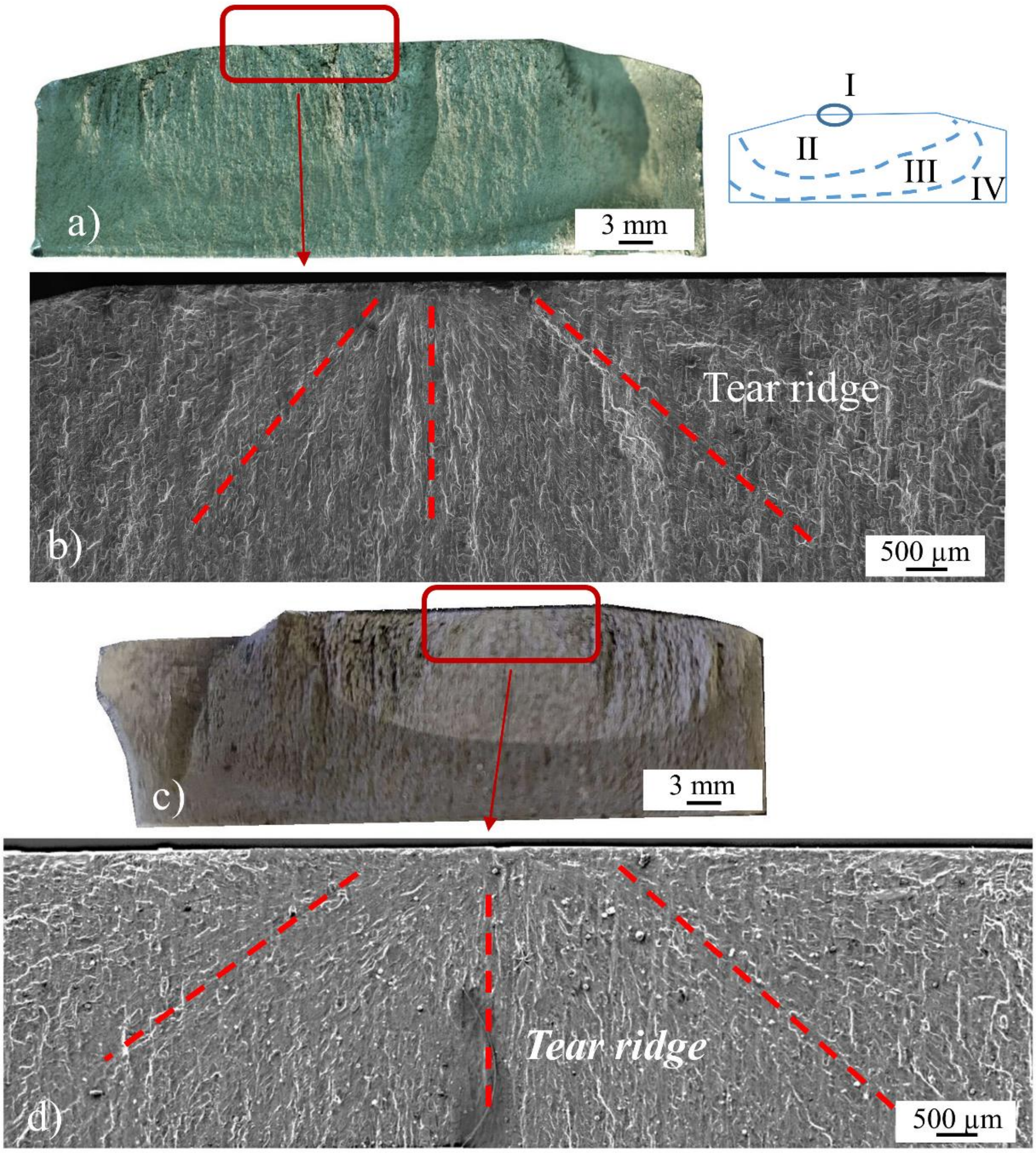

Figure 4-18: *SEM images of the As M. and As M.+TSA fatigue specimens in HCF regimes: a and c) representative macrographs of an overall view of the fracture surface of As M.+TSA-03 and As M.-08 specimens after fatigue tests, respectively; b and d) SEM enlarged images of the spot fringe at 50X where the tear ridges that run across the entire crack propagation area can be observed.*

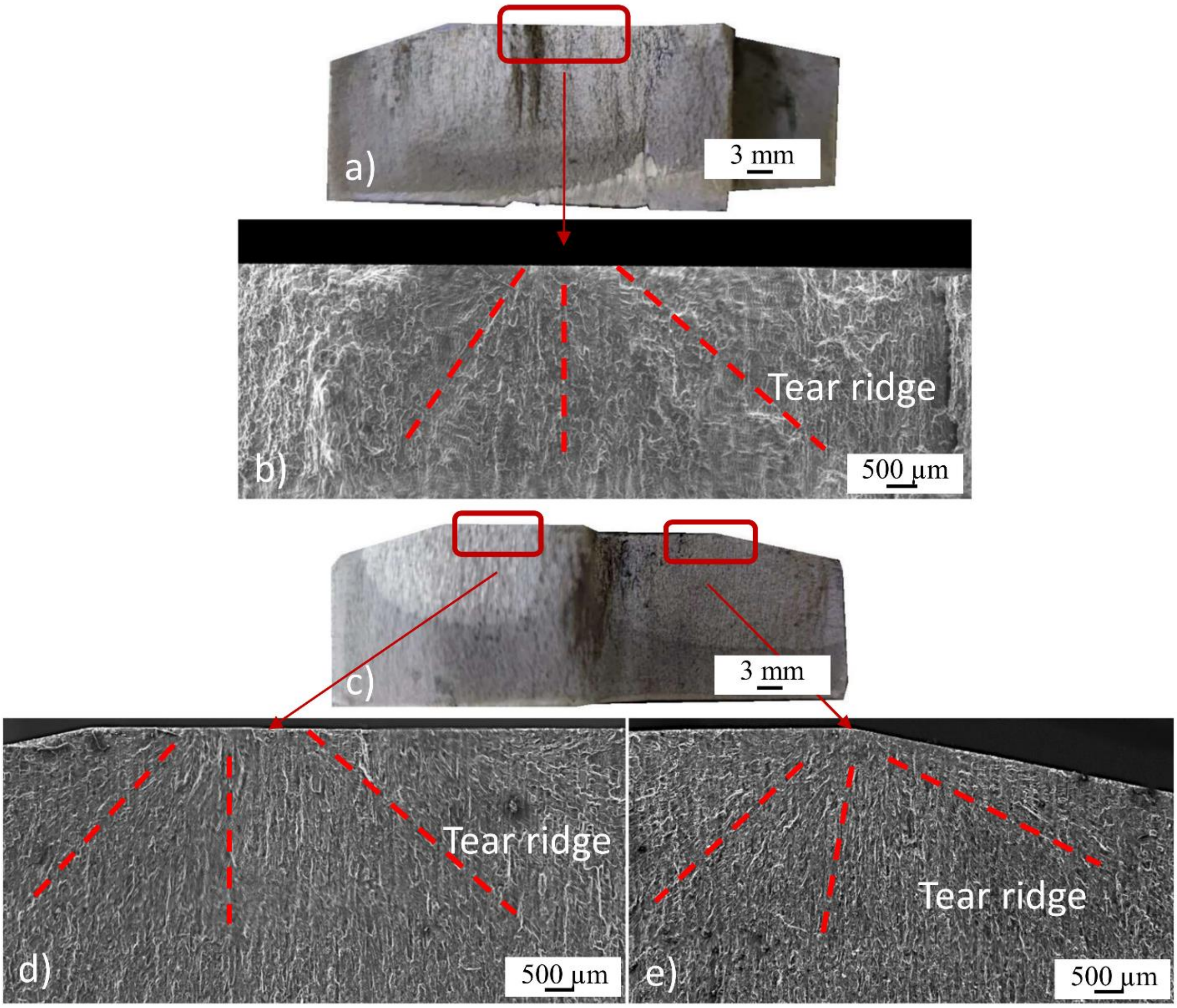

Figure 4-19: *SEM images of the As M. and As M.+TSA fatigue specimens in LCF regimes: a and c) representative macrographs of an overall view of the fracture surface of As M.-04 and As M.+TSA-01 specimens after fatigue tests, respectively; b and d) SEM enlarged images of the spot fringe at 50X where the tear ridges that run across the entire crack propagation area can be observed.*

It was observed that the fracture morphology of all specimens exhibits distinctive fatigue regimes: crack initiation (I), slow crack propagation (II), fast crack propagation (III) and final fracture (IV) (see the schematic representation in Figure 4-18). In general, crack growth can be characterized by the size of fatigue striations. In agreement with the studies reported in the literature, it was observed that the crack initiation sites mainly occurred on the surface for both As M. and As M.+TSA specimens. More specifically, it was observed that the As M. specimens both in the LCF and HCF regimes (Figures 4-18a, b and 4-19a, b) as well as the As M.+TSA specimen in the HCF regime (Figure 4-18c, d) usually have a single surface crack, while As M.+TSA specimens in LCF regime (Figure 4-19c, d) often have multiple initiation locations on the fracture plane. Moreover, this fatigue crack originates at the surface pin-holes for As M. specimens and in correspondence to the cavities and micro-voids for As M.+TSA ones. So, the presence of angular cavities and/or pores cluster leads to a significant effect on crack nucleation (Figure 4-20c, d). On the other hand, it is well known that the presence of pre-existing stress concentrations originated by defects determines localized deformation [200]. Nevertheless, some other minor crack initiation sites were also detected such as the specimen corner. In other words, it was found that when the maximum applied stress is higher, the number of cracks that grow during fatigue is greater. This is because as the applied stress increases, the potential crack initiation sites are more numerous. Therefore, in this situation, the final rupture will occur through the joining of those growing cracks which have been independently nucleated. Conversably, for intermediate and low applied stresses, a single crack will grow to a critical length. A similar conclusion was reported by Patton [223]; the authors pointed out that during the fatigue life of the same specimen several cracks can be initiated. Moreover, they claimed that the ultimate failure mechanism depends on the stress level and thus, presented a model for fatigue damage accumulation.

More interesting, from the magnified SEM images (Figs. 18b, d and 19c, d), it can be seen that the fatigue failure crack is propagated at a stable rate over an area that exhibited bright river-like tear ridges. These run across the entire crack propagation area until the final shear fracture area, indicating a fairly stable crack propagation rate throughout the thickness. However, the fracture surfaces exhibit mixed intergranular-transgranular fracture with small areas of cleavage-like fracture at the rim of the fracture surfaces (Figure 4-20a). Moreover, as can be seen in Figure 4-21b, the fracture surfaces contain regions with lots of striations in fatigue crack expansion area. These striations are generally generated via a repeated plastic blunting-sharpening process because of the slip of dislocations in the plastic zone in front of the fatigue crack tip and the change of their distance is related to the ΔK at the crack front region [224,225].

The extension of the stable fatigue crack propagation region is approximately 10 mm, or half the thickness of the tested components. In the case of specimens that showed failure in the high-cycle region, analysis of the fracture surfaces showed an average value of the spacing between fatigue striations of about 1.13 µm in the case of the anodized specimen and 0.5 µm in the case of the non-anodized specimen, both evaluated at a distance of 5 mm from the crack initiation site.

Compared with the As M. specimens, the specimen subjected TSA treated exhibits a distance between fatigue striations slight larger in the crack expansion area than As M. specimen, which indicates a slight faster fatigue crack growth rate.

Furthermore, also dimples, intergranular cracks and voids were observed by SEM and are shown in Figures 21a and b.

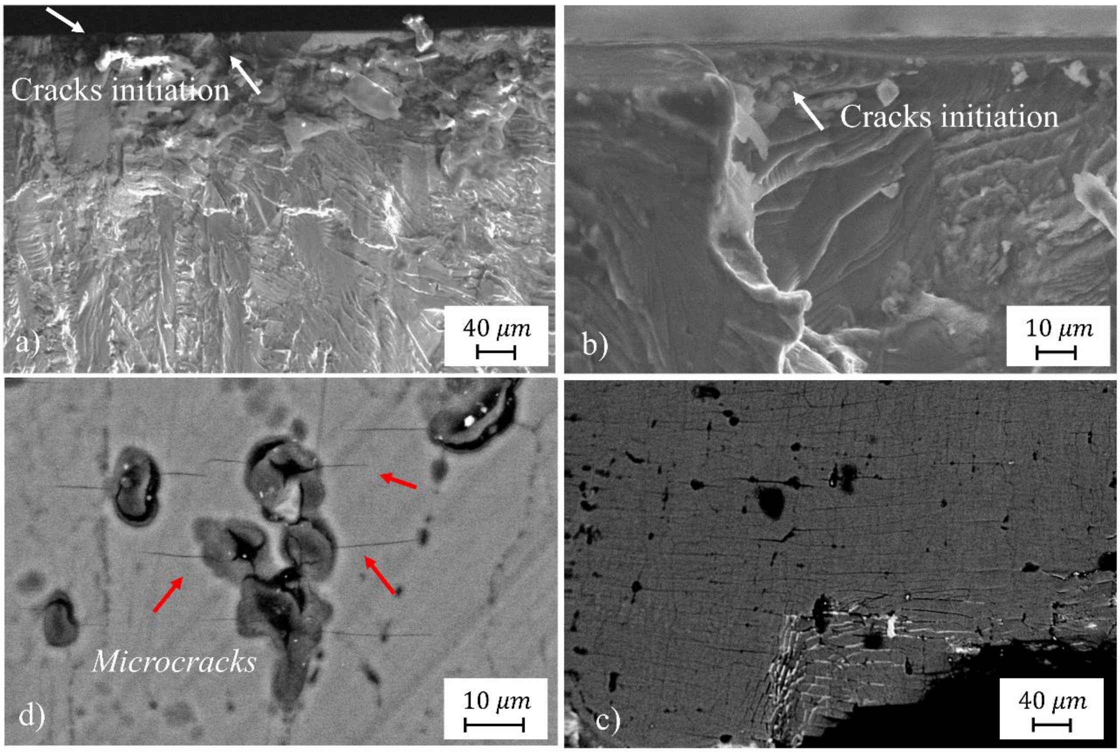
Cracks initiation
a)
40 μm
Cracks initiation
b)
10 μm
Microcracks
d)
10 μm
c)
40 μm

Figure 4-20: *SEM analysis of the fracture surface of the treated sample: a) cross-section of fracture surface in the region of the crack initiation due to defects: crack initiation occurs at the surface. Moreover, fracture surface exhibits cleavage-like fracture. b) crack initiation sites occurred on the surface, c) longitudinal section of fracture surface showing defects with angular morphology that act as stress concentrations points, resulting in areas with micro-crack formation and d) magnification of the fracture surface showing the presence of the voids at the vertices of which the micro-cracks occur.*

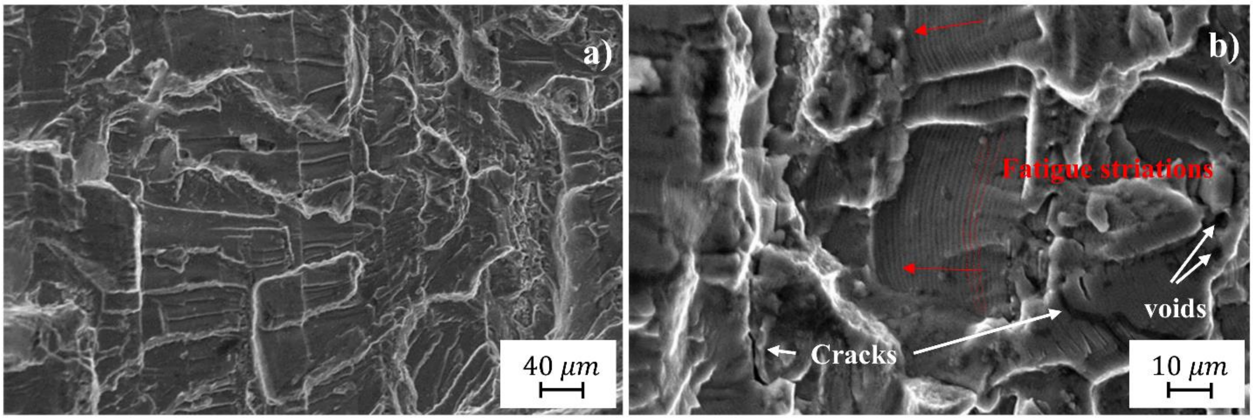
a)
40 μm
b)
Fatigue striations
voids
Cracks
10 μm

Figure 4-21: *SEM analysis of the fracture surface of the treated sample: a) magnification of fracture surface of region of stable crack growth and b) fracture surface contains regions with lots of striations. Striation's width is about 1.13 µm.*

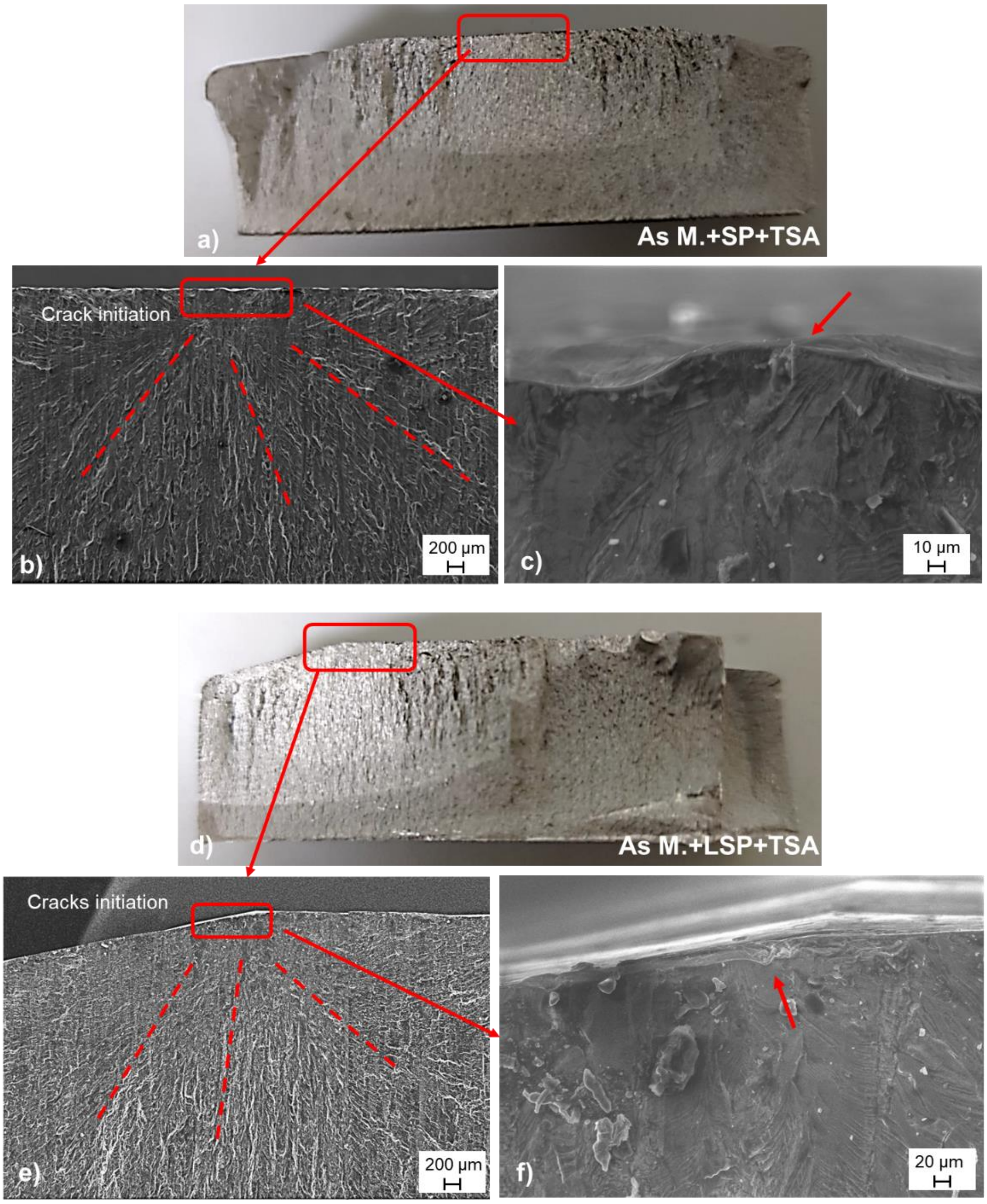

Figure 4-22: *SEM images of the As M.+SP+TSA and As M.+LSP+TSA fatigue specimens in HCF regimes: a and d) representative macrographs of an overall view of the fracture surface of As M.+SP+TSA-05 and As M.+LSP+TSA-04 specimens after fatigue tests, respectively; b-c and e-f) SEM enlarged images of the spot fringe where the tear ridges that run across the entire crack propagation area can be observed.*

Figure 4-22 shows the fracture surfaces related to two specimens belonging to the As M.+SP+TSA and As M.+LSP+TSA groups, respectively, that experienced failure in the HCF regime of fatigue curves. The crack nucleation sites are located on the surface of the component, as also observed in the case of the As M. and As M.+TSA specimens. A shift of the crack nucleation point to the subsurface region of the component could be expected due to the presence of a strong compressive stress state induced by the two peening processes. However, the four-point bending load configuration is characterized by maximum bending stresses just at the surface of the part, with a decreasing linear trend in depth and a sign reversal at the neutral axis, thus making the surface the most stressed region despite the superposition of the residual stress state. Crack nucleation sites are predominantly located at geometric discontinuities, such as the valleys of roughness profiles in the case of As M.+SP+TSA components or the connection zone on the tensile surface of flexure bars, or at pores or microcracks induced by the anodizing process, as previously observed in the case of As M.+TSA specimens. No multiple fatigue crack propagation fronts are observed in both laser peened and shot peened components.

4.5. Summary

This chapter has dealt with the effect of anodic film and peening processes as pre-treatment to anodizing on fatigue behavior of 7050-T7451 aluminum alloy, which was anodized by electrochemical process in tartaric-sulfuric acid (TSA) bath. The conclusions involve the following points:

- The surface of the anodic layer is characterized by the presence of numerous pores or microvoids between 0.6 and 20.5 μm in diameter that locally agglomerate to form clusters of defects that act as preferential sites of stress concentration. The formation of the pores is mainly attributed to the difference in reactivity of the intermetallic particles present in the 7050-T7451 alloy. The use of different anodizing times allowed the development of anodic layers of different thicknesses on As M.+SP+TSA (2 μm) and As M.+LSP+TSA (4 μm) specimens, in order to verify whether the LSP process is able to counterbalance the negative effects of the presence of the anodic layer on the fatigue properties of the material by offering results comparable to those provided by an optimized shot peening process.
- Analysis of the residual stress fields on the surfaces of the four groups of specimens showed that the TSA treatment does not induce significant changes in the residual stress state compared with the reference stress values measured on the untreated material. The shot peening and laser shock peening processes, on the other hand, induce a strong uniform compressive state on the examined surface, the intensity of which turns out to be generally less than -200 MPa. The in-depth residual stress profile of As M.+LSP+TSA components was also evaluated to verify the correct application of the laser shock peening treatment and the possible effects of the subsequent anodizing process. At the previously identified LSP optimized process parameters, the laser peening treatment induces a stress profile that exhibits a compressive maximum stress of -350 MPa at a depth of about 0.4 mm from the treated surface and a penetration depth of more than 1 mm, in accordance with the design requirements.

- Four-point bending fatigue tests were performed to evaluate the effects of the anodizing process on fatigue properties of the alloy. An overall reduction of the lifetime at all stress levels was observed due to anodizing: specifically, the discrepancy between S-N data of As M. and TSA specimens increases as the applied maximum stress shifts toward lower values, while it is less pronounced in the LCF region where the presence of pits has a lower effect on crack initiation. It is reasonable to assume that the residual stress state determined by the anodizing process did not influence the fatigue performance of the components as a consequence of the adopted process parameters. Both shot peening and laser shock peening result in a significant increase in material fatigue life. However, differences are observed between the fatigue behaviors of As M.+SP+TSA and As M.+LSP+TSA specimens: in the LCF regime, the two fatigue curves are almost overlapping, while in the HCF regime, the two curves diverge and the fatigue limit of As M.+SP+TSA specimens turns out to be higher than that of As M.+LSP+TSA specimens. This discrepancy can be associated with the higher thickness of the anodic layer on the laser shock peened specimens and the resulting higher density and size of defects caused by the anodizing process.

CHAPTER 5

EVALUATION OF FATIGUE BEHAVIOR OF SINGLE EDGE NOTCHED COMPONENTS SUBJECTED TO LASER SHOCK PEENING PROCESS

5.1. Preface

In the previous chapters, the possibility of employing Laser Shock Peening technology as an alternative to the Shot Peening process for improving the fatigue performance of 7xxx aluminum alloy aircraft components was investigated. The first objective was to identify a set of process parameters that would provide an optimum balance between the characteristics of the induced residual stress field and the impact on the surface integrity of the component, as assessed by some commonly used roughness parameters. Then, through the execution of four-point bending fatigue tests, the effective ability of the LSP technology to provide fatigue performance benefits comparable to those offered by the already established and optimized shot peening process was highlighted; in addition, the possibility of using the LSP process in combination with a recently developed anodizing treatment such as Tartaric-Sulfuric acid anodizing was evaluated, highlighting its ability to counterbalance the detrimental effects caused by the presence of the anodic layer on fatigue performance. However, the analysis focused only on the application of LSP on smooth, notch-free components characterized by ideal process conditions. Real aerospace components are instead characterized by complex geometries, often featuring the presence of notches, fillets, and holes, which can alter the distribution and intensity of residual stresses induced by the peening process, thus compromising its ability to increase the mechanical properties of the component. For this reason, the focus in this chapter will be directed toward the application of the LSP process on notched components, i.e., with stress concentration factors K_t greater than 1. A representative geometry of a real aircraft component will be defined and the local applicability of the LSP process at the notch will be evaluated by analyzing the residual surface stress fields induced by the process. Fatigue tests will then be performed to evaluate the influence of the geometric characteristics of the component on the ability of the LSP process to increase its fatigue strength.

5.2. Introduction

The proper selection of laser peening process parameters allows for uniform, high-intensity residual compressive stress fields to be obtained providing a significant increase in the fatigue properties of the component. The plastic deformation of the surface and subsurface region of the material caused by the oriented plasma expansion and pressure wave propagation results in an elastic reaction of the surrounding material which is responsible for the generation of the residual stresses. The amount of surrounding elastic material and its distribution affect the location of tensile residual stresses that balance the compressive stresses locally induced by the LSP process. Based on these considerations, it is logical to expect that the presence of a geometric discontinuity, such as a notch, may alter the distribution of residual stresses induced by the LSP process compared to that which would be obtained by applying the same treatment on a smooth component. Some scientific papers have tried to verify whether the curvature of a surface plays a critical role in defining the resulting residual stress state by creating numerical finite element models of curved geometries. In particular, Vasu [226], starting from the results of numerical analyses of laser shock peened curved components, developed a mathematical relationship linking residual stresses and the radius of curvature of the surface: he found that increasing the radius of curvature in a concave geometry reduces the compressive stress state, conversely increasing the radius of curvature in a convex geometry increases the compressive residual stresses. In addition, the relationship between the radius of curvature and the intensity of residual stresses turns out to be approximately linear for both convex and concave surfaces (Figure 5-1). In the author's opinion, this difference in behavior was attributable to the different deformation compatibility of the curved geometry compared to a flat geometry.

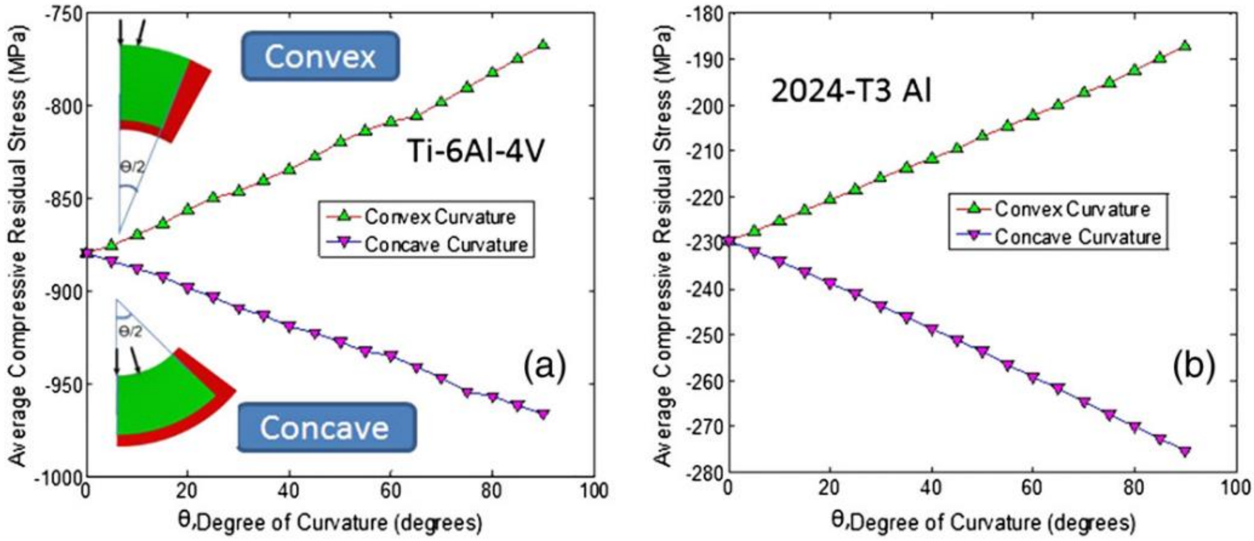

Figure 5-1: *Influence of radius of curvature on the residual stress field induced by LSP process on convex and concave geometry: a) Ti-6Al-4V, b) AA 2024-T3* [226].

Thus, it can be said that the compressive residual stresses induced by the laser shock peening process turn out to be higher in a concave geometry and lower in a convex geometry compared with a flat surface, given the same input conditions.

Gang [227] studied the applicability of the LSP process to curved surfaces and the effects of surface curvature on the radial, axial, and depth distributions of residual stresses in 316L stainless steel. The results obtained are in agreement with those previously emerging from Vasu's work: indeed, the residual stress distributions showed that the compressive stresses induced by the LSP process decrease as surface curvature increases and that the magnitude of compressive residual stresses is larger in concave geometries than in convex ones (Figure 5-2).

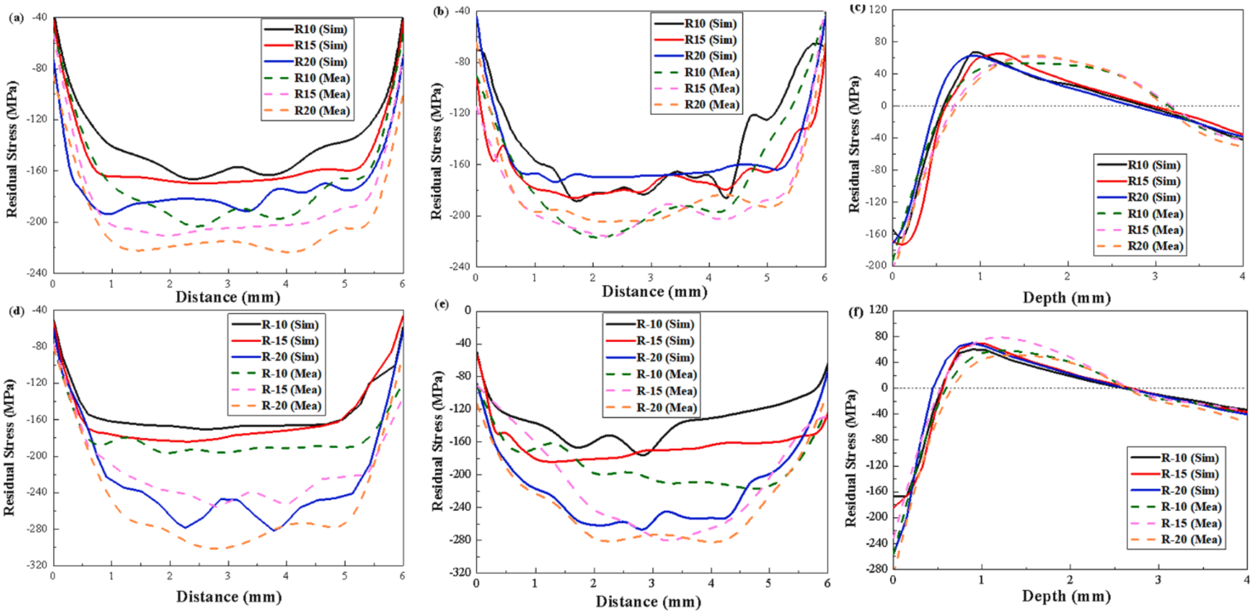

Figure 5-2: *Comparison between simulated and measured tri-directional residual stress distributions on convex and concave geometry: a-b-c) convex geometry; d-e-f) concave geometry; a-d) axial direction; b-e) radial direction; c-f) depth* [227].

As expected, a significant influence of boundary effects on the distribution of axial and radial stresses was observed, and consequently a non-homogeneity of surface residual stress intensities within the treated area was found. It is a phenomenon of relevant importance when considering the possibility of applying LSP treatment on the thickness of notched components: the fillet connecting the lateral surface and the main flat surface of the component will represent a particularly critical geometric region since it is affected simultaneously by boundary phenomena and the presence of curved surfaces.

Another interesting application was proposed by Cuellar [228] and concerned the application of different LSP patterns at holes to prevent or delay the phenomenon of fatigue crack nucleation under cyclic loads. Specifically, an open-hole notched specimen with a notch factor of 3.1 and four different types of laser peening patterns were considered in order to evaluate the residual stress distribution at the notched region and identify the most advantageous design solution. Using the contour method, the authors proposed different residual stress maps generated at each LSP pattern and then performed fatigue tests to evaluate the benefits induced by each process (Figure 5-3). It was shown that when not properly applied, the LSP process can have a negative effect on the mechanical performance of the material due to the undesirable development of tensile residual stresses in the vicinity of high-stressed regions.

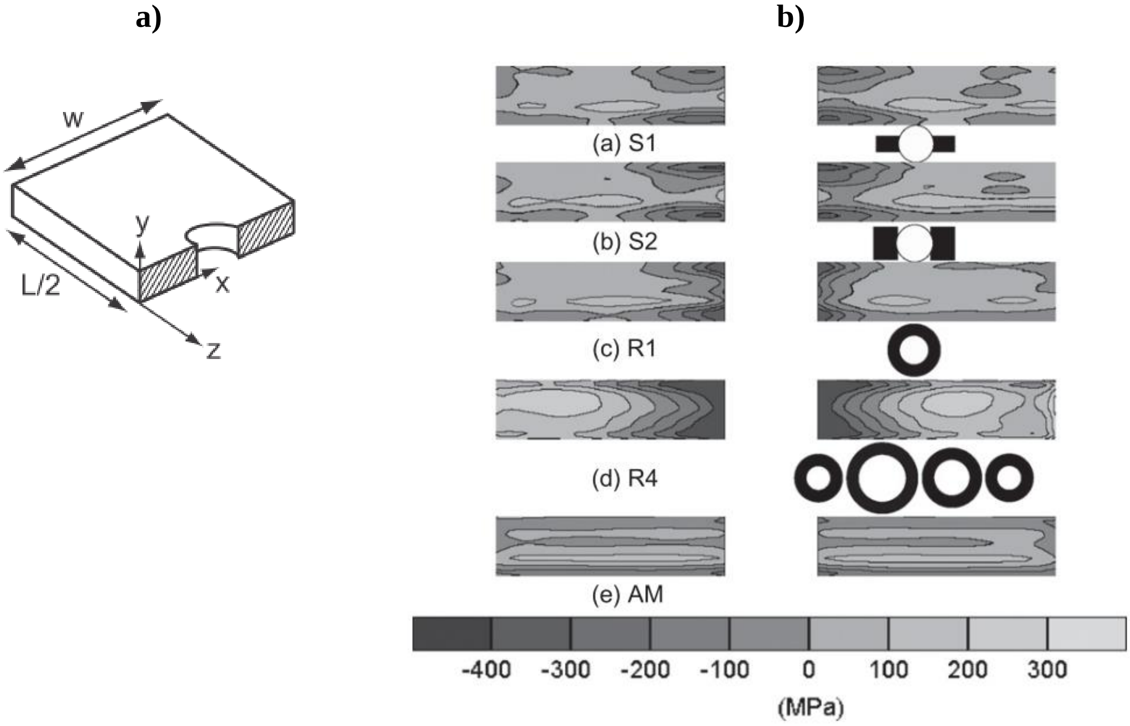

Figure 5-3: *a) Cross section of the hole region and identification of measurement surfaces by contour method; b) stress maps obtained by contour method using different LSP patterns* [228].

Several other works of a purely numerical nature have attempted to address the issue of the effects of geometry in the laser shock peening process: Dewald [229,230] used eigenstrain theory for the prediction of residual stresses induced by the LSP process in three-dimensional components with different geometries; similarly, Coratella [231,232] verified the feasibility of applying the eigenstrain method for predicting residual stresses in a notched sample when eigenstrain are determined from a simple geometry sample. The predicted residual stresses were compared to experimental results obtained by incremental hole drilling, contour method, synchrotron X-ray diffraction and neutron diffraction. It was found that eigenstrain approach is quite efficient when the geometry of the sample is similar to that from which eigenstrains are derived, while some discrepancies were observed when the reference sample and the analyzed one have very different geometries (Figure 5-4). Li [232] used

FEM for the simulation of residual stress fields on the surface of a titanium alloy blade verifying that the curvature of the surface results in a reduction of compressive residual stresses in the radial direction near the edge of the component.

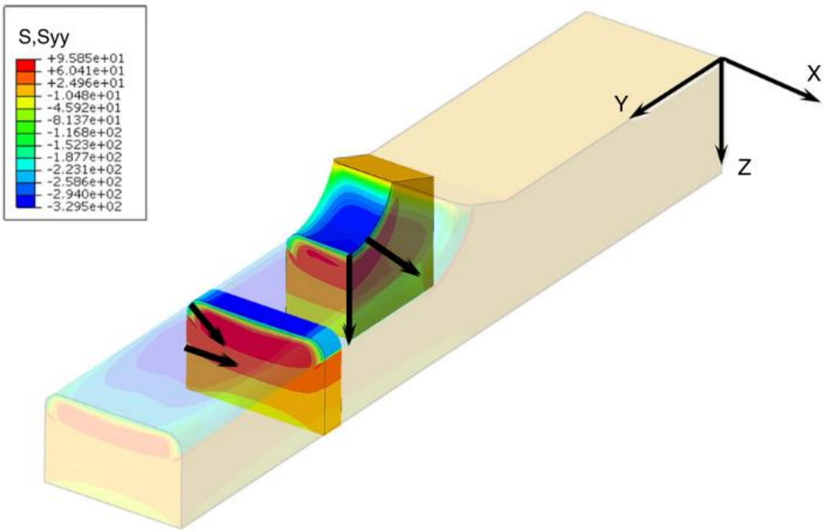

Figure 5-4: *Residual stress maps in different cross sections of a notched component subjected to laser peening obtained by FEM based on eigenstrain theory* [231].

All reviewed scientific publications agree that the presence of a geometric discontinuity is a likely source of modification of the residual stress distribution within the component and that the laser peening strategy and geometric characteristics of the workpiece are key factors in defining the residual stress field. In the previous chapters, a combination of LSP process parameters was identified at which an optimal balance between surface integrity and residual stress profile properties is guaranteed and, as a result, the fatigue life of the component following the treatment is increased compared to the untreated component. The effectiveness of the identified treatment was also tested in combination with a tartaric-sulfuric acid anodizing process to provide the corrosion resistance required for critical aircraft structural applications, and the results showed that the LSP process achieves fatigue performance nearly comparable to an optimized shot peening process despite more severe anodizing conditions. The logical final step of analysis is to verify the effectiveness of the LSP process when applied to anodized components that feature geometric discontinuities or notches and are thus representative of real structural parts.

To the author's knowledge, no scientific article has evaluated the fatigue properties of a notched component subjected simultaneously to the LSP process and TSA anodizing. To achieve this goal, this chapter will initially design a notched component with a notch factor $K_t>1$ representative of a real component for aircraft applications. An LSP pattern with optimized process parameters will be locally applied at the notch before undergoing TSA anodizing treatment. The surface residual stress field will be evaluated using the X-ray diffraction method to assess any alteration of the stress state from values measured on the unnotched smooth component. The components will then be subjected to constant amplitude uniaxial fatigue tests to evaluate the effectiveness of the laser peening treatment and, as in the case of the four-point bending fatigue specimens, the results will be compared with the fatigue properties obtained from shot peened components.

5.3. Experimental activity

5.3.1. Definition of material and sample geometry

The objective of the experimental activity is to analyze the fatigue behavior of a notched component made of aircraft aluminum alloy 7050-T7451 characterized by a stress concentration factor K_t of 1.5 subjected to Laser Shock Peening process and tartaric-sulfuric acid anodizing treatment. The stress concentration factor was chosen in accordance with the industrial partner to make the component representative of an aircraft structural part that has a critical geometric feature at which a laser pattern is expected to be applied and for which a stress concentration factor of approximately 1.5 was numerically calculated.

The geometric characteristics of the analyzed component are shown in Figure 5-5. The components are made of the same material as the four-point bending fatigue test specimens analyzed in the previous chapter and are obtained from an 80 mm thick AA 7050 rolled plate supplied in T7451 condition. For completeness, the composition and mechanical properties of the material are reported again in Tables 5-1 and 5-2.

Table 5-1: *Chemical composition of 7050-T7451 aluminum alloy in wt.%*

Elements	Zn	Mg	Cu	Zr	Fe	Si	Mn	Cr	Ti
Concentration (%)	6.2	2.25	2.3	0.1	0.15	0.12	≤0.10	≤0.04	≤0.06

Table 5-2: *Mechanical properties of 7050-T7451 aluminum alloy.*

Tensile Yield Strength, σy	Ultimate Tensile Strength, σu	Ductility	Modulus of elasticity, E	Poisson’s ratio, ν
MPa	*MPa*	*%*	*GPa*	*#*
469	524	11	71.7	0.33

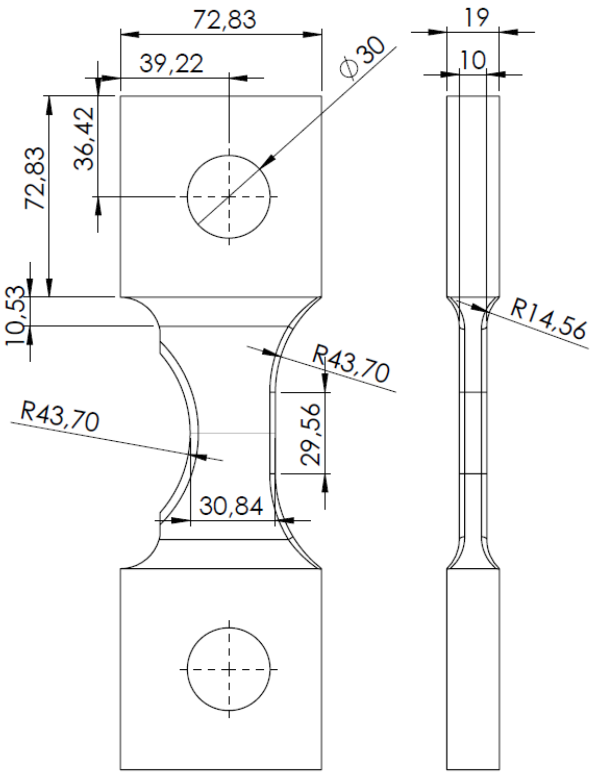

Figure 5-5: *Geometric properties of single edge notch fatigue specimen.*

The geometry of the component is characterized by the presence of a circular-shaped notch with a radius of 43.7 mm that extends over a 10-mm-thick region. The clamping surfaces have two 30 mm diameter circular through holes eccentric to the main axis of the component. An important feature of the adopted geometry is that it can be easily modified to allow the fabrication of components with a different stress concentration factor. It is in fact sufficient to vary the length of the flat section opposite the circular notch while holding all other dimensions and geometric relationships constant to obtain different values of the stress concentration factor.

Another interesting point is that the component can be subjected to two different load configurations: pin-load configuration or full-clamped configuration (Figure 5-6). In the pin-load configuration, the axial load is applied using two cylindrical pins inserted into the holes in the component's clamping region and connected to the loading machine by means of U-shaped forks. The pins must be free to rotate within the seat of the holes in order to accommodate the deformations caused by the bending associated with the eccentricity of the load axis with respect to the main axis of the component. In the full-clamped configuration, the component is simply clamped into the clamping wedges of the testing machine and subjected to axial stress. Obviously, the two loading configurations result in different stress distributions within the component and thus different stress concentration factors at the notch.

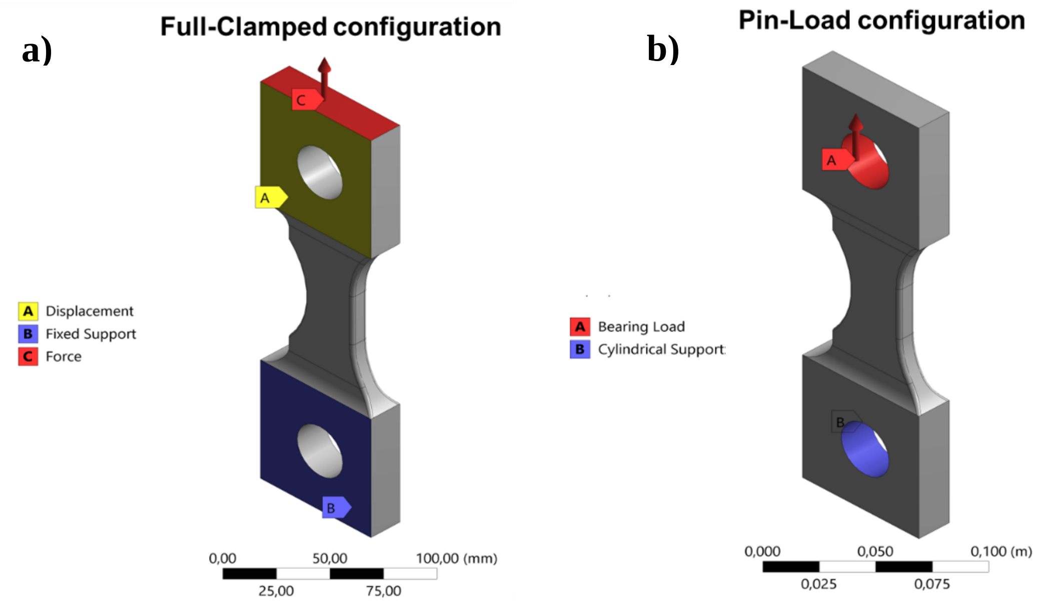
a)
Full-Clamped configuration
A Displacement
B Fixed Support
C Force
A
B
C
0,00
50,00
100,00 (mm)
25,00
75,00
b)
Pin-Load configuration
A Bearing Load
B Cylindrical Support
A
B
0,000
0,050
0,100 (m)
0,025
0,075

Figure 5-6: *Schematic definition of the two different loading configurations: a) full-clamped configuration and b) Pin-Load configurations.*

5.3.2. Evaluation methods of stress concentration factor

The stress concentration factor will be evaluated the two different load configurations by both finite element method and experimental evaluation methods.

The two load configurations adopted are pin load and full-clamped configuration, as defined in the previous paragraph.

Numerical simulation will be carried out in the Ansys Workbench environment assuming the application of static axial load and evaluating the stress concentration factor at the notch as the ratio of the maximum axial stress value to the nominal axial stress calculated with respect to the minimum section of the component. The volume of the component was discretized using a tetrahedral mesh made by an automatic patch-conforming algorithm. Elements with an average size of 3 mm were used throughout the entire volume of the component except for the notch and loading holes for which a surface refinement factor of three was used to obtain more accurate solutions at the most stressed regions. Overall, the model consists of 856522 elements with a total of 1225009 nodes (Figure 5-7).

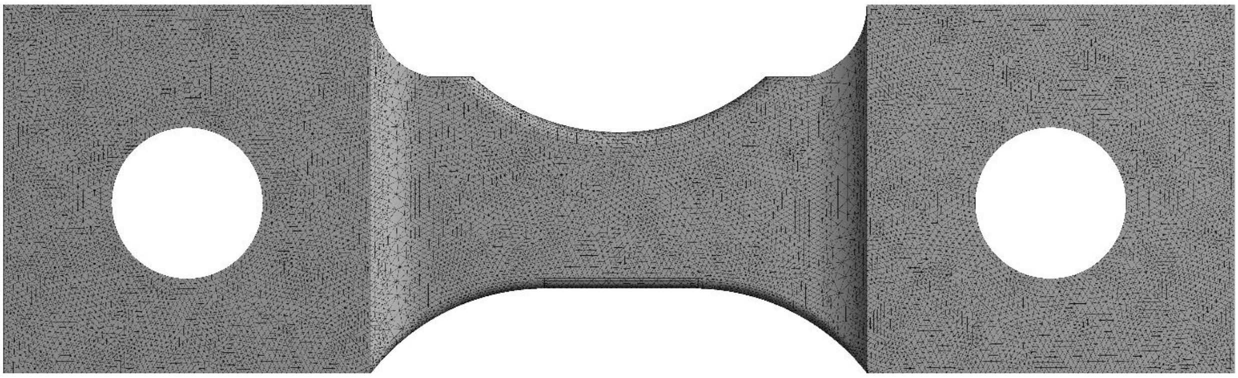

__Figure 5-7:__ Details of the employed tetrahedral mesh on single edge notched component.

In the case of the full-clamped configuration, the load was applied to the top surface of the component, while a fixed constraint was set in the clamping region opposite the surface where the load was applied and a normal displacement constraint was set on both clamping surfaces (Figure 5-6a). In the case of pin-load configuration, bearing loads are used to model the force transmitted between the loading pin and the hole. Cylindrical support, on the other hand, is used to simulate constraint conditions on the opposite pin in order to ensure free rotation around the main axis of the pin (Figure 5-6b). A monotonically increasing static load was applied in both loading configurations.

Based on the numerical results, it will be identified the loading configuration that allow for a stress concentration factor of 1.5 at the notch to be obtained and ensure the absence of addtional highly stressed critical regions other than the notch.

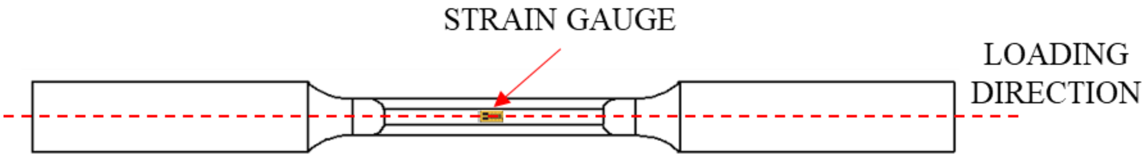

__Figure 5-8:__ Location of strain gauge for the experimental evaluation of the stress concentration factor at the notch.

Once the components are fabricated based on the identified geometry, the stress concentration factor will be experimentally verified by installing a uniaxial strain gauge (HBM type 3/120 LY11) in the notch section (Figure 5-8). The components will then be subjected to static uniaxial stresses in the elastic field, and the strain data obtained will be used to calculate the axial stress value in the most stressed region of the component. Further verification will be carried out by application of the Digital Image Correlation (DIC) technique: DIC is a full-field, noncontact optical technique that allows a map of displacements and/or deformations of the surface under examination to be determined at different instants of time. One of the two main surfaces of the component will be prepared by depositing a layer of opaque white paint and then making a random, non-repetitive dotted pattern of black paint on the white layer (Figure 5-9). Displacement information can then be obtained by correlating pattern images acquired during load application using a digital camera at different instants with a reference image obtained at a zero-load condition.

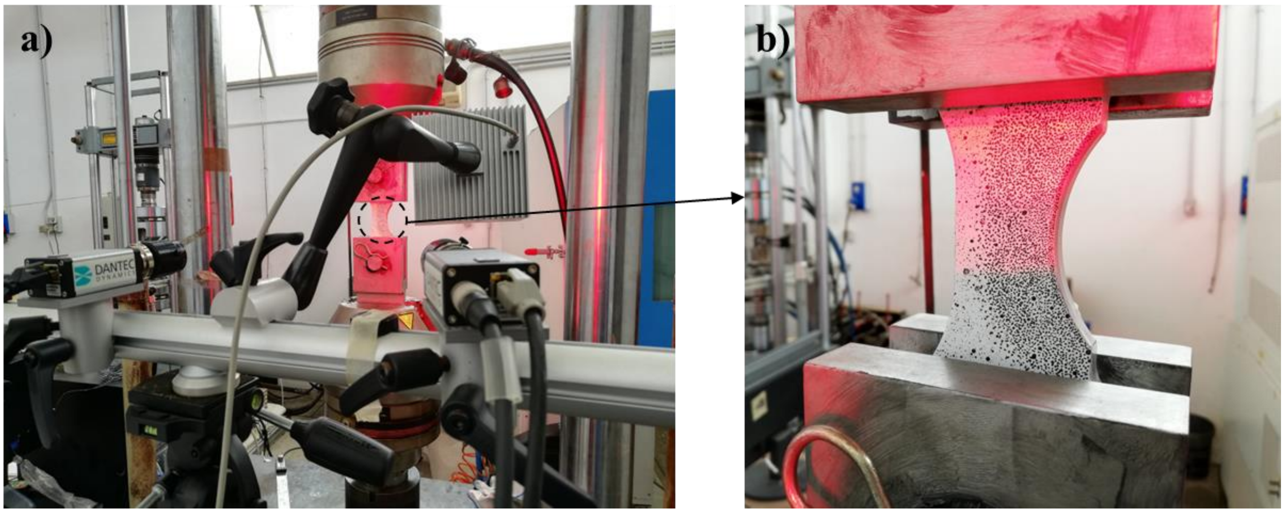

Figure 5-9: *Setup for digital image correlation measurement: a) Overall view of the measurement system; b) detail of the black dotted pattern on the surface of the single edge notched component.*

Measurement of displacements and deformations of the portion of the surface under investigation was performed through the DIC Dantec Dynamics Q400 system (Dantec Dynamics A/S, Skovlunde, Denmark) equipped with INSTRA 4D software (Dantec Dynamics A/S, Skovlunde, Denmark). The Dantec Dynamics system includes: two GigE CCD Manta cameras of 1628 x 1436 pixels, manufactured by AVT (Allied Vision Technologies GmbH, Stadtroda, Germany); a tripod equipped with a support bar on which the cameras are mounted to compensate for vibrations; an LED light to stably and uniformly illuminate the area to be analyzed; the control unit that includes the PC on which the INSTRA software is installed and, finally, the synchronization units. Given the extent of the area to be analyzed, the two cameras were equipped with Ricoh FL-CC1614 high-resolution lenses, with 2M resolution, F1.4 - 16 aperture and 16.0 mm focal length. The strain data obtained by DIC will then be compared with the numerical values obtained at the loading configuration adopted to validate the numerical model.

5.3.3. Classification of components for fatigue testing

Four different groups of components classified according to the surface treatments to which they were subjected were considered: as machined (As M.) condition, simply tartaric-sulfuric acid anodized (As

M.+TSA) condition, shot peened and TSA anodized condition (As M.+SP+TSA) and laser shock peened and TSA anodized condition (As M.+LSP+TSA). Each group of components consists of 8 specimens each of one is identified by an alphanumeric code indicating the treatments performed and the sequential number, as shown in Table 5-3.

Table 5-3: *Classification of components for fatigue testing according to the surface treatments they were subjected.*

Group 1	
As Machined	As M.-01
	As M.-02
	As M.-03
	As M.-04
	As M.-05
	As M.-06
	As M.-07
	As M.-08

Group 2	
TSA Anodized	As M.+TSA-01
	As M.+TSA-02
	As M.+TSA-03
	As M.+TSA-04
	As M.+TSA-05
	As M.+TSA-06
	As M.+TSA-07
	As M.+TSA-08

Group 3	
Shot peened +TSA	As M.+SP+TSA-01
	As M.+SP+TSA-02
	As M.+SP+TSA-03
	As M.+SP+TSA-04
	As M.+SP+TSA-05
	As M.+SP+TSA-06
	As M.+SP+TSA-07
	As M.+SP+TSA-08

Group 4	
Laser Peened + TSA	As M.+LSP+TSA-01
	As M.+LSP+TSA-02
	As M.+LSP+TSA-03
	As M.+LSP+TSA-04
	As M.+LSP+TSA-05
	As M.+LSP+TSA-06
	As M.+LSP+TSA-07
	As M.+LSP+TSA-08

Shot peening treatment was applied to all external surfaces of the component in the 10-mm-thick region (Figure 5-10b). The specimens were initially shot peened to full coverage using cast steel shots with an average size of 600 μm at an intensity of 0.20 to 0.24 mmA. Next, the specimens were subjected to a decontamination process using glass shots of smaller size (300 μm) and with a resulting Almen intensity of 0.26-0.32 mmN.

Laser Shock Peening treatment was applied locally at the circular notch of the component. Peening was performed successively on both the main surfaces and the side surface of the component (notch side) by rotating the specimen with respect to its main longitudinal axis during the process (Figure 5-10c).

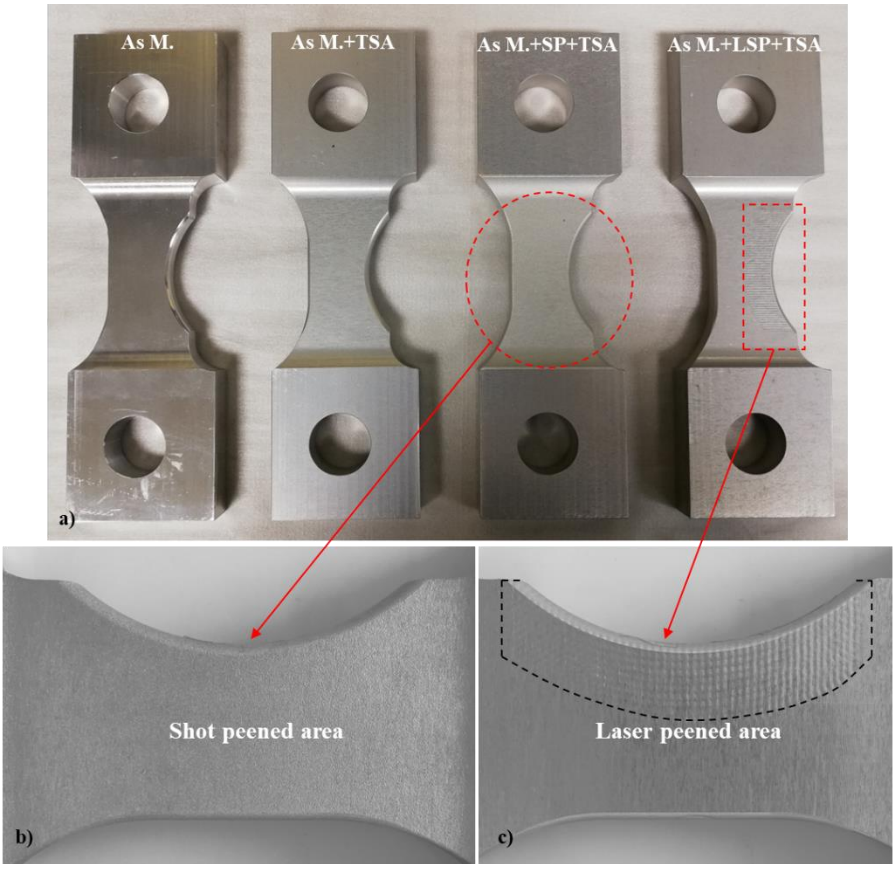

Figure 5-10: *Single edge notched components for fatigue testing: a) overall view of each type of component; b) magnified view of the shot peened region of As M.+SP+TSA components; c) magnified view of the shot peened region of As M.+LSP+TSA components.*

An ND:YLF laser system characterized by a wavelength of 1053 nm was used for the laser shock peening process. The process parameters are identical to those used on the specimens for the four-point bending fatigue tests: the laser pulse energy was set at 2.5 J and is distributed over a circular spot with a diameter of 2 mm. With a laser pulse duration of 20 ns, a nominal power density of about 4 GW/cm^2 is obtained. The laser pattern, characterized by an overlap rate of 33% in both the scanning and overlapping directions of the laser spots, is repeated three times with a 33% offset on each of the surfaces involved in the process. The stepping direction of the laser pattern is parallel to the loading direction of the component. The surface of the component is preliminarily covered with a layer of ablative material (aluminum tape) to promote plasma formation. Instead, the pressure waves generated by the plasma expansion are directed into the thickness of the material by means of a laminar flow of water interposed between the laser source and the material substrate. The TSA process was performed in a solution consisting of tartaric acid and sulfuric acid present in the solution with a concentration of 80 g/l and 40 g/l, respectively. The process parameters were set to obtain an anodic layer of 2 µm thickness, so a voltage of 15 V, an acid bath temperature of 40°C and a solution holding time of about 22 min were selected. The anodizing treatment was performed after the surface of the components underwent degreasing pretreatment with alkaline cleaner and pickling in an aqueous solution of sulfuric acid, nitric acid and ferric sulfate.

5.3.4. Residual stress evaluation methods and fatigue testing

Residual stresses were evaluated on one of the two front surfaces and on the side surface of four randomly selected components belonging to each group, according to the classification given in Table 5-3. A measurement grid consisting of 13x11 points placed at a distance of 2 mm from each other in both X- and Y-direction was constructed close to the notch on the front surface of the component. An additional measurement grid consisting of 3x3 points was built at the center of the side surface of the component for the evaluation of residual stresses within the notch. Again, the measurement points are placed at a distance of 2 mm from each other in both generating directions of the grid (Figure 5-11). Residual stresses were evaluated by X-ray diffraction technique at each grid point along the loading direction (Y-direction).

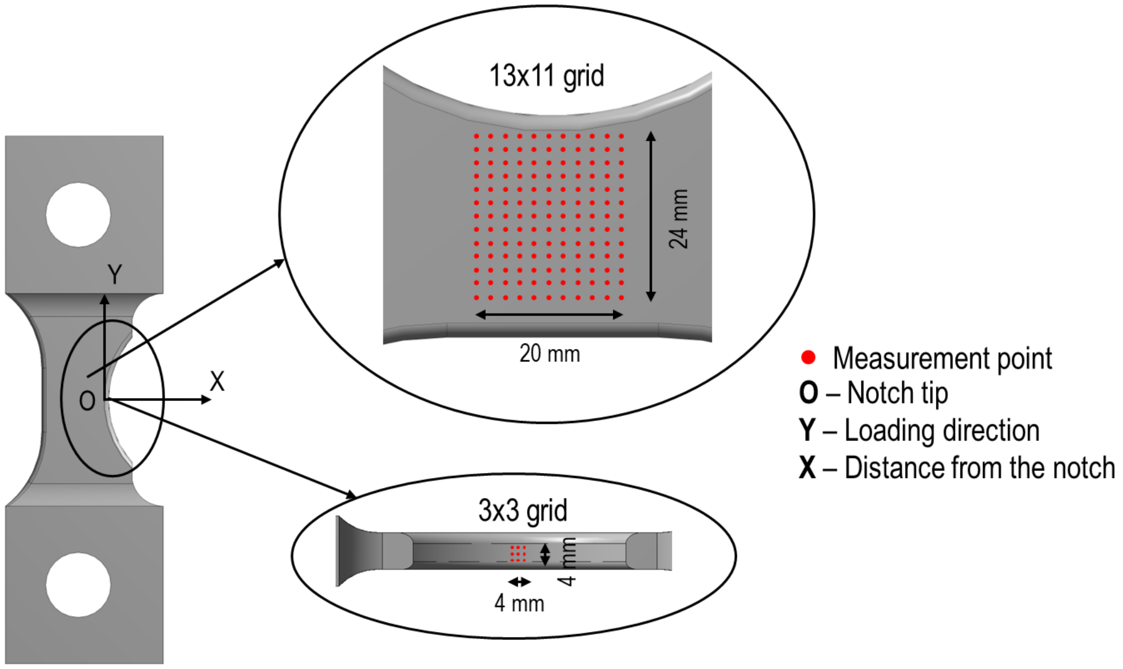

Figure 5-11: *Definition of the two measurement grids on the front surface and on the lateral surface of single edge notched components for residual stress evaluation.*

Surface residual stresses analysis was performed using Xstress 3000 G3R X-ray diffractometer (Stresstech). It was instrumented with a Cr tube (λ = 0.2291 nm) and a 2 mm collimator. The residual stress measurements were performed using the $\sin^2\Psi$ technique as required by UNI EN 15305 standard. The diffracted intensity, the peak width and the position of the diffraction peak were determined by interpolating the peak profile with the Pseudo-Voigt function.

Table 5-4 summarizes the parameters used for the residual stress measurements.

Table 5-4: *X-Ray diffraction process parameters*

Tube	Diffraction angle *[°]*	Exposure time *[sec]*	No. of tilt *[#]*	Tilt angle *[°]*	Tilt oscillation *[°]*	Collimator diameter *[mm]*	Voltage *[kV]*	Current *[mA]*
Cr	139.3	40	4	±45	±3	2	30	8

The residual stress values obtained at each point on the measurement grids were then interpolated using a third-degree polynomial interpolation function to obtain residual stress maps of the examined surfaces.

Fatigue tests were performed on a "Rumul Vibroforte 500" resonance testing machine equipped with a 500 kN load cell. All fatigue tests were performed in a full-clamped load configuration because, as will be verified in the next sections, the pin-load configuration induces a high-stress state at the contact region between the pin and the hole causing early failures in regions other than the notch, especially in the case of shot and laser peened components. The components were subjected to constant amplitude uniaxial cyclic loads with a stress ratio of 0.1. The loading frequency is a function of the mass distribution of the machine-component system and the applied load and is generally in the range of 75-85 Hz. The runout was set at 3×10^6 cycles. After the fatigue tests were completed, four components, one from each category, were selected to conduct fracture surface analyses to identify the failure modes and nucleation sites of fatigue cracks.

5.4. Results

5.4.1. Stress concentration factor

5.4.1.1. Numerical evaluation of the stress concentration factor

The objective of the numerical analysis is to identify the loading configuration that allow for a stress concentration factor of 1.5 to be obtained at the notch, so that the component is representative of a real critical structural part for aircraft applications. The stress distributions were obtained assuming the application of monotonically increasing static load according to pin load and full-clamped load configurations up to a maximum load of 40 kN. Maximum axial stress values in the notch as a function of applied load were then extrapolated and compared with nominal stress values calculated as the ratio of the applied load to the minimum section of the component. The slope of the linear regression line of maximum stress in the notch and nominal stress represents the value of the stress concentration factor. Figure 5-12 shows the stress distributions obtained under the assumptions of pin load and full-clamped configuration, respectively. The maps were obtained at an applied load of 40 kN.

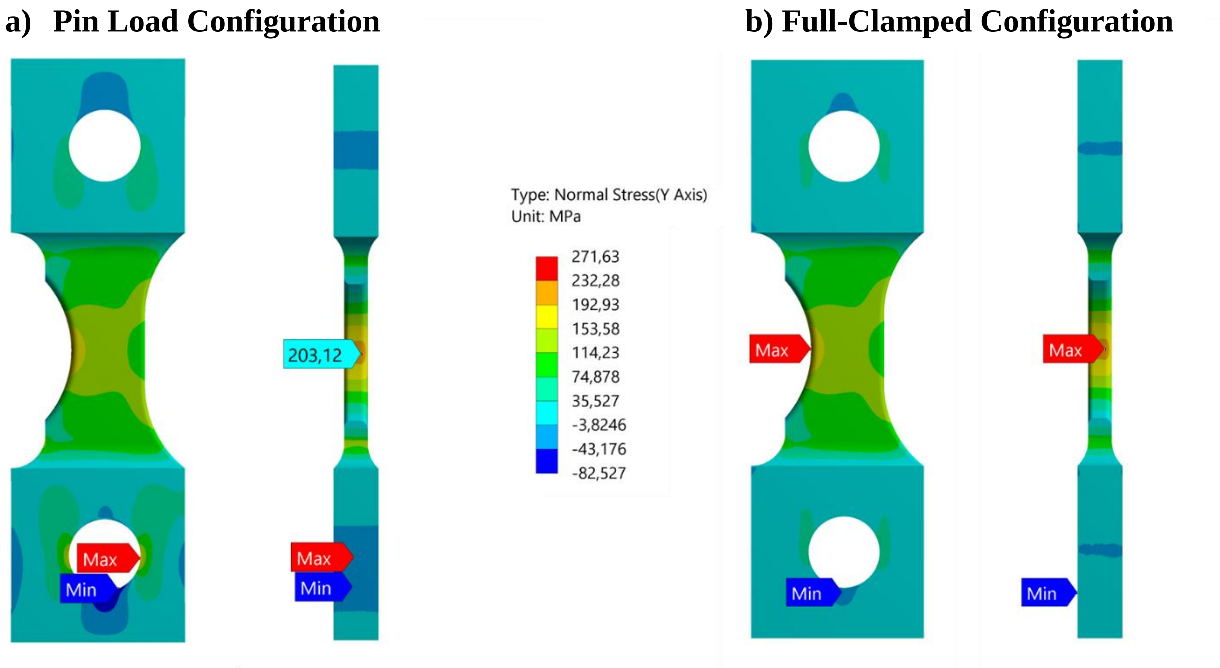
a) Pin Load Configuration
b) Full-Clamped Configuration
203,12
Max
Min
Type: Normal Stress(Y Axis)
Unit: MPa
271,63
232,28
192,93
153,58
114,23
74,878
35,527
-3,8246
-43,176
-82,527
Max
Min
Max
Min

Figure 5-12: Normal stress maps (Y-direction) of single-edge notched components under pin load (a) and full clamped (b) load configurations.

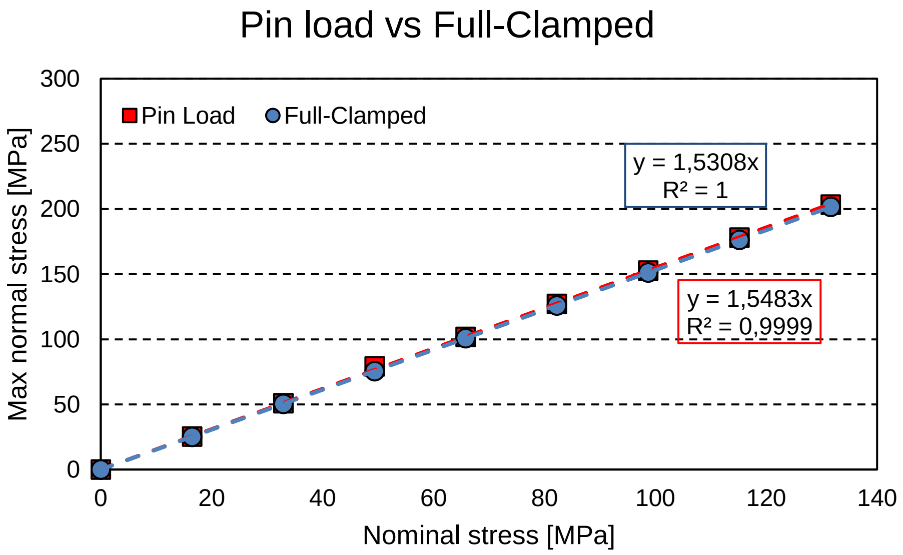

***Figure 5-13:** Maximum normal stress at the notch as a function of nominal stress in single-edge notched components under pin load and full clamped load configurations.*

The maximum normal stress values in the notch are found to be 203 MPa and 201 MPa in the case of pin load and full-clamped configuration, respectively. Given the minimum cross section of the component, which is approximately 304 mm^2, it is then possible to calculate the nominal stress associated with the applied load and consequently the value of the stress concentration factor in the two load configurations. Specifically, a K_t of about 1.54 is measured at the notch in both cases (Figure 5-13). A careful analysis of the two stress maps reveals also that the two stress distributions at the notch on the front surface of the component are comparable. However, attention should be paid to the stress state in the clamping region: in the case of pin load configuration, forces are exchanged through the contact between the pin and the inner surface of the hole causing a local increase in the stress state. As a result, the stress value at the pin-hole contact region turns out to be slightly higher than the maximum stress value measured in the notch. Under this condition, it is highly likely that the fatigue crack will nucleate at the pin-hole contact region rather than in the notch. In the full-clamped configuration the stress intensification due to the presence of the hole in the clamping region is significantly lower than in the case of pin-load configuration confirming the notch area as the most stressed region of the component. Another region that could be critical under fatigue stress is the fillet placed in the transition zone between gauge and clamping area. When local reinforcement by laser shock peening is applied in the notch region, this region has the highest value of stress concentration factor (K_t=1.15) and is therefore a candidate as a critical region for the occurrence of fatigue crack nucleation phenomena. These observations based on numerical results were verified experimentally through a series of preliminary tests conducted for verification and initial installation of the experimental loading setup.

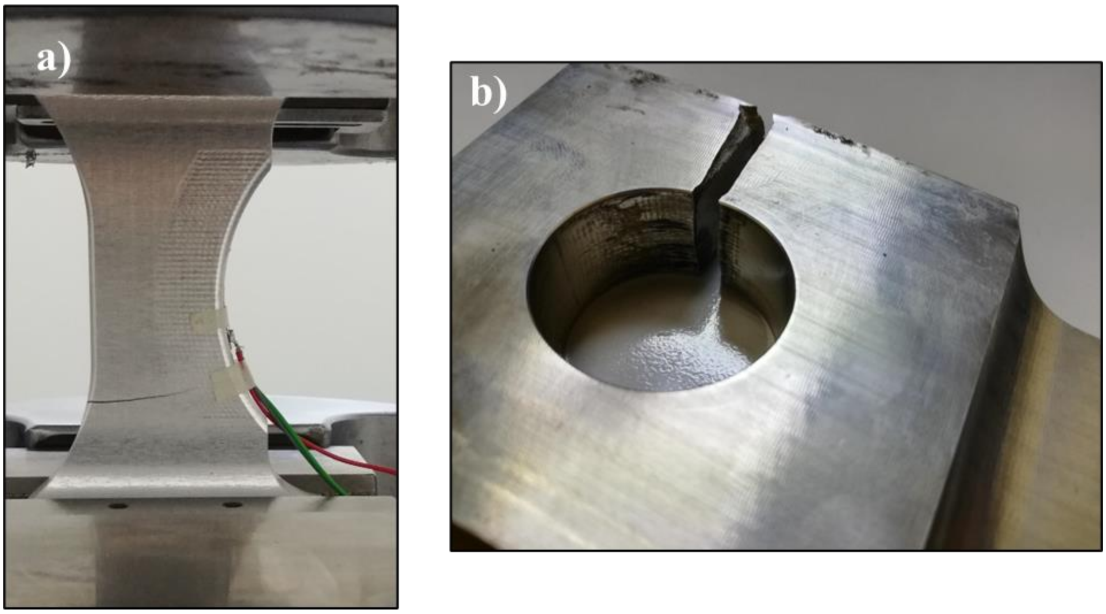

Figure 5-14: *Unexpected failures of single edge notched components: a) fatigue crack starting from the transition zone between flat section and clamping region; b) fatigue crack nucleating at the most stressed part of the loading hole.*

Figure 5-14a shows the case of an As M.+LSP+TSA component fatigue-tested in a full-clamped loading configuration in which the fatigue crack is nucleated in the transition region between flat section and the clamping region. Figure 5-14b, on the other hand, shows the case of an As M. component tested in a pin load configuration that exhibited failure at the most stressed area of the inner surface of the loading hole.

Based on the obtained results, a component with a stress concentration factor of 1.5 can be obtained by indifferently adopting the defined geometry in combination with either of the two load configurations. However, the pin load configuration results in a concentration of stresses at the loading holes due to contact between the pin and the inner surface of the hole, which can lead to unexpected crack nucleation in a region other than the notch. Consequently, in accordance with the industrial partner, it was agreed to adopt the full-clamped load configuration.

5.4.1.2. Experimental verification of stress concentration factor

Experimental verification of the stress concentration factor was carried out by applying two different experimental methods: installing strain gauges in the most stressed region of the notch to measure the deformations associated with the application of a static load and using the Digital Image Correlation technique to obtain a displacement map on one of the front surfaces of the component for validation of the numerical results. Regarding the first experimental method for testing the stress concentration factor, a HBK 120 Ω uniaxial strain gauge with a measuring grid of 1.5 mm was installed in the center of the notch section of the single edge notched specimen, as shown in the Figure 5-8. The component was then subjected to monotonically increasing static loading with a load application rate of 100 N/sec up to a maximum load of 35 kN to avoid the occurrence of local plasticization phenomena. As established in the previous section, a full-clamped load configuration was used. The stress values at each strain value acquired through the strain gauge placed in the notch are obtained under the assumption of isotropic material and linear elastic behavior using the value of Young modulus given in Table 5-2. Figure 5-15 then shows the diagram relating the maximum stress value in the notch to the nominal stress at different values of applied load. The experimental result gives a stress concentration factor value of about 1.56, which is perfectly in line with the stress concentration factor obtained by numerical analysis (K_t=1.53).

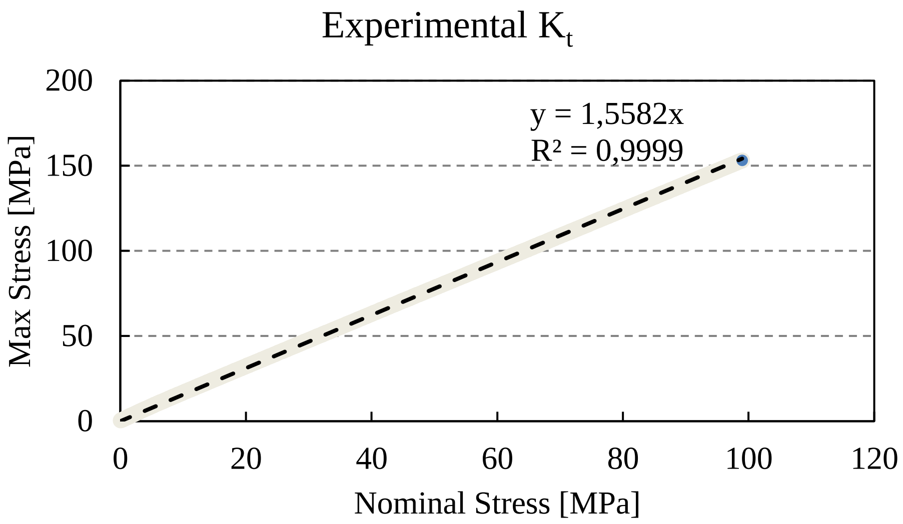

Figure 5-15: *Stress concentration factor at the notch obtained by applying an HBM strain gauge in the inner surface of the notch.*

The map of the axial displacements obtained by application of the digital image correlation technique on the front surface of the component is shown in Figure 5-16a. The map is compared with the axial displacement field obtained by numerical simulation (Figure 5-16b). An excellent correspondence between the experimental and numerical values is observed both in terms of the intensity of the measured displacements and in their surface distribution, confirming the validity of the numerical model.

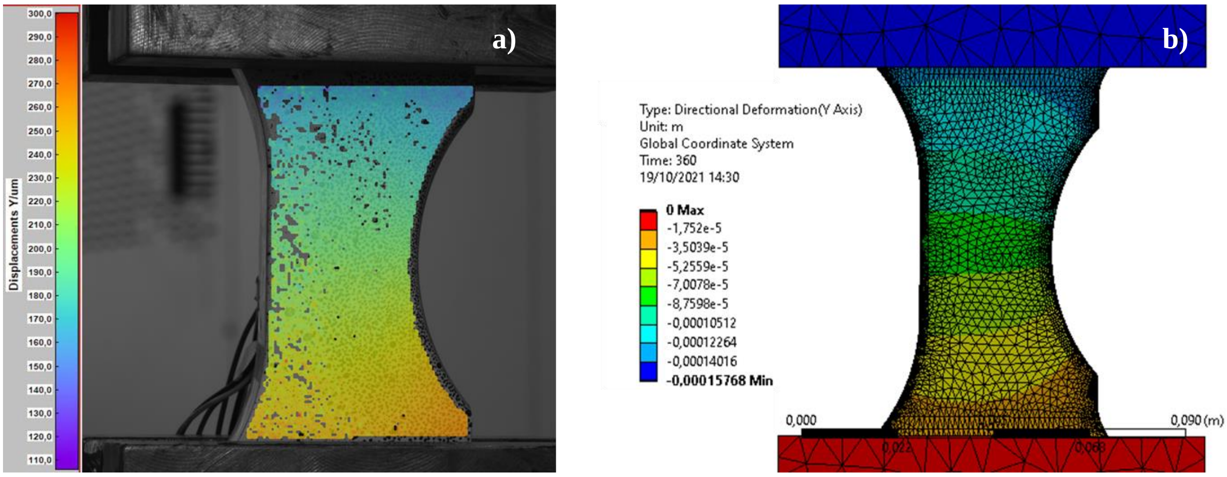
a)
Displacements Y/um
300,0
290,0
280,0
270,0
260,0
250,0
240,0
230,0
220,0
210,0
200,0
190,0
180,0
170,0
160,0
150,0
140,0
130,0
120,0
110,0
b)
Type: Directional Deformation(Y Axis)
Unit: m
Global Coordinate System
Time: 360
19/10/2021 14:30
0 Max
-1,752e-5
-3,5039e-5
-5,2559e-5
-7,0078e-5
-8,7598e-5
-0,00010512
-0,00012264
-0,00014016
-0,00015768 Min
0,000
0,090 (m)
0,022
0,068

Figure 5-16: *a) Displacement map obtained by Digital Image Correlation technique applied on the front surface of the component; b) Displacement map obtained by numerical simulation.*

5.4.2. Residual stress results

Residual stresses were evaluated in two different regions of the component: on the front surface near the notch and on the inner surface of the notch, as indicated in Figure 5-11. Regarding residual stress measurements on the front surface of the component, the stress maps obtained for the four different categories of components considered are shown in Figure 5-17. If we assume that the origin of the reference system of the measurement grid is located at the tip of the notch and the X axis represents the distance of a point from the notch, it is possible to calculate the mean value of residual stresses at different distances from the notch and thus obtain a surface trend of stresses moving away from the notch. The surface residual stress trends for each component group are shown in Figure 5-18.

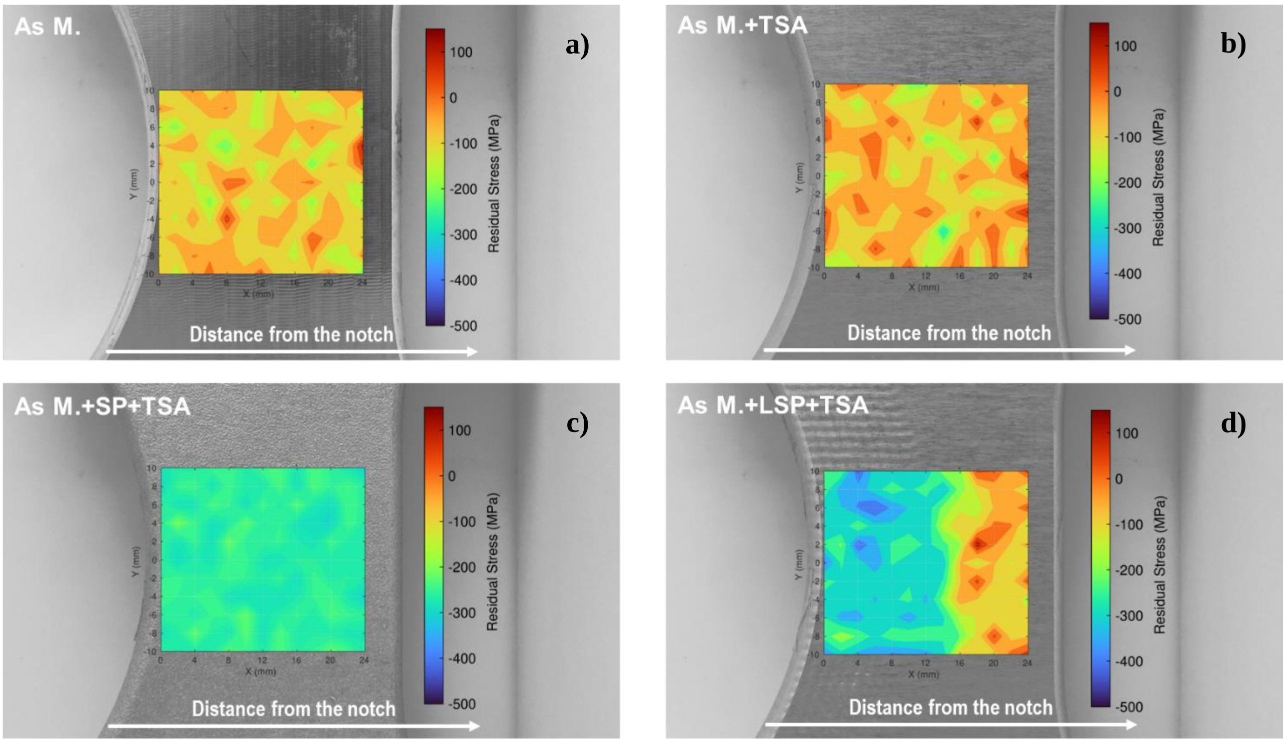

__Figure 5-17:__ Residual stress maps on the front surfaces of single-edge notched components; a) As M.; b) As M.+TSA; c) As M.+SP+TSA and d) As M.+LSP+TSA.

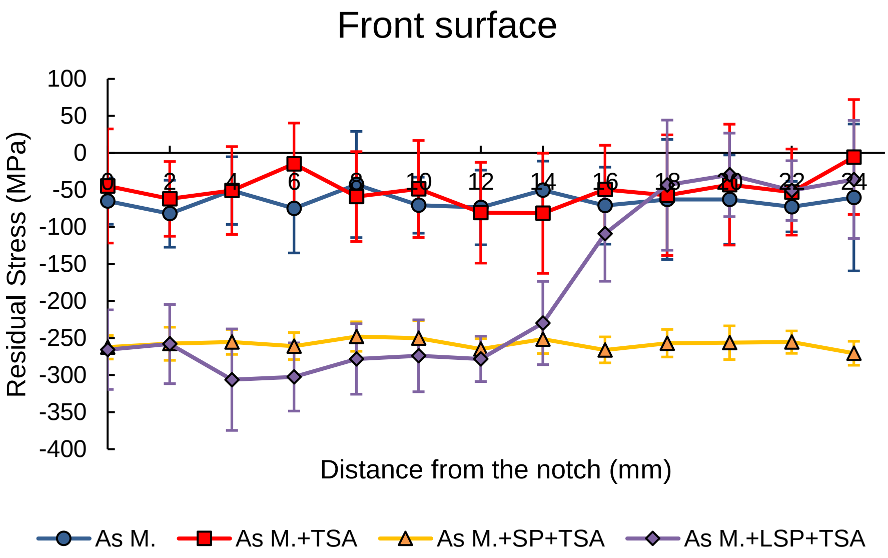

__Figure 5-18:__ Average values of residual stresses as a function of the distance from the notch tip.

As M. components exhibit a slightly compressive residual stress state on the surface. The average stress value over the entire surface is about -65 MPa, which is compatible with residual stresses induced by technological machining process. The TSA anodizing process does not determine a significant change in the residual stress state: the mean value of residual stresses on the surface, which is about -50 MPa, appears to be almost identical to that measured in As M. components, and the stress distribution does not appear to be affected by the anodizing process. It is worth mentioning that the measurement of residual stresses by X-ray diffraction is not limited to the volume of anodic layer but also affects the part of the substrate immediately in contact with the anodic film. Consequently, the numerical result of residual stresses should be considered as an indication of the influence of the presence of the anodic layer on the stress state of the base material and not as the value of residual stresses within the anodic layer. On the other hand, both shot peening and laser shock peening processes induce a strong compressive stress state on the surface of the component. The intensity of residual stresses in the two processes are almost coincident, with average values settling at -260 MPa in the case of shot peening and -280 MPa in the case of laser shock peening (in the treated region). A closer analysis of the surface residual stress profile of the As M.+LSP+TSA components, however, reveals two peculiarities: first, at the notch tip the residual stresses take on average lower values than those measured at greater distances from the notch; second, it is interesting to observe the residual stress gradient at the interface between the region subjected to the LSP process and the untreated region with residual stresses extending well beyond the region involved in the peening process until they stabilize at values close to those of the As M. and As M.+TSA components. Thus, a reduction in the compressive residual stresses induced by the LSP process in the notch tip area is observed. To verify whether there is indeed an influence of geometry on the distribution and intensity of residual stresses, the residual stress state was also evaluated within the notch surface (Figure 5-11). The measurement grid was placed at the center of the flat inner surface of the notch at a minimum distance of 2 mm from the two lateral fillets. The values of residual stresses at each point on the measurement grid was interpolated using a cubic polynomial function in order to obtain stress maps within the component notch. The values assumed by residual stresses at the measurement grid points located on the inner surface of the notch are reported in Table 5-5, while the stress maps for each category are shown in Figures 5-19 and 5-20.

Table 5-5: *Values assumed by residual stresses at the measurement grid points located on the inner surface of the notch.*

		As M.		
		x [mm]		
		-2	**0**	**2**
y [mm]	**-2**	-25,3	-40,2	-87,8
	0	3,2	-7,5	-42,4
	2	8,3	-60	11,2

		As M.+TSA		
		x [mm]		
		-2	**0**	**2**
y [mm]	**-2**	4,5	-22,1	-11
	0	-34	1,1	-8
	2	-25,3	-31	-2,3

		As M.+SP+TSA		
		x [mm]		
		-2	**0**	**2**
y [mm]	**-2**	-238,4	-244,2	-288,3
	0	-254,4	-249,1	-239,3
	2	-261,4	-268,5	-239,2

		As M.+LSP+TSA		
		x [mm]		
		-2	**0**	**2**
y [mm]	**-2**	-187,1	-213,7	-179
	0	-201,3	-228,1	-209,2
	2	-194,1	-249,3	-192,4

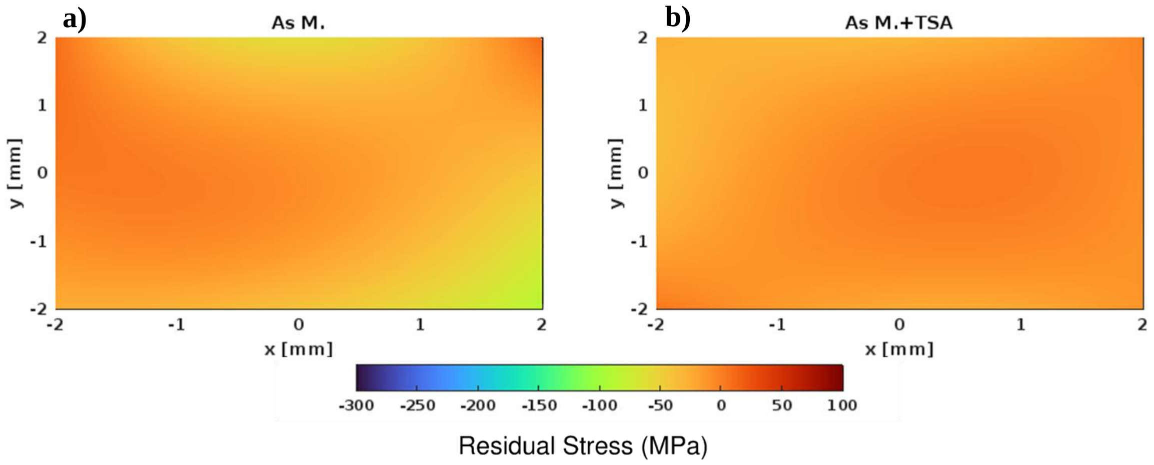

Figure 5-19: *Residual stress maps in the inner surface of the notch of a) As M. and b) As M.+TSA components.*

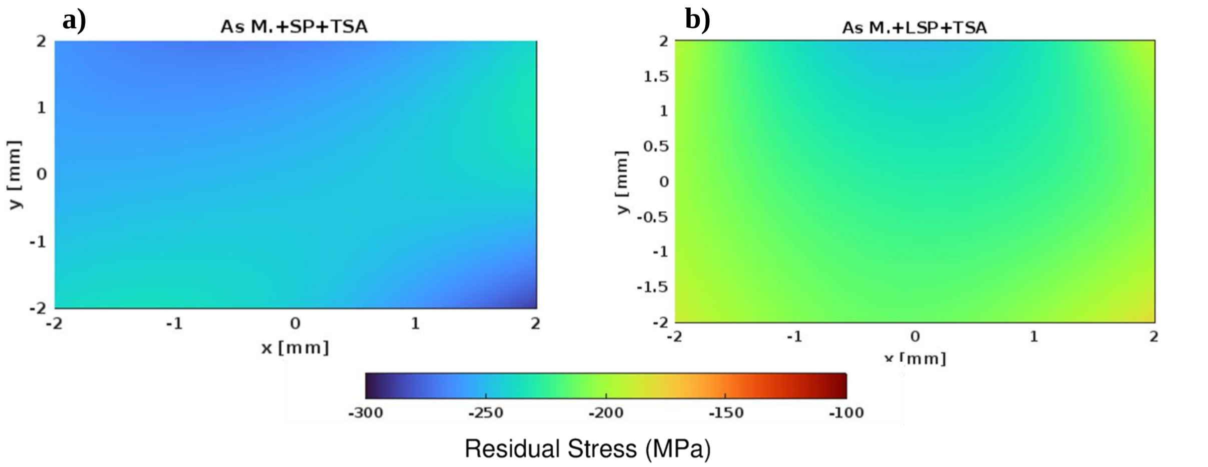

Figure 5-20: *Residual stress maps in the inner surface of the notch of a) As M.+SP+TSA and b) As M.+LSP+TSA components.*

The average values of residual stresses in the case of As M. and As M.+TSA components are comparable with those measured on the front surface of the component. The same is found in the case of As M.+SP+TSA components, with a constant stress distribution on the inner surface of the notch and an average value of about -250 MPa. In contrast, a significant difference is observed in the case of As M.+LSP+TSA components: the average value of residual stresses on the inner surface of the notch is about 205 MPa, about 27% less than the average value measured in the laser peened region of the front surface of the component. In particular, a drastic reduction in the values of residual stresses is observed at the measurement grid points closest to the lateral fillets. One possible motivation behind the reduction in residual stress values near the fillets can be attributed to the size of the laser spot adopted for the LSP process. Due to the curvature of the treated surface, the laser spot will be projected onto a non-planar region resulting in inhomogeneity and reduced pressure values at the treated surface. This phenomenon will be more noticeable the larger the size of the laser spot employed as a larger curved region is targeted. Smaller laser spots can be adopted to solve this drawback; however, it is necessary to recall that the size of the laser spot is one of the critical parameters of the LSP process and that the rate of attenuation of the pressure wave generated by plasma expansion within the material and consequently the penetration depth and the intensity of the induced residual stresses are closely related to this parameter.

5.4.3. Results of fatigue test on single edge notched components

Fatigue tests were conducted in a full-clamped loading configuration by subjecting the components to constant amplitude uniaxial cyclic loads. Four different fatigue curves were then obtained, each relating to a specific category of components based on the classification proposed in Table 5-3. The fatigue data were interpolated using the 4-parameter Weibull equation shown in Equation 1:

$$S = b(N + B)^{a} + S_{e} \tag{1}$$

The fatigue life values at each stress level are given in Table 5-6. The stress value given in the table corresponds to the maximum net cyclic stress calculated with respect to the minimum section of the component. To know the maximum stress value in the notch, the indicated stress value must be multiplied by the stress concentration factor corresponding to the adopted geometry (in this case K_t=1.55). The values of the interpolation parameters of the Weibull function are given in Table 5-7 for each component category.

Table 5-6: *Number of cycles to failure and maximum net stress level for each component: a) As M. components; b) As M.+TSA components; c) As M.+SP+TSA components; d) As M.+LSP+TSA components.*

a)

ID Code	Maximum net stress [MPa]	Cycles to failure
As M.-01	250	36000
As M.-02	230	50500
As M.-03	235	380100
As M.-04	225	53700
As M.-05	200	106600
As M.-06	185	>3×10^6
As M.-07	195	154900
As M.-08	215	96200

b)

ID Code	Maximum net stress [MPa]	Cycles to failure
As M.+TSA-01	250	29700
As M.+TSA-02	230	39300
As M.+TSA-03	200	72600
As M.+TSA-04	180	85300
As M.+TSA-05	160	>3×10^6
As M.+TSA-06	210	65700
As M.+TSA-07	220	62000
As M.+TSA-08	170	163800

c)

ID Code	Maximum net stress [MPa]	Cycles to failure
As M.+SP+TSA-01	230	329300
As M.+SP+TSA 02	250	141400
As M.+SP+TSA-03	240	218700
As M.+SP+TSA-04	220	836200
As M.+SP+TSA-05	225	312600
As M.+SP+TSA-06	210	790400
As M.+SP+TSA-07	205	>3×10^6
As M.+SP+TSA-08	215	635300

d)

ID Code	Maximum net stress [MPa]	Cycles to failure
As M.+LSP+TSA-01	240	98200
As M.+LSP+TSA-02	230	155600
As M.+LSP+TSA-03	250	80200
As M.+LSP+TSA-04	220	149900
As M.+LSP+TSA-05	210	265900
As M.+LSP+TSA-06	200	>3×10^6
As M.+LSP+TSA-07	205	410000
As M.+LSP+TSA-08	200	344200

Table 5-7: *Estimated values of Weibull parameters using non-linear regression analysis based on the least square method.*

Weibull parameters	As M.	As M.+TSA	As M.+SP+TSA	As M.+LSP+TSA
b	10×10^8	3.69×10^7	1.09×10^7	1.83×10^7
B	24900	15930	72120	62080
a	-1.51	-1.199	-1.005	-1.071
S_e	186	156	202	190

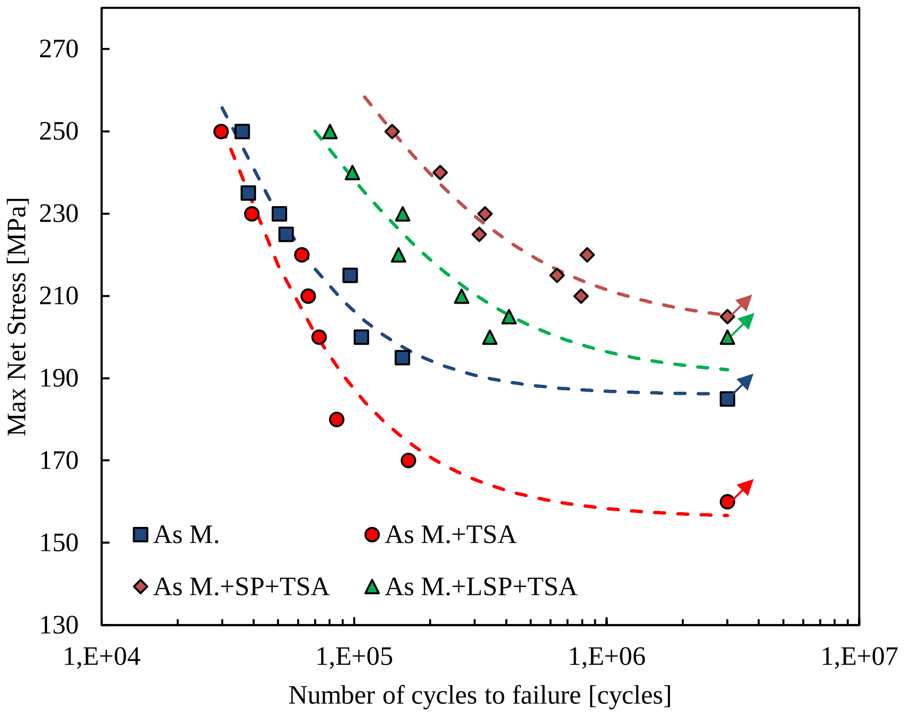

Figure 5-21: *S-N fatigue curves of single edge notched components under constant amplitude uniaxial cyclic loading.*

The fatigue curves shown in Figure 5-21 recall the fatigue trends observed in the previous chapter in relation to the four-point bending fatigue tests of unnotched bending bars (K_t=1). If we compare the fatigue curves of As M. and As M.+TSA components, the negative effects of the anodizing process on the fatigue life of the component can be observed immediately. This phenomenon has already been noted and discussed in the previous analyses and was associated with the brittleness of the anodic layer and the presence of pore or microvoid-type defects in the surface and subsurface region of the component that act as preferential sites for fatigue cracks nucleation. Due to the presence of pore or defect clusters, the fatigue life of the anodized component is significantly reduced in the HCF regime of fatigue curves compared to the LCF regime. Based on experimental results, it was estimated a reduction of the theoretical fatigue limit by 18% following TSA anodizing at the adopted combination of process parameters. In contrast, in the LCF region of the fatigue curves, the As M. and As M.+TSA components show comparable trends probably because macroscopic plasticity occurs, residual stresses are relaxed and material defects have a low impact on the resistance due to material elastic-plastic accommodation. The main difference from the fatigue results of unnotched specimens is found by analyzing the fatigue behavior of As M.+SP+TSA and As M.+LSP+TSA components. In this analysis, both SP and LSP components were subjected to the same TSA anodizing process, as a result they both have an anodic layer of approximately 2 μm thickness. Thus, a very similar fatigue behavior between the two types of specimens was expected since the results of the four-point bending fatigue tests had shown the ability of the LSP process to provide excellent results in the LCF regime of fatigue curves and only a slight reduction in the theoretical fatigue limit due to the increased thickness of the anodic layer. Contrary to expectations, however, an overall better fatigue behavior of As M.+SP+TSA components is observed compared to As M.+LSP+TSA components at all considered stress levels. This behavior may be related to the reduction of the residual stress field in the inner region of the notch observed in As M.+LSP+TSA components. This claim can be verified by analyzing the fracture surfaces of the components to identify the fatigue crack nucleation site and verify whether it is located at the region of the fillets or a different location in the component. Although As M.+LSP+TSA components exhibit lower fatigue life values than As M.+SP+TSA components at the same stress level, the benefits of the LSP process on the fatigue properties of the untreated and simply anodized material should still be emphasized. Laser peening is still able to provide a fatigue life increase factor greater than 2 in the LCF and MCF regimes of the fatigue curves, while still presenting a fatigue limit comparable with that of the untreated material but still about 20% higher than that of the simply anodized material. Thus, if the objective of the analysis were to demonstrate that the LSP process is able to compensate for the reduction in fatigue life caused by the application of the tarta-sulfuric acid anodizing treatment the answer would certainly be affirmative; however, the specific process parameters used in the present study do not allow for comparable benefits to those offered by an optimized shot peening treatment because of the difficulty of applying LSP at geometric discontinuities such as the low radius fillets present on the investigated component.

5.4.4. Analisys of fatigue fracture surfaces

As expected, all components subjected to uniaxial fatigue tests showed failure at the central section of the circular notch, as shown in Figure 5-22. The failure mode is consistent with the results of numerical and experimental analyses for stress concentration factor evaluation, as the notch was found to be the most stressed region based on the geometry and loading configuration adopted.

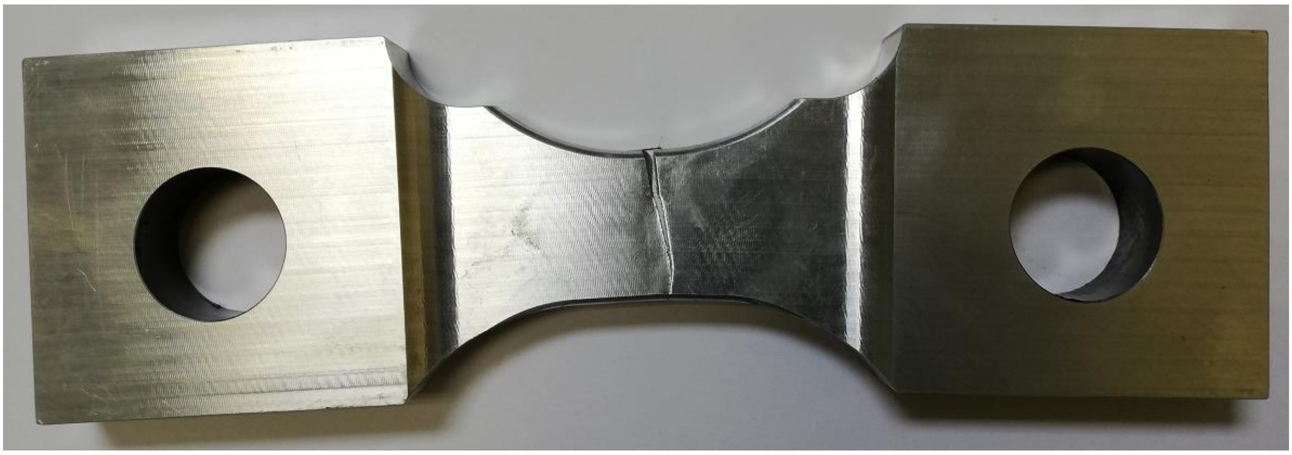

Figure 5-22: *Typical failure mode of a single edge notched component subjected to uniaxial fatigue test.*

To better understand the failure mechanisms and to identify fatigue crack nucleation sites, four tested components, one from each category, that showed failure in the MCF regime of fatigue curves were selected and their respective fracture surfaces were analyzed by scanning electron microscopy (SEM). Figures 5-23, 5-24, 5-25 and 5-26 show SEM micrographs for each component category showing different magnifications of the fatigue crack nucleation region. Fracture surface analyses indicated the curved region of the fillet as the main site of fatigue cracks nucleation for all examined components. Although the nucleation zone is the same, the microstructural features that promote crack initiation are different in the various components. The fracture surface of the As M. component shows no particular geometric features from which the fatigue crack likely originated. However, secondary cracks propagating radially from the crack nucleation site can be observed in Figure 5-23c.

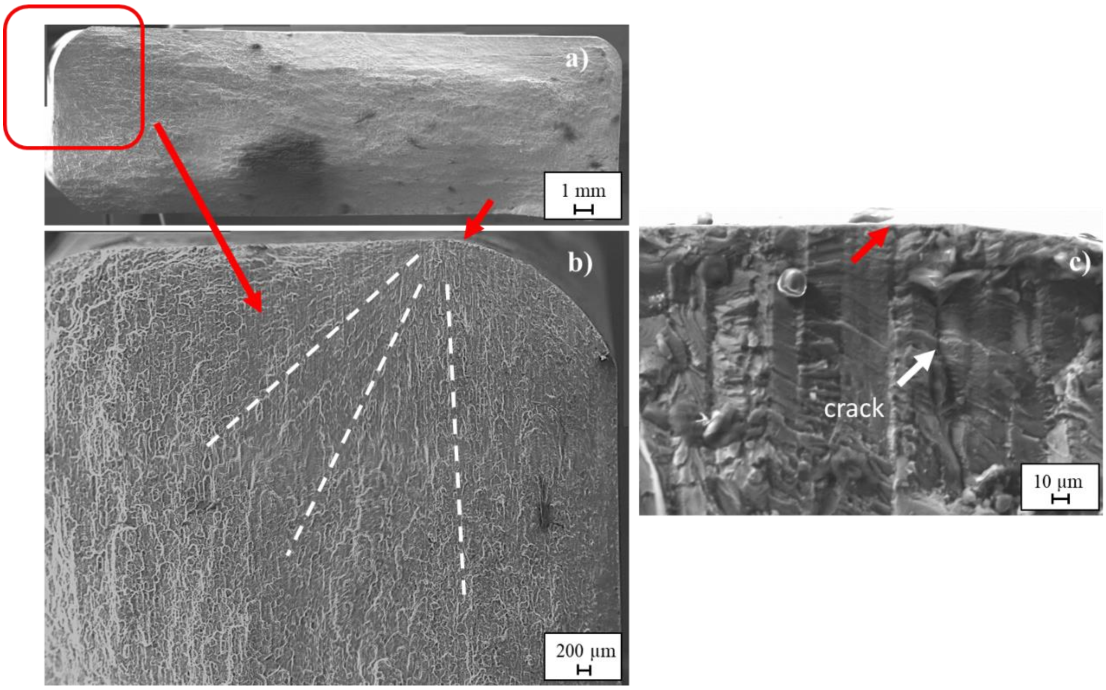

Figure 5-23: *Fracture surface of As M. component at different magnifications: a) overall view of the fracture surface; b) location of the crack nucleation site; c) microstructural feature inducing crack nucleation.*

It is particularly interesting to observe the fracture surface of the simply anodized component, which indicates the presence of a semicircular-shaped defect with a diameter of about 20 µm from which the fatigue crack presumably originates (Figure 5-24c). The size of the defect is consistent with the size of a pore cluster typically found on the surface of the anodic layer of anodized components (see Chapter 5 for more details about the morphology of surface defects induced by the TSA anodizing process). In Figure 5-24, it is also possible to observe the presence of the TSA layer developed on the substrate material as a result of the anodizing process, and in particular, it can be verified that its thickness is approximately 2 µm.

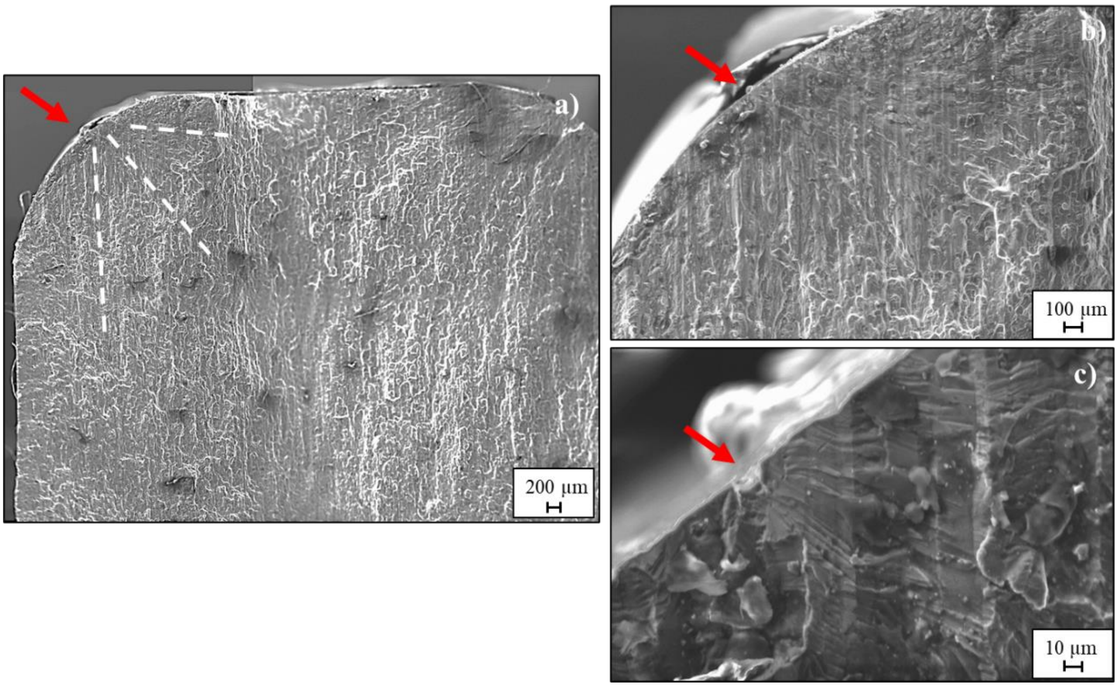

Figure 5-24: *Fracture surface of As M.+TSA component at different magnifications: a) overall view of the fracture surface; b) location of the crack nucleation site; c) semicircular-shaped defect inducing fatigue crack nucleation.*

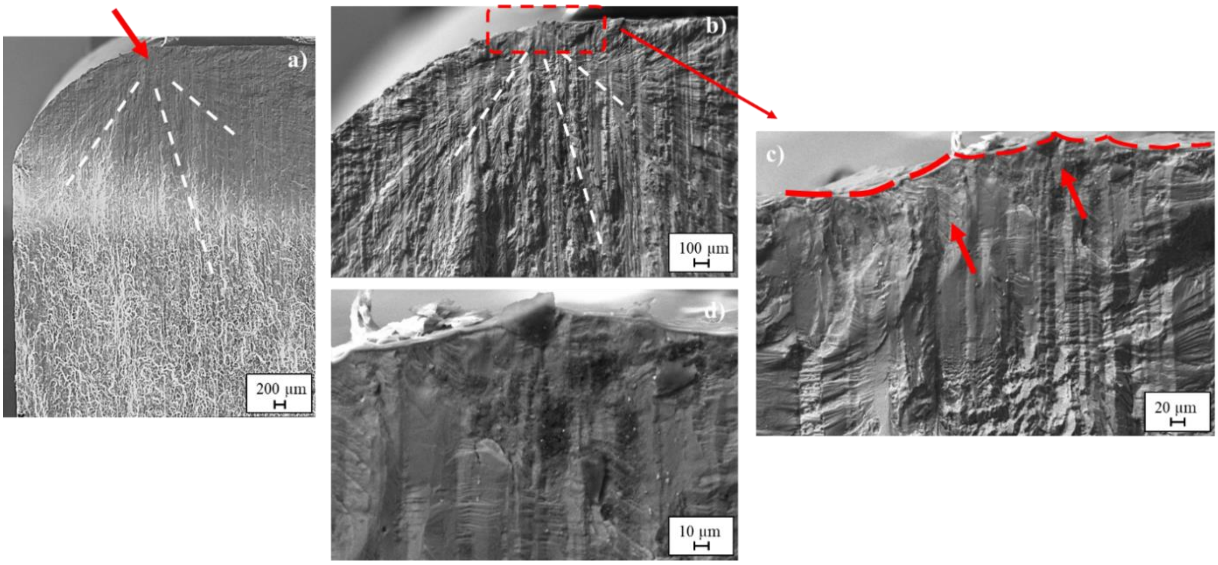

Figure 5-25: *Fracture surface of As M.+SP+TSA component at different magnifications: a) overall view of the fracture surface; b-c) location of the crack nucleation site; d) magnification of the boundary region between two indentation footprints.*

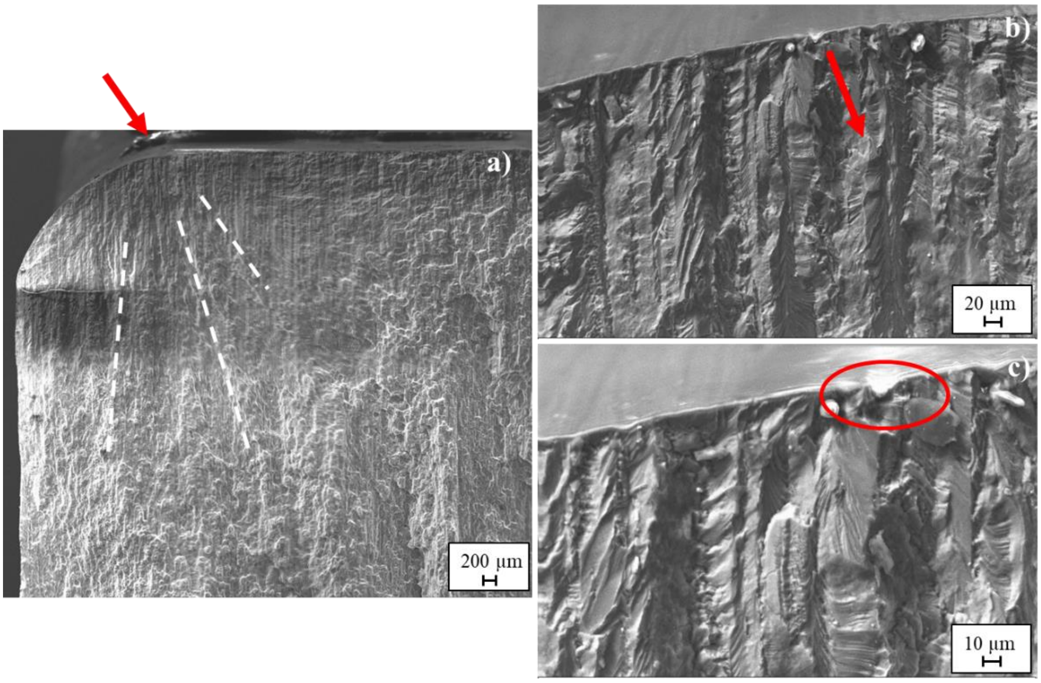

Figure 5-26: *Fracture surface of As M.+LSP+TSA component at different magnifications: a) overall view of the fracture surface; b) location of the crack nucleation site; d) magnification of the boundary region between two indentation footprints.*

In As M.+SP+TSA components (Figure 5-25), the influence of the accentuated roughness average parameter induced by the shot peening process is significantly greater. In fact, fatigue cracks appear to nucleate at the valleys of the surface roughness profile induced by the successive impacts of the shots on the surface (Figure 5-25d). In contrast, the As M.+LSP+TSA component (Figure 5-26) shows a very similar situation to that observed in the case of simply anodized component. In fact, also in this case it is possible to identify on the surface of the component a defect of semicircular shape with a smaller diameter than previously observed (about 10 mm) to which the onset of fatigue failure of the component can probably be associated.

A further observation is necessary to justify the surface location of the fatigue crack nucleation site. While in the case of As M. and As M.+TSA components it is logical to expect the fatigue crack to originate on the surface of the part, in the case of shot peened and laser peened components the presence of the compressive residual stress field could result in a shift of the nucleation site to a more unfavorable region in terms of stress state. Actually, there are two factors that prevent this phenomenon from occurring: the existence of surface defects induced by the presence of the anodizing process; and the change in the tensional state near the notch. The presence of the notch results in a local increase in the stress state defined by the stress concentration factor: as the distance from the notch increases, the maximum stress decreases and the stress state tends to the nominal stress calculated with respect to the minimum section of the component. Similarly, the residual stress field induced by LSP or SP processes exhibits a maximum at a depth from the treated surface between 200 and 500 µm and then exhibits an increasing trend toward tensile values. Residual stresses near the surface mitigate the maximum stresses near the notch tip by theoretically promoting the displacement of the crack nucleation site to the subsurface region. This is not the case, however, because microscale defects present on the surface of the anode layer (pores and pore clusters) and at the interface between the anodic layer and the aluminum substrate (microcracks) in turn change the local stress state by raising the stress values right at the surface of the component. As a result, the near-surface stress state, given by the sum of the external stress state (notch effect), the compressive residual stresses and the local stress intensification caused by the presence of the microstructural defects, is comparable to the external stress state, consequently no shift in the crack nucleation point should be expected; on the other hand, the subsurface stress state is affected by the presence of the compressive residual stresses induced by the peening processes (above 100 µm depth) and determine the slowing down of the fatigue crack propagation phenomenon, ensuring the fatigue life benefits observed in the LCF and MCF regime of fatigue curves.

5.5. Summary

In this chapter, the effect of the presence of geometric discontinuities on the residual stress state induced by the LSP process and on the fatigue life of components successively subjected to peening and anodizing treatment was evaluated. The results obtained can be summarized as follows:

- the stress concentration factor induced by the presence of a circular notch in a single-edge notched component subjected to two different loading configurations (pin load and full-clamped) was evaluated both numerically and experimentally. To be representative of a real aircraft component, the investigated component must have a stress concentration factor of about 1.5 at the notch. It has been shown that the full-clamped load configuration allows this design requirement to be met.
- The residual stress field was evaluated in two different regions near the notch: on the front surface of the component and on the inner surface of the notch. Measurements by X-ray diffraction revealed the difficulty of the laser shock peening process to effectively induce a compressive residual stress field in the vicinity of small geometric discontinuities (fillet radii), as a consequence of the size of the laser spot in comparison with the characteristic size of the geometric feature. Specifically, a 27% reduction in the mean value of compressive residual stresses measured at the inner surface of the notch was estimated compared to the mean value of compressive residual stresses measured at the front surface of the component. The use of a smaller spot size could promote the development of a more uniform residual stress field at the notch but could cause a reduction in the intensity and depth of residual stress penetration due to the higher rate of pressure wave attenuation. Similar phenomena were not observed in shot peened components.
- Fatigue test results demonstrated the possibility of increasing the fatigue life of a component by applying a laser shock peening pattern at a critical region (notch) prior to the anodizing process. In general, the LSP treatment employed provides a fatigue life increase factor greater than 2 in the LCF and MCF regimes of fatigue curves compared to untreated or simply anodized components. The theoretical fatigue limit of As M.+LSP+TSA components is about 20% higher than that of As M.+TSA components and slightly higher than that of untreated components. However, As M.+SP+TSA components exhibit higher fatigue properties than As M.+LSP+TSA components at all examined stress levels, despite identical anodizing conditions. One possible motivation can be associated with the reduction in the residual compressive stress state observed at the notch region in laser peened components.

CONCLUSIONS

I. Summary

Over the past few decades, the Laser Shock Peening process has emerged in the industrial landscape for its ability to induce deep and high compressive residual stress fields within the material. These characteristics enable significant benefits in terms of fatigue life and damage tolerance in highly stressed structures typical of aircraft applications. In order to demonstrate and quantify the effectiveness of the LSP treatment applied to the 7050-T7451 aluminum alloy of aeronautical interest, an extensive experimental campaign was conducted. This initially included evaluation of the residual stress fields induced by different combinations of LSP process parameters to identify the one that offered the best compromise in terms of compressive residual stress properties (maximum intensity and depth of penetration) and the least impact on the surface integrity of the component, as assessed using the most common roughness parameters. Once this combination of parameters was identified, a mechanical testing activity was planned aimed at evaluating the fatigue properties of unnotched and notched components subjected simultaneously to LSP and tartaric-sulfuric acid anodizing processes, in order to verify the ability of the LSP process to compensate for the reduction in fatigue life caused by the presence of the anodic layer and, at the same time, to offer a fatigue life increase factor in line with the requirements of typical critical structural applications in the aeronautical field. The effectiveness of the LSP treatment on anodized components was evaluated by comparing the fatigue results of LSP components with those obtained for identical components subjected to an optimized SP process still used in an industrial environment.

In light of the above objectives, the following conclusions can be drawn:

- The nominal power density and number of laser passes, i.e., the number of layers, turned out to be the most influential factors affecting roughness properties, determining an increasing trend of both R_a and R_t values shifting from the lowest to the highest level of each parameter. Moving from the minimum (2.5 GW/cm^2) to the maximum (4.5 GW/cm^2) nominal power density level results in an increase in R_a value of about 37% and an increase in the R_t value of about 42%. Typical average roughness values associated with the highest power density levels are around 1.9 µm, significantly lower than the typical average roughness values of SP-treated components (usually in the range 4-5 µm). Similar to laser power density, the use of a higher number of layer results in a deterioration of the surface roughness of the laser peened component. However, the R_a value measured at the highest employed number of layers is significantly lower than maximum average roughness value at the highest power density. This observation suggests the possibility to adopt this peening strategy to applications that require high surface integrity of the component and low roughness parameters (wear resistance, fretting fatigue, etc.). The thickness and the LSP strategy parameters do not significantly affect the surface integrity of the component.

- A reduction in compressive residual stresses was observed on the surface of 10-mm-thick components compared with 30-mm-thick components. This reduction could be associated with the phenomenon of reflection of the elastic waves on the lower surface of the specimen, although this phenomenon is more typically found in components with a slightly lower thickness. In addition, it was observed that compressive residual stresses on the surface of the specimens increase with the number of layers and that the maximum compressive stress is comparable with that obtained using the maximum nominal power density. Comparable values of surface residual stresses were measured both in the scanning and stepping direction of the laser, confirming the validity of the adopted laser peening strategy. In-depth residual stress analysis revealed that specimens that were laser peened using higher values of nominal power density showed higher values of maximum compressive stress both along scanning and stepping direction and that residual stresses remained approximately constant up to a depth of about 0.7-0.8 mm beneath the treated surface. In specimens in which more layers were used, the peak of compressive residual stresses is located about 0.1-0.2 mm from the treated surface, and its intensity is significantly lower than that measured in specimens treated with higher power densities (on average a reduction of 37%). Therefore, the strategy of using more layers instead of increasing the laser power density can be effective in non-critical structural applications where surface integrity is prioritized over residual stress field characteristics. In contrast, when high compressive residual stresses and penetration depths are required, the use of high power densities is recommended over the use of a greater number of layers. As a result, it was concluded that 30 mm-thick samples that were laser peened using NPD values of 3.5 and 4.5 GW/cm^2 accurately met the residual stress design requirements for fatigue critical applications.

- Evaluation of the residual stress field on the surface of the bending specimens for four-point bending fatigue testing showed that the anodizing process does not result in a change in residual stresses, as was expected based on previous studies on the subject. This is probably related to the reduced thickness of the anodic layer and the impossibility of limiting the measurement of residual stresses to the thickness of the layer alone (about 2 µm). Both Shot

Peening and Laser Shock Peening processes induce the presence of a strong residual compressive stress field on the surface of anodized components, with values generally between 200 and 250 MPa in both the scanning and laser stepping directions. As concerns four-point bending fatigue test results of untreated, simply anodized, shot peened and laser peened components, it turned out that the presence of the anodic film on the surface of anodized specimens determined an overall reduction in the fatigue performance of the base material. The main reason for the decrease in fatigue performance of anodized components can be primarily ascribed to the presence of micro-voids/pits that facilitate crack initiation resulting in an abrupt reduction in the theoretical fatigue limit due to the greater influence of the presence of defects on the HCF regime of fatigue curves. Only a slight reduction in fatigue life in anodized components is observed in the LCF regime due to the plasticization phenomena which tend to reduce the stress gradients that develop at the stress concentration sites (TSA-induced defects). Both shot peening and laser shock peening result in a significant increase in material fatigue life. However, differences are observed between the fatigue behaviors of As M.+SP+TSA and As M.+LSP+TSA specimens: in the LCF regime, the two fatigue curves are almost overlapping, while in the HCF regime, the two curves diverge and the fatigue limit of As M.+SP+TSA specimens turns out to be higher than that of As M.+LSP+TSA specimens. This discrepancy can be associated with the higher thickness of the anodic layer on the laser shock peened specimens and the resulting higher density and size of defects caused by the anodizing process.

- Analysis of surface residual stresses performed on single edge notched components subjected to laser peening showed a reduction in the intensity of compressive residual stresses near the geometric discontinuity represented by the circular notch. Specifically, a 27% reduction in the mean value of compressive residual stresses measured at the inner surface of the notch was estimated compared to the mean value of compressive residual stresses measured at the front surface of the component. One possible motivation behind the reduction in residual stress values near the fillets can be attributed to the size of the laser spot adopted for the LSP process: due to the curvature of the treated surface, the laser spot was projected onto a non-planar region resulting in inhomogeneity and reduced pressure values at the treated surface. Fatigue test results demonstrated the possibility of increasing the fatigue life of a component by applying a laser shock peening pattern at a critical region (notch) prior to the anodizing process. In general, the LSP treatment employed provides a fatigue life increase factor greater than 2 in the LCF and MCF regimes of fatigue curves compared to untreated or simply anodized components. The theoretical fatigue limit of As M.+LSP+TSA components is about 20% higher than that of As M.+TSA components and slightly higher than that of untreated components due to the presence of pit like defects on the surface of the component. However, As M.+SP+TSA components exhibit higher fatigue properties than As M.+LSP+TSA components at all examined stress levels, despite identical anodizing conditions. One possible motivation can be associated with the reduction in the residual compressive stress state observed at the notch region in laser peened components.

II. Future Research

This research activity represented an important step in understanding the effects of LSP surface treatment on the fatigue behavior of aircraft components. Nevertheless, it is just a first contribution towards to the enhancement of fatigue properties of fatigue-critical structural parts and offers numerous insights for new research perspectives. Some of these are summarized below:

- Improvement of surface quality. The increase in the number of layers parameter provides compressive surface residual stresses comparable with those obtained at the highest power density values. However, the penetration depth and peak intensity of residual stresses turned out to be significantly lower than that required by specific aircraft applications. It is important to mention that the strategy of adopting a high number of layers was used in combination with low nominal power density values to minimize the influence of the latter parameter on the definition of residual stresses. It would be interesting to adopt intermediate power densities in together with higher numbers of layers to combine the greater intensity and depth of penetration obtained at high power densities with the greater stability and reduced influence on surface integrity offered by higher numbers of layers.
- Role of the spot size. The presence of geometric discontinuities can locally alter the distribution and intensity of residual stresses induced by the LSP process, and that this can likely be linked to the geometric incompatibility between the laser spot size and the characteristic size of the geometric discontinuity. Therefore, the use of a smaller spot size could reduce the magnitude of the problem, allowing for more uniform compressive surface residual stress fields at the notch. However, it has been pointed out that the spot size parameter affects the propagation mode of pressure waves and may have undesirable repercussions on the magnitude of plastic deformations and the consequent development of compressive residual stresses in the subsurface region of the component. The high interconnection among the different LSP process parameters makes it complicated to identify an unambiguous

solution that perfectly fits the specific application. It is therefore advisable to analyze in detail the role of spot size in the development of residual stress fields in the vicinity of geometric discontinuities of comparable size.

- Numerical model for fatigue analysis. Further inspiration for future research activities is the numerical simulation of fatigue-related phenomena in mechanical structures subjected to peening and anodizing surface treatments. In recent years, a number of numerical techniques have been developed to simulate the presence of a residual stress field with specific properties within a component, and some of them, such as the one based on eigenstrain theory, make it possible to predict quite accurately the distribution and intensity of residual stresses even in components with complex geometries. Based on these considerations, it might be interesting to combine eigenstrain theory for the construction of the residual stress field induced by the LSP process with the theory of the critical distance for the numerical evaluation of the fatigue behavior of a notched component. The rapidity and low computational cost required by the two different methodologies would provide excellent predictive capabilities in a relatively short time.

REFERENCES

[1] Davis J.R., Corrosion of Aluminum and Aluminum Alloys, 1999. https://doi.org/10.1361/caaa1999p001.

[2] Davis J.R., Aluminum and Aluminum Alloys Introduction and Overview, 2001. https://doi.org/10.1361/autb2001p351.

[3] MIL-HDBK-5H, Department of Defense handbook metallic materials and elements for aerospace vehicle structures., 2003. http://www.everyspec.com.

[4] E.A. Starke, J.T. Staley, Application of modern aluminum alloys to aircraft, Progress in Aerospace Sciences. 32 (1996) 131–172. https://doi.org/10.1016/0376-0421(95)00004-6.

[5] G. Hénaff, F. Menan, G. Odemer, Influence of corrosion and creep on intergranular fatigue crack path in 2XXX aluminium alloys, Eng Fract Mech. 77 (2010) 1975–1988. https://doi.org/10.1016/J.ENGFRACMECH.2010.03.039.

[6] B. Zhou, B. Liu, S. Zhang, The advancement of 7xxx series aluminum alloys for aircraft structures: A review, Metals (Basel). 11 (2021). https://doi.org/10.3390/met11050718.

[7] A.C.U. RAO, V. VASU, M. GOVINDARAJU, K.V.S. SRINADH, Stress corrosion cracking behaviour of 7xxx aluminum alloys: A literature review, Transactions of Nonferrous Metals Society of China (English Edition). 26 (2016) 1447–1471. https://doi.org/10.1016/S1003-6326(16)64220-6.

[8] A. Azarniya, A.K. Taheri, K.K. Taheri, Recent advances in ageing of 7xxx series aluminum alloys: A physical metallurgy perspective, J Alloys Compd. 781 (2019) 945–983. https://doi.org/10.1016/j.jallcom.2018.11.286.

[9] S.G. Pantelakis, N.D. Alexopoulos, Assessment of the ability of conventional and advanced wrought aluminum alloys for mechanical performance in light-weight applications, Mater Des. 29 (2008) 80–91. https://doi.org/10.1016/J.MATDES.2006.12.004.

[10] L. Xianghuai, Recent advance in surface treatment and its applications in China, Surf Coat Technol. 131 (2000) 261–266. https://doi.org/10.1016/S0257-8972(00)00791-X.

[11] S. Qutaba, M. Asmelash, K. Saptaji, A. Azhari, A review on peening processes and its effect on surfaces, International Journal of Advanced Manufacturing Technology. 120 (2022) 4233–4270. https://doi.org/10.1007/s00170-022-09021-6.

[12] L. Wagner, Mechanical surface treatments on titanium, aluminum and magnesium alloys, Materials Science and Engineering: A. 263 (1999) 210–216. https://doi.org/10.1016/S0921-5093(98)01168-X.

[13] R. Sundar, P. Ganesh, R.K. Gupta, G. Ragvendra, B.K. Pant, V. Kain, K. Ranganathan, R. Kaul, K.S. Bindra, Laser Shock Peening and its Applications: A Review, Lasers in Manufacturing and Materials Processing. 6 (2019) 424–463. https://doi.org/10.1007/s40516-019-00098-8.

[14] C.S. Montross, T. Wei, L. Ye, G. Clark, Y.-W. Mai, Laser shock processing and its effects on microstructure and properties of metal alloys: a review, 2002. www.elsevier.com/locate/ijfatigue.

[15] A.K. Gujba, M. Medraj, Laser peening process and its impact on materials properties in comparison with shot peening and ultrasonic impact peening, Materials. 7 (2014) 7925–7974. https://doi.org/10.3390/ma7127925.

[16] P.P. Yre, L. Berthe, X. Scherpereel, R. Fabbro, Laser-shock processing of aluminium-coated 55C1 steel in water-confinement regime, characterization and application to high-cycle fatigue behaviour, 1998.

[17] P. Peyre, R. Fabbro, P. Merrien, H.P. Lieurade, MATIEIUALS SCIENCE & ENGINEERING A Laser shock processing of aluminium alloys. Application to high cycle fatigue behaviour, 1996.

[18] M. Turski, S. Clitheroe, A.D. Evans, C. Rodopoulos, D.J. Hughes, P.J. Withers, Engineering the residual stress state and microstructure of stainless steel with mechanical surface treatments, Appl Phys A Mater Sci Process. 99 (2010) 549–556. https://doi.org/10.1007/s00339-010-5672-6.

[19] W. Zinn, B. Scholtes, Mechanical Surface Treatments of Lightweight Materials-Effects on Fatigue Strength and Near-Surface Microstructures, n.d.

[20] M.P. Martínez-Viademonte, S.T. Abrahami, T. Hack, M. Burchardt, H. Terryn, A review on anodizing of aerospace aluminum alloys for corrosion protection, Coatings. 10 (2020) 1–30. https://doi.org/10.3390/coatings10111106.

[21] H. Liu, H. Liu, P. Bocher, C. Zhu, Z. Sun, Effects of case hardening properties on the contact fatigue of a wind turbine gear pair, Int J Mech Sci. 141 (2018) 520–527. https://doi.org/10.1016/J.IJMECSCI.2018.04.010.

[22] Y. Liu, M. Wang, J. Shi, W. Hui, G. Fan, H. Dong, Fatigue properties of two case hardening steels after carburization, Int J Fatigue. 31 (2009) 292–299. https://doi.org/10.1016/J.IJFATIGUE.2008.08.010.

[23] J. Vetter, G. Barbezat, J. Crummenauer, J. Avissar, Surface treatment selections for automotive applications, Surf Coat Technol. 200 (2005) 1962–1968. https://doi.org/10.1016/J.SURFCOAT.2005.08.011.

[24] G.A. Askar'Yan, Moroz E. M., Pressure on evaporation of matter in a radiation beam, Soviet Journal of Experimental and Theoretical Physics. 16 (1963) 1638.

[25] N.C. Anderholm, Laser-generated stress waves, Appl Phys Lett. 16 (1970) 113–115. https://doi.org/10.1063/1.1653116.

[26] A.H. Clauer, B.P. Fairand, B.A. Wilcox, Laser-hock Hardening ot Weld zones in Aluminum Alloys, (n.d.).

[27] A.H. Clauer, B.P. Fairand, B.A. Wilcox, Pulsed Laser Induced Deformation in an Fe-3 Wt Pct Si Alloy, n.d.

[28] B.P. Fairand, A.H. Clauer, R.G. Jung, B.A. Wilcox, Quantitative assessment of laser-induced stress waves generated at confined surfaces, Appl Phys Lett. 25 (1974) 431–433. https://doi.org/10.1063/1.1655536.

[29] B.P. Fairand, B.A. Wilcox, W.J. Gallagher, D.N. Williams, Laser shock-induced microstructural and mechanical property changes in 7075 aluminum, J Appl Phys. 43 (1972) 3893–3895. https://doi.org/10.1063/1.1661837.

[30] A.H. Clauer, B.P. Fairand, J.E. Slater, Laser Shocking of 2024 and 7075 Aluminum Alloys, 1977.

[31] C.S. Montross, T. Wei, L. Ye, G. Clark, Y.W. Mai, Laser shock processing and its effects on microstructure and properties of metal alloys: a review, Int J Fatigue. 24 (2002) 1021–1036. https://doi.org/10.1016/S0142-1123(02)00022-1.

[32] Adaption of LSP Capability for USe on F-22 Raptor Primary Structure at an Aircraft Modification Depot - David Jensen, (n.d.).

[33] M.J. Leap, J. Rankin, J. Harrison, L. Hackel, J. Nemeth, J. Candela, Effects of laser peening on fatigue life in an arrestment hook shank application for Naval aircraft, Int J Fatigue. 33 (2011) 788–799. https://doi.org/10.1016/J.IJFATIGUE.2010.12.016.

[34] J.N. Johnson, R.W. Rohde, Dynamic deformation twinning in shock-loaded iron, J Appl Phys. 42 (1971) 4171–4182. https://doi.org/10.1063/1.1659750.

[35] R. Fabbro, J. Fournier, P. Ballard, D. Devaux, J. Virmont, Physical study of laser-produced plasma in confined geometry, J Appl Phys. 68 (1990) 775–784. https://doi.org/10.1063/1.346783.

[36] D. Devaux, R. Fabbro, L. Tollier, E. Bartnicki, Generation of shock waves by laser-induced plasma in confined geometry, J Appl Phys. 74 (1993) 2268–2273. https://doi.org/10.1063/1.354710.

[37] C.S. Montross, V. Florea, M. v Swain, The influence of coatings on subsurface mechanical properties of laser peened 2011-T3 aluminum, n.d.

[38] J.E. Masse, G. Barreau, Laser generation of stress waves in metal, Surf Coat Technol. 70 (1995) 231–234. https://doi.org/10.1016/0257-8972(95)80020-4.

[39] P. Peyre, L. Berthe, X. Scherpereel, R. Fabbro, E. Bartnicki, Experimental study of laser-driven shock waves in stainless steels, J Appl Phys. 84 (1998) 5985–5992. https://doi.org/10.1063/1.368894.

[40] X. Hong, S. Wang, D. Guo, H. Wu, J. Wang, Y. Dai, X. Xia, Y. Xie, Confining Medium and Absorptive Overlay: Their Effects on a Laser-induced Shock Wave, 1998.

[41] L. Berthe, R. Fabbro, P. Peyre, L. Tollier, E. Bartnicki, Shock waves from a water-confined laser-generated plasma, J Appl Phys. 82 (1997) 2826–2832. https://doi.org/10.1063/1.366113.

[42] D. Devaux, R. Fabbro, L. Tollier, E. Bartnicki, Generation of shock waves by laser-induced plasma in confined geometry, J Appl Phys. 74 (1993) 2268–2273. https://doi.org/10.1063/1.354710.

[43] A. Kruusing, Underwater and water-assisted laser processing: Part 1-general features, steam cleaning and shock processing, 2004.

[44] R. Fabbro, P. Peyre, L. Berthe, X. Scherpereel, Physics and applications of laser-shock processing, J Laser Appl. 10 (1998) 265–279. https://doi.org/10.2351/1.521861.

[45] L. Berthe, R. Fabbro, P. Peyre, E. Bartnicki, Wavelength dependent of laser shock-wave generation in the water-confinement regime, J Appl Phys. 85 (1999) 7552–7555. https://doi.org/10.1063/1.370553.

[46] L. Petan, J.L. Ocaña, J. Grum, Influence of laser shock peening pulse density and spot size on the surface integrity of X2NiCoMo18-9-5 maraging steel, Surf Coat Technol. 307 (2016) 262–270. https://doi.org/10.1016/j.surfcoat.2016.08.088.

[47] Y. Hu, Z. Yao, Overlapping rate effect on laser shock processing of 1045 steel by small spots with

Nd:YAG pulsed laser, Surf Coat Technol. 202 (2008) 1517–1525. https://doi.org/10.1016/j.surfcoat.2007.07.008.

[48] Y. Sano, M. Obata, T. Kubo, N. Mukai, M. Yoda, K. Masaki, Y. Ochi, Retardation of crack initiation and growth in austenitic stainless steels by laser peening without protective coating, Materials Science and Engineering A. 417 (2006) 334–340. https://doi.org/10.1016/j.msea.2005.11.017.

[49] C. Rubio-González, C. Felix-Martinez, G. Gomez-Rosas, J.L. Ocaña, M. Morales, J.A. Porro, Effect of laser shock processing on fatigue crack growth of duplex stainless steel, Materials Science and Engineering A. 528 (2011) 914–919. https://doi.org/10.1016/j.msea.2010.10.020.

[50] S. Srinivasan, D.B. Garcia, M.C. Gean, H. Murthy, T.N. Farris, Fretting fatigue of laser shock peened Ti–6Al–4V, Tribol Int. 42 (2009) 1324–1329. https://doi.org/10.1016/J.TRIBOINT.2009.04.014.

[51] A.H. Clauer, D.F. Lahrman, Laser shock processing as a surface enhancement process, Key Eng Mater. 197 (2001) 121–142. https://doi.org/10.4028/www.scientific.net/kem.197.121.

[52] S. Spanrad, J. Tong, Characterisation of foreign object damage (FOD) and early fatigue crack growth in laser shock peened Ti–6Al–4V aerofoil specimens, Materials Science and Engineering: A. 528 (2011) 2128–2136. https://doi.org/10.1016/J.MSEA.2010.11.045.

[53] T. Joshua Spradlin, T. Joshua, Process Sequencing for Fatigue Life Extension of Large Scale Process Sequencing for Fatigue Life Extension of Large Scale Laser Peened Components Laser Peened Components Repository Citation Repository Citation, n.d. https://corescholar.libraries.wright.edu/etd_all://corescholar.libraries.wright.edu/etd_all/495.

[54] Y. WANG, X. PAN, X. WANG, Z. LIU, S. LIU, W. WAN, P. WANG, Influence of laser shock peening on surface integrity and tensile property of high strength low alloy steel, Chinese Journal of Aeronautics. 34 (2021) 199–208. https://doi.org/10.1016/J.CJA.2020.09.004.

[55] X. Meng, X. Leng, C. Shan, L. Zhou, J. Zhou, S. Huang, J. Lu, Vibration fatigue performance improvement in 2024-T351 aluminum alloy by ultrasonic-assisted laser shock peening, Int J Fatigue. 168 (2023) 107471. https://doi.org/10.1016/J.IJFATIGUE.2022.107471.

[56] G. Ivetic, I. Meneghin, E. Troiani, G. Molinari, J. Ocaña, M. Morales, J. Porro, A. Lanciotti, V. Ristori, C. Polese, J. Plaisier, A. Lausi, Fatigue in laser shock peened open-hole thin aluminium specimens, Materials Science and Engineering: A. 534 (2012) 573–579. https://doi.org/10.1016/J.MSEA.2011.12.010.

[57] Y. Sano, K. Masaki, T. Gushi, T. Sano, Improvement in fatigue performance of friction stir welded A6061-T6 aluminum alloy by laser peening without coating, Materials & Design (1980-2015). 36 (2012) 809–814. https://doi.org/10.1016/J.MATDES.2011.10.053.

[58] Y. Sano, T. Adachi, K. Akita, I. Altenberger, M.A. Cherif, B. Scholtes, K. Masaki, Y. Ochi, T. Inoue, Enhancement of Surface Property by Low-Energy Laser Peening without Protective Coating, Key Eng Mater. 345–346 (2007) 1589–1592. https://doi.org/10.4028/www.scientific.net/kem.345-346.1589.

[59] M.B. Toparli, M.E. Fitzpatrick, Residual stresses induced by laser peening of thin aluminium plates, in: Materials Science Forum, Trans Tech Publications Ltd, 2011: pp. 504–509. https://doi.org/10.4028/www.scientific.net/MSF.681.504.

[60] Y. Ta N, G. Wu, J.-M. Yang, T. Pan, Laser shock peening on fatigue crack growth behaviour of aluminium alloy The mechanical effects of a laser-induced shock wave have, n.d.

[61] C. Cellard, D. Retraint, M. François, E. Rouhaud, D. le Saunier, Laser shock peening of Ti-17 titanium alloy: Influence of process parameters, Materials Science and Engineering: A. 532 (2012) 362–372. https://doi.org/10.1016/J.MSEA.2011.10.104.

[62] S.Q. Jiang, J.Z. Zhou, Y.J. Fan, S. Huang, J.F. Zhao, Prediction on residual stress and fatigue life of magnesium alloy treated by laser shot peening, in: Materials Science Forum, Trans Tech Publications Ltd, 2009: pp. 393–398. https://doi.org/10.4028/www.scientific.net/MSF.626-627.393.

[63] O. Hatamleh, J. Lyons, R. Forman, Laser and shot peening effects on fatigue crack growth in friction stir welded 7075-T7351 aluminum alloy joints, Int J Fatigue. 29 (2007) 421–434. https://doi.org/10.1016/J.IJFATIGUE.2006.05.007.

[64] O. Hatamleh, A comprehensive investigation on the effects of laser and shot peening on fatigue crack growth in friction stir welded AA 2195 joints, Int J Fatigue. 31 (2009) 974–988. https://doi.org/10.1016/J.IJFATIGUE.2008.03.029.

[65] O. Hatamleh, R.S. Mishra, O. Oliveras, Peening effects on mechanical properties in friction stir welded AA 2195 at elevated and cryogenic temperatures, Mater Des. 30 (2009) 3165–3173. https://doi.org/10.1016/J.MATDES.2008.11.010.

[66] S. Wang, Y. Li, M. Yao, R. Wang, Compressive residual stress introduced by shot peening, J Mater

Process Technol. 73 (1998) 64–73. https://doi.org/10.1016/S0924-0136(97)00213-6.
[67] O. Unal, Optimization of shot peening parameters by response surface methodology, Surf Coat Technol. 305 (2016) 99–109. https://doi.org/10.1016/J.SURFCOAT.2016.08.004.
[68] M. Guagliano, Relating Almen intensity to residual stresses induced by shot peening: a numerical approach, J Mater Process Technol. 110 (2001) 277–286. https://doi.org/10.1016/S0924-0136(00)00893-1.
[69] H.Y. Miao, S. Larose, C. Perron, M. Levesque, An analytical approach to relate shot peening parameters to Almen intensity, Surf Coat Technol. 205 (2010) 2055–2066. https://doi.org/10.1016/J.SURFCOAT.2010.08.105.
[70] Modern Mechanical Surface Treatment States, Stability, Effects, n.d.
[71] R.C. McClung, A literature survey on the stability and significance of residual stresses during fatigue, Fatigue Fract Eng Mater Struct. 30 (2007) 173–205. https://doi.org/10.1111/j.1460-2695.2007.01102.x.
[72] M. Aghaie-Khafri, M. Amin, A.H. Momeni, Life assessment and life extension of an aircraft wheel, Advances in Mechanical Engineering. 2012 (2012). https://doi.org/10.1155/2012/326971.
[73] K.K. Liu, M.R. Hill, The effects of laser peening and shot peening on fretting fatigue in Ti–6Al–4V coupons, Tribol Int. 42 (2009) 1250–1262. https://doi.org/10.1016/J.TRIBOINT.2009.04.005.
[74] C.A. Rodopoulos, J.S. Romero, S.A. Curtis, E.R. de Los Rios, P. Peyre, Effect of Controlled Shot Peening and Laser Shock Peening on the Fatigue Performance of 2024-T351 Aluminum Alloy, 2024.
[75] U. Sánchez-Santana, C. Rubio-González, G. Gomez-Rosas, J.L. Ocaña, C. Molpeceres, J. Porro, M. Morales, Wear and friction of 6061-T6 aluminum alloy treated by laser shock processing, Wear. 260 (2006) 847–854. https://doi.org/10.1016/J.WEAR.2005.04.014.
[76] A.E. Hughes, N. Birbilis, J.M.C. Mol, S.J. Garcia, X. Zhou, G.E. Thompson, High Strength Al-Alloys: Microstructure, Corrosion and Principles of Protection, n.d. www.intechopen.com.
[77] A. Boag, A.E. Hughes, N.C. Wilson, A. Torpy, C.M. MacRae, A.M. Glenn, T.H. Muster, How complex is the microstructure of AA2024-T3?, Corros Sci. 51 (2009) 1565–1568. https://doi.org/10.1016/J.CORSCI.2009.05.001.
[78] E. McCafferty, Introduction to corrosion science, Springer New York, 2010. https://doi.org/10.1007/978-1-4419-0455-3.
[79] A. Eftekhari, Nanostructured materials in electrochemistry, Wiley-VCH, 2008.
[80] S.P. den Braver-Sewradj, J. van Benthem, Y.C.M. Staal, J. Ezendam, A.H. Piersma, E.V.S. Hessel, Occupational exposure to hexavalent chromium. Part II. Hazard assessment of carcinogenic effects, Regulatory Toxicology and Pharmacology. 126 (2021) 105045. https://doi.org/10.1016/J.YRTPH.2021.105045.
[81] M. García-Rubio, P. Ocón, A. Climent-Font, R.W. Smith, M. Curioni, G.E. Thompson, P. Skeldon, A. Lavía, I. García, Influence of molybdate species on the tartaric acid/sulphuric acid anodic films grown on AA2024 T3 aerospace alloy, Corros Sci. 51 (2009) 2034–2042. https://doi.org/10.1016/J.CORSCI.2009.05.034.
[82] A. Doublet, M. Kjellberg, B. Jousselme, M. Pinault, G. Deniau, R. Cornut, G. Charrier, Bifunctional coatings: Coupling an organic adhesion promoter with an anticorrosion inorganic layer, RSC Adv. 9 (2019) 24043–24049. https://doi.org/10.1039/c9ra03657a.
[83] D. Solé Verdaguer, ALTERNATIVE SURFACE TREATMENTS WITHOUT CHROMIUM CONTENT IN AERONAUTICAL ALUMINIUM ALLOYS Tartaric sulphuric anodising, n.d.
[84] Corrosion: Fundamentals, Testing, and Protection ASM INTERNATIONAL ® Publication Information and Contributors, n.d.
[85] E. Cirik, K. Genel, Effect of anodic oxidation on fatigue performance of 7075-T6 alloy, Surf Coat Technol. 202 (2008) 5190–5201. https://doi.org/10.1016/J.SURFCOAT.2008.06.049.
[86] E. Lee, Y. Jeong, S. Kim, S-N fatigue behavior of anodized 7050-t7451 produced in different electrolytes, Metall Mater Trans A Phys Metall Mater Sci. 43 (2012) 2002–2011. https://doi.org/10.1007/s11661-011-1044-x.
[87] R.G. Rateick, T.C. Binkowski, B.C. Boray, Effect of hard anodize thickness on the fatigue of AA6061 and C355 aluminium, 1996.
[88] R. Sadeler, Effect of a commercial hard anodizing on the fatigue property of a 2014-T6 aluminium alloy, J Mater Sci. 41 (2006) 5803–5809. https://doi.org/10.1007/s10853-006-0725-0.
[89] B. Lonyuk, I. Apachitei, J. Duszczyk, The effect of oxide coatings on fatigue properties of 7475-T6 aluminium alloy, Surf Coat Technol. 201 (2007) 8688–8694.

https://doi.org/10.1016/J.SURFCOAT.2006.02.002.

[90] G.W. Critchlow, D.M. Brewis, Review of surface pretreatments for aluminium alloys, Int J Adhes Adhes. 16 (1996) 255–275. https://doi.org/10.1016/S0143-7496(96)00014-0.

[91] G.W. Critchlow, K.A. Yendall, D. Bahrani, A. Quinn, F. Andrews, Strategies for the replacement of chromic acid anodising for the structural bonding of aluminium alloys, Int J Adhes Adhes. 26 (2006) 419–453. https://doi.org/10.1016/J.IJADHADH.2005.07.001.

[92] S.Y. Park, W.J. Choi, H.S. Choi, H. Kwon, S.H. Kim, Recent trends in surface treatment technologies for airframe adhesive bonding processing: A review (1995-2008), Journal of Adhesion. 86 (2010) 192–221. https://doi.org/10.1080/00218460903418345.

[93] G.D. Sulka, K.G. Parkoła, Temperature influence on well-ordered nanopore structures grown by anodization of aluminium in sulphuric acid, Electrochim Acta. 52 (2007) 1880–1888. https://doi.org/10.1016/J.ELECTACTA.2006.07.053.

[94] D.J. Arrowsmith, A.W. Clifford, Morphology of anodic oxide for adhesive bonding of aluminum, Int J Adhes Adhes. 3 (1983) 193–196. https://doi.org/10.1016/0143-7496(83)90093-3.

[95] M. Curioni, P. Skeldon, E. Koroleva, G.E. Thompson, J. Ferguson, Role of Tartaric Acid on the Anodizing and Corrosion Behavior of AA 2024 T3 Aluminum Alloy, J Electrochem Soc. 156 (2009) C147. https://doi.org/10.1149/1.3077602.

[96] M. Saenz de Miera, M. Curioni, P. Skeldon, G.E. Thompson, The behaviour of second phase particles during anodizing of aluminium alloys, Corros Sci. 52 (2010) 2489–2497. https://doi.org/10.1016/J.CORSCI.2010.03.029.

[97] T. Vignoli Machado, P. Atz Dick, G.H. Knörnschild, L.F.P. Dick, The effect of different carboxylic acids on the sulfuric acid anodizing of AA2024, Surf Coat Technol. 383 (2020) 125283. https://doi.org/10.1016/J.SURFCOAT.2019.125283.

[98] ASTM E837-13a, Standard Test Method for Determining Residual Stresses by the Hole-Drilling Strain-Gage Method, Standard Test Method E837-13a. (2013) 1–16.

[99] H. Leth-Olsen, J.H. Nordlien, K. Nisancioglu, Filiform corrosion of aluminium sheet. iii. microstructure of reactive surfaces, Corros Sci. 40 (1998) 2051–2063. https://doi.org/10.1016/S0010-938X(98)00094-8.

[100] R. Ambat, A.J. Davenport, A. Afseth, G. Scamans, Electrochemical Behavior of the Active Surface Layer on Rolled Aluminum Alloy Sheet, J Electrochem Soc. 151 (2004) B53. https://doi.org/10.1149/1.1635828.

[101] X. Zhou, Y. Liu, G.E. Thompson, G.M. Scamans, P. Skeldon, J.A. Hunter, Near-surface deformed layers on rolled aluminum alloys, Metall Mater Trans A Phys Metall Mater Sci. 42 (2011) 1373–1385. https://doi.org/10.1007/s11661-010-0538-2.

[102] Y. Ma, X. Zhou, G.E. Thompson, P. Skeldon, Surface texture formed on AA2099 Al–Li–Cu alloy during alkaline etching, Corros Sci. 66 (2013) 292–299. https://doi.org/10.1016/J.CORSCI.2012.09.032.

[103] D.J. Arrowsmith, D.A. Moth, C.M. Vickery, Etching aluminium for adhesive bonding, Transactions of the IMF. 66 (1988) 112–115. https://doi.org/10.1080/00202967.1988.11870819.

[104] Y. Suzuki, K. Kawahara, T. Kikuchi, R.O. Suzuki, S. Natsui, Corrosion-Resistant Porous Alumina Formed via Anodizing Aluminum in Etidronic Acid and Its Pore-Sealing Behavior in Boiling Water, J Electrochem Soc. 166 (2019) C261–C269. https://doi.org/10.1149/2.0221912jes.

[105] Y. Murakami, Metal fatigue: Effects of small defects and nonmetallic inclusions, 2019. https://doi.org/10.1016/C2016-0-05272-5.

[106] J. Lemaitre, R. Desmorat, Engineering damage mechanics: Ductile, creep, fatigue and brittle failures, 2005. https://doi.org/10.1007/b138882.

[107] U. Krupp, Fatigue Crack Propagation in Metals and Alloys: Microstructural Aspects and Modelling Concepts, 2007. https://doi.org/10.1002/9783527610686.

[108] J. Rösler, H. Harders, M. Bäker, Mechanical behaviour of engineering materials: Metals, ceramics, polymers, and composites, 2007. https://doi.org/10.1007/978-3-540-73448-2.

[109] DAVID OSMAN BUSSE, Extending Fatigue Life of Aircraft Fuselage Structures Using Laser-Peening, SCHOOL OF AEROSPACE, TRANSPORT AND MANUFACTURING, 2018.

[110] Norman E. Dowling, Mechanical Behavior of Materials: Engineering Methods for Deformation, Fracture, and Fatigue, 4th ed., 2013.

[111] S. Stanzl-Tschegg, Very high cycle fatigue measuring techniques, Int J Fatigue. 60 (2014) 2–17. https://doi.org/10.1016/j.ijfatigue.2012.11.016.

[112] B. Pyttel, D. Schwerdt, C. Berger, Very high cycle fatigue - Is there a fatigue limit?, Int J Fatigue. 33 (2011) 49–58. https://doi.org/10.1016/j.ijfatigue.2010.05.009.

[113] C. Li, S. Wu, J. Zhang, L. Xie, Y. Zhang, Determination of the fatigue P-S-N curves – A critical review and improved backward statistical inference method, Int J Fatigue. 139 (2020). https://doi.org/10.1016/j.ijfatigue.2020.105789.

[114] P. Strzelecki, T. Tomaszewski, Application of Weibull distribution to describe S-N curve with using small number specimens, AIP Conf Proc. 1780 (2016). https://doi.org/10.1063/1.4965939.

[115] J. Ling, J. Pan, A maximum likelihood method for estimating P-S-N curves, Int J Fatigue. 19 (1997) 415–419. https://doi.org/10.1016/S0142-1123(97)00037-6.

[116] W.D. Pilkey, D.F. Pilkey, Peterson's Stress Concentration Factors, Third Edition, 2008. https://doi.org/10.1002/9780470211106.

[117] N. MacGregor, C. W. & Grossman, Effects of Cyclic Loading on Mechanical Behavior of 24S-T4 and 75S-T6 Aluminum Alloys and SAE 4130 Steel, National Advisory Committee for Aeronautics,. (1952).

[118] H.M. Westergaard, Bearing Pressures and Cracks, J Appl Mech. 6 (1939) A49-53.

[119] Irwin G. R., Plastic zone near a crack and fracture toughness, in: 7th Sagamore Conf. 1960, 1960: pp. IV–63.

[120] F. Paris, P.C. and Erdogan, A Critical Analysis of Crack Propagation Laws, Journal of Basic Engineering. 85 (1963) 528-533.

[121] P.C. PARIS, Extensive Study of Low Fatigue Crack Growth Rates in A533 and A508 Steels, in: Proceedings of the 1971 National Symposium on Fracture Mechanics, 1971: pp. 141–176.

[122] P.J. Withers, Residual stress and its role in failure, Reports on Progress in Physics. 70 (2007) 2211–2264. https://doi.org/10.1088/0034-4885/70/12/R04.

[123] M. Beghini, L. Bertini, Fatigue crack propagation through residual stress fields with closure phenomena, Eng Fract Mech. 36 (1990) 379–387. https://doi.org/10.1016/0013-7944(90)90285-O.

[124] X.D. Ren, Y.K. Zhang, J.Z. Zhou, J.Z. Lu, L.C. Zhou, Influence of compressive stress on stress intensity factor of hole-edge crack by high strain rate laser shock processing, Mater Des. 30 (2009) 3512–3517. https://doi.org/10.1016/J.MATDES.2009.03.005.

[125] Y.K. Zhang, X.D. Ren, J.Z. Zhou, J.Z. Lu, L.C. Zhou, Investigation of the stress intensity factor changing on the hole crack subject to laser shock processing, Mater Des. 30 (2009) 2769–2773. https://doi.org/10.1016/J.MATDES.2008.09.033.

[126] D. Schnubel, N. Huber, Retardation of fatigue crack growth in aircraft aluminium alloys via laser heating – Numerical prediction of fatigue crack growth, Comput Mater Sci. 65 (2012) 461–469. https://doi.org/10.1016/J.COMMATSCI.2012.07.047.

[127] Y.E. Ma, P. Staron, T. Fischer, P.E. Irving, Size effects on residual stress and fatigue crack growth in friction stir welded 2195-T8 aluminium – Part I: Experiments, Int J Fatigue. 33 (2011) 1417–1425. https://doi.org/10.1016/J.IJFATIGUE.2011.05.006.

[128] G.S. Schajer, Relaxation Methods for Measuring Residual Stresses: Techniques and Opportunities, Exp Mech. 50 (2010) 1117–1127. https://doi.org/10.1007/s11340-010-9386-7.

[129] E.F. Rybicki, J.R. Shadley, W.S. Shealy, A consistent-splitting model for experimental residual-stress analysis, Exp Mech. 23 (1983) 438–446. https://doi.org/10.1007/bf02330061.

[130] N. Tebedge, G. Alpsten, L. Tall, Residual-stress measurement by the sectioning method - A procedure for residual-stress measurements by the sectioning method is described. Two different hole-drilling methods were performed and the results are compared, Exp Mech. 13 (1973) 88–96. https://doi.org/10.1007/BF02322389.

[131] R.G. Treuting, W.T. Read Jr., A mechanical determination of biaxial residual stress in sheet materials, J Appl Phys. 22 (1951) 130–134. https://doi.org/10.1063/1.1699913.

[132] S. Keil, EXPERIMENTAL DETERMINATION OF RESIDUAL STRESSES WITH THE RING-CORE METHOD AND AN ON-LINE MEASURING SYSTEM, Exp Tech. 16 (1992) 17–24. https://doi.org/10.1111/j.1747-1567.1992.tb00701.x.

[133] M.B. Prime, Cross-sectional mapping of residual stresses by measuring the surface contour after a cut, J Eng Mater Technol. 123 (2001) 162–168. https://doi.org/10.1115/1.1345526.

[134] G.S. Schajer, Practical Residual Stress Measurement Methods, 2013. https://doi.org/10.1002/9781118402832.

[135] D.C. Jiles, Review of magnetic methods for nondestructive evaluation, NDT International. 21 (1988) 311–319. https://doi.org/10.1016/0308-9126(88)90189-7.

[136] T. Leon-Salamanca, D.F. Bray, Residual stress measurement in steel plates and welds using critically

refracted longitudinal (LCR) Waves, Research in Nondestructive Evaluation. 7 (1996) 169–184. https://doi.org/10.1080/09349849609409576.

[137] J.G. Wong, A. K., Dunn, S. A., Sparrow, Residual stress measurement by means of the thermoelastic effect, Nature. 332 (1988) 613–615.

[138] M. Hetenyi, Handbook of experimental stress analysis, Wiley, New York, 1950.

[139] S.S. Chiang, D.B. Marshall, A.G. Evans, The response of solids to elastic/plastic indentation. I. Stresses and residual stresses, J Appl Phys. 53 (1982) 298–311. https://doi.org/10.1063/1.329930.

[140] ASTM E 837-01, Standard Test Method for Determining Residual Stresses by the Hole drilling Strain-Gauge Method, (2001).

[141] G.S. Schajer, Hole-drilling residual stress profiling with automated smoothing, J Eng Mater Technol. 129 (2007) 440–445. https://doi.org/10.1115/1.2744416.

[142] H. Wern, Measurement of non-uniform residual stresses using the hole drilling method, a new integral formalism, Strain. 31 (1995) 63–68. https://doi.org/10.1111/j.1475-1305.1995.tb00959.x.

[143] M. Scafidi, E. Valentini, B. Zuccarello, Error and uncertainty analysis of the residual stresses computed by using the hole drilling method, Strain. 47 (2011) 301–312. https://doi.org/10.1111/j.1475-1305.2009.00688.x.

[144] M. Beghini, L. Bertini, L.F. Mori, Evaluating non-uniform residual stress by the hole-drilling method with concentric and eccentric holes. Part II: Application of the influence functions to the inverse problem, Strain. 46 (2010) 337–346. https://doi.org/10.1111/j.1475-1305.2009.00684.x.

[145] J. Epp, X-ray diffraction (XRD) techniques for materials characterization, Materials Characterization Using Nondestructive Evaluation (NDE) Methods. (2016) 81–124. https://doi.org/10.1016/B978-0-08-100040-3.00004-3.

[146] N.S. Rossini, M. Dassisti, K.Y. Benyounis, A.G. Olabi, Methods of measuring residual stresses in components, Mater Des. 35 (2012) 572–588. https://doi.org/10.1016/J.MATDES.2011.08.022.

[147] Schajer Gary S., Practical residual stress measurement methods, 2013.

[148] C.E. Murray, Invariant x-ray elastic constants and their use in determining hydrostatic stress, J Appl Phys. 110 (2011). https://doi.org/10.1063/1.3667294.

[149] W. Guo, H. Wang, G. He, P. Peng, D. He, G. Han, J. Yan, Comparison of mechanical and corrosion properties of 7050 aluminum alloy after different laser shock peening, Opt Laser Technol. 151 (2022). https://doi.org/10.1016/j.optlastec.2022.108061.

[150] B. Sun, J. Zhao, H. Qiao, Y. Lu, Effects of square spot size and beam quality on residual stress of 7050 aluminum alloy by laser shock peening, Mater Chem Phys. 284 (2022). https://doi.org/10.1016/j.matchemphys.2022.126023.

[151] R. Sikhamov, F. Fomin, B. Klusemann, N. Kashaev, The influence of laser shock peening on fatigue properties of AA2024-T3 alloy with a fastener hole, Metals (Basel). 10 (2020). https://doi.org/10.3390/met10040495.

[152] J.P. Nobre, C. Polese, S.N. van Staden, Incremental Hole Drilling Residual Stress Measurement in Thin Aluminum Alloy Plates Subjected to Laser Shock Peening, Exp Mech. 60 (2020) 553–564. https://doi.org/10.1007/s11340-020-00586-5.

[153] Z. Kallien, S. Keller, V. Ventzke, N. Kashaev, B. Klusemann, Effect of laser peening process parameters and sequences on residual stress profiles, Metals (Basel). 9 (2019). https://doi.org/10.3390/met9060655.

[154] H. Gu, P. Yan, L. Jiao, S. Chen, Y. Song, S. Zou, X. Wang, Effect of laser shock peening on boring hole surface integrity and conformal contact fretting fatigue life of Ti-6Al-4 V alloy, Int J Fatigue. 166 (2023). https://doi.org/10.1016/j.ijfatigue.2022.107241.

[155] D. He, L. Li, J. Chi, H. Zhang, G. Zhang, G. He, J. Yan, H. Zhang, W. Guo, Gradient microstructure response in different phases of Ti<inf>2</inf>AlNb alloy with laser shock peening, Materials Science and Engineering A. 862 (2023). https://doi.org/10.1016/j.msea.2022.144497.

[156] W. Guo, Y. Zhang, H. Sun, H. Zhang, Y. Zhu, Microstructure evolution and fatigue properties subjected to optimized coverage areas of laser shock peened TB10 titanium alloy, Opt Laser Technol. 158 (2023). https://doi.org/10.1016/j.optlastec.2022.108851.

[157] D. He, L. Li, Y. Zhang, J. Chi, H. Zhang, R. Sun, Z. Che, H. Zhang, W. Guo, Gradient microstructure and fatigue properties of TC21 titanium alloy processed by laser shock peening, J Alloys Compd. 935 (2023). https://doi.org/10.1016/j.jallcom.2022.168139.

[158] L. Azevedo, N. Kashaev, C. Horstmann, V. Ventzke, C. Furtado, P.M.G.P. Moreira, P.J. Tavares, Fatigue behaviour of laser shock peened AISI D2 tool steel, Int J Fatigue. 165 (2022).

https://doi.org/10.1016/j.ijfatigue.2022.107226.
[159] C. Wang, K. Luo, J. Cai, J. Lu, Obvious improvement in electrochemical and long-term immersion corrosion resistance of AISI 420 martensitic stainless steel using laser shock peening, Corros Sci. 209 (2022). https://doi.org/10.1016/j.corsci.2022.110688.
[160] X. Chen, J. Sun, Z. Xu, J. Chen, Q. Jiang, Y. Li, J. Li, J. Cheng, Optimization of Laser Shock Process Parameters for 40Cr Steel, Coatings. 12 (2022). https://doi.org/10.3390/coatings12121872.
[161] D. Wang, J. Dang, Y. Li, Z. Liu, H. Wang, M. Chen, Study on the surface integrity distribution of 300M ultrahigh strength steel subjected to different surface modification treatments, Surf Coat Technol. 451 (2022). https://doi.org/10.1016/j.surfcoat.2022.129033.
[162] D. Furfari, U.C. Heckenberger, V. Holzinger, E. Hombergsmeier, J. Vignot, N. Ohrloff, Is the civil aerospace industry ready to implement laser shock peening into maintenance environment? questions to be answered and minimum requirements from aircraft manufacturer’s perspective, in: Lecture Notes in Mechanical Engineering, Springer, 2020: pp. 643–657. https://doi.org/10.1007/978-3-030-21503-3_52.
[163] D. Furfari, Laser shock peening to repair, design and manufacture current and future aircraft structures by residual stress engineering, in: Adv Mat Res, Trans Tech Publications, 2014: pp. 992–1000. https://doi.org/10.4028/www.scientific.net/AMR.891-892.992.
[164] S. Gencalp Irizalp, N. Saklakoglu, Laser peening of metallic materials, in: Comprehensive Materials Finishing, Elsevier Inc., 2017: pp. 408–440. https://doi.org/10.1016/B978-0-12-803581-8.09160-8.
[165] H. Kovacı, Y.B. Bozkurt, A.F. Yetim, M. Aslan, A. Çelik, The effect of surface plastic deformation produced by shot peening on corrosion behavior of a low-alloy steel, Surf Coat Technol. 360 (2019) 78–86. https://doi.org/10.1016/j.surfcoat.2019.01.003.
[166] H. Kovacı, Hacısalihoğlu, A.F. Yetim, A. Çelik, Effects of shot peening pre-treatment and plasma nitriding parameters on the structural, mechanical and tribological properties of AISI 4140 low-alloy steel, Surf Coat Technol. 358 (2019) 256–265. https://doi.org/10.1016/j.surfcoat.2018.11.043.
[167] S. Bagherifard, S. Slawik, I. Fernández-Pariente, C. Pauly, F. Mücklich, M. Guagliano, Nanoscale surface modification of AISI 316L stainless steel by severe shot peening, Mater Des. 102 (2016) 68–77. https://doi.org/10.1016/j.matdes.2016.03.162.
[168] A. Siddaiah, B. Mao, Y. Liao, P.L. Menezes, Surface characterization and tribological performance of laser shock peened steel surfaces, Surf Coat Technol. 351 (2018) 188–197. https://doi.org/10.1016/j.surfcoat.2018.07.087.
[169] X. Shen, P. Shukla, S. Nath, J. Lawrence, Improvement in mechanical properties of titanium alloy (Ti-6Al-7Nb) subject to multiple laser shock peening, Surf Coat Technol. 327 (2017) 101–109. https://doi.org/10.1016/j.surfcoat.2017.08.009.
[170] E. Maawad, H.G. Brokmeier, L. Wagner, Y. Sano, C. Genzel, Investigation on the surface and near-surface characteristics of Ti-2.5Cu after various mechanical surface treatments, Surf Coat Technol. 205 (2011) 3644–3650. https://doi.org/10.1016/j.surfcoat.2011.01.001.
[171] S. Zou, J. Wu, Y. Zhang, S. Gong, G. Sun, Z. Ni, Z. Cao, Z. Che, A. Feng, Surface integrity and fatigue lives of Ti17 compressor blades subjected to laser shock peening with square spots, Surf Coat Technol. 347 (2018) 398–406. https://doi.org/10.1016/j.surfcoat.2018.05.023.
[172] M.B. Toparli, M.E. Fitzpatrick, Residual stresses induced by laser peening of thin aluminium plates, Materials Science Forum. 681 (2011) 504–509. https://doi.org/10.4028/www.scientific.net/MSF.681.504.
[173] D. Glaser, C. Polese, R.D. Bedekar, J. Plaisier, S. Pityana, B. Masina, T. Mathebula, E. Troiani, Laser shock peening on a 6056-T4 aluminium alloy for airframe applications, in: Adv Mat Res, Trans Tech Publications, 2014: pp. 974–979. https://doi.org/10.4028/www.scientific.net/AMR.891-892.974.
[174] A. Salimianrizi, E. Foroozmehr, M. Badrossamay, H. Farrokhpour, Effect of Laser Shock Peening on surface properties and residual stress of Al6061-T6, Opt Lasers Eng. 77 (2016) 112–117. https://doi.org/10.1016/j.optlaseng.2015.08.001.
[175] M. Turski, S. Clitheroe, A.D. Evans, C. Rodopoulos, D.J. Hughes, P.J. Withers, Engineering the residual stress state and microstructure of stainless steel with mechanical surface treatments, Appl Phys A Mater Sci Process. 99 (2010) 549–556. https://doi.org/10.1007/s00339-010-5672-6.
[176] L. Petan, J.L. Ocaña, J. Grum, Influence of laser shock peening pulse density and spot size on the surface integrity of X2NiCoMo18-9-5 maraging steel, Surf Coat Technol. 307 (2016) 262–270. https://doi.org/10.1016/j.surfcoat.2016.08.088.
[177] H. Luong, M.R. Hill, The effects of laser peening and shot peening on high cycle fatigue in 7050-T7451

aluminum alloy, Materials Science and Engineering A. 527 (2010) 699–707. https://doi.org/10.1016/j.msea.2009.08.045.

[178] Y.K. Gao, Improvement of fatigue property in 7050-T7451 aluminum alloy by laser peening and shot peening, Materials Science and Engineering A. 528 (2011) 3823–3828. https://doi.org/10.1016/j.msea.2011.01.077.

[179] Y.F. Jiang, B. Ji, X.D. Gan, C. Hua, X. Li, H. Zhu, Study on the effect of laser peening with different power densities on fatigue life of fastener hole, Opt Laser Technol. 106 (2018) 311–320. https://doi.org/10.1016/j.optlastec.2018.04.025.

[180] M.B. Toparli, M.E. Fitzpatrick, Residual stresses induced by laser peening of thin aluminium plates, in: Materials Science Forum, Trans Tech Publications Ltd, 2011: pp. 504–509. https://doi.org/10.4028/www.scientific.net/MSF.681.504.

[181] ISO, BN EN ISO 4288:1998. Geometrical Product Specifications (GPS)- Surface texture: Profile method- Rules and procedures for the assessment of surface texture, Geometrical Product Specifications (GPS). (1998) 1–8. https://bsol-bsigroup-com.sheffield.idm.oclc.org/Bibliographic/BibliographicInfoData/000000000001345614.

[182] European Commitee for Standardization (2008) EN 15305:2008 E, Non-destructive Testing – Test Method for Residual Stress analysis by X-ray Diffraction, (2008).

[183] P. Peyre, R. Fabbro, P. Merrien, H.P. Lieurade, Laser shock processing of aluminium alloys. Application to high cycle fatigue behaviour, Materials Science and Engineering A. 210 (1996) 102–113. https://doi.org/10.1016/0921-5093(95)10084-9.

[184] H. Luong, M.R. Hill, The effects of laser peening and shot peening on high cycle fatigue in 7050-T7451 aluminum alloy, Materials Science and Engineering A. 527 (2010) 699–707. https://doi.org/10.1016/j.msea.2009.08.045.

[185] H. Luong, M.R. Hill, The effects of laser peening on high-cycle fatigue in 7085-T7651 aluminum alloy, Materials Science and Engineering A. 477 (2008) 208–216. https://doi.org/10.1016/j.msea.2007.05.024.

[186] A. Salimianrizi, E. Foroozmehr, M. Badrossamay, H. Farrokhpour, Effect of Laser Shock Peening on surface properties and residual stress of Al6061-T6, Opt Lasers Eng. 77 (2016) 112–117. https://doi.org/10.1016/j.optlaseng.2015.08.001.

[187] Y. Hu, Z. Yao, J. Hu, 3-D FEM simulation of laser shock processing, Surf Coat Technol. 201 (2006) 1426–1435. https://doi.org/10.1016/j.surfcoat.2006.02.018.

[188] S. Huang, J.Z. Zhou, J. Sheng, K.Y. Luo, J.Z. Lu, Z.C. Xu, X.K. Meng, L. Dai, L.D. Zuo, H.Y. Ruan, H.S. Chen, Effects of laser peening with different coverage areas on fatigue crack growth properties of 6061-T6 aluminum alloy, Int J Fatigue. 47 (2013) 292–299. https://doi.org/10.1016/j.ijfatigue.2012.09.010.

[189] X.C. Zhang, Y.K. Zhang, J.Z. Lu, F.Z. Xuan, Z.D. Wang, S.T. Tu, Improvement of fatigue life of Ti-6Al-4V alloy by laser shock peening, Materials Science and Engineering A. 527 (2010) 3411–3415. https://doi.org/10.1016/j.msea.2010.01.076.

[190] A. Umapathi, S. Swaroop, Residual Stress Distribution and Microstructure of a Multiple Laser-Peened Near-Alpha Titanium Alloy, J Mater Eng Perform. 27 (2018) 2466–2474. https://doi.org/10.1007/s11665-018-3336-4.

[191] P. Peyre, L. Berthe, X. Scherpereel, R. Fabbro, Laser-shock processing of aluminium-coated 55C1 steel in water-confinement regime, characterization and application to high-cycle fatigue behaviour, J Mater Sci. 33 (1998) 1421–1429. https://doi.org/10.1023/A:1004331205389.

[192] P. Mylavarapu, C. Bhat, M.K.R. Perla, K. Banerjee, K. Gopinath, T. Jayakumar, Identification of critical material thickness for eliminating back reflected shockwaves in laser shock peening – A numerical study, Opt Laser Technol. 142 (2021) 107217. https://doi.org/10.1016/j.optlastec.2021.107217.

[193] M.Z. Mubarok, Wahab, Sutarno, S. Wahyudi, Effects of Anodizing Parameters in Tartaric-Sulphuric Acid on Coating Thickness and Corrosion Resistance of Al 2024 T3 Alloy, Journal of Minerals and Materials Characterization and Engineering. 03 (2015) 154–163. https://doi.org/10.4236/jmmce.2015.33018.

[194] F. Campbell, Manufacturing Technology for Aerospace Structural Materials, 2006. https://doi.org/10.1016/B978-1-85617-495-4.X5000-8.

[195] D.S. Verdaguer, Alternative surface treatments without chromium content in aeronautical aluminium alloys, MSc thesis, 2015.

[196] G. Renna, P. Leo, G. Casalino, E. Cerri, Repairing 2024 Aluminum Alloy via Electrospark Deposition Process: A Feasibility Study, Advances in Materials Science and Engineering. 2018 (2018). https://doi.org/10.1155/2018/8563054.

[197] G. Renna, P. Leo, C. Casavola, Effect of ElectroSpark process parameters on the WE43 magnesium alloy deposition quality, Applied Sciences (Switzerland). 9 (2019) 1–14. https://doi.org/10.3390/app9204383.

[198] J. R. Davis, ASM Specialty Handbook: Aluminum and Aluminum Alloys, ASM International, 1993. http://www.asminternational.org/home/-/journal_content/56/10192/06610G/PUBLICATION/.

[199] D.A. Porter, K.E. Easterling, M.Y. Sherif, Phase transformations in metals and alloys, third edition, 2009.

[200] I. Polmear, D. st. John, J.F. Nie, M. Qian, Light Alloys: Metallurgy of the Light Metals: Fifth Ed., 2017.

[201] F. Snogan, C. Blanc, G. Mankowski, N. Pébère, Characterisation of sealed anodic films on 7050 T74 and 2214 T6 aluminium alloys, Surf Coat Technol. 154 (2002) 94–103. https://doi.org/10.1016/S0257-8972(01)01717-0.

[202] M.H. Setianto, A.A. Korda, Characterization of Tartaric-Sulphuric Acid Anodized 2024-T3 Aluminium Alloys with Anodizing Potential Variation, J Phys Conf Ser. 1204 (2019). https://doi.org/10.1088/1742-6596/1204/1/012039.

[203] F. MUSEUX, R. THEILMANN, Introducing more eco-efficient chemical treatments for aircraft structure, (2009). https://www.airbus.com/search.html?q=Introducing+more+eco-efficient+chemical+treatments+for+aircraft+structure#searchresult-document-all.

[204] S. Dhanish, G. Yoganandan, J.N. Balaraju, Development of TSA anodized/MnVO sealed coating using a statistical approach for Al 7075 alloy and a study of its corrosion behaviour, Surf Coat Technol. 402 (2020) 126316. https://doi.org/10.1016/j.surfcoat.2020.126316.

[205] V.R. Capelossi, M. Poelman, I. Recloux, R.P.B. Hernandez, H.G. de Melo, M.G. Olivier, Corrosion protection of clad 2024 aluminum alloy anodized in tartaric-sulfuric acid bath and protected with hybrid sol-gel coating, Electrochim Acta. 124 (2014) 69–79. https://doi.org/10.1016/j.electacta.2013.09.004.

[206] M. García-Rubio, M.P. de Lara, P. Ocón, S. Diekhoff, M. Beneke, A. Lavía, I. García, Effect of postreatment on the corrosion behaviour of tartaric-sulphuric anodic films, Electrochim Acta. 54 (2009) 4789–4800. https://doi.org/10.1016/j.electacta.2009.03.083.

[207] M. García-Rubio, P. Ocón, A. Climent-Font, R.W. Smith, M. Curioni, G.E. Thompson, P. Skeldon, A. Lavía, I. García, Influence of molybdate species on the tartaric acid/sulphuric acid anodic films grown on AA2024 T3 aerospace alloy, Corros Sci. 51 (2009) 2034–2042. https://doi.org/10.1016/j.corsci.2009.05.034.

[208] E. Harscoet, D. Froelich, Use of LCA to evaluate the environmental benefits of substituting chromic acid anodizing (CAA), J Clean Prod. 16 (2008) 1294–1305. https://doi.org/10.1016/j.jclepro.2007.06.010.

[209] J. sheng Zhang, X. hui Zhao, Y. Zuo, J. ping Xiong, The bonding strength and corrosion resistance of aluminum alloy by anodizing treatment in a phosphoric acid modified boric acid/sulfuric acid bath, Surf Coat Technol. 202 (2008) 3149–3156. https://doi.org/10.1016/j.surfcoat.2007.10.041.

[210] M. Chaussumier, C. Mabru, M. Shahzad, R. Chieragatti, F. Rezai-Aria, A predictive fatigue life model for anodized 7050 aluminium alloy, Int J Fatigue. 48 (2013) 205–213. https://doi.org/10.1016/j.ijfatigue.2012.11.002.

[211] M. Shahzad, M. Chaussumier, R. Chieragatti, C. Mabru, F. Rezai-Aria, Surface characterization and influence of anodizing process on fatigue life of Al 7050 alloy, Mater Des. 32 (2011) 3328–3335. https://doi.org/10.1016/j.matdes.2011.02.027.

[212] E. Lee, Y. Jeong, S. Kim, S-N fatigue behavior of anodized 7050-t7451 produced in different electrolytes, Metall Mater Trans A Phys Metall Mater Sci. 43 (2012) 2002–2011. https://doi.org/10.1007/s11661-011-1044-x.

[213] J.A.M. de Camargo, H.J. Cornelis, V.M.O.H. Cioffi, M.Y.P. Costa, Coating residual stress effects on fatigue performance of 7050-T7451 aluminum alloy, Surf Coat Technol. 201 (2007) 9448–9455. https://doi.org/10.1016/j.surfcoat.2007.03.032.

[214] N. Li, H. Li, J. Zhou, H. Liu, C. Liu, S. Qu, Influence of different surface treatments on fatigue life of 7050 Al alloy, Materials Science Forum. 944 MSF (2018) 142–148. https://doi.org/10.4028/www.scientific.net/MSF.944.142.

[215] B. Hadzima, F. Nový, L. Trško, F. Pastorek, M. Jambor, S. Fintová, Shot peening as a pre-treatment to anodic oxidation coating process of AW 6082 aluminum for fatigue life improvement, International

Journal of Advanced Manufacturing Technology. 93 (2017) 3315–3323. https://doi.org/10.1007/s00170-017-0776-1.

[216] British Standards Institution, European Committee for Standardization, BS EN 6072 : 2010 BSI Standards Publication Aerospace series — Metallic materials — Test methods — Constant amplitude fatigue testing, (2010).

[217] J. hua Liu, M. Li, S. mei Li, M. Huang, Effect of the microstructure of Al 7050-T7451 on anodic oxide formation in sulfuric acid, International Journal of Minerals, Metallurgy and Materials. 16 (2009) 432–438. https://doi.org/10.1016/S1674-4799(09)60076-5.

[218] L.E. Fratila-Apachitei, H. Terryn, P. Skeldon, G.E. Thompson, J. Duszczyk, L. Katgerman, Influence of substrate microstructure on the growth of anodic oxide layers, Electrochim Acta. 49 (2004) 1127–1140. https://doi.org/10.1016/j.electacta.2003.10.024.

[219] C. Fares, L. Hemmouche, M.A. Belouchrani, A. Amrouche, D. Chicot, E.S. Puchi-Cabrera, Coupled effects of substrate microstructure and sulphuric acid anodizing on fatigue life of a 2017A aluminum alloy, Mater Des. 86 (2015) 723–734. https://doi.org/10.1016/j.matdes.2015.07.120.

[220] T.P. Savas, J.C. Earthman, Fatigue crack nucleation studies on sulfuric acid anodized 7075-T73 aluminum, J Mater Eng Perform. 23 (2014) 2131–2138. https://doi.org/10.1007/s11665-014-1000-1.

[221] L. Hemmouche, C. Fares, M.A. Belouchrani, Influence of heat treatments and anodization on fatigue life of 2017A alloy, Eng Fail Anal. 35 (2013) 554–561. https://doi.org/10.1016/j.engfailanal.2013.05.003.

[222] K. Chanyathunyaroj, W. Samit, C. Poonthananiwatkul, S. Phetchcrai, Effect of Coatings on the Mechanical Properties and Fatigue Life of 6061 Aluminum Alloys, Transactions of the Indian Institute of Metals. 74 (2021) 2135–2147. https://doi.org/10.1007/s12666-021-02296-5.

[223] G. Patton, C. Rinaldi, Y. Bréchet, G. Lormand, R. Fougères, Study of fatigue damage in 7010 aluminum alloy, Materials Science and Engineering: A. 254 (1998) 207–218. https://doi.org/10.1016/S0921-5093(98)00762-X.

[224] B. Nie, Z. Zhang, Z. Zhao, Q. Zhong, Effect of anodizing treatment on the very high cycle fatigue behavior of 2A12-T4 aluminum alloy, Mater Des. 50 (2013) 1005–1010. https://doi.org/10.1016/j.matdes.2013.03.083.

[225] P. Dai, X. Luo, Y. Yang, Z. Kou, B. Huang, J. Zang, J. Ru, The Fracture Behavior of 7085-T74 Al Alloy Ultra-Thick Plate During High Cycle Fatigue, Metall Mater Trans A Phys Metall Mater Sci. 51 (2020) 3248–3255. https://doi.org/10.1007/s11661-020-05759-4.

[226] A. Vasu, R. v. Grandhi, Effects of curved geometry on residual stress in laser peening, Surf Coat Technol. 218 (2013) 71–79. https://doi.org/10.1016/J.SURFCOAT.2012.12.029.

[227] G. Xu, H. Lu, K. Luo, F. Dai, J. Lu, Effects of surface curvature on residual stress field of 316L stainless steel subjected to laser shock peening, Opt Laser Technol. 144 (2021) 107420. https://doi.org/10.1016/J.OPTLASTEC.2021.107420.

[228] S.D. Cuellar, M.R. Hill, A.T. Dewald, J.E. Rankin, Residual stress and fatigue life in laser shock peened open hole samples, Int J Fatigue. 44 (2012) 8–13. https://doi.org/10.1016/J.IJFATIGUE.2012.06.011.

[229] A.T. Dewald, M.R. Hill, Eigenstrain-based model for prediction of laser peening residual stresses in arbitrary three-dimensional bodies. Part 1: Model description, Journal of Strain Analysis for Engineering Design. 44 (2009) 1–11. https://doi.org/10.1243/03093247JSA417.

[230] A.T. Dewald, M.R. Hill, Eigenstrain-based model for prediction of laser peening residual stresses in arbitrary three-dimensional bodies. Part 2: Model verification, Journal of Strain Analysis for Engineering Design. 44 (2009) 13–27. https://doi.org/10.1243/03093247JSA420.

[231] S. Coratella, M. Sticchi, M.B. Toparli, M.E. Fitzpatrick, N. Kashaev, Application of the eigenstrain approach to predict the residual stress distribution in laser shock peened AA7050-T7451 samples, Surf Coat Technol. 273 (2015) 39–49. https://doi.org/10.1016/J.SURFCOAT.2015.03.026.

[232] P. Li, S. Huang, H. Xu, Y. Li, X. Hou, Q. Wang, W. Fu, Y. Fang, Numerical simulation and experiments of titanium alloy engine blades based on laser shock processing, Aerosp Sci Technol. 40 (2015) 164–170. https://doi.org/10.1016/J.AST.2014.10.017.